A single-cell genomic based investigation of immune cells in the aorta and adipose tissue during metabolic disease progression

Yasemin-Xiomara Zurke

Kennedy Institute of Rheumatology

St Edmund Hall

University of Oxford



A thesis submitted for the degree of Doctor of Philosophy in Cardiovascular Science

Hilary Term 2023

Abstract

Metabolic diseases such as obesity, type 2 diabetes and atherosclerosis are characterised by chronic inflammation that leads to the accumulation of immune cells in affected organs like the adipose tissue and arteries. Macrophages in the obese adipose tissue and the atherosclerotic plaque show transcriptional, phenotypic and functional heterogeneity. The accumulation of $CD11c^+$ macrophages has been associated with both atherosclerosis and obesity progression, suggesting the presence of conserved macrophage phenotypes in metabolic tissues. This thesis aimed to 1) characterise shared and distinct features of monocytes and macrophages in the aorta and adipose tissue in the context of metabolic disease 2) investigate the role of the transcription factor IRF5 on the modulation of myeloid phenotype in both diseases. Both aims were addressed using single-cell techniques.

Single-cell RNA sequencing of chimeric mice during a time course of metabolic disease progression and data integration with non-irradiated community datasets demonstrated that resident macrophages in the adipose tissue could be replenished by monocyte-derived macrophages, while the perturbation of the vascular macrophage niche via irradiation resulted in transcriptional activation of macrophages and loss of some of the bona fide transcriptional features of vascular resident macrophages. Integrated analysis of the aortic and adipose tissue mononuclear phagocyte compartments revealed that resident macrophages in the aorta and adipose tissue display tissue-specific transcriptional programs. Although vascular resident $Folr2^+Lyve1^+$ macrophages were identifiable also within the adipose tissue, the majority of resident adipose tissue macrophages expressed genes associated with lipid metabolism, cell adhesion and proliferation, highlighting that cell maintenance and function of tissue resident macrophages differ between the aorta and adipose tissue.

In my analysis, two $CD11c^+$ macrophage subsets were identified according to their expression of CD226 and CD63/TREM2 using both scRNAseq and CyTOF. $CD11c^+$ macrophage subsets were conserved across multiple metabolic disease models and shared transcriptional signatures between metabolic tissues. In disease, $CD11c^+Trem2^{hi}$ foamy macrophages expanded in the aorta and the adipose tissue, while $CD11c^+CD226^+$ macrophages did not. The transcription factor IRF5, a potential regulator of $CD11c^+$ macrophages in metabolic disease, has been shown to induce atherosclerotic lesion formation and insulin resistance in experimental models of atherosclerosis and obesity. IRF5 promoted expansion of $Trem2^{hi}$ macrophages in the aorta in chimeras, but not in the adipose tissue, further highlighting that tissue niche affects macrophage activation and transcriptional regulation patterns.

In conclusion, macrophages in the adipose tissue and atherosclerotic aorta show both conserved and tissue specific transcriptional phenotypes and dynamics in response to genotoxic damage and during metabolic disease progression. Understanding similarities and differences between the two tissues will be important to inform identification of new therapeutic targets for cardiometabolic diseases.

Acknowledgements

My DPhil experience in Oxford was an incredible adventure and I am grateful for everyone who was part of my journey and supported me during the past five years in and out of the lab.

First and foremost, I would like to thank my supervisors Prof Claudia Monaco, Dr Stephen Sansom and Dr Lea Dib. Your scientific guidance and continuous support throughout the project have been invaluable. Claudia – thank you for the opportunity to pursue my DPhil in the Monaco lab, and for providing the space and encouragement to grow as a scientist and person. Steve – thank you for the opportunity to join the Sansom lab and for supporting me on my journey to become a bioinformatician. Lea – you found the right encouragement and advice in every situation; I admire your optimism and will always be grateful for not having to filter my thoughts and emotions around you.

I would also like to thank all present and past members of the Monaco and Sansom Labs for being amazing colleagues and for creating a warm, supportive and inspiring atmosphere. In particular, I would like to thank Dr Inhye Park for supporting and teaching me in the lab, for her great scientific advice, and for being a good friend. I wouldn't want to miss the many hours we spent talking in the BSU, or during lunch and coffee breaks. I would also like to thank Dr Suzanne Engelen and Alice Robinson, I am forever grateful for sharing the DPhil experience with you – being 1 of 3 musketeers made all the ups of it even higher and all the lows much more COPEable. I am proud of each of our journeys and cannot wait for many reunions in the future.

My DPhil would not have been the same without the people who made Oxford my home. Agata, you truly are family to me, not only because we merged into an old married couple during our four years in RHC, but also because I know I can depend on you no matter what – I am beyond grateful to have you in my life. Carolina, I am not sure what I would have done without you and the hours we spent walking and talking and finding balance in stressful times. The rest of the Teddy Hall crew: Jules, Charlie, Marc and Tom, I am happy to call you my friends and can't wait to make new memories with you all around the world. Lucy, Flavia, Clelia, Mev, Kadi and Michelle, you made our house a home. It's a privilege to be your friend and the last year would have been a lot more difficult without you.

Finally, I would like to thank my family for the infinite love and support through every moment in life. You helped me to grow into the person that I am today, and without you my DPhil journey would not have been possible. I would like to especially thank my parents, Anke and Thomas, my siblings Josephine, Laura and Johannes, and my grandma Gisela. Thank you for the constant encouragement to pursue my dreams even when I was and still am doubting myself. Thank you for uncountable phone calls, always listening and unconditional support from afar. Your support means the world to me. Danke!

Table of Contents

Chapter 1. Introduction 9

1.1. Introduction to metabolic diseases 9

1.2. The pathophysiology of atherosclerosis 10

1.3. The pathophysiology of obesity 11

1.4. Immune cells in the aorta and adipose tissue 13
1.4.1. T lymphocytes 13
1.4.2. Mononuclear phagocytes 15
1.4.2.1. Dendritic cells 15
1.4.2.2. Monocytes 15
1.4.2.3. Macrophages 16

1.5. The transcription factor IRF5 19

1.6. Hypothesis and aims 20

Chapter 2. A single-cell atlas of the aorta and adipose tissue during metabolic disease progression 22

2.1. Introduction 22

2.2. Generation of a scRNAseq dataset of the aorta and epididymal white adipose tissue during metabolic disease progression and analysis strategy 24

2.3. Defining the aortic immune cell landscape of mixed bone marrow chimeras during metabolic disease progression using scRNAseq 27
2.3.1. Defining the T and NK cell landscape in the aorta using scRNAseq 31
2.3.2. Defining the myeloid landscape in the aorta using scRNAseq 35
2.3.2.1. Validation of clusters identified in the aorta of mixed bone marrow chimeras using published scRNAseq datasets 42

2.4. Defining the epididymal white adipose tissue immune cell landscape of mixed bone marrow chimeras during metabolic disease progression using scRNAseq 50
2.4.1. Defining the T and NK cell landscape in the epididymal white adipose tissue using scRNAseq 54
2.4.2. Defining the MNP landscape in the epididymal white adipose tissue using scRNAseq 57
2.4.2.1. Validation of clusters identified in the epididymal white adipose tissue of mixed bone marrow chimeras using published scRNAseq datasets 62

2.5. Discussion 68

Chapter 3. Comparison of the immune cell landscapes of the aorta and the adipose tissue using scRNAseq and CyTOF 74

3.1. Introduction 74

3.2. Comparison of T cells 77
3.2.1. A combined T and NK cell atlas of the aorta and epididymal white adipose tissue during metabolic disease progression 77
3.2.2. T cell exhaustion is a shared feature of metabolic disease progression in the aorta and epididymal white adipose tissue 78

3.3. Comparison of myeloid cells 82
3.3.1. A combined myeloid cells atlas of the aorta, epididymal white adipose tissue and blood during metabolic disease progression 82
3.3.2. Dendritic cells 85
3.3.3. Monocytes 85
3.3.4. Macrophages 91
3.3.4.1. Resident macrophages in the adipose tissue distinctly express CCR2 93
3.3.4.2. *Itgax*$^{+}$ macrophages share transcriptional features in the aorta and epididymal white adipose tissue 97

3.4. Discussion 101

Chapter 4. The role of IRF5 in shaping monocyte and macrophage heterogeneity during metabolic disease progression. 105

4.1. Introduction 105

4.2. IRF5 deficiency affects age dependent myelopoiesis 106

4.3. IRF5 promotes accumulation of disease associated CD11c$^+$CD63$^+$ macrophages in the aorta 113

4.4. Discussion 116

Chapter 5. Discussion 118

5.1. The aortic and adipose tissue Folr2$^+$ macrophage pools display divergent tissue specific transcriptional programs 119

5.2. CD11c$^+$ macrophages in the aorta and adipose tissue share fundamental transcriptional signatures but display differential regulation by IRF5 122

5.3. Future directions 124

Chapter 6. Materials and Methods 126

6.1. Maintenance and breeding of mice 126

6.2. Genotyping 126
6.2.1. DNA extraction and polymerase chain reaction (PCR) 126
6.2.2. Blood sampling and flow cytometry 127

6.3. In vivo experimental procedures 128
6.3.1. Competitive mixed bone marrow chimeras (MBMC) 128
6.3.2. Non-Competitive bone marrow chimeras (BMC) 128
6.3.3. Glucose tolerance testing 128

6.4. Single cell dissociation of murine tissues 129
6.4.1. Bone marrow 129
6.4.2. Blood leukocytes 129
6.4.3. Aorta 129
6.4.4. Adipose tissue 130

6.5. Flow cytometry 131

6.6. In vitro experimental procedures 132
6.6.1. Bone marrow derived macrophages 132
6.6.2. Apoptosis Assay 132
6.6.3. Proliferation Assay 132

6.7. Single-cell RNA sequencing of mixed competitive bone marrow chimeras 133
6.7.1. Sample preparation 133
6.7.2. Data analysis strategy 136
6.7.3. Quality control and draft analysis 136
6.7.4. Resolving the immune cell landscape of the aorta and epididymal white adipose tissue. 140
6.7.5. Comparison of the MNP landscapes of the aorta and epididymal white adipose tissue with community datasets 143
6.7.6. Cross-tissue integration of the aorta, epididymal white adipose tissue and blood 144
6.7.7. Differential gene expression within clusters 144
6.7.8. Composition analysis 145
6.7.8.1. Cell density plots 145
6.7.8.2. scCODA 145
6.7.9. Pseudotime analysis 145
6.7.9.1. scVelo 145
6.7.9.2. Preprocessing 145
6.7.9.3. Velocity computation 146
6.7.10. cellrank 146
6.7.11. Slingshot 146

6.8. Mass cytometry 147
6.8.1. Sample preparation 147
6.8.2. Data Analysis 149

Appendix A **Supplemental data** 150

Appendix B **Abbreviations** 174

Appendix C **List of Publications** 176

Appendix D **Bibliography** 177

List of Figures

Figure 2.1: **Generation of a scRNAseq dataset of the aorta, epiWAT and blood during metabolic disease progression.** 25

Figure 2.2: **Defining the aortic immune cell landscape of mixed bone marrow chimeras (MBMCs) in metabolic disease using scRNAseq.** 29

Figure 2.3: **Defining the aortic immune cell landscape of mixed bone marrow chimeras (MBMCs) in metabolic disease using CyTOF** 30

Figure 2.4: **The single-cell landscape of mature T and NK cells in the aorta of mixed bone marrow chimeras (MBMCs).** 33

Figure 2.5: **The single-cell mononuclear phagocyte landscape in the aorta of mixed bone marrow chimeras (MBMCs).** 38

Figure 2.6: **The single-cell landscape of macrophages in the aorta of mixed bone marrow chimeras (MBMCs).** 40

Figure 2.7: **Integrated analysis of 7 scRNAseq studies of the aorta**. 43

Figure 2.8: **Comparison of aortic macrophage cluster composition between mixed bone marrow chimeras (MBMCs) and community datasets.** 46

Figure 2.9: **Trajectory analysis of aortic mononuclear phagocyte clusters in mixed bone marrow chimeras (MBMCs) and community datasets at steady state and in disease.** 49

Figure 2.10: **Defining the epiWAT immune cell landscape of mixed bone marrow chimeras (MBMCs) in metabolic disease using scRNAseq.** 52

Figure 2.11: **Defining the epiWAT immune cell landscape of mixed bone marrow chimeras (MBMCs) in metabolic disease using CyTOF.** 53

Figure 2.12: **The single-cell landscape of mature T and NK cells in the epiWAT of mixed bone marrow chimeras (MBMCs).** 56

Figure 2.13: **The single-cell mononuclear phagocyte landscape in the epiWAT of mixed bone marrow chimeras (MBMCs).** 58

Figure 2.14: **The single-cell landscape of macrophages in the epiWAT of mixed bone marrow chimeras (MBMCs).** 60

Figure 2.15: **Integrated analysis of 4 scRNAseq studies of the epiWAT.** 64

Figure 2.16: **Comparison of epiWAT macrophage cluster composition between mixed bone marrow chimeras (MBMCs) and community datasets.** 66

Figure 2.17: **Trajectory analysis of epiWAT mononuclear phagocyte clusters in mixed bone marrow chimeras (MBMCs) and community datasets at steady state and in disease.** 67

Figure 3.1: **A combined T cell atlas of the aorta and epiWAT from mixed bone marrow chimeras (MBMCs) during metabolic disease progression.** 80

Figure 3.2: **T cells in the aorta and epiWAT acquire exhaustion marker expression during metabolic disease progression.** 81

Figure 3.3: **A combined mononuclear phagocyte atlas of the aorta and epiWAT from mixed bone marrow chimeras (MBMCs) during metabolic disease progression** 84

Figure 3.4: **The combined single-cell landscape of monocytes in the aorta, epiWAT and blood using scRNAseq.** 87

Figure 3.5 **Monocytes transcriptionally adapt to the aorta and epiWAT microenvironments.** 90

Figure 3.6: **The combined single-cell landscape of macrophages in the aorta and epiWAT of mixed bone marrow chimeras (MBMCs) using scRNAseq.** 92

Figure 3.7: **Resident macrophages in the aorta and epiWAT show tissue specific transcriptomes.** .. 95

Figure 3.8: **Resident macrophages in the adipose tissue distinctly express CCR2**. 97

Figure 3.9: **Two distinct CD11c^{+} macrophage populations can be identified in the aorta and epiWAT using scRNAseq and CyTOF.** 98

Figure 3.10 **Macrophage dynamics in the aorta and epiWAT using scRNAseq and CyTOF.** 100

Figure 4.1: **Myeloid WT cells outcompete IRF5$^{-/-}$ cells 20 weeks after bone marrow transfer in the blood, aorta and epiWAT.** 108

Figure 4.2: **WT cells and IRF5$^{-/-}$ cells equally reconstitute the bone marrow of mixed bone marrow chimera.** 110

Figure 4.3: **WT cells outcompete IRF5$^{-/-}$ bone marrow derived cells in vitro.** 112

Figure 4.4: **IRF5 deficiency does not affect monocyte maturation to Ly6C^{lo} monocytes or monocyte-derived macrophages in the blood, epiWAT or aorta.** 113

Figure 4.5: **IRF5 promotes expansion of disease associated CD11c^{+}CD63^{+} macrophages in the atherosclerotic aorta**. 115

Figure 6.1: **Representative sorting strategies for single-cell RNA sequencing analysis.** 134

Figure 6.2: **Scatter plot of number of genes and. % mitochondrial reads per sample coloured by % mitochondrial reads. Quality control filtering thresholds are indicated using red dotted lines.** 138

Figure 6.3: **Overview of cell numbers and quality control metrics of scRNAseq samples.** 139

Figure 6.4: **Subsetting of and reclustering of mature T cells in the aorta.** 141

Figure 6.5: **Merging strategy of aortic mononuclear phagocyte (MNP) clusters.**..... 142

Figure S 1: **Overrepresented gene sets in macrophage subsets identified in the aorta of mixed bone marrow chimeras (MBMCs).**..... 151

Figure S 2: **The single-cell landscape of monocytes and dendritic cells in the aorta of mixed bone marrow chimeras (MBMCs).**..... 152

Figure S 3: **Additional aortic mononuclear phagocyte marker genes**..... 153

Figure S 4: **Comparison of aortic myeloid clusters identified in analysis of mixed bone marrow chimeras (MBMCS) and integrated analysis with community aortic datasets.**..... 154

Figure S 5: **Differential gene expression analysis between aortic macrophages clusters from mixed bone marrow chimeras (MBMCS) and community datasets.** 155

Figure S 6: **The single-cell landscape of monocytes and dendritic cells in the epiWAT of mixed bone marrow chimeras (MBMCs).**..... 156

Figure S 7: **Additional epiWAT mononuclear phagocyte marker genes**. 157

Figure S 8: **Comparison of epiWAT myeloid clusters identified in analysis of mixed bone marrow chimeras (MBMCs) and integrated analysis with community epiWAT datasets.**..... 158

Figure S 9: **Differential gene expression analysis between epiWAT macrophages clusters from MBMCS and community datasets.**..... 159

Figure S 10: **Analysis strategy of combined T cell atlas of the aorta and epiWAT during metabolic disease progression.**..... 160

Figure S 11: **Cluster composition per sample of mononuclear phagocyte clusters identified in combined analysis of blood, aorta and epiWAT and additional cluster marker genes for monocytes and macrophages.** 162

Figure S 12: **The combined single-cell landscape of dendritic cells of the aorta and epiWAT using scRNAseq.**..... 163

Figure S 13: **Differential gene expression between monocytes of the aorta, epiWAT and blood at steady state and 12 w WD.** 164

Figure S 14**: Comparison of macrophage clusters identified in separate analysis of the aorta and epiWAT to integrated analysis of aorta, epiWAT and blood.** 165

Figure S 15: **Identification of Trem2^{hi} and Ccr2^{+}Cd226^{+} macrophages in publicly available scRNAseq datasets from the aorta and epiWAT.**..... 168

Figure S 16: **Composition of WT and IRF5$^{-/-}$ macrophage clusters identified in combined analysis of the aorta and epiWAT of mixed bone marrow chimera during metabolic disease progression.**..... 169

Figure S 17: **Representative gating strategy for the myeloid populations in the blood of MBMCs.** 170

Figure S 18: **Representative gating strategies for myeloid progenitors in the bone marrow.**..... 171

List of Tables

Table 2.1: Overview of samples included to define the aortic immune cell, T/NK and mononuclear phagocyte landscapes during metabolic disease progression. 27

Table 2.2: Overview of samples included to define the epididymal white adipose immune cell and mononuclear phagocyte landscapes during metabolic disease progression. 50

Table 2.3: Overview of samples included to define the epididymal white adipose tissue T and NK cells landscapes during metabolic disease progression. 54

Table 3.1 Overview of samples included to define the integrated aortic and epididymal white adipose tissue T and NK cells landscape during metabolic disease progression. 77

Table 3.2 Overview of samples included to define the integrated aortic and epididymal white adipose tissue mononuclear phagocyte landscape. 82

Table 6.1: PCR primers used for genotyping. 127

Table 6.2: PCR run parameters for genotyping. 127

Table 6.3: List of antibodies used for flow cytometry. 131

Table 6.4: Overview of single-cell RNA sequencing samples and corresponding cellranger outputs. 135

Table 6.5: Analysis parameters for sub analysis per tissue. 143

Table 6.6: List of CyTOF antibodies. 148

Table S 1: Gene set overrepresentation analysis of differentially expressed genes between Folr2^{+} macrophages of the aorta and epiWAT at steady state. 166

Table S 2: Gene set overrepresentation analysis of differentially expressed genes between Folr2^{+} macrophages of the aorta and epiWAT at 12w WD. 167

Table S 3: Overview of community datasets. 173

Chapter 1. Introduction

1.1. Introduction to metabolic diseases

Cardiovascular disease (CVD) is the leading cause of death in the western world[1]. Metabolic syndrome describes a cluster of conditions including obesity, insulin resistance, hypercholesterolaemia and high blood pressure that often coexist, all of them contributing to the continuously increasing burden of CVD[2,3]. The prevalence of obesity has risen significantly over the past three decades in adults and children leading to an increased incidence of type 2 diabetes (T2D) and CVD[4]. Both obesity and atherosclerosis, are multifactorial chronic inflammatory diseases that share common pathophysiological pathways. Research over the past decades has determined a detrimental role of inflammation as a driver of obesity, insulin resistance and atherosclerosis[5,6]. The accumulation of immune cells, and especially macrophages, in both the adipose tissue and the intimal space of arteries is a hallmark of obesity-associated insulin resistance and atherosclerosis, respectively. Currently, treatment strategies for atherosclerosis predominantly depend on surgical interventions or aim at targeting risk factors like hypercholesteremia through low density lipoprotein (LDL)-cholesterol-lowering[7,8]. The CANTOS trial[9], for the first time, demonstrated that targeting inflammation in cardiovascular disease could be beneficial. In addition, the anti-inflammatory drug colchicine reduced cardiovascular events in patients with chronic coronary artery disease[10] and recent myocardial infarction[11], highlighting that targeting inflammation in cardiovascular disease could be a viable approach to target the remaining CVD burden.

Obesity, defined as excess body fat, was historically targeted through: lifestyle approaches including both dietary and physical activity regimens, surgery including gastric bypass and pharmacological approaches targeting metabolic pathway such as

glucagon-like peptide-1 (GLP-1) receptor agonists (Tirzepatide[12]) or GLP1 analogues (Semaglutide[13]). GLP1 belongs to the family of incretins known to stimulate insulin secretion post-prandially[14]. GLP1 based drugs were originally designed as T2D therapeutic agents, highlighting the interconnected pathways and causality between different metabolic disorders. Interestingly, GLP1-targeting drugs demonstrated anti-inflammatory effects independent to their glucose lowering role[15,16]. This is in line with the finding that many other diabetes-designed drugs such as biguanides, sulfonylureas and thiazolidinediones exhibit anti-inflammatory effects, the result of which can contribute to their overall effect on the management of diabetes beyond their glucose regulatory effects[17]. The reverse relation also applies where know anti-inflammatory drugs such as salicylates have been found to exert a beneficial effect on glycemia control[18]. These findings demonstrate the interlink between metabolic and inflammatory disorders and highlight the potential of targeting inflammation to treat metabolic disease and vice versa.

1.2. The pathophysiology of atherosclerosis

Atherosclerosis is initiated by the accumulation of modified lipoproteins, such as oxidized LDL (oxLDL), in the subendothelial space of medium to large size arteries[19]. This occurs primarily in areas of low shear stress, such as curvatures and bifurcations. Lipoproteins serve as both antigens activating the adaptive immune response and adjuvant molecular patterns triggering the innate immune response[20–23]. The resulting immune cell activation leads to inflammation through various mechanisms like cytokine production, neutrophil extracellular trap release, and monocyte recruitment to the plaque. Plaque macrophages, originating from monocyte differentiation, local proliferation or vascular smooth muscle cell transdifferentiation, take up lipoproteins in the plaque and become lipid-laden foam cells that contribute to plaque necrotic core formation. Antigen presenting cells, including macrophages, dendritic cells, and B cells, present lipid and peptide antigens to T cells and

invariant natural killer T cells, triggering adaptive immune responses. These processes collectively contribute to endothelial dysfunction, exacerbating inflammation, monocyte recruitment, lipoprotein uptake, vascular smooth muscle cell (VSMC) activation and proliferation, and fibroblast migration, ultimately leading to the development of atherosclerotic plaques[24].

In advanced atherosclerosis, complex chronic inflammation leads to the creation of plaques with thin fibrous caps and large necrotic cores. These morphologies increase the risk of rupture and subsequent ischemic events[25]. Recent research highlights the multifactorial nature of atherogenesis, with contributions from organs like including the bone marrow, spleen and adipose tissue[26,27].

1.3. The pathophysiology of obesity

The adipose tissue (AT) is a central metabolic organ with endocrine and homeostatic functions including energy storage, thermal insulation and protection from mechanical damage. Two major adipose tissue depots with distinct morphologies and function can be distinguished: brown (BAT) and white (WAT) adipose tissue. The primary function of the brown adipose tissue is body temperature regulation through thermogenesis. It is abundant in new-born babies, and depots decrease with age (<1-2% of total fat mass in adults)[28]. In mice and humans BAT depots are located in interscapular and supraclavicular regions, as well as around the kidneys, heart, aorta, pancreas and the trachea. Brown adipose tissue is associated with improved metabolic health in obesity, but underlying mechanisms are still unknown. Adipocytes express β-adrenergic receptors, and their activation can stimulate metabolism of BAT to increase mitochondrial ATP dissipation through upregulation of the mitochondrial protein, uncoupling protein 1 (UCP1), a protein highly expressed and specific to BAT. Adrenergic stimulation, whether pharmacologic or through cold exposure, can also lead to a “browning” phenotype in WAT, whereas white adipocytes, especially in the subcutaneous areas, can acquire a

reversible brown-like phenotype and increase their UCP1 expression, these cells are referred to as beige or brite adipocytes in WAT depots[29–31].

White adipose tissue (WAT) is the predominant type of adipose tissue in adult humans and mice and is primarily responsible for energy storage. The WAT can be further classified into subcutaneous (SAT) the most prominent WAT depot in lean, healthy individuals and visceral white adipose tissue (VAT) which is located intra-abdominally, adjacent to internal organs. Lean healthy individuals have small amounts of visceral fat. Subcutaneous adipose tissue is the primary recipient of excess lipid during increased energy intake or limited energy expenditure. The development of obesity is associated with the expansion of both SAT and WAT compartments, however increase in VAT mass, i.e. increase in ectopic fat deposition surrounding organs including kidneys, the liver and the heart, shows the highest correlation with development of metabolic syndrome including hyperinsulinemia, dyslipidaemia, chronic inflammation and atherosclerosis. AT expansion includes both increase in adipocyte size (hypertrophy) and adipocyte number (hyperplasia) which depends on differentiation of adipocyte progenitor cells in the stroma fraction of the adipose tissue[32]. AT expansion is also accompanied with increased angiogenic and extracellular matrix deposition programs[33]. Excess fat deposition leads to pathological expansion of adipocytes size or hypertrophy, and eventually adipocyte necrosis, accompanied by enhanced secretion of adipokines, cytokines and chemokines promoting inflammation, insulin resistance and enhanced immune cell recruitment[34]. A variety of innate and adaptive immune cells resides in the WAT during homeostasis and contribute to the maintenance of the tissue[35]. The expansion of AT in obesity results in changes of the AT environment affecting both immune cell composition and activation. Adipose tissue macrophages (ATMs) macrophages expand in obesity from 10% of stromal cells in in healthy AT to 50% of stromal cells in obese mice[36] and humans[37]. Both, infiltrating monocytes and proliferating

macrophages contribute to macrophage accumulation in the obese adipose tissue[36,38–40]. Disease associated CD11c$^+$ macrophages form crown-like structures surrounding hypertrophic adipocytes and act as debris and lipid-droplet scavengers[41,42]. In addition, CD11c$^+$ macrophages have been associated with insulin resistance[43,44], highlighting the importance of macrophages in the pathogenesis of obesity.

1.4. Immune cells in the aorta and adipose tissue

Immune mechanisms in both atherosclerosis and obesity are very complex and the emergence of single-cell technologies including single-cell RNA sequencing (scRNAseq) and mass cytometry are starting to unravel previously unappreciated immune cell heterogeneity. While B cells, eosinophils and neutrophils are important in atherosclerosis and obesity, in this thesis I focus on T lymphocytes and primarily on mononuclear phagocyte immune mechanism in the aorta and adipose tissue during metabolic disease progression.

1.4.1. T lymphocytes

Resident T cells and innate lymphoid cells contribute to aortic and adipose tissue homeostasis. In disease, the lymphocyte compartment contributes to the inflammatory environment of the tissue and disease manifestation[35,45,46].

T lymphocytes are divided into two main groups: CD8$^+$ and CD4$^+$ T cells. CD8$^+$ T cells recognise antigens that are presented by major histocompatibility complex class I (MHC I) molecules. As they mature, they acquire cytotoxic effector T cell features and kill virus-infected or abnormal cells. CD8$^+$ T cells outnumber CD4$^+$ T cells in advanced human atherosclerotic plaques[47,48]. CD8$^+$ T cells have been shown to be proatherogenic, however they might also exhibit some antiatherogenic roles through their action on antigen presenting cells (APCs)[45]. In addition, CD8$^+$ T cell numbers increase in blood of coronary artery disease (CAD) patients[49,50]. In mice, CD8$^+$ T cells were shown to promote unstable plaque phenotypes and plaque erosion[48,51]. In obesity, CD8$^+$ cells have a largely

proinflammatory role. CD8-deficient mice show reduced macrophage accumulation and improved insulin sensitivity, while adoptive transfer of $CD8^+$ T cells into CD8-deficient mice aggravated adipose tissue inflammation[52].

Contrary to what has been shown in advanced human plaques, $CD4^+$ T cells dominate the mouse atherosclerotic plaque T cell compartment, and display a pro-inflammatory T helper 1 (TH1) phenotype[46]. $CD4^+$ T cells have been shown to clonally expand during atherosclerosis and show upregulation of cytotoxic markers including GZMA and GZMK[53]. TH1 cells express pro-inflammatory cytokines IFNγ, TNFα and *Tbx21*, encoding for T-bet. TH1 cells have been consistently shown to drive lesion development and plaque instability suggesting a pro-atherogenic role[5]. In the adipose tissue, TH1 cells numbers are increased in obese individuals and mice, and their activation is associated with insulin resistance[54–56].

Treg cells express the transcription factor FOXP3. In line with their expression of the anti-inflammatory cytokines IL10 and TGFβ, they are thought to have atheroprotective functions[45]. Treg numbers decrease during atherogenesis and obesity[57–59]. Single-cell technologies are helping to decipher T cell heterogeneity and plasticity in atherosclerosis and obesity. For example, it was recently shown that $FOXP3^+$ Tregs can acquire T effector cytotoxic transcriptional and functional phenotypes, while losing FOXP3 expression[60–64]. This is in line with recent reports showing that T cell tolerance checkpoints are broken down in atherosclerosis[53,65]. Interestingly, this phenotypic switch of Tregs has also been described in autoimmune conditions, including type 1 diabetes[66].

The role of $CD4^+$ T helper 2 (TH2) and T helper 17 (TH17) cells in atherosclerosis and obesity remains less investigated[35,45]. TH2 cells are regulated by the transcription factor GATA3 and secrete IL4, IL5 and IL13. Innate lymphoid cells that express IL5 and IL13 have been identified in atherosclerotic plaques[67,68], and cell type specific functional studies should be performed.

1.4.2. Mononuclear phagocytes

1.4.2.1. Dendritic cells

Dendritic cells are antigen presenting cells that contribute to immune responses in atherosclerosis and obesity by eliciting adaptive immune responses[69]. Three main DC subsets can be distinguished: plasmacytoid dendritic cells (pDCs), type 1 conventional dendritic cells (cDC1) and type 2 conventional dendritic cells (cDC2). Plasmacytoid dendritic cells are rare in metabolic tissues and are more abundant in the blood and lymphoid tissues, where they produce type 1 interferon after interaction with pathogens[70,71].

cDC1s cross-present antigens to lymphocytes and cDC2s are primarily responsible for T cell priming[72]. In atherosclerosis, dendritic cells can exhibit both pro-atherogenic and anti-atherogenic roles[73–75] and in humans, plaque vulnerability was associated with increased dendritic cell numbers[76]. DCs have both a positive and detrimental effect on Tregs. A specific DC subset has been shown to suppress Treg responses in the plaque through secretion of CCL17[77]. In contrast, depletion of cDC1 using $FLT3^{-/-}$ mice resulted in decreased Treg numbers and exacerbation of atherosclerosis in mice[78]. Similarly , FLT3l deficiency which also reduces numbers of DCs[79], promoted insulin sensitivity[80]. Similarly, the role of dendritic cells in obesity is also unclear in terms of benefit to harm. $CSF2^{-/-}$ mice showed reduced cDC2 numbers in the AT and increased body weight[35]. However, this effect cannot be solely mapped to cDC2, in fact CSF2 (colony stimulating factor 2/ GMCSF) is important for maturation of other immune cells including macrophages, neutrophils and eosinophils and all or some of these cells might have contributed to the obesity phenotype recorded in these $CSF2^{-/-}$ mice.

1.4.2.2. Monocytes

In mice and humans two main monocyte populations can be distinguished: classical ($Ly6C^{hi}$ in mice and $CD14^{+}CD16^{-}$ in humans) and nonclassical ($Ly6C^{lo}$ in mice and

$CD14^{lo}CD16^{+}$ in humans) monocytes. Hypercholesterolaemia, hyperglycaemia, stress and inflammation induce myelopoiesis in the bone marrow as well as extramedullary haematopoiesis in the spleen[81–84], resulting in increased monocyte numbers in the blood. In atherosclerosis and obesity, classical/$Ly6C^{hi}$ monocytes, are the main monocyte subset recruited to plaques and the obese adipose tissue[36,38,81,85,86], where they can differentiate into heterogenous populations of dendritic cells and macrophages[87,88]. On the other hand, $Ly6C^{lo}$ monocytes, also referred to as patrolling monocytes, preferentially differentiated into disease-associated $CD11c^{+}$ myeloid cells during atherogenesis[87]. In agreement with this finding, a subset of non-classical monocytes was found to be enriched in the blood of patients with coronary artery disease using mass cytometry[89]. Nonclassical monocytes, derive from classical monocytes[90] in a Nur77-dependent manner. In steady state, patrolling monocytes promote vascular endothelial cell homeostasis; they remove damaged cells and debris from the vasculature and are associated with healthy vascular remodelling[91–93]. Deficiency of Nur77 has been shown to increase atherosclerosis and obesity, suggesting an atheroprotective role of patrolling monocytes in line with their homeostatic functions described above[93–96]. However, their differentiation into a subset of disease-associated $CD11c^{+}$ macrophage subset in the plaque as discussed above, warrants more investigation into this subset in the context of inflammatory disease.

1.4.2.3. Macrophages

The plaque and obese adipose tissue microenvironments are rich with cytokines and lipid mediators shaping macrophage functions and phenotypes[97–100]. Macrophages have various roles in metabolic tissues, including the clearance of apoptotic cells (efferocytosis), phagocytosis of debris, lipid handling and production of pro- and anti-inflammatory cytokines[34,101]. Until recently, macrophages were defined based on two phenotypes: proinflammatory M1 macrophages and anti-inflammatory M2 macrophages. This dichotomy however does not represent the variety of macrophage states observed *in*

vivo. Advances in single-cell technologies showcased the importance of macrophage heterogeneity in atherosclerosis and obesity by challenging the strict M1/M2 classification. Single-cell techniques like single-cell RNA sequencing and mass cytometry (Cytometry of Time of Flight (CyTOF)) are helping to decipher macrophage landscapes in the aorta and the adipose tissue in health and disease[102,103,112–116,104–111]. In both tissues four main groups of macrophages have been described in mice and humans based on their transcriptional signatures: resident-like, foamy *Trem2*, inflammatory, and proliferating macrophages suggesting striking transcriptional similarities of myeloid cells in metabolic disease.

Resident-like macrophages in the healthy and atherosclerotic aorta also express *Timd4, Lyve1, Folr2, Pf4, F13a1*, *C1qa* and *Mrc1*[103,105,117] and could be further distinguished by CD209 expression using CyTOF or scRNAseq[109,117]. Embryonic derived *Tim4*$^{+}$*Lyve1*$^{+}$*Folr2*$^{+}$ (TLF) macrophages have been identified across multiple organs[118].

In the aorta, two anatomic niches; the intima and the adventitia harbour different populations of resident macrophages which are maintained through proliferation in healthy aortas[119–121]. Intimal resident macrophages, recently referred to as aortic intima resident macrophages or Mac^{AIR}, are monocyte derived and seeded after birth[119]. Mac^{AIR} express *Cd72*, *Mmp12* and *Il1b* in addition to *Trem2* associated marker genes (*Cd9*, *Spp1*, *Itgax*, *Lpl*). Depletion of these macrophages suggests a pro-atherogenic role in early atherogenesis[119]. Adventitial resident macrophages, the bona fide TLFs, derive from embryonic precursors and postnatal monocyte seeding[120,121]. Adventitial macrophages, TLFs, maintain vessel homeostasis by inhibiting collagen production of vascular smooth muscle cells thereby regulating arterial stiffness[122].

In adipose tissue, a subset of resident adipose tissue macrophages is identified through expression of CD206, TIM4 and LYVE1. These macrophages are referred to as vascular associated macrophages (VAMs), are associated with blood vessels, are highly endocytic

and are shown to contribute to angiogenesis giving them an overall homeostatic phenotype[115,123,124].

Foamy cells arise during atherogenesis or obesity and can be derived from monocytes, macrophages, dendritic cells as well as VSMCs[105,112,125]. Foamy macrophages in both tissues express high levels of genes associated with lipid metabolism, cholesterol efflux and oxidative phosphorylation including *Trem2*, *Cd9*, *Lpl*, *Fabp5*, *Plin2*, *Abcg1*, *Spp*1 and *Itgax* and do not express inflammatory gene signatures suggesting a homeostatic lipid handling role in atherosclerosis[105,112]. Recently, two subsets of *Trem2* macrophages have been defined using scRNAseq[117]: *Gpnmb*^{hi}*Trem2*^{hi} macrophages displayed the known homeostatic lipid handling signature, while Slamf9^{hi}*Trem2*^{hi} macrophages expressed a more inflammatory gene signature (*Tnf*, *Ccl3*, *Ccl4*, *Nfkbiz*) and less lipid handling gene signature when compared to *Gpnmb*^{hi}*Trem2*^{hi} macrophages. A subset that exhibit both a high lipid signature and inflammatory score was recently identified in human carotid plaques: these inflammatory lipid-associated macrophages were referred to as PLIN2^{hi}/TREM1^{hi} due to the highest expression of lipid-droplet associated gene perilipin (PLIN2) and the triggering receptor expressed on myeloid cells 1 (TREM1) known to be the inflammatory "antagonist" of TREM2[126]. However, a murine macrophage equivalent to this population was not identified when analysing all available murine datasets and the closest population with similar characteristics was found in a disease-associated monocyte population[126]. Understanding the relationship and ontogeny between the lipid-associated and inflammatory macrophage subsets is important to understand how foam cells might contribute to disease progression.

Pro-inflammatory CD11c^{+} macrophages are a hallmark of obesity[127] and CD11c^{+} ATMs express higher levels of proinflammatory cytokines compared to CD11c^{-} macrophages[128]. Inflammatory macrophages express high levels chemokines, cytokines and

inflammasome associated genes (*Ccl2*, *Ccl4*, *Ccl7*, *Il1b*, *Nlrp3*, *Tnf*)[104,105], suggesting they drive disease progression.

In addition to these pro-inflammatory macrophages, *Trem2* macrophages, known to lack any inflammatory signature, also express high levels of *Itgax*, the gene encoding for CD11c[67,105]. This shows that CD11c$^+$ cells constitute a heterogenous populations, indeed, using reporter mice, scientists were able to identify at least two CD11c$^+$ macrophage populations with distinct migratory and transcriptional profiles[107], suggesting a more complex picture of CD11c macrophages dynamics during metabolic disease progression.

1.5. The transcription factor IRF5

Interferon regulatory factor 5 is a transcription factor that is known to induce a pro-inflammatory phenotype in macrophages[129,130] and dendritic cells[131]. In addition, IRF5 is upregulated during monocyte[132] and neutrophil maturation[133]. IRF5 gain of function polymorphisms are associated with various autoimmune diseases, including systemic lupus erythematosus (SLE), rheumatoid arthritis, inflammatory bowel disease, and multiple sclerosis[133].

Global IRF5 deficiency reduces atherosclerotic burden, necrotic core formation and CD11c$^+$ macrophage accumulation in *Apoe*$^{-/-}$ mice on chow diet [134]. Similarly, myeloid IRF5 deficiency resulted in a more stable plaque phenotype in *Apoe*$^{-/-}$ mice fed a high cholesterol diet for 12 weeks, suggesting that IRF5 affects lesional macrophage proliferation and foam cell formation[135]. Recently, IRF5 was shown to induce plaque rupture upon aortic ligation in *Apoe*$^{-/-}$ mice and was associated with CD11c expression and a vulnerable plaque phenotype in human carotid plaques[136]. In a mouse model of diet induced obesity, global and myeloid IRF5 deficiency improved insulin sensitivity and resulted in expansion of CD206$^+$ macrophages[137]. After short term high fat diet feeding, IRF5 promotes metabolic adaption to caloric excess[138]. In addition, IRF5 deficiency

promoted expansion of $CD206^+$, markers for resident/homeostatic, macrophages over $CD11c^+$ macrophage development in the inflamed colon[139].

1.6. Hypothesis and aims

The rise in single cell technologies helped decipher immune cell/myeloid heterogeneity in different tissues and organs in both human and animal models. Adipose tissue and atherosclerotic vasculature immune cell atlases are being completed and potential conserved transcriptional programs and macrophage activation states are being identified across tissues, disease models and species. However, so far, no inter-tissue comparison of atherosclerotic aortas and the obese adipose tissues has been done. In addition, available datasets from both tissues address specific questions, and most of them rely on mouse models that either induce atherosclerosis or obesity. Given the frequent co-existence of both diseases in the general population and the similarities between macrophage subsets in both metabolic diseases and tissues, it is crucial to further dissect the interrelatedness and biological divergence of macrophages in the aorta and adipose tissue to better understand cellular mechanisms of metabolic disease progression and co-morbidity.

Hypothesis:

Macrophages in metabolic tissues share transcriptional profiles and link atherosclerosis and obesity.

Aims:

1) Generate a comprehensive murine single-cell atlas of the aorta and the adipose tissue during metabolic disease progression.
2) Identify shared and unique mononuclear phagocyte transcription profiles and compositional changes in the artery and adipose tissue during metabolic disease progression.
3) Investigate the cell-intrinsic role of IRF5 in modulating monocyte and macrophage cell distribution, phenotype, transcriptional signatures and function during metabolic disease progression.

Chapter 2. A single-cell atlas of the aorta and adipose tissue during metabolic disease progression

2.1. Introduction

Metabolic diseases, such as obesity and atherosclerosis, are chronic inflammatory disorders that often coexist and contribute to the global burden of cardiovascular disease (CVD)[140–142]. Immune processes in both atherosclerosis and obesity are being increasingly elucidated and found to contribute to disease progression[6,143].

A diet with elevated fat, cholesterol and sugar, commonly referred to as a "western diet" (WD) is highly correlated to the development of both atherosclerosis and obesity[144]. Excess circulating lipids in the form of lipoproteins can have detrimental effects on the overall metabolic profile and its associated co-morbidities[145]. In the vasculature, especially at locations of low shear stress, endothelial cell activation and the retention and accumulation of low-density lipoproteins in the subendothelial space of the arterial wall leads to immune cell recruitment, differentiation and activation[145]. This eventually leads to the formation of lipid-rich plaques in medium and large sized arteries. In the adipose tissue, immune cells including ATMs reside in the interstitial spaces between adipocytes and perform homeostatic functions. Upon weight gain, the adipose tissue expands through adipocyte hypertrophy and eventual necrosis, leading to enhanced secretion of adipokines, cytokines and chemokines promoting infiltration of circulating immune cells and their activation contributing to both local and systemic metabolic dysfunction, fibrosis and insulin resistance[142,146].

Both atherosclerosis and obesity are characterised by dysfunctional lipid metabolism and inflammation, and macrophages in particular, play a central role in both aspects contributing to disease progression[100,147]. Single-cell studies of aortas and the adipose tissue in health and disease have emphasised the complexity of immune cell phenotypes

in general and macrophages in particular in both tissues during metabolic disease progression in mice and humans[47,67,111,116,148–153,102–107,109,110]. Tissue niche and ontogeny affect macrophage functions, phenotypes, and transcriptomes[154]. In disease, local proliferation of tissue resident macrophages and recruitment of circulating blood monocytes contribute hand in hand to macrophage accumulation in the atherosclerotic plaque and the obese adipose tissue, however the contribution from these origins may differ between tissues[40,120]. Genetic lineage tracing and monocyte fate mapping studies are just starting to explore monocyte and local progenitor contributions to distinct macrophage subpopulations in atherosclerosis and obesity[81,104,119,121]. Macrophages have various roles in the plaque and adipose tissue ranging from homeostatic functions including the clearance of apoptotic cells, phagocytosis of debris and lipid handling to pathogenic roles such as production of pro- and anti-inflammatory cytokines. Some of these functions are associated with specific subsets. Lipid-associated macrophages (LAMs) are an important example of a disease-associated macrophage population. LAMs have been identified in multiple metabolic diseases, such as atherosclerosis, obesity, fatty liver and cancer[155–158]. LAMs are characterised by a conserved lipid-associated transcriptional signature involved in lipid uptake, lysosomal metabolism, anti-oxidative functions, matrix remodelling, cholesterol metabolism and efflux[105,112].

In recent years, the rise in single cell technologies helped decipher immune cell/myeloid heterogeneity in different tissues and organs in both human and animal models. Conserved transcriptional programs and macrophage activation states are being identified across various tissues. Murine and human atlases of the obese adipose tissue and atherosclerotic plaques are becoming more and more available. However, no inter-tissue comparison of atherosclerotic aortas and the obese adipose tissues has been done yet. Although both diseases often coexist in humans, datasets from both tissues rely on mouse models that either induce atherosclerosis or obesity. To improve our understanding of

cellular mechanisms underlying metabolic disease progression and co-morbidity, it is important to further dissect the interrelatedness and biological divergence of macrophages in the aorta and adipose tissue

To allow an in-depth definition of tissue-specific immune cell phenotype while limiting confounding factors (Chapter 3), I used single-cell approaches to characterise aorta and epididymal white adipose tissue immune cell populations using the same animal. In this chapter, I sought to define separate immune cell landscapes of the aorta and epididymal white adipose tissue (epiWAT) across different time points of metabolic disease progression in both aortas and in the same mouse using single-cell approaches. Since the transcription factor IRF5 is a master regulator of macrophage transcriptional state[159] and it has a known role in atherosclerosis and obesity[134,135,137,138], I selected it as model molecule to study its cell intrinsic effects at the single cell level.

2.2. Generation of a scRNAseq dataset of the aorta and epididymal white adipose tissue during metabolic disease progression and analysis strategy

In order to generate an inclusive atlas of immune cells in metabolic tissues, I focused on the below specific aims:

To (i) characterise the immune cell dynamics in the aorta and epiWAT of mixed bone marrow chimera during metabolic disease progression (Chapter 2), (ii) compare immune cells between the aorta and the epiWAT (Chapter 3) and (iii) investigate cell intrinsic effects of the myeloid master regulator transcription factor IRF5 in modulating myeloid heterogeneity in the aorta and epiWAT (Chapter 4), I generated a scRNAseq dataset of immune cells from the blood, aorta and epiWAT during a time course of metabolic disease progression in a murine model where obesity and atherosclerosis were induced simultaneously by western diet feeding(Figure 2.1A,B). Briefly, C57BL/6J or LDLR$^{-/-}$ (CD45.1^{+}) mice were sub-lethally irradiated and reconstituted with 50% bone marrow

from CD45.1^{+}CD45.2^{+}CX3CR1$^{GFP/+}$ WT mice and 50% bone marrow from CD45.2^{+}CX3CR1$^{GFP/+}$ IRF5$^{-/-}$ mice. Steady state control samples were collected after 9 weeks recovery from the bone marrow transfer and metabolic disease was induced by feeding a high fat, high cholesterol, high sugar western diet (WD) for 12 weeks or 18 weeks after 6 weeks recovery from the bone marrow transfer. For each time point cells from 4-9 mice were pooled and WT and IRF5$^{-/-}$ immune cells from the aorta, epiWAT and blood were sorted (Figure 2.1A) for sequencing (see Methods 6.3.1, 6.7.1).

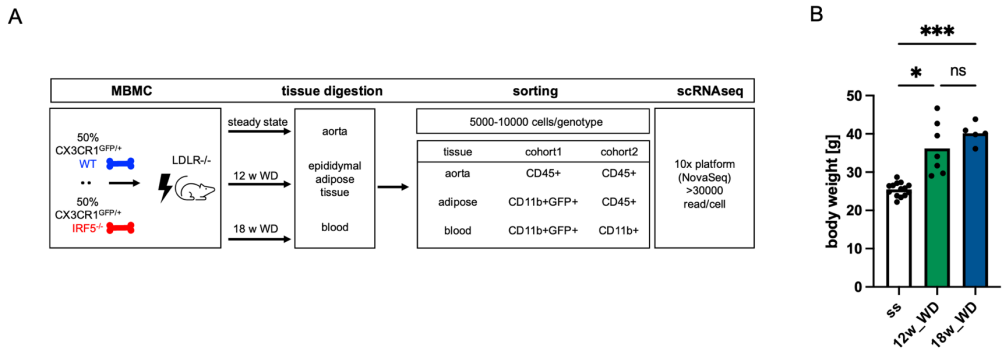


Figure 2.1: ***Generation of a scRNAseq dataset of the aorta, epiWAT and blood during metabolic disease progression.*** *A. Schematic of scRNAseq sample acquisition. Mixed bone marrow chimeras (MBMCs) received 50% CX3CR1-GFP$^{+/-}$IRF5$^{-/-}$ and 50% CX3CR1-GFP$^{+/-}$IRF5$^{+/+}$ (WT) bone marrow. Mice were fed a chow diet (steady state) or western diet (WD) for 12 or 18 weeks to induce metabolic disease. Single cell suspension from blood and digested epidydimal adipose tissue (epiWAT) and aortas from 4-9 mice per time point were pooled, immune cells were sorted per genotype and scRNAseq using the 10x Genomics platform was performed. B. MBMC mouse body weight during the time course of metabolic disease progression. Brown-Forsythe ANOVA test with Dunnett's T3 multiple comparison test * p <0.05, *** p < 0.0005.*

In this chapter I characterised the overall immune cell landscapes in the aorta and epiWAT of mixed bone marrow chimera with particular focus on the mononuclear phagocyte compartment and compositional changes of WT cells during metabolic disease progression. First, I performed an integrated analysis of sorted leukocytes including steady state, 12w WD and 18 w WD samples from both genotypes for the aorta (n=5 samples per genotype) and epiWAT (n=5 samples per genotype). After quality control (see Methods 6.7.3) 49484 high quality aortic leukocytes and 50927 high quality epididymal leukocytes were first clustered at low resolution to identify major immune cell types, followed by detailed sub analysis of the T/NK cell and mononuclear phagocyte compartment. Finally, clusters identified in the mononuclear phagocyte (MNP)

compartments of the aorta and epiWAT were integrated with and compared to publicly available single-cell datasets (see Methods 6.7.5).

2.3. Defining the aortic immune cell landscape of mixed bone marrow chimeras during metabolic disease progression using scRNAseq

Table 2.1: Overview of samples included to define the aortic immune cell, T/NK and mononuclear phagocyte landscapes during metabolic disease progression.

tissue	disease time point	genotype	batch	number of mice in pool	Sorting strategy
aorta	steady state	WT	A	6	Live CD45+
aorta	steady state	KO	A	6	Live CD45+
aorta	12w WD	WT	B	4	Live CD45+
aorta	12w WD	KO	B	4	Live CD45+
aorta	steady state	WT	C	10	Live CD45+
aorta	steady state	KO	C	10	Live CD45+
aorta	12w WD	WT	D	7	Live CD45+
aorta	12w WD	KO	D	7	Live CD45+
aorta	18 w WD	WT	E	6	Live CD45+
aorta	18 w WD	KO	E	6	Live CD45+

First, an integrated analysis of aortic samples from WT and IRF5$^{-/-}$ cells from steady state, 12w WD and 18w WD was performed (Table 2.1). Low resolution clustering was applied and 7 leukocyte clusters were annotated based on expression of the given cell type markers and singleR annotations: 3 T cell clusters (*Cd3e*), 1 NK cell cluster (*Nkg7*), 1 B cell cluster (*Cd79a*), a mixed B cell/plasma cell cluster (*Jchain*, *Sdc1*), a neutrophil cluster (*Retnlg*, *Csf3r*), a dendritic cell (DC) cluster (*Flt3*, *Cd209a*), a macrophage cluster (*Itgam*, *Adgre1*), a monocyte cluster (*Plac8*, *Ace*, *Ly6c2*) and a mixed macrophage/DC cluster (Figure 2.2A-C). All cell types were well represented in all 10 integrated aortic samples regardless of disease time point or genotype (Figure 2.2E). Plasma cells are primarily found in the spleen and bone marrow[160–162] and therefore it is not surprising that only 3/10 samples contained more than 5 cells in the mixed B cell/plasma cell cluster (Figure 2.2E). To generate an overview of the general immune cell composition clusters were aggregated to major cell lineages (Figure 2.2D): mononuclear phagocytes (MNPs), B/plasma cells, T/NK cells and neutrophils. At steady state and in metabolic disease,

immune cells in the aorta were primarily comprised of mononuclear phagocytes (steady state: 38.68±18.20%, 12w WD: 24.23±0.61%), T/NK cells (steady state:42.18±24.41%, 12 WD:54.58±6%), and B/plasma cells (steady state:17.51±6.19%, 12w WD:20.09±6.76%), while neutrophils comprised only 1-2 % of immune cells (steady stae:1.63±0.02%, 12w WD:1.10±0.16%) (Figure 2.2F). T/NK cells and mononuclear phagocytes showed high variability in their abundance in the aorta at steady state (Figure 2.2F). To validate the frequencies of major cell lineages I also performed CyTOF mass cytometry on aortas of mixed bone marrow chimera at steady state and 12w WD feeding (Figure 2.3). I identified major cell lineage clusters of MNPs (F4/80, CD68, CD64, CD11c), neutrophils (Ly6G), eosinophils (SiglecF), B cells (B220, CD19) and T/NK cells (CD90.2, CD3, CD4, CD8) (Figure 2.3A,C). Again, MNPs and T/NK cells constituted the biggest leukocyte populations at steady state (MNPs: 51.12±20.08%, T/NK cells: 30.44±15.56) and in disease (MNPs: 47.14±7.42%, T/NK cells: 36.35±6.55) (Figure 2.3B). In addition to the cell lineages, that were identified using scRNAseq, I also identified eosinophils using CyTOF. In line with previous reports[109,148,163], eosinophils constituted ~2% of immune cells in the aorta (steady state: 1.98±0.85%, 12w WD: 1.30±0.06%) (Figure 2.3C). The absence of eosinophils in the scRNAseq dataset was likely due to the fact that eosinophils express high levels of cellular ribonucleases[164], and therefore might be filtered out with low quality cells during quality control due to low RNA content. This finding was consistent with scRNAseq studies of eosinophilic esophagitis, a pathology that is characteries by eosinophil accumulation[164]. Overall, no significant compositional changes as assessed by scCODA[165] during metabolic disease progression were observed in any cell lineage using CyTOF or scRNAseq.

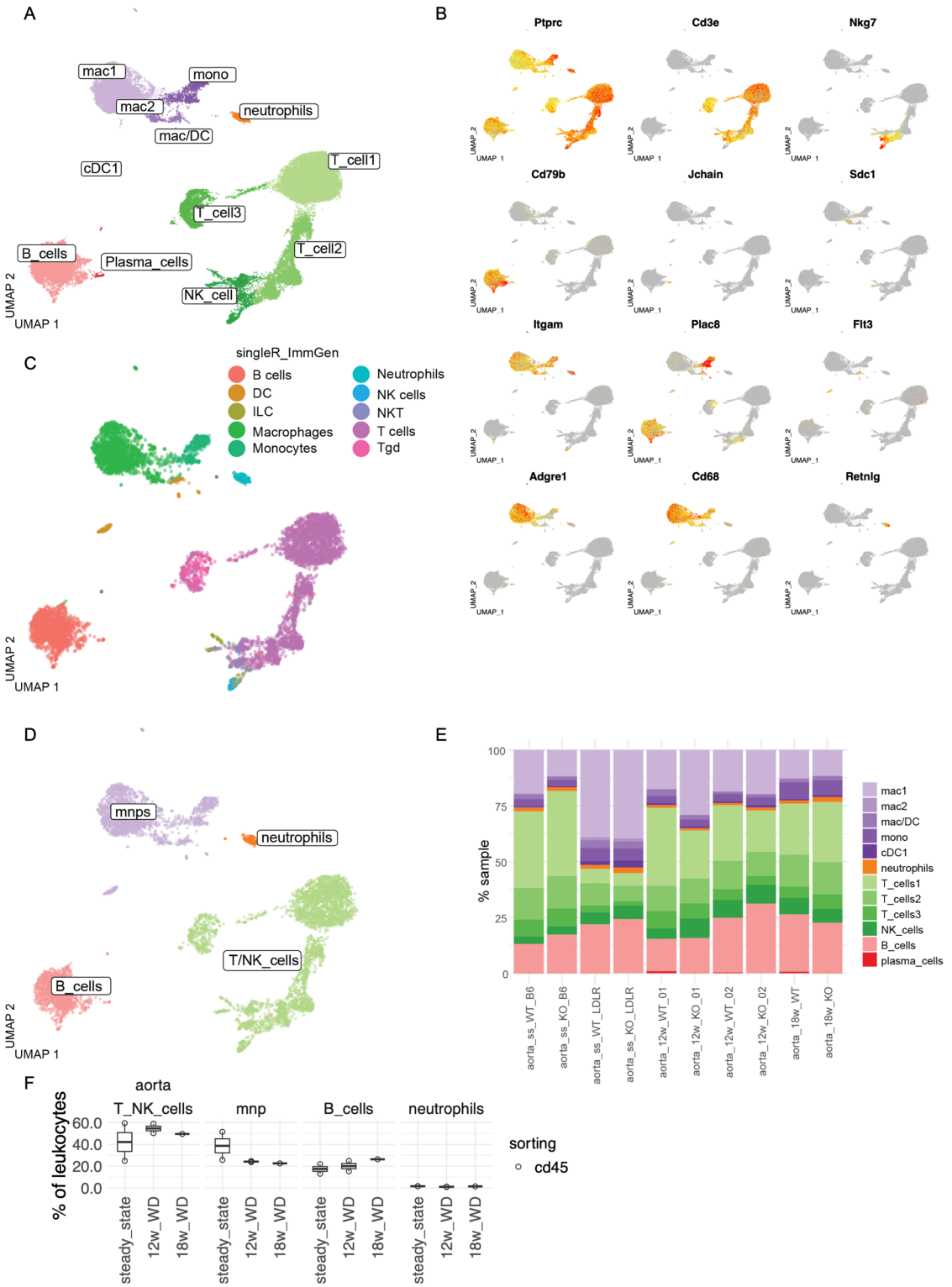


Figure 2.2: ***Defining the aortic immune cell landscape of mixed bone marrow chimeras (MBMCs) in metabolic disease using scRNAseq.*** *scRNAseq was performed on CD45^{+} sorted WT and IRF5$^{-/-}$ samples from MBMC aortas at steady state (n=2 per genotype), 12w western diet (WD) (n=2 per genotype), 18w WD (n=1 per genotype). 49484 leukocytes were analysed to get an overview of immune cell composition in the aorta. A. Leiden clustering identified 12 leukocyte clusters. B. Expression of selected cluster marker genes (BH-adjusted P < 0.05, two-sided Wilcoxon tests) and known cell type markers used for cell type annotation C. Automatic cell type annotation using singleR and the ImmGen database as a reference. D. Identified clusters were grouped into major cell lineages based on classical marker expression and singleR annotations (B,C). E. The bar plots show the cluster composition within each sample. F. The box plots show percentages of WT cells that were found in each major cell lineage. No credible changes in composition were identified at 12w WD or 18w WD when compared to steady state using scCODA.*

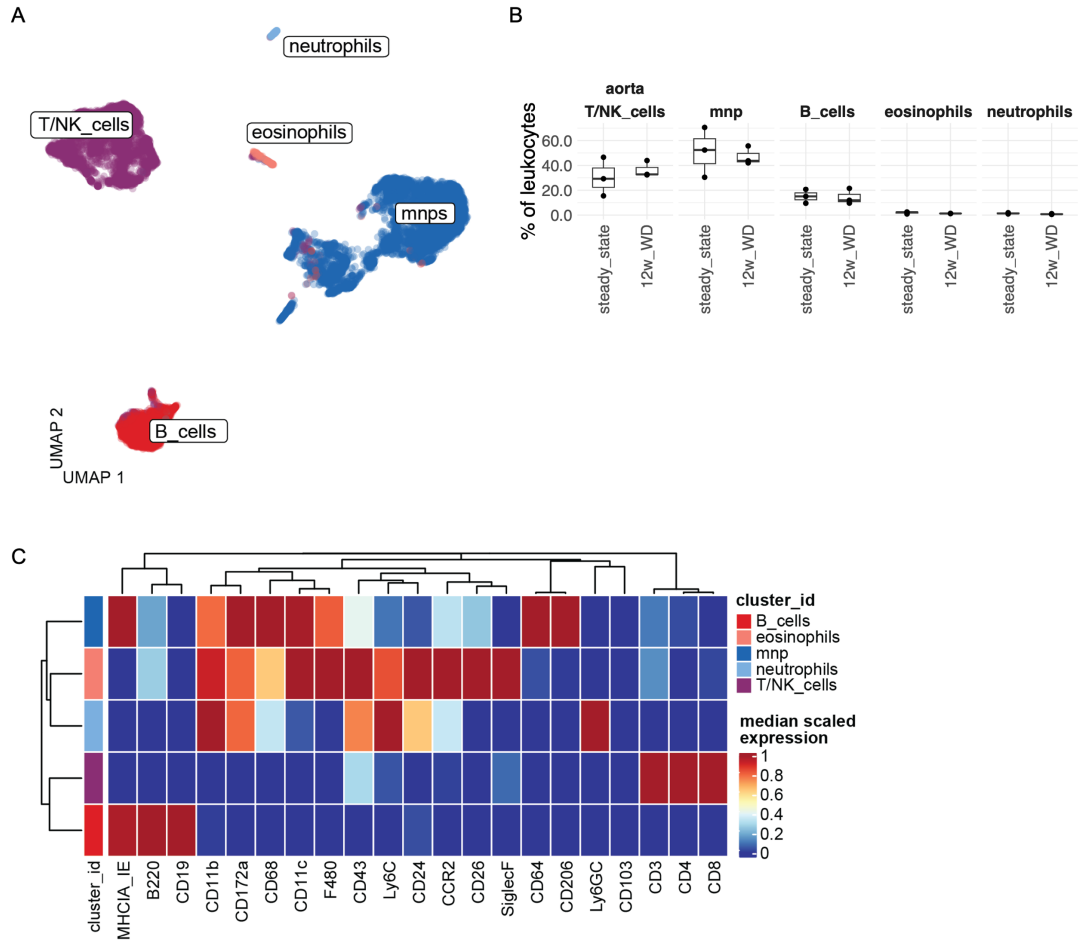


Figure 2.3: ***Defining the aortic immune cell landscape of mixed bone marrow chimeras (MBMCs) in metabolic disease using CyTOF****. CyTOF was performed on aortas from MBMCs at steady state and 12w western diet (WD). A. CD45^{+} cells were analysed using FlowSOM clustering. Clusters were merged based on major cell lineage marker expression (CD19, CD3, CD11b, Ly6G/C, SiglecF). B. The box plots show percentages of WT cells that were found in each major cell lineage. No credible changes in composition were identified at 12w WD or 18w WD when compared to steady state using scCODA. C. The heatmap shows the median scaled surface marker expression levels of cell lineage markers that were used for FlowSOM clustering.*

2.3.1. Defining the T and NK cell landscape in the aorta using scRNAseq

To investigate the cellular heterogeneity present within the T/NK lymphocytes, I reanalysed T and NK cell clusters from the overall analysis (Figure 2.4A, Table 2.1). The majority of T cells in the aorta displayed a *Cd4*$^{+}$*Cd8a*$^{+}$*Rag1*$^{+}$ double positive thymocyte-like phenotype and therefore were excluded from downstream analysis (Figure 6.4). 6793 T/NK cells from 10 aortic samples were reanalysed and 17 T/NK cell populations were identified (Figure 2.4B-E). I identified 6 CD4^{+} T cell clusters consisting of 3 naïve CD4 T cell clusters (*Ccr7*, *Sell*, *Il7r, Lef1),* TH1 CD4 T cells (*Cxcr3, Ccr5, Cxcr6*, *Cd40lg, Slamf6*), CD4 Tregs (*Foxp3, Ctla4*) and TH17 CD4 T cells (Rorc, *Il17, Il23r, Ccr6)*. The 5 CD8^{+} T cell clusters identified were: 3 naïve CD8 T cell clusters (*Ccr7*, *Sell*, *Il7r, Lef1)*, activated/cytotoxic CD8 T cells (*Gzmk*, *Eomes, Ccl5),* and a mixed activated cluster expressing markers of CD8 T cell activation, effector functions and survival (*Ly6c2*, *Il2rb*, *Txk*, *Bcl2*) as well as markers that can be expressed in other lymphocytes including NK cells, Tregs and γδ-T cells (*Klrd1*, *Klrc1*, *Prf1*, *Gzmm*). ILC2 cells were negative for CD3-encoding transcripts (*Cd3d*, *Cd3g*) and expressed ILC2 signature genes (*Rora*, *Gata3*, *Areg*, *Il1rl1*). I also identified a NK cell cluster that expressed high levels of *Klrbc1* (encoding for NK1.1)*, Klra9 (*encoding for Ly49C*)* and *Gzma*, as well as NKT cells expressing NK markers (*Klrbc1*, *Klra9)* in addition to CD3-encoding transcripts, *Cd4*, *Ifng* and *Il4*. Finally, I identified a small cluster of cycling T cells (*Mki67*, *Top2a*) as well as a remaining small cluster of *Rag1* and *Rag2* expressing double positive thymocytes (Figure 2.4B-E).

I identified all T/NK cell phenotypes previously described using scRNAseq[67,103,110,111,148], except for a γδ-T cell cluster which have only been identified using scRNAseq combined with scTCR-seq[65] or CITE-seq[114]. γδ-T cells often express T cell activation markers and likely cluster with other activated T cells. A subset of cells in the mixed activated CD8

cluster was annotated as γδ-T cells using singleR. This cluster was the only cluster that differentially expressed genes encoding for gamma and delta T cell receptor chain components (not shown). In addition, cluster marker genes *Klrd1* and *Prf1* and *Gzmm* are often expressed on γδ-T cells. Therefore, the mixed activated CD8 cluster likely contained γδ-T cells.

Compositional analysis of the aortic lymphocyte population showed that the majority of $CD4^+$ and $CD8^+$ T cells displayed a naïve phenotype at steady state (38.69% mean frequency, Figure 2.4F). However, with disease progression, lymphocyte composition shifted towards $CD4^+$ and $CD8^+$ effector T cell phenotypes including TH1, TH17 $Cd4^+$ T cells and activated/cytotoxic $CD8^+$ T cells suggesting an association between T cell activation and disease progression (Figure 2.4F).

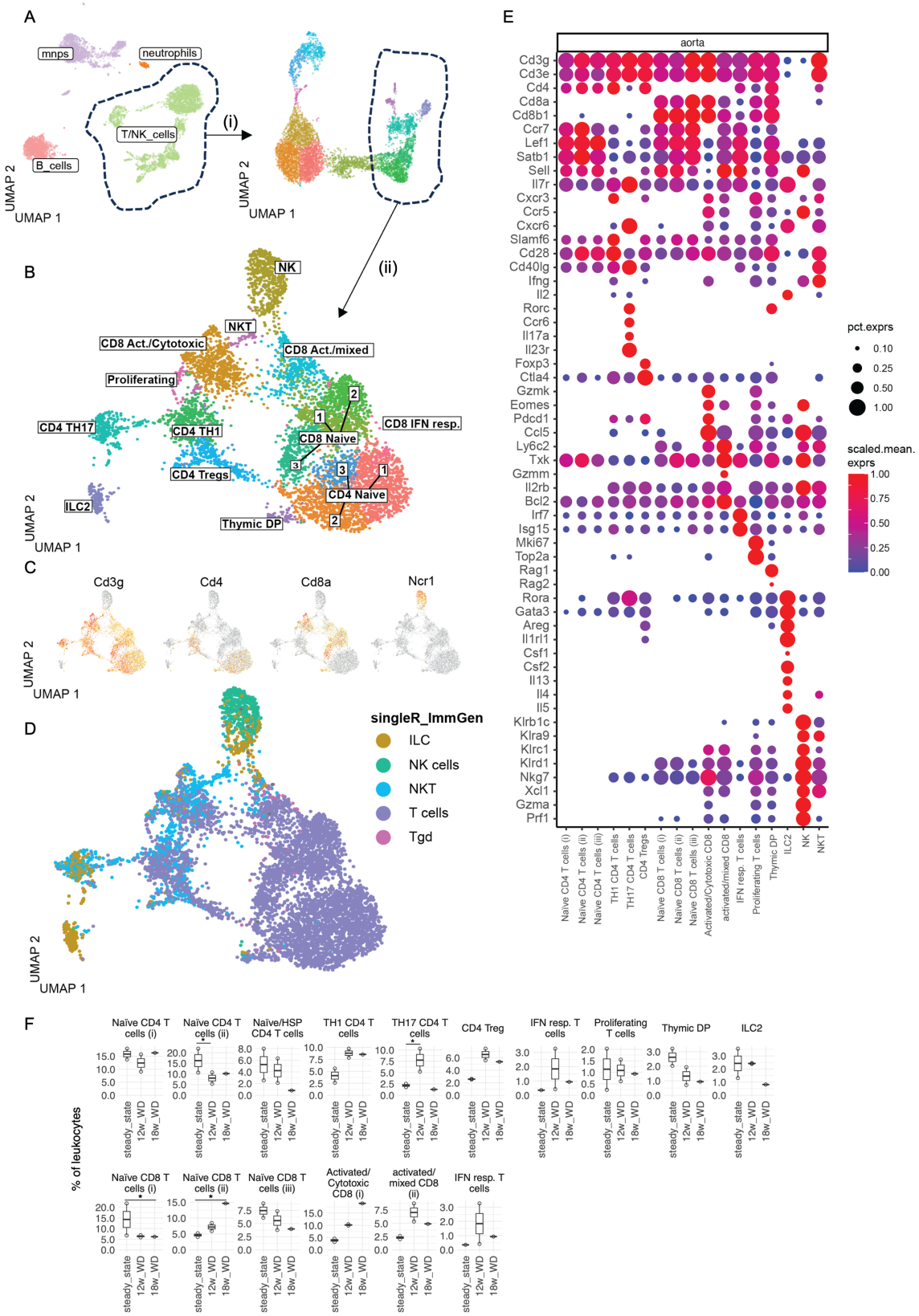


Figure 2.4: ***The single-cell landscape of mature T and NK cells in the aorta of mixed bone marrow chimeras (MBMCs).*** *scRNAseq was performed on CD45^{+} sorted WT and IRF5$^{-/-}$ samples from MBMC aortas at steady state (n=2 per genotype), 12w western diet (WD) (n=2 per genotype), 18w WD (n=1 per genotype). A/B. Reanalysis strategy of T and NK cells int the aorta. 25905 T and NK cells were reanalysed first(i). In a second step 6793 mature T cells (Rag1 negative/Itm2a negative) were reanalysed (ii) to improve resolution in the mature lymphocyte compartment. B. Leiden clustering of mature T and NK cells identified 15 T and 1 NK cell clusters. C. Expression of selected T and NK cell markers used for cell type annotation.* ***(continued page 34)***

(continued) *Figure 2.4:* ***The single-cell landscape of mature T and NK cells in the aorta of mixed bone marrow chimeras (MBMCs).*** *D. Automatic cell type annotation using singleR and the ImmGen database as a reference. E. The dot plot shows the expression of selected cluster marker genes (BH-adjusted $P < 0.05$, two-sided Wilcoxon tests) and known cell-type marker genes. The colour of the dots represents the scaled average expression and their size reflects the percentage of cells within a cluster expressing the gene. Dots were only plotted for genes that were expressed in > 10% of cells in a cluster. F. The box plots show percentages of WT cells that were found in identified T and NK cell clusters. Composition at 12w WD and 18w WD were compared to steady state using scCODA.*

2.3.2. Defining the myeloid landscape in the aorta using scRNAseq

Both my scRNAseq and CYTOF analysis showed, in agreement with the literature, mononuclear phagocytes as one of the most abundant cell types in the aorta. Hence, to investigate plaque myeloid cell diversity in more detail I performed a separate analysis of the monocyte, macrophage and dendritic cell clusters identified in Figure 2.2 (see 6.7.4, Table 2.1). My myeloid-focused reanalysis of 12672 MNPs revealed 2 monocyte clusters (*Plac8*), 4 dendritic cell (DC) subsets (*Flt3*) and 16 macrophage clusters (*Adgre1*) (Figure 2.5A, B, E). Cell identities were confirmed using singleR annotations using the ImmGen database as a reference (Figure 2.5B).

Aortic monocytes were divided into *Ly6c2*$^{+}$ monocytes (*Ly6c2*, Cd177, Sell) and *Ace*$^{+}$ monocytes (*Ace, Spp, Treml4*) (Figure 2.5D,Figure S 2C), reflecting Ly6C^{hi} and Ly6C^{lo} monocyte subsets. Marker genes of both monocyte clusters were over-represented in phagocytic and monocyte trafficking pathways including "phagocytosis" (odds ratio (OR): *Ly6c2*$^{+}$:4.49, *Ace*$^{+}$:6.18) and "cellular extravasation" (OR: *Ly6c2*$^{+}$:5.45, *Ace*$^{+}$:6.73). Abundance of monocytes was similar at steady state (mean frequencies of MNPs: *Ly6c2*$^{+}$: 5.21%, *Ace*$^{+}$: 7.27%) and 12 w WD (mean frequencies: *Ly6c2*$^{+}$: 4.52%, *Ace*$^{+}$: 6.78%) (Figure S 2D). Notably, there was a significant increase in both monocyte populations at 18w WD (mean frequencies: *Ly6c2*$^{+}$: 9.06%, *Ace*$^{+}$: 20.26%), indicating monocyte recruitment to the aortic wall intensified after 18w of WD. *Ace*$^{+}$ monocytes were slightly more abundant than *Ly6c2*$^{+}$ at all time points.

As described above, my myeloid analysis led to the identification of 4 distinct dendritic cell populations; a cDC1 population characterised by expression of *Clec9a* and *Irf8*, a cDC2 population (*Cd209a,Clec10a*), a pDC population (*Siglech, Cd7*) and a *Ccr7*^{hi} DC subset that also expressed *Fscn1*, *Ccl22* which are associated with DC activation maturation[166,167] (Figure 2.5A,Figure S 2A,C). Dendritic cells (DCs) constituted 5-10% of the aorta MNP population throughout the different time points (mean frequencies of

MNPs: steady state=6.35%, 12w WD=9.43%, 18w WD 7.26%) with cDC2s and cDC1s forming the majority of DC populations at all time points, however no significant differences of subset abundances across the time course of metabolic disease progression were identified.

Previously published studies using scRNAseq have identified three major macrophage populations with different inflammatory properties in both murine and human atherosclerotic plaques[117]. These include inflammatory macrophages, lipid associated non-inflammatory macrophage, and resident homeostatic macrophages. Similarly, macrophages in my dataset could broadly be separated into three groups: 2 clusters of *Ccr2*$^{+}$ 'inflammatory' monocytic macrophages (mono/macs), 3 clusters of *Cd9*$^{+}$ macrophages, and 10 clusters of resident-like *Folr2*$^{+}$ macrophages. In addition, I identified one cluster of proliferating *Mki67*$^{+}$ macrophages (Figure 2.5A,D; Figure 2.6C). *Ccr2*$^{+}$ macrophages could further be distinguished by *Il1b* and *Cd226* expression (Figure 2.6C). The *Ccr2*$^{+}$*Ilb*$^{+}$ cluster also expressed high levels *Nlrp3* and monocyte associated genes including *Plac8*, and *Ms4a4c* suggesting a less mature monocyte-macrophage phenotype (mono/mac) (Figure S 3C). Marker genes for *Ccr2*$^{+}$*Ilb*$^{+}$ mono/macs were overrepresented in inflammatory response pathways, such as "I-kappaB kinase/NF-kappaB signaling" (OR: 3.26), suggesting an inflammatory phenotype (Figure S 1). Using CyTOF, a CCR2^{+} mono-mac population in murine atherosclerosis that positively correlated with disease progression has been described[109]. Consistent with this finding, *Ccr2*$^{+}$*Ilb*$^{+}$ mono/macs showed a significant increase in abundance at 18w WD when compared to steady state (Figure 2.6B). *Cd226* macrophages expressed *Itgax* which encodes for disease-associated macrophage marker CD11c, *Retnla* (encoding for Relm-alpha), *Ear2* and *Il6 (*Figure S 3*C)*. Relm-alpha is a marker for alternatively activated macrophages *in vitro* and *Retnla*^{hi} macrophages have been previously described in the aorta[67,104,117] using scRNAseq and shown to display similar gene signatures to peritoneal

macrophages, however their function is still unknown. In my dataset, *Ccr2*$^{+}$*Cd226*$^{+}$ marker genes were over-represented in pathways associated with insulin secretion, cell adhesion and migration as well as metabolic processes, i.e. “positive regulation of insulin secretion” (OR 3.18), “cellular response to fatty acid” (OR 10.9) (Figure S 1).

Cd9^{+} macrophages formed three clusters: First, *Plin2*^{hi} mono/macs expressed markers of lipid associated macrophages including *Cd9*, *Plin2*, *Fabp5*, *Spp1*, *Lgals3*, *Abcg1* and *Gpnmb* (Figure S 3B). This cluster displayed marker genes that were overrepresented in homeostatic LAM associated pathways like “Lysosome - Mus musculus (house mouse)” (OR 3.97), “Cholesterol metabolism - Mus musculus (house mouse)” (OR 7.45) (Figure S 1). However, this cluster did not differentially express *Trem2*, and in contrast to previous reports of the non-inflammatory transcriptome of LAMs, *Plin2*^{hi} mono/macs expressed pro-inflammatory genes including *Hif1a, Il1b*, *Osm* and *Cd274* as well as markers of recently recruited monocyte derived macrophages (mono/macs) such as *Cd44*, *Ly6c2* and *Ccr2* (Figure S 3B). While this cluster was not detected at steady state (mean frequency < 0.01%), its abundance significantly increased in disease indicating a disease associated phenotype (mean frequencies: 12w WD=2.21%, 18w WD=4.57%) (Figure 2.6B). The second *Cd9*$^{+}$ cluster, *Mmp12*$^{+}$ macrophages, constituted 1-2% of MNPs and displayed similar signature to that of the recently described Mac^{AIR} gene signature (*Cd9*, *Spp1*, *Cd72* and *Mmp12*) (Figure S 3B) [119]. The third *Cd9*$^{+}$ cluster I identified was *Saa3*$^{+}$ macrophages. *Saa3* is a member of acute-phase serum amyloid (SAA) apolipoproteins that are released in response to inflammation[168]. SAA proteins have been implicated in atherosclerosis[169–171] and obesity[172–174]. In male mice *Saa3* deficiency attenuated atherosclerosis[175,176] and obesity[177].

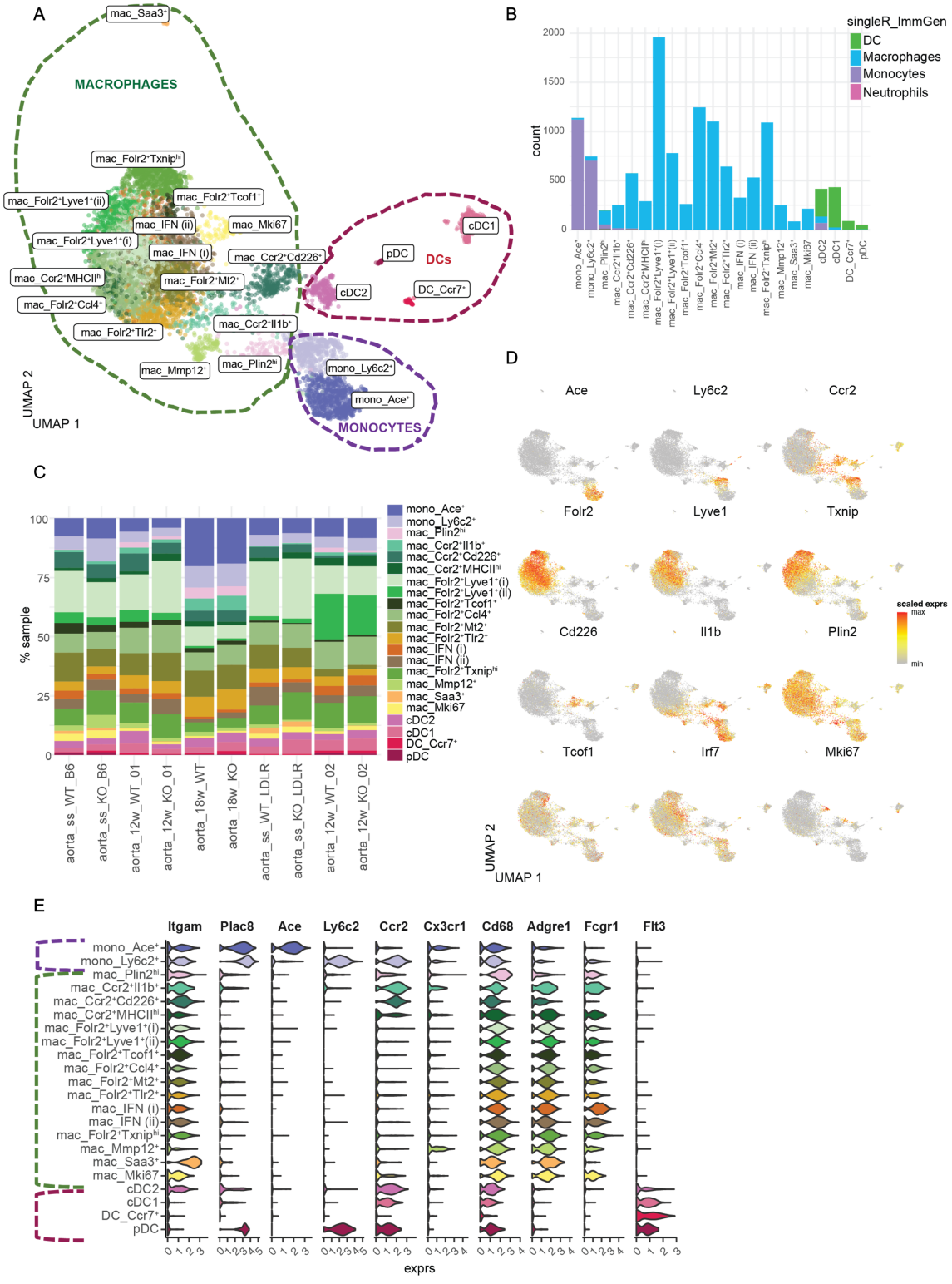


Figure 2.5: ***The single-cell mononuclear phagocyte landscape in the aorta of mixed bone marrow chimeras (MBMCs).*** *12672 mononuclear phagocytes (MNPs) from CD45^{+} sorted WT and IRF5$^{-/-}$ samples from MBMC aortas at steady state (n=2 per genotype), 12w western diet (WD) (n=2 per genotype), 18w WD (n=1 per genotype) were analysed A. Leiden clustering identified 2 monocyte clusters, 4 dendritic cell clusters and 16 macrophage clusters. B. Bar plots represent the number of cells in each cluster and are coloured by automatic cell type annotation using singleR and the ImmGen database as a reference. C. The bar plots show the cluster composition within each sample. D. Expression of selected cluster marker genes (BH-adjusted P < 0.05, two-sided Wilcoxon tests). E. The violin plot shows classical marker expression of monocyte, macrophage and dendritic cell markers.*

Folr2^{+}macrophages consisted of 2 *Folr2*$^{+}$*Lyve1*$^{+}$ homeostatic resident-like macrophage subsets that also expressed other markers of tissue resident macrophage gene signatures[118] including *Cd209f* and *Mrc1*. In my dataset, resident macrophages lacked expression of the bona fide resident marker *Timd4* (Figure S 3C), suggesting that monocyte derived donor macrophages in MBMCs cannot acquire *Timd4* expression. *Folr2*$^{+}$*Lyve1*$^{+}$ *(i) and (ii)* macrophages expressed high levels of *Stat3*, the transcription factor mediating anti-inflammatory effects of IL10[178,179], suggesting a homeostatic role. The *Folr2*$^{+}$*Lyve1*$^{+}$ *(i)* macrophage cluster was the most abundant cell cluster identified at steady state (mean frequency of MNPs: 20.29) (Figure 2.6B), and it significantly decreased with disease. In contrast *Folr2*$^{+}$*Lyve1*$^{+}$ *(ii)* macrophages showed a significant increase in abundance at 12 w WD, where they constituted the majority of MNPs (mean frequency of MNPs: 12.11%). *Folr2*$^{+}$*Lyve1*$^{+}$ *(ii)* macrophages expressed high levels of *Mertk* and marker genes were overrepresented in endocytosis associated pathways (i.e. "endocytosis involved in viral entry into host cell" (OR 8.11)) (Figure S 1, Figure S 3C). In addition, this cluster differentially expressed genes associated with cholesterol export including *Abca1, Abca9*. This transcriptional phenotype suggested *Folr2*$^{+}$*Lyve1*$^{+}$ (ii) to be highly adapted to the atherosclerotic plaque environment.

Folr2^{+}*Tcof1*$^{+}$ macrophages expressed *Pde4c* which encodes for the cAMP phosphodiesterase 4 (PDE4). PDE4 inhibitors suppress inflammatory responses in human PBMCs by specific downregulation of PDE4A and PDE4B, and upregulation of PDE4C[180]. *Tcof1* encodes for Treacle which plays an important role in physiological processes including ribosomal DNA transcription, DNA damage response and mitotic regulation[181].

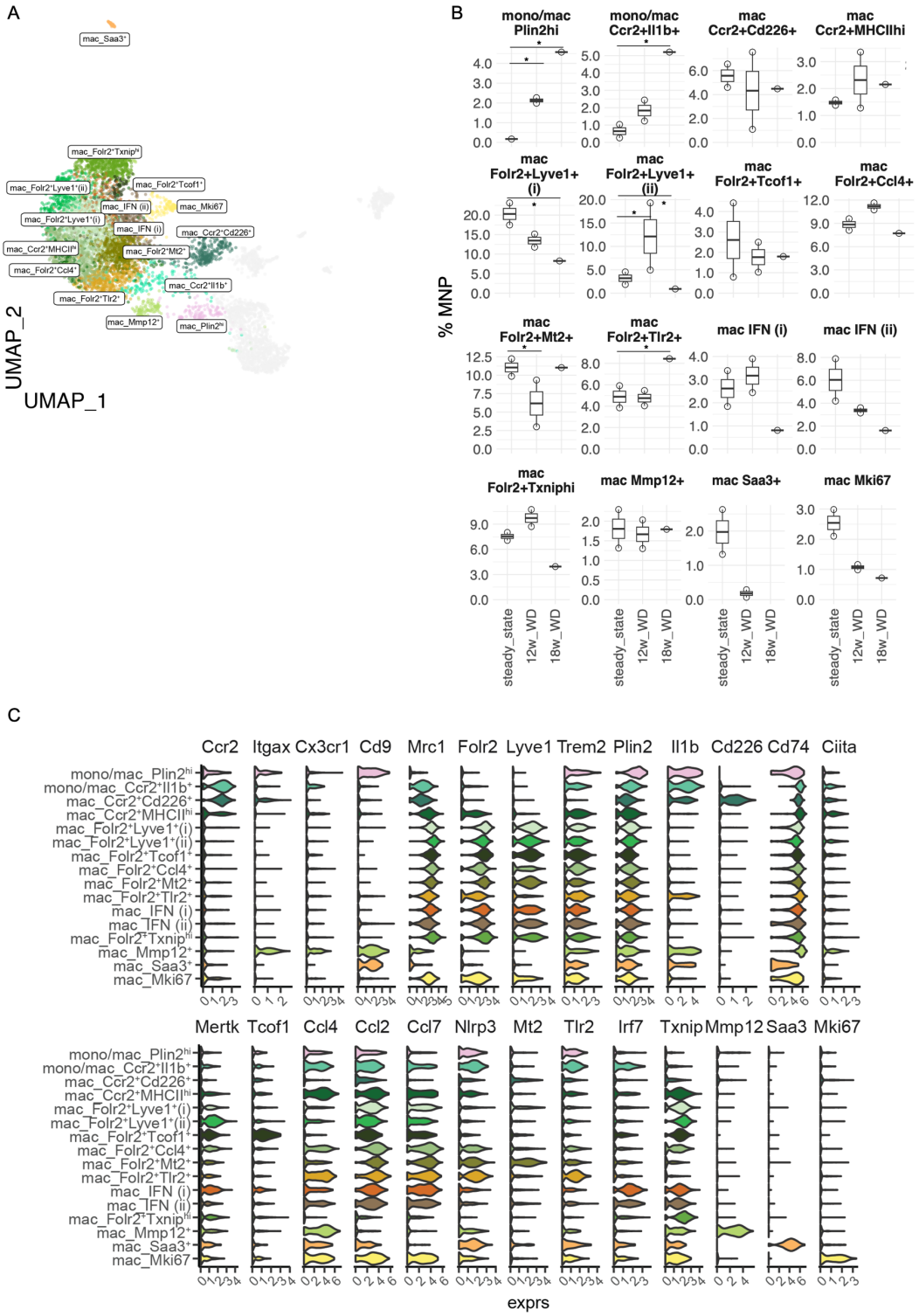


Figure 2.6: ***The single-cell landscape of macrophages in the aorta of mixed bone marrow chimeras (MBMCs).*** *12672 mononuclear phagocytes (MNPs) from CD45$^+$ sorted WT and IRF5$^{-/-}$ samples from MBMC aortas at steady state (n=2 per genotype), 12w western diet (WD) (n=2 per genotype), 18w WD (n=1 per genotype) were analysed. A. Leiden clustering of the MNPs in the aorta identified 16 macrophage clusters that could be further grouped into 2 Ccr2$^+$ cluster, 3 Cd9$^+$ clusters and 10 Folr2$^+$ cluster and 1 Mki67$^+$ cluster. B. The box plots show percentages of WT cells that were found in identified clusters. Compositions at 12w WD and 18w WD were compared to steady state using scCODA. C. The violin plots show the expression levels of selected cluster marker genes (BH-adjusted $P < 0.05$, two-sided Wilcoxon tests) in each of the identified macrophage clusters.*

Marker genes of *Folr2*$^{+}$*Tcof1*$^{+}$ macrophages were over-represented in pathways associated with transcriptional regulation ("stem cell differentiation" OR: 2.82) and extracellular sensing ("glycosaminoglycan binding" OR:5.23, "sensory perception of mechanical stimulus" OR:4.36). This suggests that *Folr2*$^{+}$*Tcof1*$^{+}$ macrophages might be more stem-like homeostatic macrophages (Figure S 1). *Folr2*$^{+}$*Txnip*^{hi} macrophages expressed high levels of thioredoxin-interacting protein (TXNIP) which controls the acidification of phagosomes in macrophages after the engulfment of bacteria[118] and the cluster markers were over-represented in endocytosis pathways ("positive regulation of endocytosis" OR: 2.89), suggesting that they are phagocytic tissue resident macrophages (Figure S 1).

In addition, I identified 3 *Folr2*$^{+}$*Nlrp3*$^{+}$ activated macrophages subsets whose cluster markers were overrepresented in pathways associated with chemokine and growth factor signalling (Figure S 1): *Folr2*$^{+}$*Ccl4*$^{+}$ macrophages expressed high levels of chemokines *Ccl2, Ccl4, Ccl7, Ccl3* as well as *Il10*, indicating a role in modulating inflammation in the aorta. Marker genes for *Folr2*$^{+}$*Mt2*$^{+}$ macrophages included metallothionein encoding genes *Mt1* and *Mt2* as well as *Emp1*, in addition to the chemokine signature identified for *Folr2*$^{+}$*Ccl4*$^{+}$ macrophages. *Folr2*$^{+}$*Mt2*$^{+}$ gene signature displayed some similarity to that of the previously described Mox macrophages[182]. Mox are atherosclerosis-associated macrophages that form in response to plaque lipids and are known to promote monocyte chemotaxis[182]. Mox have been shown to upregulate redox-regulated genes including *Mt2* have been described in the context of atherosclerosis[149,182] and hypertension[183]. *Folr2*$^{+}$*Tlr2*$^{+}$macrophages expressed high levels of *Il1b, Nlrp3* and *Tnf* suggesting a resident subset with a pro-inflammatory phenotype (Figure S 3B).

Finally, two *Folr2*$^{+}$ *IFN* responsive macrophage subsets were identified by expression of *Irf7* and *Isg15*.

2.3.2.1. Validation of clusters identified in the aorta of mixed bone marrow chimeras using published scRNAseq datasets

To validate the MNP transcriptomic signatures in my mixed bone marrow chimera model, I next performed an integrated analysis of MNPs combining the here presented dataset with 6 previously published scRNAseq datasets of healthy and atherosclerotic murine aortas (Methods 6.7.5). In the combined analysis I identified a total of 26 clusters including 2 monocyte clusters, 4 dendritic cell clusters and 20 macrophage clusters (Figure 2.7A). Clusters were annotated using marker genes discussed in the previous section. All monocyte and dendritic cell clusters identified in my dataset described in the previous section were also identified in the combined integrated analysis (Figure 2.7,Figure S 4). I also identified similar clusters across both analyses in the macrophage compartment (Figure S 4). Clusters with highest conservation of cells across both analyses included*:* *Ccr2*$^{+}$*Cd226*$^{+}$ mono/macs, *Folr2*$^{+}$*Lyve1*$^{+}$ macrophages, *Folr2*$^{+}$*Tcof1*$^{+}$ macrophages, *Folr2*$^{+}$*Txnip*^{hi} macrophages, *Folr2*$^{+}$*Ccl4*$^{+}$ macrophages, IFN responsive macrophages, *Mmp12*$^{+}$ macrophages, *Saa3*$^{+}$ macrophages and cycling *Mki67*$^{+}$ macrophages. Some resident-like *Folr2*$^{+}$ clusters identified in my dataset now clustered together forming one chemokine expressing population referred to as *Ccl2*$^{+}$*Ccl7*$^{+}$ macrophages. In addition, *Folr2*$^{+}$*Mt2*$^{+}$ and *Folr2*$^{+}$*Tlr2*$^{+}$ macrophages could not be separated in the integrated analysis and were merged into one cluster referred to as *Folr2*$^{+}$*Nlrp3*$^{+}$ macrophages (Figure S 4). I also identified in the community integrated analysis 2 *Trem2*^{hi} LAM clusters that could be distinguished by *Gpnmb* and *Slamf9* expression as previously reported[103] with *Gpnmb*$^{+}$ population expressing the highest lipid-associated signature with a notable lack of inflammatory genes in agreement with the previous published murine *Trem2*^{hi} LAM populations[105,117].

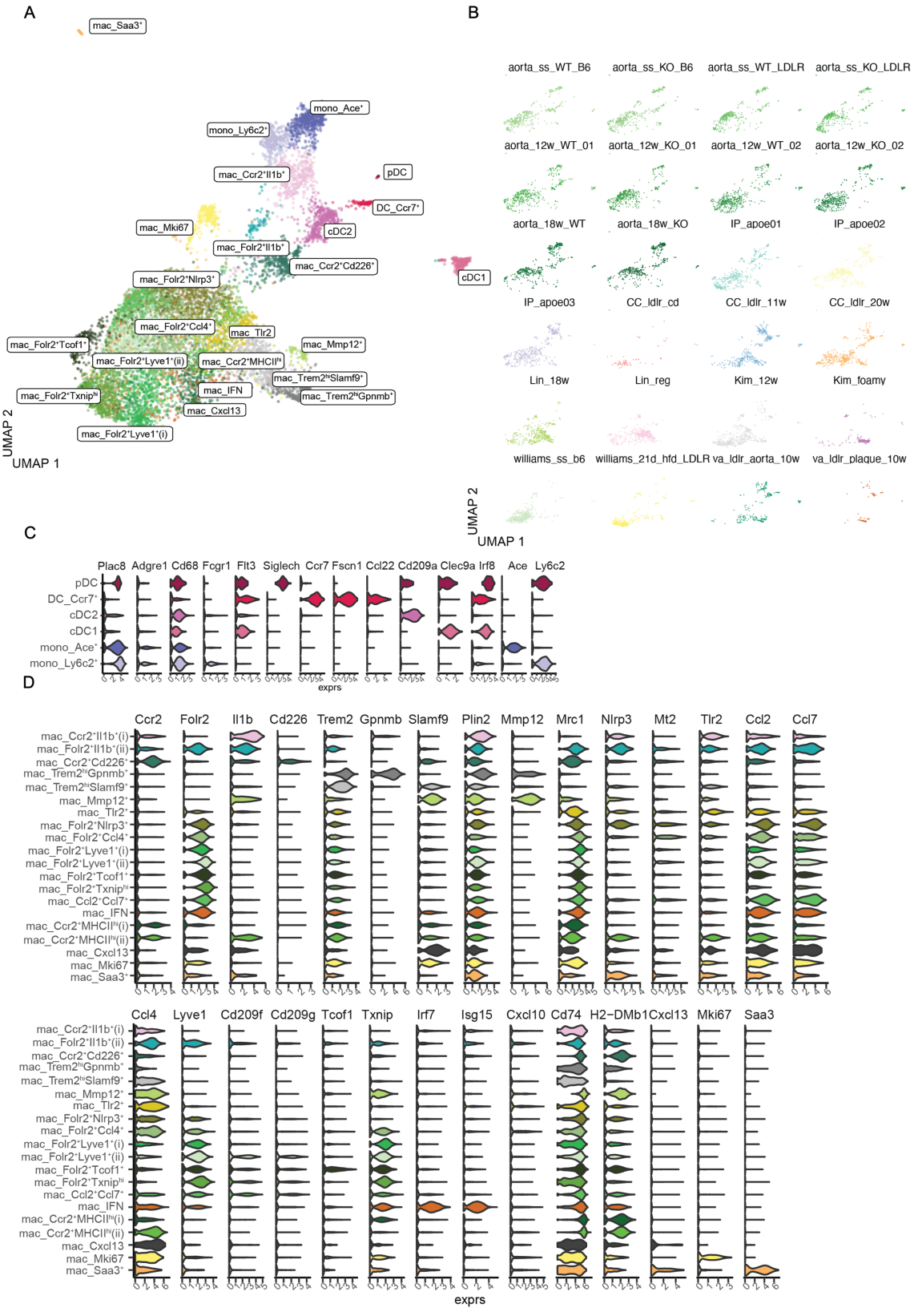


Figure 2.7: ***Integrated analysis of 7 scRNAseq studies of the aorta****. An aortic mononuclear phagocyte (MNP) atlas was constructed by integrated analysis of 6 publicly available scRNAseq datasets (Table S 3) of healthy and atherosclerotic aortas and 12672 mononuclear phagocytes (MNPs) from CD45^{+} sorted WT and IRF5$^{-/-}$ samples from mixed bone marrow chimera (MBMC) aortas. A. The UMAP shows the integrated dataset. Leiden clustering identified 2 monocyte clusters, 4 dendritic cell clusters and 20 macrophage clusters. B. The UMAP shows the cells faceted by study. C./D. The violin plot shows marker gene expression (BH-adjusted P < 0.05, two-sided Wilcoxon tests) of selected monocytes and dendritic cell markers clusters (C.) and macrophage clusters (D.)*

I did not identify similar *Trem2^{hi}* populations in my competitive chimera dataset, however, the population with the highest lipid associated gene signature in the MBMC dataset, the *Plin2^{hi}* mono/macs, clustered with *Ccr2^{+}Il1b^{+}* mono/macs and only few clustered with Tem2^{hi} LAMs (Figure S 4). This suggested that Plin2^{hi} mono/macs identified in the MBMC dataset most likely represented a mixed clusters of mostly inflammatory *Ly6c2^{+}Plin2^{+}* mono/macs and a few *Trem2^{hi}* LAMs. The lack of bona fide LAMs in my dataset could be a result of the irradiation treatment where lipid accumulation and hematopoietic cells might be compromised[184–187] which could affect *Trem2^{hi}* LAMs progenitor cells in the blood and plaque.

After showing conservation of most myeloid cluster signature between my dataset and the community datasets, I investigated whether compositional distribution of these defined clusters differed between my MBMCs data and the community datasets from whole aorta digestion at steady state, in disease (12-16w diet) and at a later disease time point (> 16 w diet) using scCODA (Figure 2.8).

At steady state, *Ace2^{+}* (log2FC abundance: 2.28) and *Ly6c2^{+}* (log2FC abundance: 1.91) monocytes as well as *Ccr2^{+}Cd226^{+}* macrophages (log2FC abundance: 21.31) were significantly more abundant in the MBMC dataset compared to non-irradiated community datasets (Figure 2.8). After irradiation, the myeloid niche in the aorta is primarily reconstituted through monocyte recruitment[188] which might contribute to higher monocyte abundance in my competitive chimera model as compared to the non-irradiated models. In addition, at steady state resident macrophages were distributed differently between my dataset and the non-irradiated community samples: *Folr2^{+}Lyve1^{+}* (i) macrophages constituted the majority of resident macrophages in non-irradiated samples at steady state (mean frequency of MNPs: 30.95%), but were absent in MBMCs at steady state (mean frequency: 0.75%). In contrast, *Folr2^{+}Lyve1^{+}* (ii) (mean frequency of MNPs: MBMC=9.75%, community=4.19%) and *Ccl2^{+}Ccl7^{+}* (mean frequency:

MBMC=26.50%, community=1.27%) macrophages constituted the majority of resident macrophages in MBMCs at steady state (Figure 2.8). Both of the latter clusters expressed high levels of chemokines (*Ccl2, Ccl7*) (Figure 2.7B) suggesting a more activated and chemotactic signature in aortic resident macrophages in MBMCs at steady state when compared to non-irradiated aortas. This was possibly due to the dynamic recruitment happening post-irradiation. *Trem2^{hi}Slamf9^{+}* macrophages were also more abundant at steady state in non-irradiated samples than in MBMCs (mean frequency: MBMC=0.55%, community=3.05%) whereas *Trem2^{hi}Gpnmb^{hi}* macrophages were minimal and non-existent in community and my dataset respectively at steady state (Figure 2.8).

After 12-16w diet and >16w diet non-irradiated community samples showed significantly higher abundance of *Trem2^{hi}Gpnmb^{+}*, *Trem2^{hi}Slamf9^{+}* and *Ccr2^{+}MHCII^{hi}* (i)/(ii) macrophage clusters. Accumulation of LAMs and antigen presenting cells in plaques is a hallmark of disease progression[105,112], and the lack of thereof in the MBMCs suggests a delayed disease progression and/or a compromised disease progression phenotype. The reduced numbers of LAMs in our aortic scRNAseq dataset might be due to (i) an effect of irradiation on lipid accumulation in macrophages, (ii) an irradiation effect on the transcriptome of resident-like macrophages at steady state that might be precursors for disease-associated phenotypes, (iii) an irradiation effect on the transcriptome on non-immune cells that might affect the aortic microenvironment through differences in chemokine production, (iv) the aortic microenvironment driven by differences in diet composition or the presence of IRF5$^{-/-}$ cells.

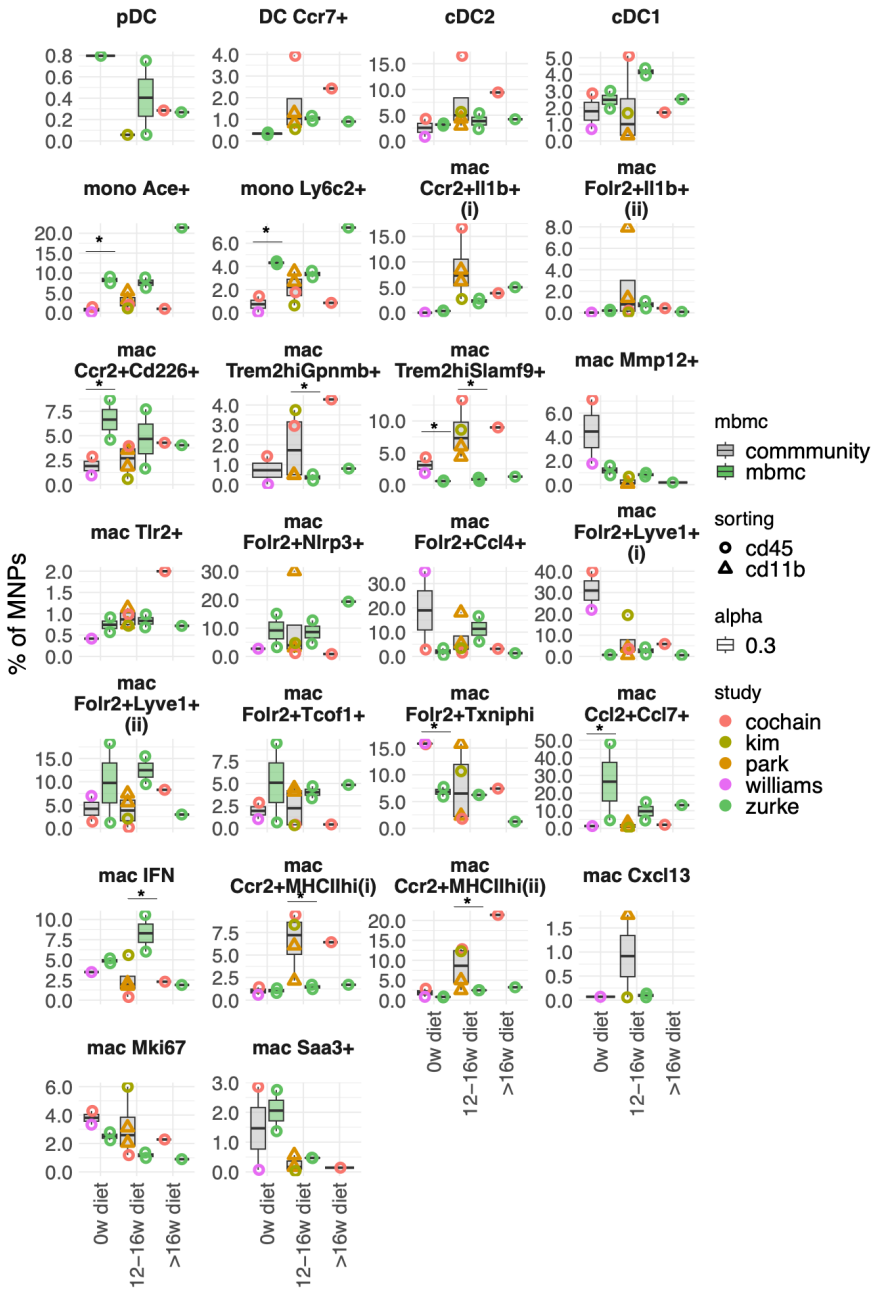


Figure 2.8: ***Comparison of aortic macrophage cluster composition between mixed bone marrow chimeras (MBMCs) and community datasets.*** *The box plots show percentages of WT cells from CD11b$^+$ or CD45$^+$ enriched datasets that were found in identified clusters. Composition between MBMC and non-irradiated community datasets was compared at steady state (0 week diet) and 12-16 week diet using scCODA.*

Next, I investigated transcriptional differences between macrophages from MBMCs and community datasets. For that purpose, differential gene expression analysis of pseudobulk data was applied using edgeR (Methods) (Figure S 5). For steady state analysis, I used the non-irradiated dataset from Williams *et al*[119] for comparison. Macrophages from steady state MBMCs differentially upregulated pro-inflammatory genes (*Il1b, Nlrp3, Osm, Cxcl1*) as well as genes associated with myeloid chemotaxis, macrophage differentiation and activation (*Nr4a1, Cebpb, Cxcr4, Lyz1, Ccr2*) whereas the non-irradiated dataset of Williams *et al* showed differentially higher expression of bona fide resident macrophage markers including *Timd4* and *Cxc3cr1* as well as cell survival cues (*Bcl2* and *Hsph1*) (Figure S 5A).

To investigate differential gene expression in disease, I compared macrophages from my MBMCs dataset to that of Kim *et al*[105]. Kim *et al* was the best fit study to use for comparative analysis since they used a similar experimental design (minus irradiation) to my experimental model in terms of dietary intervention length (12weeks), murine strain ($LDLR^{-/-}$) and gender (male), sorting strategy (CD45 sorting) as well as number of cells recovered. DEGs in MBMCs included chemokines *Il12b*, *Ccl2*, *Ccl4*. In contrast DEGs upregulated in Kim *et al* included *Timd4*, *Col14a1*, and *Mmp14* known to be involved in vascular homeostasis and tissue remodelling. In addition, macrophages in Kim *et al* showed significantly higher expression of genes associated with the *Trem2*^{hi} LAM signature (*Acp5, Itgax, Cd9, Spp1, Fabp4, Fabp5, Cd72*), reflecting the minimal presence of bona fide LAMs in our irradiated model and highlighting the compositional differences in macrophages described above (Figure S 5B). In line with the overall more homeostatic phenotype of macrophages in the Kim *et al* dataset, *Trem2*^{hi} LAMs in mouse and humans have been described to show a homeostatic transcriptional signature.

Finally, since the *Trem2*^{hi} LAM population was the cluster were my dataset mostly differed from the community analysis compositionally, and given the transcriptional

differences in resident-like macrophages at steady state, I set up to investigate whether compositional differences in the *Trem2*^{hi} LAM compartment in disease were due to differences in its progenitor population. To explore the possibility that only bona fide resident macrophages could give rise to *Trem2*^{hi} LAMs, I performed trajectory analysis of MBMCs and selected community datasets at steady state and disease (12-16w diet) using scVelo and cellrank (Methods) (Figure 2.9).

At steady state, both Williams *et al* and the MBMC dataset trajectory analysis suggested that the resident macrophage compartment was self-contained with minimum contribution form monocytes or cycling *Mki67*$^{+}$ macrophages (Figure 2.9A,B). Velocity streams pointed towards a direction of macrophage activation with *Folr2*$^{+}$*Txnip*^{hi} macrophages, the least activated macrophage cluster, being the root and *Folr2*$^{+}$*Ccl4*$^{+}$ and *Folr2*$^{+}$*Nlrp3*$^{+}$ forming the end of the velocity streams. At 12w WD, I still observed the same activation trajectory within the *Folr2*$^{+}$ macrophage compartment, from least to more activated phenotype, in both my MBMCs and the community datasets (Kim *et al*[105] and *Park et al*[149]) (Figure 2.9E-J).

Trem2^{hi} LAMs on the other hand did not seem to have a distinct root cluster. In both community datasets, only some *Mki67*$^{+}$ cycling macrophages were projected into the *Trem2*^{hi} LAMs cluster (Figure 2.9E-H). In contrast, in the MBMC dataset the few *Trem2*^{hi} LAMs identified using integrated analysis were projected to come from monocytes, further suggesting that the LAMs identified in the MBMC datasets are mostly monocytic. Overall, the origin of *Trem2*^{hi} LAMs could not be determined from this velocity analysis. Differences in LAM abundance between community datasets and my MBMC dataset may therefore be due to differences in the precursor due to irradiation and/or differences in microenvironment or diet.

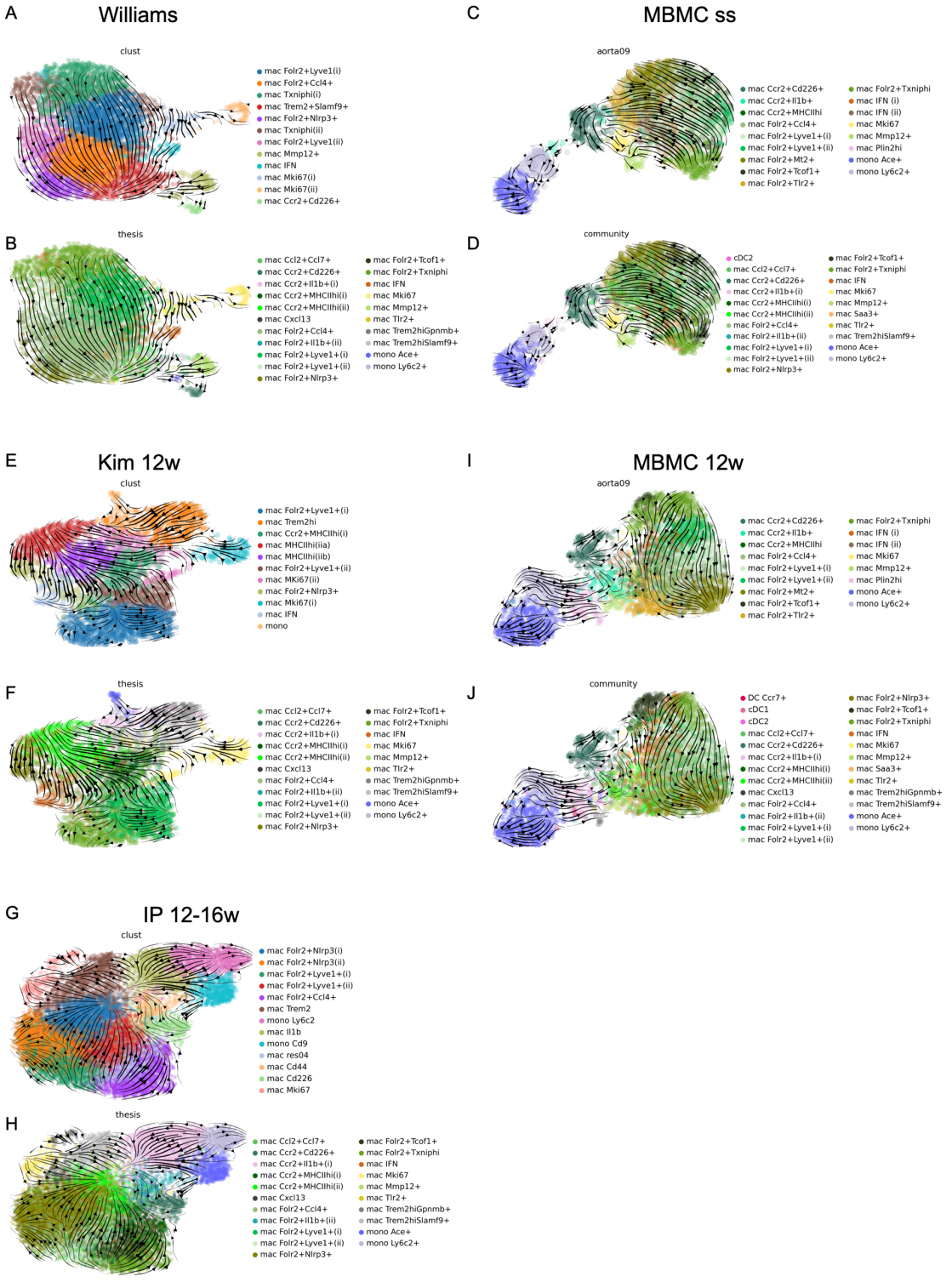


Figure 2.9: ***Trajectory analysis of aortic mononuclear phagocyte clusters in mixed bone marrow chimeras (MBMCs) and community datasets at steady state and in disease.*** *Pseudotime velocity analysis was performed on steady state and disease MBMC and community (Table S 3) samples using scVelo. A-H. PAGA initialised UMAP representations of velocity streams for Williams et al (A-B), MBMC at steady state (C-D), Kim et al at 12w diet (E-F), Park et al at 12-16 w diet (H-G) and MBMC at 12w WD (I-J). Cells in A,C,E,I,G are coloured by clusters identified when studies were analysed separately (see 6.7.9.1). Cells in B,D,F,H,J are coloured by clusters identified in the integrated analysis (see 6.7.5). Arrows indicate directions of predicted future transcriptional states.*

2.4. Defining the epididymal white adipose tissue immune cell landscape of mixed bone marrow chimeras during metabolic disease progression using scRNAseq

Table 2.2: Overview of samples included to define the epididymal white adipose immune cell and mononuclear phagocyte landscapes during metabolic disease progression.

tissue	disease time point	genotype	batch	number of mice in pool	Sorting strategy
epiWAT	steady state	WT	A	6	Live CD45+
epiWAT	steady state	KO	A	6	Live CD45+
epiWAT	12w WD	WT	B	4	Live CD45+
epiWAT	12w WD	KO	B	4	Live CD45+
epiWAT	steady state	WT	C	10	Live Lineage-Cd11b+CX3CR1+
epiWAT	steady state	KO	C	10	Live Lineage-Cd11b+CX3CR1+
epiWAT	12w WD	WT	D	7	Live Lineage-Cd11b+CX3CR1+
epiWAT	12w WD	KO	D	7	Live Lineage-Cd11b+CX3CR1+
epiWAT	18 w WD	WT	E	6	Live Lineage-Cd11b+CX3CR1+
epiWAT	18 w WD	KO	E	6	Live Lineage-Cd11b+CX3CR1+

Two sorting strategies were applied to epiWAT samples for scRNAseq at steady state and 12w WD: live $CD45^+$ cells were sorted to acquire an overview of the whole immune cell compartment, and live $CD11b^+CX3CR1\text{-}GFP^+$ cells were sorted to enrich for monocyte derived mononuclear phagocytes. To resolve the immune cell landscape of MBMCs during a time course of metabolic disease progression, I integrated WT and $IRF5^{-/-}$ cells from epiWAT samples from steady state, 12w WD and 18w WD from both sorting strategies (n=5 samples per genotype, Table 2.2). Low resolution clustering was applied and 7 leukocyte clusters were annotated based on expression of cell type markers and singleR annotations: 2 T cell clusters (*Cd3e*), 1 NK cell cluster (*Nkg7*), 1 B cell cluster

(*Cd79a*), a plasma cell cluster (*Jchain*, *Sdc1*), a neutrophil cluster (*Retnlg*, *Csf3r*), 3 dendritic cell clusters (*Flt3*, *Cd209a*), 5 macrophage clusters (*Itgam*, *Adgre1*), and a monocyte cluster (*Plac8*, *Ace*, *Ly6c2*) (Figure 2.10A-C). All cell types were represented in the 4 live $CD45^+$ samples, while live $CD11b^+CX3CR1\text{-}GFP^+$ samples, as expected, only contained mononuclear phagocyte clusters (Figure 2.10D). Next, clusters were aggregated to major cell lineages: mononuclear phagocytes (MNPs), B/plasma cells, T/NK cells and neutrophils. At steady state and in metabolic disease, immune cells in the epiWAT were primarily comprised of mononuclear phagocytes (steady state:45.12%, 12 WD:55.11%), T/NK cells (steady state:35.76%, 12 WD:30.26%), B/plasma cells (steady state:30.9%, 12w WD:23.93%), and neutrophils (steady stae:1.62%, 12w WD:0.85%) (Figure 2.10F). Next, cell lineage abundances were validated using CyTOF (Figure 2.11): mononuclear phagocytes (steady state:45.12±9.12%, 12 WD:59.10±10.88%), T/NK cells (steady state:24.21±1.08%, 12 WD:25.09±6.91%), B/plasma cells (steady state:15.71±5.98%, 12w WD:12.18±2.81%), neutrophils (steady stae:2.52±1.71%, 12w WD:0.97^+±01.21%) and eosinophils (steady stae:11.43±6.56%, 12w WD:2.64±0.96%). Similar to the aorta, I identified eosinophils only using CyTOF but not scRNAseq likely due to the high expression levels of ribonucleases in eosinophils. A small increase in MNPs in the epiWAT was observed at 12 weeks WD using both scRNAseq (Figure 2.10F) and CYTOF (Figure 2.11C), however no statistical significance was reached when assessed by scCODA.

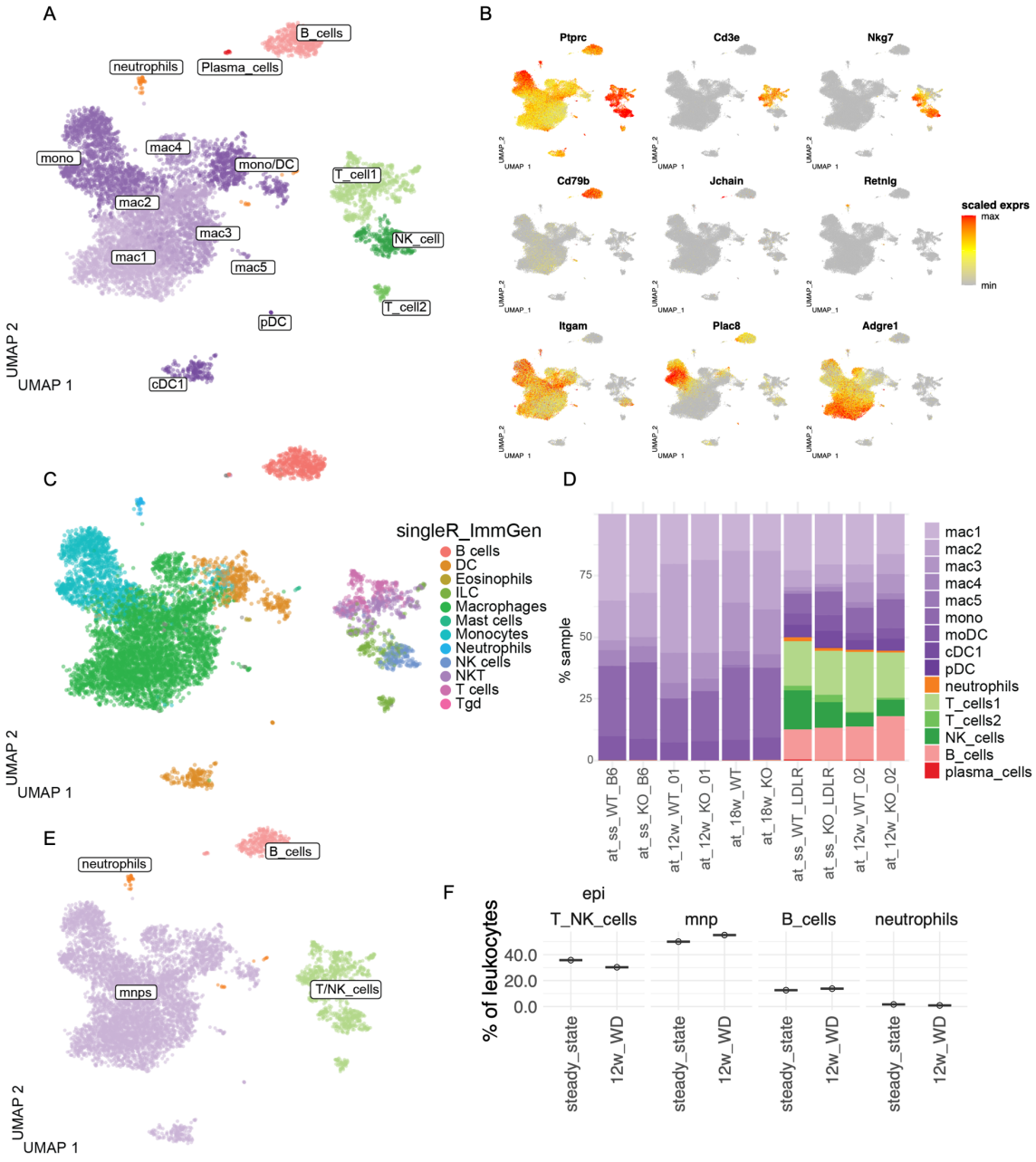


Figure 2.10: ***Defining the epiWAT immune cell landscape of mixed bone marrow chimeras (MBMCs) in metabolic disease using scRNAseq.*** *scRNAseq was performed on CD45$^+$ and Lin$^-$CD11b$^+$CX3CR1$^+$ sorted WT and IRF5$^{-/-}$ samples from MBMC epiWAT at steady state (n=1 per genotype and sorting strategy), 12w western diet (WD) (n=1 per genotype and sorting strategy), 18w WD (n=1 per genotype sorted for Lin-CD11b$^+$CX3CR1$^+$). 50927 leukocytes were analysed to get an overview of immune cell composition in the epiWAT. A. Leiden clustering identified 15 leukocyte clusters. B. Expression of selected cluster marker genes (BH-adjusted P < 0.05, two-sided Wilcoxon tests) and known cell type markers used for cell type annotation C. Automatic cell type annotation using singleR and the ImmGen database as a reference. D. The bar plots show the cluster composition within each sample. E. Identified clusters were grouped into major cell lineages based on classical marker expression and singleR annotations (B,D). F. The bar plots show percentages of WT cells from CD45$^+$ sorted samples that were found in each major cell lineage.*

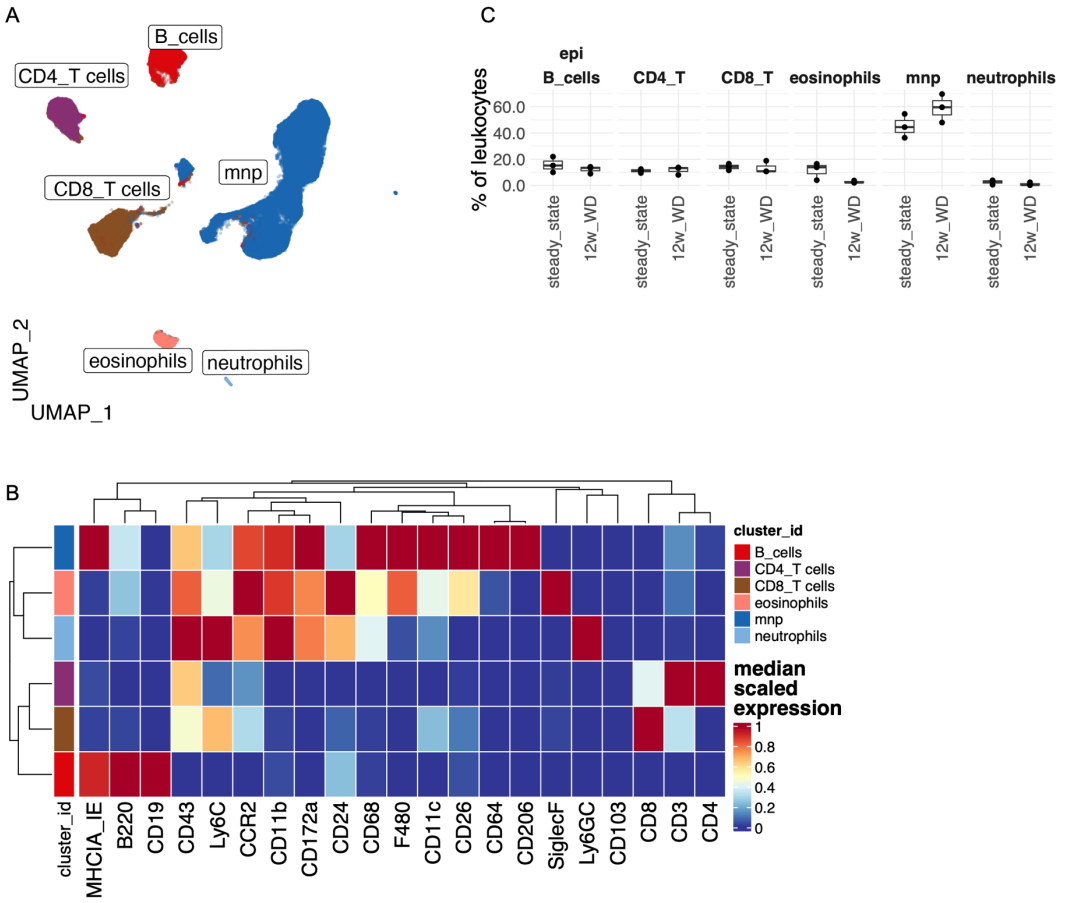


Figure 2.11: ***Defining the epiWAT immune cell landscape of mixed bone marrow chimeras (MBMCs) in metabolic disease using CyTOF.*** *CyTOF was performed on epiWAT from MBMCs at steady state (n=3) and 12w WD (n=3). A. CD45^{+} cells were analysed using FlowSOM clustering. Clusters were merged based on major cell lineage marker expression (CD19, CD3, CD11b, Ly6G/C, SiglecF). B. The box plots show percentages of WT cells that were found in each major cell lineage. No significant changes in composition were identified at 12w WD when compared to steady state using scCODA. C. The heatmap shows the median scaled surface marker expression levels of cell lineage markers that were used for FlowSOM clustering.*

2.4.1. Defining the T and NK cell landscape in the epididymal white adipose tissue using scRNAseq

Table 2.3: Overview of samples included to define the epididymal white adipose tissue T and NK cells landscapes during metabolic disease progression.

Tissue	disease time point	genotype	batch	number of mice in pool	Sorting strategy
epiWAT	steady state	WT	A	6	Live CD45+
epiWAT	steady state	KO	A	6	Live CD45+
epiWAT	12w WD	WT	B	4	Live CD45+
epiWAT	12w WD	KO	B	4	Live CD45+

Granular reanalysis of 5688 T/NK cells identified in live $CD45^+$ sorted samples (n=2 samples per timepoint and genotype, Table 2.3) resulted in 17 clusters (Figure 2.12A-C): 1 mixed naïve T cell clusters containing $CD4^+$ and $CD8^+$ cells, 6 $CD4^+$ T cell clusters, 3 activated $CD8^+$ clusters, IFN responsive T cells, proliferating T cells, a $NCR1^+$ ILC3 cluster, an ILC2 cluster and 3 NK cell clusters. $CD4^+$ clusters could be divided into central memory CD4 T cells (CD4 TCM) expressing naïve T cell markers in addition to *Cd200* and *Il6ra*, TH1 CD4 T cells expressing *Cx3cr1* and high levels of *Ifng*, TH2 CD4 T cells expressing *Il2*, *Il3*, *Il4* and *Il13*, TH17 CD4 T cells expressing *Rorc*, *Il17a* and *Il23r*, CD4 Tregs expressing *Foxp3* and *Ctla4*, and CD4 T follicular helper cells (Tfh) expressing *Cxcr5*, *Bcl6* and *Il21*. CD8 T cell clusters exhibited an activated phenotype with high expression levels of *Ccl5*, *Ly6c2* and *Txk* and formed 2 clusters, an activated/cytotoxic CD8 T cell cluster characterised by high expression of cytotoxicity markers *Gzmk*, *Eomes* and *Pdcd1* and an activated/mixed Cd8 T cell cluster characterised by expression of *Klrb1c*, *Klra9* and *Nkg7* markers also expressed in NK cells suggesting that this cluster might also contain NK cells or NKT cell. Innate lymphoid cell (ILC) clusters were negative for CD3-, CD4-, and CD8- encoding genes and the three NK clusters could be distinguished by high *Xcl1* expression ($Xcl1^+$ NK cells), expression of cytotoxicity markers *Gzma*, *Prf1* (cytotoxic NK cells) and expression of *Ikzf1* (immature NK cells) a

transcription factor known to be relevant for NK cell maturation[164]. NK cells and other ILCs comprised the majority of T/NK cells in the adipose tissue at steady state (NK cells = 34.23%, ILC2=5.31%, ILC3=9.21%) (Figure 2.12E). Unlike in the aorta, even at steady state T cells showed an activated phenotype (cytotoxic CD8 T cells=9.65%, CD4 TH1=6.5%) rather than a naïve phenotype (naïve T cells=6.9%). At 12w WD, activated/cytotoxic $Cd8^{+}$ T cells (25.70%) became the majority of cells in the adipose tissue.

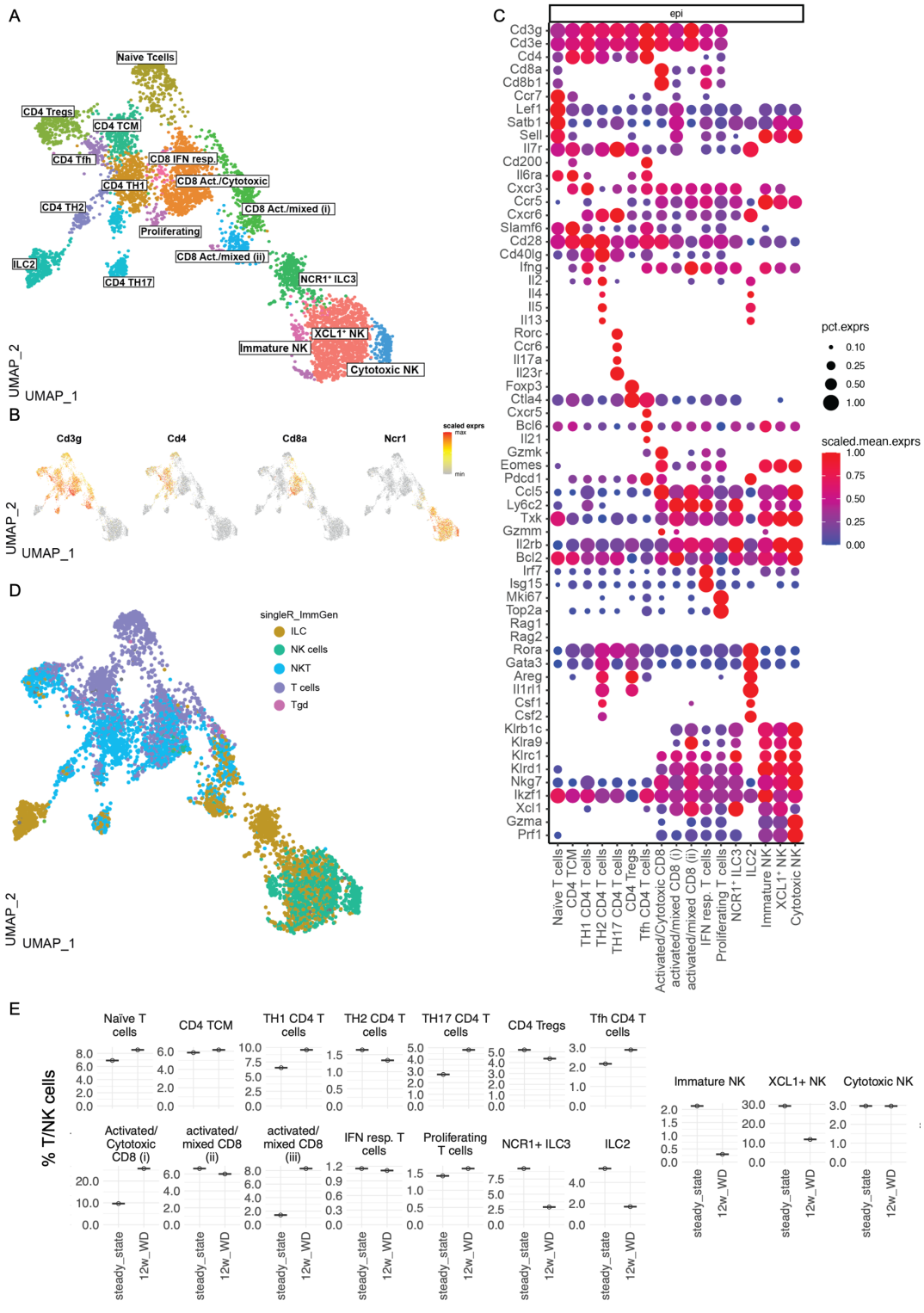


Figure 2.12: ***The single-cell landscape of mature T and NK cells in the epiWAT of mixed bone marrow chimeras (MBMCs).*** *scRNAseq was performed on CD45$^+$ and Lineage$^-$CD11b$^+$CX3CR1$^+$ sorted WT and IRF5$^{-/-}$ samples from MBMC epiWAT at steady state (n=1 per genotype and sorting strategy), 12w western diet (WD) (n=1 per genotype and sorting strategy), 18w WD (n=1 per genotype sorted for Lin-CD11b$^+$CX3CR1$^+$). T and NK cells identified in CD45$^+$ sorted samples were reanalysed. A. Leiden clustering of 5688 T and NK cells identified 14 T and 3 NK cell clusters. B. Expression of selected T and NK cell markers used for cell type annotation C. The dot plot shows the expression of selected cluster marker genes (BH-adjusted P < 0.05, two-sided Wilcoxon tests) and known cell-type marker genes. The colour of the dots represents the scaled average expression and its size reflects the percentage of cells within a cluster expressing the gene. Dots were only plotted for genes that were expressed in > 10% of cells within the cluster. D. Automatic cell type annotation using singleR and the ImmGen database as a reference. E. The box plots show percentages of WT cells that were found in identified clusters.*

2.4.2. Defining the MNP landscape in the epididymal white adipose tissue using scRNAseq

Next, I reanalysed the 42455 MNPs from all epiWAT samples (n=5 samples per genotype, Table 2.2), including samples sorted for live $CD45^+$ and live $Lineage^-$ $Cd11b^+CX3CR1^+$ cells, to phenotype the MNP compartment in the epiWAT during metabolic disease progression better. Reanalysis identified 17 MNP clusters: 11 macrophage clusters (*Adgre1*), 2 monocyte clusters (Plac8, *Ly6c2*, *Ace*) and 4 DC (*Flt3, Dpp4*) cluster (Figure 2.13A,D). Cell type identities were also confirmed using singleR (Figure 2.13B).

The same monocyte and dendritic cell populations described in the aorta were identified in the epiWAT analysis (Figure S 6A-D): monocytes were comprised of $Ly6c2^+$ monocytes (*Ly6c2, Cd177, Sell*) and Ace^+ monocytes (*Ace, Spp, Treml4*), and identified dendritic cell populations were cDC1(*Clec9a*, *Irf8*), cDC2 (*Cd209a,Clec10a*), pDC (*Siglech,Ly6d*) and a $Ccr7^{hi}$ DC subset that also expressed *Fscn1*, *Ccl22* which are associated with DC activation, migration and maturation[166,167] (Figure S 6). Similar to the aorta, marker genes of both monocyte clusters were over-represented in phagocytic and monocyte trafficking pathways including "positive regulation of phagocytosis" (odds ratio: $Ly6c2^+$:5.31, Ace^+:5.52), "cellular extravasation" (odds ratio: $Ly6c2^+$:5.83, Ace^+:4.44) (Figure S 6).

Macrophages in the epiWAT were classified into 4 resident-like macrophage clusters (*Pf4, C1qa, C1qc*), 4 $Ccr2^{hi}$ macrophage clusters, LAMs ($Cd9^+Trem2^{hi}$), $Fcgr4^+$ macrophages and cycling $Mki67^+$ macrophages (Figure 2.14).

$Folr2^+Lyve1^+$ macrophages expressed a gene signature (*Cd209f/g*, *Mertk*, *Cd163*) associated with the highly endocytic resident vascular associated macrophages (VAMs) identified in lean and obese adipose tissue[164]. Accordingly, $Folr2^+Lyve1^+$ marker genes

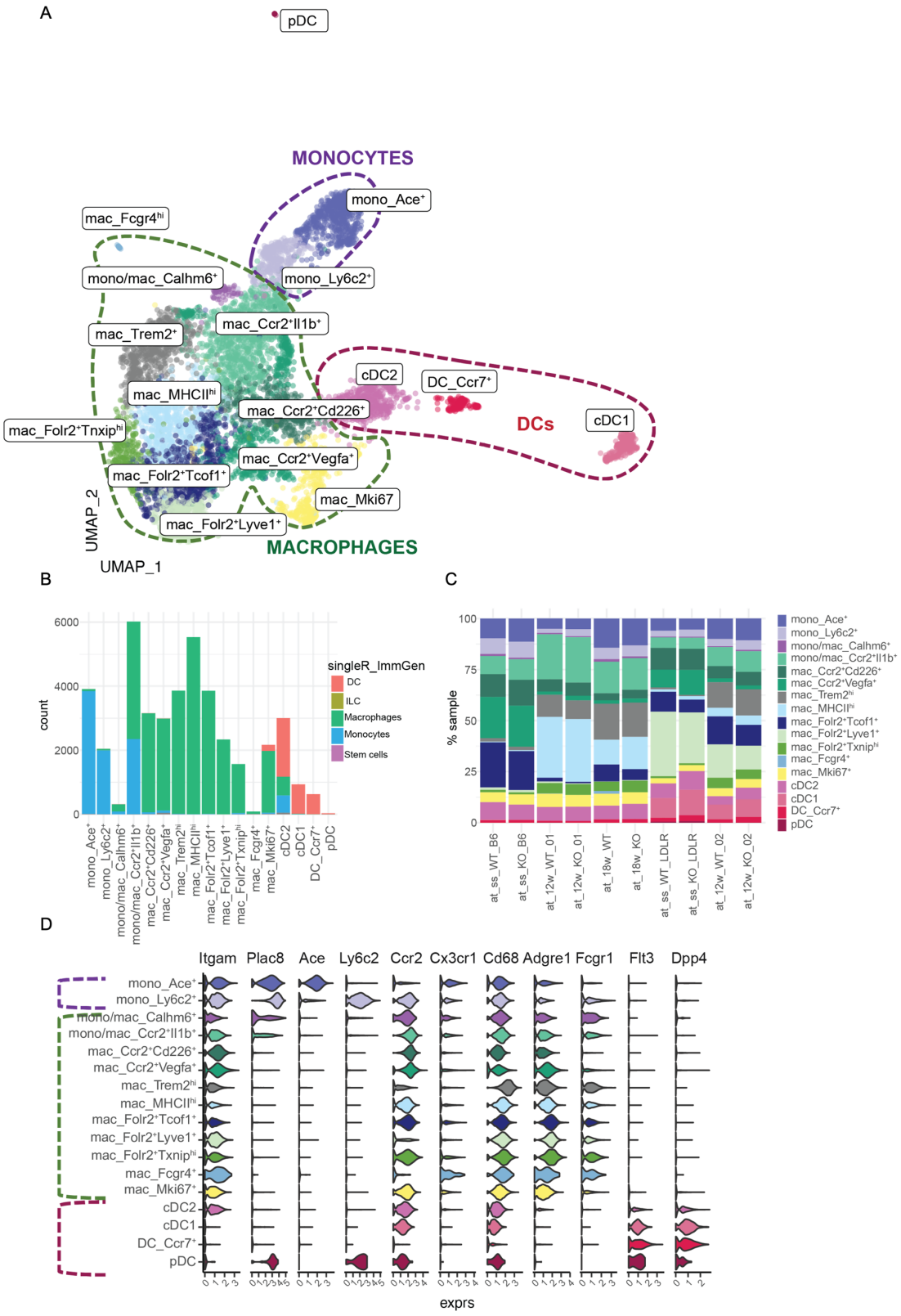


Figure 2.13: ***The single-cell mononuclear phagocyte landscape in the epiWAT of mixed bone marrow chimeras (MBMCs).*** *42455 mononuclear phagocytes (MNPs) from CD45^{+} sorted and Lineage^{-} CD11b^{+}CX3CR1^{+} sorted WT and IRF5$^{-/-}$ samples from epiWAT of MBMCs at steady state (n=1 per genotype and sorting strategy), 12w western diet (WD) (n=1 per genotype and sorting strategy), 18w WD (n=1 per genotype sorted for Lineage^{-}CD11b^{+}CX3CR1^{+}) were analysed A. Leiden clustering identified 2 monocyte clusters, 4 dendritic cell clusters and 11 macrophage clusters. B. Bar plots represent the number of cells in each cluster and are coloured by automatic cell type annotation using singleR and the ImmGen database as a reference. C. The bar plots show the cluster composition within each sample. D. The violin plot shows selected markers classically expressed in monocyte, macrophage and dendritic cells.*

were overrepresented in pathways involving homeostatic functions and blood vessel maintenance, including "vasculogenesis involved in coronary vascular morphogenesis" (OR 23.6); "complement activation, alternative pathway" (OR 19.6) and "endosomal vesicle fusion" (OR 11.8) (Figure 2.14C). *Folr2*$^{+}$*Tcof1*$^{+}$ macrophages, *Folr2*$^{+}$*Txnip*^{hi} macrophages and *MHCII*^{hi} macrophages also expressed tissue resident macrophage markers including *Mrc1, C1qa, C1qc* and *Pf4*, but did not express CD209 encoding genes (Figure S 7C). *Folr2*$^{+}$*Tcof1*$^{+}$ macrophage marker genes were overrepresent in pathways including cell proliferation and growth factor signalling ("macrophage cytokine production" OR 6.28, "CCR2 chemokine receptor binding" OR 26.3) (Figure 2.14C) and they did not express endocytosis associated genes, suggesting, similar to the aorta's *Folr2*$^{+}$*Tcof1*$^{+}$ cells, a more immature less endocytic resident-like macrophage phenotype. *Folr2*$^{+}$*Txnip*^{hi} macrophages, like in the aorta, showed cluster markers that were overrepresented in phagocytic pathways ("phagocytosis, recognition" OR 9.75; "positive regulation of receptor-mediated endocytosis" OR 3.8) (Figure 2.14C). In addition, *Folr2*$^{+}$*Txnip*^{hi} macrophages showed high expression of MHCII genes, especially when compared to the other two *Folr2*$^{+}$ clusters, and overrepresentation of marker genes in lipid associated processes ("lipid export from cell" OR 5.8). Therefore, *Folr2*$^{+}$*Txnip*^{hi} macrophages likely represented a homeostatic phagocytic macrophage phenotype that also processes lipids for antigen presentation. *MHCII*^{hi} macrophages expressed *Vcam1* and chemokines including *Ccl2, Ccl4*, *Ccl7* and *Ccl12*. This suggests either an activated resident macrophage phenotype, or a recently recruited tissue adapting phenotype (Figure S 7C).

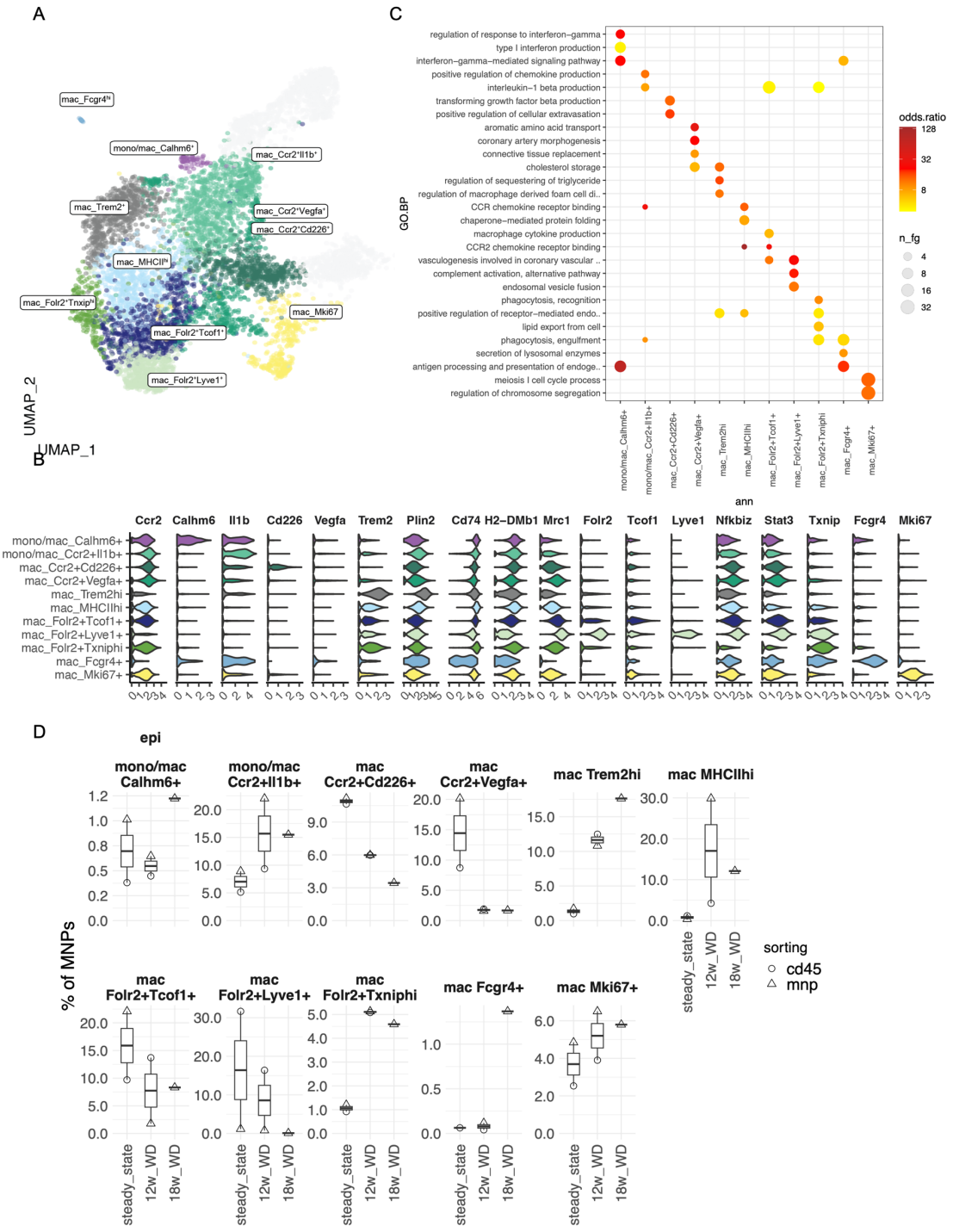


Figure 2.14: ***The single-cell landscape of macrophages in the epiWAT of mixed bone marrow chimeras (MBMCs).*** *42455 mononuclear phagocytes (MNPs) from CD45$^+$ sorted and Lineage$^-$CD11b$^+$CX3CR1$^+$ sorted WT and IRF5$^{-/-}$ samples from epiWAT of MBMCs at steady state (n=1 per genotype and sorting strategy), 12w western diet (WD) (n=1 per genotype and sorting strategy), 18w WD (n=1 per genotype sorted for Lineage$^-$CD11b$^+$CX3CR1) were analysed. A. Leiden clustering of the MNPs in the aorta identified 11 macrophage clusters that could be further grouped into 4 Ccr2$^+$ clusters, 1 Cd9$^+$ cluster and 5 resident clusters and 1 Mki67$^+$ cluster. B. The violin plots show the expression levels of selected cluster marker genes (BH-adjusted P < 0.05, two-sided Wilcoxon tests) in each of the identified clusters. C. The dot plot shows selected GO biological process and KEGG categories that showed a significant overrepresentation in cluster marker genes (Fisher test, BH adjusted p-value < 0.001). The colour of dots represents the odds ratio and the dot size represents number of differentially expressed marker genes that are part of this pathway category. D. The box plots show percentages of WT cells that were found in identified clusters.*

Ccr2^{hi} clusters included *Ccr2*$^{+}$*Calhm6*$^{+}$ mono/macs, *Ccr2*$^{+}$*Il1b*$^{+}$ mono/macs, *Ccr2*$^{+}$*Cd226*$^{+}$ macrophages and *Ccr2*$^{+}$*Vegfa*$^{+}$ macrophages. *Ccr2*$^{+}$*Calhm6*$^{+}$ mono/macs expressed *Cxcl9, Cxcl10, Irf7* and *Isg15* suggesting an interferon responsive macrophage phenotype (Figure S 7A). In agreement with singleR annotations (Figure 2.13B), *Ccr2*$^{+}$*Calhm6*$^{+}$ mono/macs showed high *Ccr2, Plac8*, *Ly6c2* and *Vcam1* expression indicative of recently recruited monocytes (Figure S 7B). This contrasts the aorta where interferon responsive macrophages displayed a *Folr2*$^{+}$ resident-like phenotype (Figure 2.5). Markers for *Ccr2*$^{+}$*Il1b*$^{+}$ mono/macs were overrepresented in *Il1b* related, inflammatory and chemotactic pathways, i.e. "positive regulation of chemokine production" (OR 12.1), "interleukin-1 beta production" (7.82) (Figure 2.14C). *Ccr2*$^{+}$*Cd226*$^{+}$ macrophages also expressed marker genes identified for *Ccr2*$^{+}$*Cd226*$^{+}$ macrophage in the aorta including *Itgax, Ear2, Retnla*, and *Il6* (Figure S 7A). Their marker genes were overrepresented in pathways associated with inflammation and tissue repair[164] ("transforming growth factor beta production" OR 13.3, "positive regulation of cellular extravasation" OR 17.4) suggesting an immune-regulatory role. *Ccr2*$^{+}$*Vegfa*$^{+}$ macrophage marker genes were overrepresented in homeostatic metabolic pathways including "aromatic amino acid transport" (OR 34) and "cholesterol storage" (OR6.4) as well as pathways involved in tissue homeostasis, such as and "coronary artery morphogenesis" (OR 21.3) and "connective tissue replacement" (OR 8.51) (Figure 2.14C).

Trem2^{hi} LAMs in the adipose tissue have been well characterised[112,158] and as previously reported, marker genes were overrepresented in lipid handling pathways: "regulation of sequestering of triglyceride" (OR 16.5), "cholesterol storage" (OR 12.9), "regulation of macrophage derived foam cell differentiation" (OR 11.9) (Figure 2.14C).

Finally, *Fcgr4*$^{+}$ macrophages have been described as macrophages that promote obesity regression during caloric restriction through phagocytosis of dying adipocytes[110]. Here

marker genes of *Fcgr4*$^+$ macrophages were overrepresented in pathways associated with phagocytosis ("phagocytosis, engulfment" OR 4.67; "secretion of lysosomal enzymes" OR 8.76) and antigen presentation ("antigen processing and presentation of endogenous peptide antigen" OR 18.4).

Folr2$^+$*Lyve1*$^+$ macrophages, cDC1s and pDCs were absent in the live lineage-Cd11b$^+$CX3CR1-GFP$^+$ sorted samples (Figure 2.14D, Figure S 6). VAMs, the equivalent of our *Folr2*$^+$*Lyve1*$^+$ cells, have been shown to have low CX3CR1 expression[123], hence sorting live lineage-Cd11b$^+$CX3CR1-GFP$^+$ enriched for monocyte derived MNPs and might have led to underrepresentation of *Folr2*$^+$*Lyve1*$^+$cells (Figure 2.14D). However, in the CD45$^+$ sort, *Folr2*$^+$*Lyve1*$^+$ macrophages represent 42.78% of macrophages at steady state and 17.25% of macrophages at 12w WD suggesting they constituted a main population in epiWAT and decrease with disease. Since, sorting strategies led to differences in frequencies of captured cells, no formal composition analysis could be done for the epiWAT. However, the data suggests that *Ccr2*$^+$*Il1b*$^+$ macrophages (mean frequencies of MNPS: steady state = 7.01%, 12w =15.69%), *Trem2*^{hi} macrophages (mean frequencies of MNPS: steady state = 1.35%, 12w =11.64%) and *Folr2*$^+$*Txnip*^{hi} macrophages (mean frequencies of MNPS: steady state = 1.06%, 12w =5.10%) accumulate in disease, as an increase in abundance was observed at 12w WD when compared to the steady state sample using the same sorting strategy. Similarly, a decrease in abundance of *Ccr2*$^+$*Cd226*$^+$ (mean frequencies of MNPS: steady state = 10.90%, 12w =5.98%) and *Ccr2*$^+$*Vegfa*$^+$ (mean frequencies of MNPS: steady state = 14.43%, 12w =1.76%) macrophages was observed (Figure 2.14D).

2.4.2.1. Validation of clusters identified in the epididymal white adipose tissue of mixed bone marrow chimeras using published scRNAseq datasets

Next, I performed an integrated analysis of epiWAT MNPs from MBMCs with datasets from 3 previously published scRNAseq studies containing samples from healthy, obese,

weight loss and weight cycling murine epiWAT (Methods 6.7.5). Using the integrated dataset, I confirmed transcriptional profiles of 16 out 17 clusters identified in the previous section (1.4.2) (Figure 2.15A,C,D). The only cluster that was identified in the analysis presented in 1.4.2 and not in the integrated analysis were *Folr2*$^{+}$*Txnip*^{hi} macrophages. In addition, I identified a small *Saa3*$^{+}$ macrophage cluster in the integrated analysis, similar to the *Saa3*$^{+}$ macrophage cluster I identified in the aortic analyses (Figure 2.5). The presented alluvial plot highlights the overlap of clusters between the two analyses (Figure S 8).

To understand whether irradiation had an effect on cell composition at steady state and in disease, I next compared cluster compositions from CD45^{+} enriched samples (Figure 2.16).

At steady state, no credible compositional differences were observed between MBMC and non-irradiated samples. In disease (>12 w diet) community datasets showed a higher *Trem2*^{hi} LAM content than MBMCs (Figure 2.16) which was in accordance with my observation in the aorta. This might be due to the same above listed reasons reflecting differences in experimental designs such as irradiation effects, dietary intervention length and composition or due to the fact that MBMCs display delayed disease progression.

To test whether MBMCs affected macrophage transcriptional signatures, I next performed DEG analysis between the MBMC dataset and a publicly available dataset (Cottam et al[114]) at steady state and in disease (>12w diet) (Figure S 9). Macrophages from steady state MBMCs differentially upregulated pro-inflammatory genes (*Nfkb, Rel, Nfat5*) and genes associated with myeloid chemotaxis macrophage differentiation and activation (*Egr3, Pd4ec, Tcof1, Nr4a1, Ndnf1*) when compared to the non-irradiated dataset of Cottam *et al*. On the other hand, Cottam data showed differentially higher expression of bona fide VAM markers including *Cd209a, Cd209b*, and *Cd209c* (Figure S 9A).

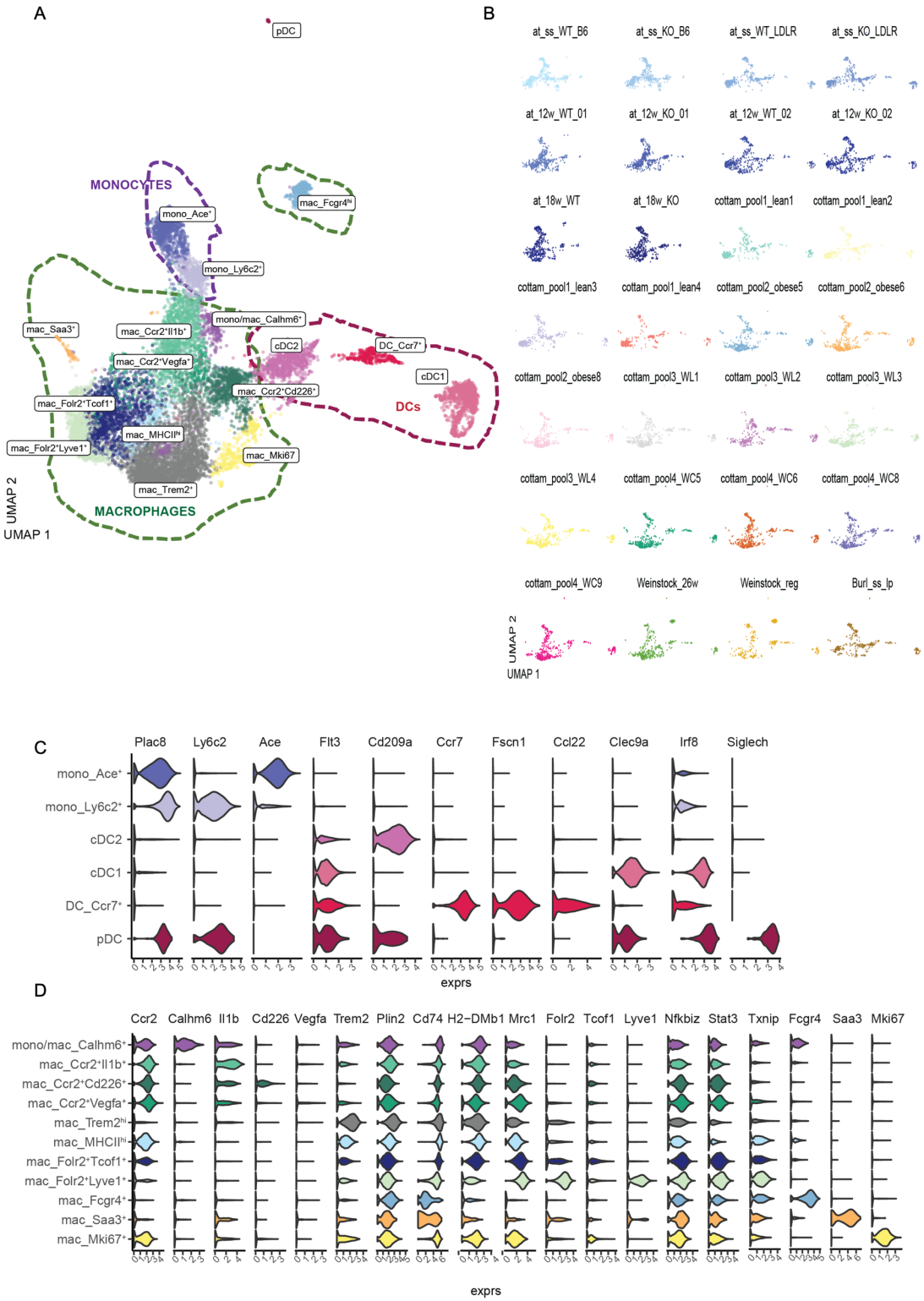


Figure 2.15: ***Integrated analysis of 4 scRNAseq studies of the epiWAT.*** *An epiWAT MNP atlas was constructed by integrated analysis of 3 publicly available scRNAseq datasets of healthy and obese epiWAT (Table S 3) and 42455 mononuclear phagocytes (MNPs) from CD45$^+$ and Lineage$^-$CD11b$^+$CX3CR1$^+$ sorted WT and IRF5$^{-/-}$ samples from mixed bone marrow chimera (MBMC) epiWAT. A. The UMAP shows the integrated dataset. Leiden clustering identified 2 monocyte clusters, 4 dendritic cell clusters and 10 macrophage clusters. B. The UMAP shows the cells faceted by sequencing sample. C/D. The violin plots show cluster marker gene expression (BH-adjusted P < 0.05, two-sided Wilcoxon tests) of monocytes and dendritic cell markers clusters (C.) and macrophage clusters (E.)*

In disease, Cottam *et al* macrophages differentially expressed LAM markers like *Trem2, Cd63* and *Spp1*, most likely due to higher LAM abundance in that dataset (Figure S 9B). Other DEGs included metabolic genes associated with iron metabolism (*Heph, Hepb1, Hmox2*), oxidative phosphorylation/mitochondrial genes (*mtAtp8, Ucp2, Slc25a39*), glucose metabolism (*Eno1, Aldoa, Ldha, Nr1h3*) and antioxidative functions (*Gstp1, Gpx, Prdx1*) (Figure S 9B). These data show that macrophages in the community data displayed a more lipid specialised phenotype while in my dataset, macrophages displayed a less mature more inflammatory and cell recruitment phenotype. These differences could be related to a more advanced disease progression and lack of irradiation in the Cottam *et al* compared to my dataset.

Finally, I performed pseudo-time analysis to investigate whether irradiation affected pseudotime differentiation trajectories at steady state and disease (Figure 2.17). At steady state, in both datasets the resident compartment and the monocyte-mono/mac compartment appeared quite separate with little contribution of the monocytes towards resident macrophages (Figure 2.17A-D). The activation trajectory observed in the aorta's resident populations from *Folr2*$^{+}$*Lyve1*$^{+}$ macrophages towards *Folr2*$^{+}$*Tcof1*$^{+}$ macrophages was conserved in the epiWAT in both in MBMCs and the community dataset (Figure 2.17A-H). In disease, lineage tracing and pseudo-time suggest that monocytes are projected to become *Trem2*^{hi} LAMs[112,114] and this transition was observed in the Cottam *et al* dataset (Figure 2.17E,F) whereas in the MBMCs analysis *Folr2*$^{+}$*Tcof1*$^{+}$ macrophages projected towards *Trem2*^{hi} LAMs (Figure 2.17G,H). One reason for this difference between datasets, again, could be the difference in disease time point and irradiation treatment. In Cottam *et al Folr2*$^{+}$*Tcof1*$^{+}$ macrophages were virtually absent in disease (Figure 2.16), indicating that recruited monocytes directly transition towards *Trem2*^{hi} LAMs at later disease time points once all resident macrophages have become lipid laden.

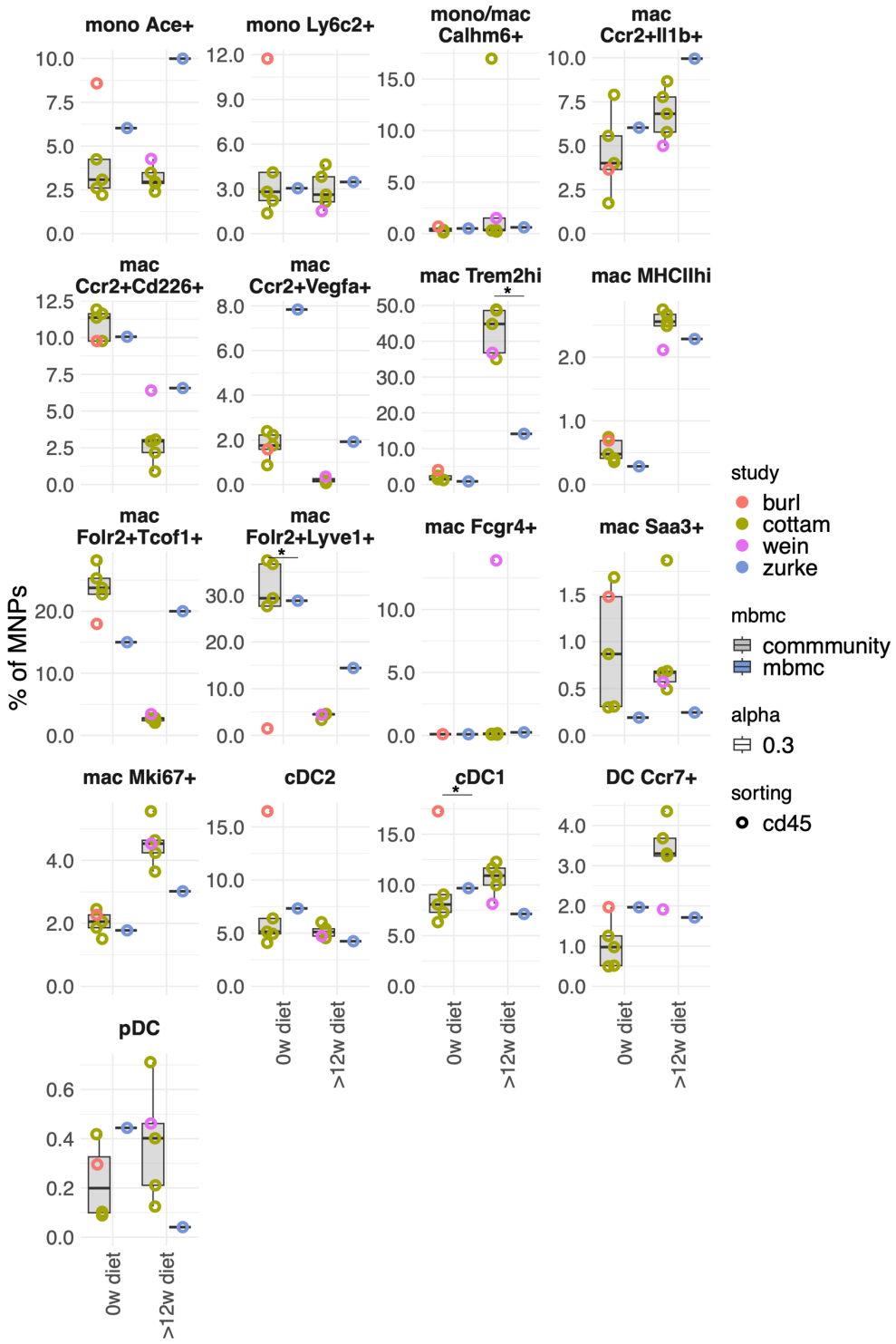


Figure 2.16: ***Comparison of epiWAT macrophage cluster composition between mixed bone marrow chimeras (MBMCs) and community datasets.*** *An epiWAT MNP atlas was constructed by integrated analysis of 3 publicly available scRNAseq datasets (Table S 3) of healthy and obese epiWAT and 42455 mononuclear phagocytes (MNPs) from CD45$^+$ and Lineage$^-$CD11b$^+$CX3CR1$^+$ sorted WT and IRF5$^{-/-}$ samples from MBMC epiWAT. The box plots show percentages of WT cells from CD45$^+$ enriched datasets that were found in identified clusters. Composition between MBMC and non-irradiated community datasets was compared at steady state (0 week diet) and 12-16 week diet using scCODA.*

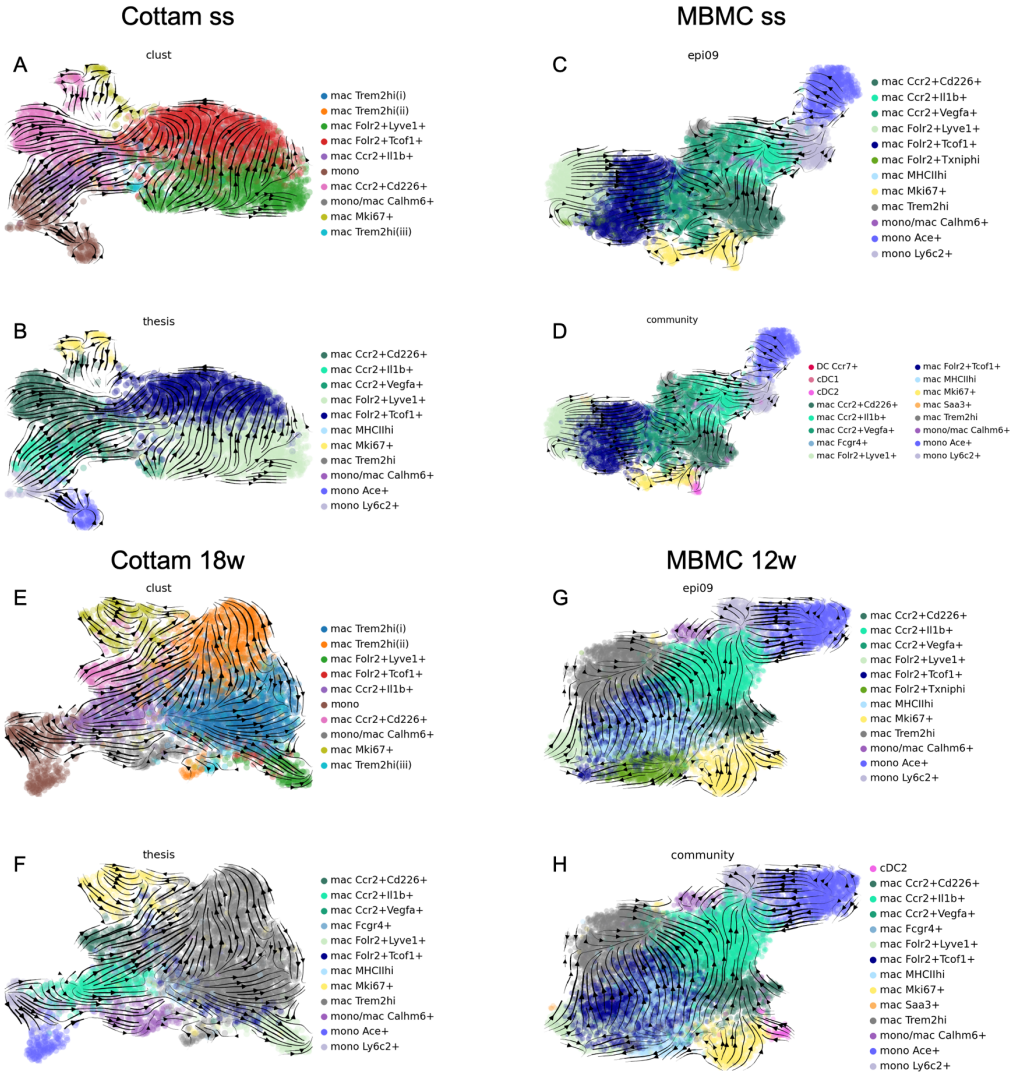


Figure 2.17: ***Trajectory analysis of epiWAT mononuclear phagocyte clusters in mixed bone marrow chimeras (MBMCs) and community datasets at steady state and in disease.*** *Pseudotime velocity analysis was performed on steady state and disease ins scRNAseq samples form MBMC and community datasets using scVelo. A-H. PAGA initialised UMAP representations of velocity streams for Cottam et al steady state (A-B) , MBMC at steady state (C-D), Cottam et al at 18 w diet (E-F). MBMC at 12 w diet (H-G) Cells in A,C,E,G are coloured by clusters identified when studies were analysed separately (see 6.7.9.1). Cells in B,D,F,H,J are coloured by clusters identified in the integrated analysis. Arrows indicate directions of predicted future transcriptional states.*

In the MBMC dataset however, *Folr2*$^{+}$*Tcof1*$^{+}$ macrophages were still present and might therefore contributed to the *Trem2*^{hi} LAM pool. The observed differences in macrophage maturation between datasets is likely to relate to differences in disease progression secondary to diet and irradiation status and it highlights the challenges we face in the field of single cell biology.

2.5. Discussion

This thesis aims to investigate similarities and differences of immune cells in the aorta and epiWAT during a time course of metabolic disease progression and how monocyte to macrophage programming varies over time in health and disease. For that purpose, I performed scRNAseq of aortic and epiWAT immune cells from the same mixed bone marrow chimera at steady state or after induction of metabolic disease through feeding of a western diet. Irradiation results in depletion of the resident myeloid compartment, which in turn is repleted by bone-marrow derived macrophages. In this chapter, I generated a single-cell atlas for both the aortic and epiWAT immune cells by integrating healthy and disease samples as well as both genotypes to gain an overview of the generated dataset.

Following integration of the cells from aorta samples or epiWAT samples, I was able to identify, based on automatic cell type predictions and manual inspection of the discovered marker genes, all major immune cell types identified in atherosclerotic plaques and obese adipose tissue[67,104,110,111,113,114,117,148,149,189] using scRNAseq and CyTOF. This included populations of T cells, B cells, mononuclear phagocytes, neutrophils and mast cells. *Cd3e*^{hi} T/NK cell frequency among all tissue leukocytes was higher in the aorta than in the epiWAT at steady state and 12w WD (42.18±24.41%, vs 35.76%, and 54.58±6% vs 30.26% respectively).

Lymphocyte-focused analysis in the aorta and adipose tissue showed that prevalence of activated T cells increased with disease progression. In the aorta, most CD4 and CD8 T cells displayed a naïve phenotype at steady state while western diet feeding led to a shift towards effector CD4 T cells and cytotoxic CD8 T cells. In the epiWAT at 12 weeks WD activated/cytotoxic CD8$^+$ T formed the majority of adipose leukocytes. These findings are in agreement with several murine studies showing that CD8$^+$ T cells are elevated in the atherosclerotic aorta[48,190] and obese adipose tissue[52] and their abundance increases as disease progresses. CD8$^+$ T cells in both tissues have been shown to have anti- and pro-

inflammatory properties and further heterogeneity is implied. They contribute to macrophage recruitment in early obesity and stimulate inflammatory macrophage polarisation[48,52,190–192].

Further, I investigated plaque and adipose tissue myeloid cell diversity in more detail by performing a separate analysis of the MNPs including monocytes, macrophages and cDC clusters identified in the overall analysis. MNPs, and especially macrophages, are known to increase in mouse models of atherosclerosis[81,193–195] and obesity[36,38,196]. In our mouse model of metabolic disease, however, cumulative MNP frequency to all leukocytes seemed to increase in the epiWAT upon WD feeding, but not in the aorta. This observation in the aorta might be driven by high variability in the frequency of aortic thymocyte-like lymphocytes I observed.

Overall, I identified 2 monocyte and 4 DC with distinct transcriptomic features in both metabolic tissues in health and disease. In addition, macrophage subsets in the aorta and epiWAT could be grouped into *Ccr2*$^{+}$ mono-macs, lipid associated macrophages, resident-like macrophages and cycling macrophages, highlighting that macrophages in both tissues show similar transcriptional signatures. This is consistent with macrophage activation trajectories that have been described across multiple murine tissues and inflammatory conditions[197]. These similarities suggest that macrophage activation stimuli might be shared between the aorta and the epiWAT and might influence transcriptional macrophage statuses more than tissues-specific programs and will be investigated further in Chapter 3.

Among the MNPs populations described and central to both atherosclerosis and obesity are lipid-scavenging macrophages known as “foamy” or lipid-associated LAM macrophages. LAMs are not unique to atherosclerosis and obesity, but also feature in neurodegenerative diseases[156,198–200] and chronic liver diseases[157,201,202]. LAMs, also referred to as *Trem2*^{hi} macrophages due to a high expression of *Trem2*, display largely a

housekeeping and protective role[112,203] aimed at scavenging lipids and cell debris[204] and accordingly display the transcriptional profile associated with an efficient lysosomal, mitochondrial and antioxidant machinery. A recent meta-analysis of published scRNAseq datasets from murine healthy and atherosclerotic aortas, identified two distinct populations of *Trem2*^{hi} macrophages: *Slamf9*^{hi}*Trem2*^{hi} macrophages expressed higher levels of inflammatory genes, while *Gpnmb*^{hi} expressed highest levels of *Trem2*^{hi} associated signature genes[117].

I identified lipid-associated MNP clusters in each tissue: *Plin2*^{hi} mono/macs in the aorta and *Trem2*^{hi} macrophages in the epiWAT were almost absent at steady state and expanded in disease, confirming that both subsets represent metabolic disease-associated populations[205,206].

Importantly, in my dataset these populations were significantly less prevalent compared to community datasets. In particular, *Plin2*^{hi} mono/macs identified in the aorta exhibited a less mature phenotype than *Trem2*^{hi} macrophages identified in community datasets, expressing monocytic markers including *Ly6c2* and *Plac8*. In addition *Plin2*^{hi} mono/macs expressed high levels of *Il1b*, especially in contrast to *Trem2*^{hi} who have been reported to show more homeostatic transcriptomes[105]. Interestingly, *Plin2*^{hi} inflammatory LAMs have recently been identified in human carotid plaques using scRNAseq, but integration with murine datasets did not identify a 1:1 equivalent in murine atherosclerosis[126]. Integration with community data revealed that very few cells with the two *Trem2*^{hi} LAM published phenotypes expressing high levels of *Trem2*, *Cd9* and *Spp1* in combination with *Slamf9* or *Gpnmb* were detected in my aortic MBMC dataset. This finding was further supported with differential gene expression analysis. Macrophages from the community datasets exhibited upregulation in genes involved in lipid handling, mitochondrial oxidation, antioxidative functions as well as *Trem2*^{hi} specific genes such as *Trem2, Cd63* and *Spp1*. My dataset, on the other hand, consistently showed upregulated

expression of genes involved in recruitment and maturation of monocytes and inflammatory genes. These findings highlight the contribution of experimental design to data interpretation. Unlike the community datasets, my experimental design was centred on a sub-lethally irradiation model and my results show that this regimen possibly leads to alterations in LAM biology. In keeping with my findings, previous studies have shown that irradiation leads to adipose tissue dysfunction with compromised lipid accumulation, dysregulation of stromal cells as well as effects on hematopoietic and circulating cells[185,187,207] as well as changes in lesion distribution including smaller thoracic lesions in $LDLR^{-/-}$ mice fed a high cholesterol diet[186], and its effect on tissue resident immune cell phenotype should be assessed. In addition to intrinsic effects of irradiation on immune cells phenotype, differences in myeloid phenotype might also be due to differential kinetics between my model and that of the community. After irradiation, all immune cells in the tissues are replenished from circulating cells including embryonically-derived resident macrophages. Hence, usual bona fide resident cells are, in irradiated models, mostly monocyte-derived. In fact, our resident population showed a more activated phenotype compared to that of the community and lacked TLF cells, the true resident population characterised by the co-expression of *Timd4, Folr2 and Lyve1*[118]. Of note, in my experimental design we only sorted for donor derived cells. Reconstitution rates (mean ± SD, n=6) in tissues of MBMC were 90.63±1.47% for the aorta and 89.73±0.84 for the epiWAT. The majority of radioresistant host derived cells were $CD3^+$ T cells in the epiWAT (73.5±3.03%), but in the aorta 34.41±6.25% of radioresistant cells were $CD11b^+F4/80^+CD206^+$ resident macrophages (data not shown). Moreover, we fed the mice a high cholesterol high fat high sugar diet at a variance from previous aortic studies with the intent of inducing atherosclerosis and obesity concomitantly, and this factor of experimental design can contribute to further variance in the dataset due to potential divergence of disease progression.

Finally, trajectory analysis showed that resident macrophages and monocytes in both aorta and adipose tissue segregated respectively within their functional niches, with resident macrophages displaying a contained trajectory from a less to a more activated state, whereas monocytes transitioned towards an inflammatory monocyte-macrophage phenotype. LAMs origin and trajectory on the other hand, was the most divergent between aorta and WAT: in line with fate mapping reports[112], adipose tissue *Trem2*^{hi} LAMs seem to partially originate from proliferating cells and monocytes, however this did not seem to be the case in the aorta where no originating cluster for TREM2^{hi} LAMs could be defined. In early atherogenesis intimal resident macrophages Mac^{AIR} take up lipids, but fate mapping studies have shown that at later disease time points minimal Mac^{AIR} derived cells can be identified in atherosclerotic lestions[119]. However, I did not see this connection in our data or the community datasets, but this might be confounded by the extreme low number of cells with a *Trem2*^{hi} cells phenotype in our data, or the very low abundance of *Mmp12*$^{+}$/Mac^{AIR} cluster in disease, possibly secondary to variations in disease progression. However, definitive origin of foamy macrophages in the aorta should be investigated using monocyte fate-mapping models like on *Ms4a3*[126] or *Cxcr4*[208].

In conclusion, in this chapter I generated single-cell immune atlases of the aorta and the epiWAT, validating cell type abundances and phenotypes by integration with available community datasets. My data showed enrichment of specific lymphocytes and MNP subsets during metabolic disease progression. Macrophages are indispensable for tissue homeostasis, but also for metabolic disease progression. Dissecting how the tissue and metabolic disease niche might influence monocyte to macrophage transitional states is crucial for understanding metabolic disease progression and how obesity might exacerbate atherosclerosis. My dataset identified similar myeloid transcriptional states in both organs at steady state and disease. In the next Chapter, I will focus in particular on

the differences in transcriptional states and monocyte to macrophage transitions existing between WAT and aorta.

Chapter 3. Comparison of the immune cell landscapes of the aorta and the adipose tissue using scRNAseq and CyTOF

3.1. Introduction

Tissue macrophages display functional, phenotypic, transcriptional and geographical heterogeneity. Single cell biology state-of-the-art techniques are helping to understand the landscape of these cells, from their proteome, transcriptome as well as their interactive network within their respective tissues in health and throughout disease progression. In recent years, this body of knowledge contributed significantly to the identification of specific macrophage phenotypes and functions in obesity and atherosclerosis alike. Myeloid cells in the aorta and WAT are grouped into different populations according to their proteo-transcriptional signature and functional features.

Resident macrophages:

In the aorta, resident macrophage populations are divided into 2 main groups depending on location, intimal versus adventitial resident macrophages[119–122,149,209]. Both resident macrophage populations originate during devolpment from embryonic and early monocyte precursors and are self-maintained throughout adulthood[119,120]. $LYVE1^+$ adventitial macrophages have homeostatic function in both health and disease[122,149].

In the adipose tissue, resident macrophages are also derived from embryonic hematopoietic precursors[210]. In lean adipose tissue, resident macrophages constitute up to 10% of cells[36]. Their functions include several homeostatic processes involved in tissue remodelling and insulin sensitivity.

$CD11c^+$ macrophages:

At steady state, intimal $CD11c^+CD68^+$ myeloid cells have been described in aortas of C57BL/6 mice in arterial regions predisposed for atherosclerosis[211,212]. These myeloid

cells, thought to be dendritic cells in the first instance, have pro-atherogenic functions. Using diphtheria toxin (DT) mediated ablation, a decrease in lesion size was achievable after depletion of CD11c myeloid cells in atherosclerotic mice[211]. In addition, $CD11c^{-/-}$ *Apoe*$^{-/-}$ mice developed smaller lesions compared to *Apoe*$^{-/-}$ mice[213] along with reduced macrophage accumulation in the lesions[213]. Using CYTOF, the Monaco lab showed that $CD11c^{+}$ macrophages were distinct from conventional dendritic cells and increased in atherosclerotic aortas in mice and human plaques[109]. $CD11c^{+}$ macrophages were further divided depending on MHCII expression[109,211]. Recently, resident $CD11c^{+}$ intimal myeloid cells have been identified as macrophages. In early atherosclerosis these aortic intimal resident $CD11c^{+}$ macrophages (Mac^{AIR}) become foamy and ablation of these macrophages prevents early lesion formation, suggesting a pro-atherogenic function[119]. In obesity, monocyte-derived $CD11c^{+}$ macrophages were central to disease development[35]. $CD11c^{+}$ adipose tissue macrophages (ATMs) expressed higher levels of proinflammatory cytokines compared to $CD11c^{-}$ macrophages[128] and selective depletion of $CD11c^{+}$ ATMs reversed insulin resistance in obesity, suggesting $CD11c^{+}$ ATMs as drivers of obesity and insulin resistance[43]. Overall, these data highlight the importance of $CD11c^{+}$ macrophages in metabolic disease. However, the transcriptional regulation and function of different $CD11c^{+}$ subsets are still unknown.

Macrophage recruitment in atherosclerosis and obesity

With atherosclerosis onset, circulating monocyte-derived cells are recruited to the atherosclerotic lesion where they differentiate into macrophages. Monocyte recruitment is chemokine-dependent through CCR2, CCR5 and CX3CR1[214]. The role of CCR2 and its ligand CCL2 in monocyte recruitment to atherosclerotic plaque and consequently atherosclerotic lesion size has been demonstrated in numerous murine knockout studies[85,215].

In adipose tissue, macrophages can increase from 10% to 50% of all cells with progression of obesity[36]. The increase of macrophages in the obese adipose tissue is also chemokine-dependent with CCL2-CCR2 axis playing a major role. In the adipose tissue, CCL2 is produced in both adipocytes and stromal vascular cells and CCL2 levels are increased in obesity[216–218]. However recent studies have shown that local macrophage proliferation is equally important in macrophage increase in the expanding adipose tissue[40].

A lot of parallels have been drawn between different macrophage subsets in different metabolic tissues and their overall signature seems to be shared, for the most part, between aortas and adipose tissue in health and disease. In Chapter 2, I have shown that lymphoid and myeloid cells show a high heterogeneity in both the aorta and epiWAT. The clusters identified in separate analyses of the aorta and the adipose tissue showed similar transcriptional signatures, suggesting conserved macrophage homeostasis and activation programs in both tissues. Furthermore, the fact that both tissues were collected from the same mouse removes a layer of confounding factor and further supports the notion of potential conserved transcriptional programs and activation states at steady state and in disease. However, a more in-depth assessment of potential tissue specific differences is warranted.

To date, no formal comparison of immune single cell transcriptome from the epiWAT and aorta has been published. In this chapter I aim to dissect similarities and differences in immune cell transcriptional phenotypes between the blood, aorta, and adipose tissue using single-cell approaches.

3.2. Comparison of T cells

3.2.1. A combined T and NK cell atlas of the aorta and epididymal white adipose tissue during metabolic disease progression

Table 3.1 Overview of samples included to define the integrated aortic and epididymal white adipose tissue T and NK cells landscape during metabolic disease progression.

tissue	disease time point	genotype	batch	number of mice in pool	Sorting strategy
aorta	steady state	WT	A	6	Live CD45+
aorta	steady state	KO	A	6	Live CD45+
epiWAT	steady state	WT	A	6	Live CD45+
epiWAT	steady state	KO	A	6	Live CD45+
aorta	12w WD	WT	B	4	Live CD45+
aorta	12w WD	KO	B	4	Live CD45+
epiWAT	12w WD	WT	B	4	Live CD45+
epiWAT	12w WD	KO	B	4	Live CD45+
aorta	steady state	WT	C	10	Live CD45+
aorta	steady state	KO	C	10	Live CD45+
aorta	12w WD	WT	D	7	Live CD45+
aorta	12w WD	KO	D	7	Live CD45+
aorta	18 w WD	WT	E	6	Live CD45+
aorta	18 w WD	KO	E	6	Live CD45+

To compare the T/NK cell compartments of the aorta and the adipose tissue, I integrated live $CD45^+$ sorted aortic (n=5 samples) and epiWAT samples (n=2 samples, Table 3.1). As described in Chapter 2 (2.3.1), the majority of T cells identified in the aorta showed a *Cd4*$^+$*Cd8a*$^+$*Rag1*$^+$ double positive thymocyte-like phenotype (Figure S 10A-C). In the epiWAT no *Cd4*$^+$*Cd8a*$^+$*Rag1*$^+$ cells were identified when clustered separately (see 2.4.1) and only very few cells, likely mature cycling T cells, clustered with aortic *Cd4*$^+$*Cd8a*$^+$*Rag1*$^+$ cells when integrated with aortic T/NK cells (Figure S 10A-C). This finding was consisted with previous reports of $CD4^+CD8^+$ double positive T cells that were only identified in the thymus, aortic arch and the mediastinal adipose tissue connecting the thymus and the aortic arch, but not in other organs or the abdominal

aorta[219]. To compare mature T cell phenotypes in the aorta and epiWAT, I next reanalysed 12495 single positive T/NK cells (Figure S 10A,D) identifying 11 subsets: naïve CD4 T cells, activated CD4 T cells, CD4 Tregs, CD4 TH17, naïve CD8 T cells, activated/cytotoxic CD8 T cells, a mixed/activated CD8 T cell cluster, *Mki67*$^{+}$ T cells, immature γδ T cells, mixed CD4/ILCs and NK cells (Figure 3.1A-C). The majority of T cells in the aorta showed a naïve phenotype at steady state (mean frequency of T cells: 61.67%) and activated T cells including activated/cytotoxic CD8 T cells (i), TH1 CD4 T cells and TH17 CD4 T cells expanded in disease (log2FC at 12w WD: activated/cytotoxic CD8 T cells=0.89, TH1 CD4 T cells=1.70, TH17 CD4 T cells=2.27) (Figure 3.1D,E), suggesting immune cell activation in disease. In the adipose tissue the naïve T cell clusters were rare at steady state and 12w WD. At steady state, NK cells (23.1% of T cells) represented the biggest cluster of T/NK cells in the adipose tissue, and activated T cell phenotypes including CD4 Tregs (log2FC 1.37), activated/mixed CD8 (ii) T cells (log2FC 3.36) were significantly more abundant than in the aorta (scCODA FDR<0.3 in >70% of iterations). (Figure 3.1D,E). At 12w WD activated/cytotoxic CD8 T cells (27.56% of T cells) constituted the majority of lymphocytes in the epiWAT and were more abundant than in the aorta. TH17/Treg imbalance is associated with autoimmunity, but has also been reported to contribute to chronic inflammation. TH17 CD4 T cells were significantly more abundant in the aorta (mean frequency of T/NK cells = 9.75%) than in the epiWAT (frequency of T/NK cells =7.19), even though their abundance increased in both tissues with disease progression (epiWAT: log2FC=1.44, aorta: mean log2FC=2.28) (Figure 3.1D,E).

3.2.2. T cell exhaustion is a shared feature of metabolic disease progression in the aorta and epididymal white adipose tissue

T cells are known to exhibit a dysfunctional state referred as T cell exhaustion, in cancer, atherosclerosis[47,65] and obesity[220–222]. Exhausted T cells differ from classical effector or

memory T cells in that they exhibit a compromised effector function with sustained expression of inhibitory receptors[223]. To explore T cell exhaustion phenotypes in disease, I generated an exhaustion score using the scanpy score genes functions (see 6.7.6) based on established gene expression features: *Pdcd1, Tox, Entpd1, Tigit*, and *Lag3*[224,225]. Effector T cells (TH1 CD4 T cells, CD4 Tregs and activate/Cytotoxic CD8 T cells (i)) in the aorta and epiWAT showed highest exhaustion signature scores (Figure 3.2B). In both tissues exhaustion gene signature scores in activated/cytotoxic T cells (i) increased significantly at 12 WD (Wilcoxon Rank sum test, $p<0.001$). In the aorta, I also observed a significant increase in exhaustion gene scores in TH1 CD4 T cells and CD4 Tregs (Figure 3.2C), consistent with a recently reported exTreg phenotype in mouse and human[63]. These observations suggest impaired adaptive immune responses in both the aorta and epiWAT during metabolic disease progression.

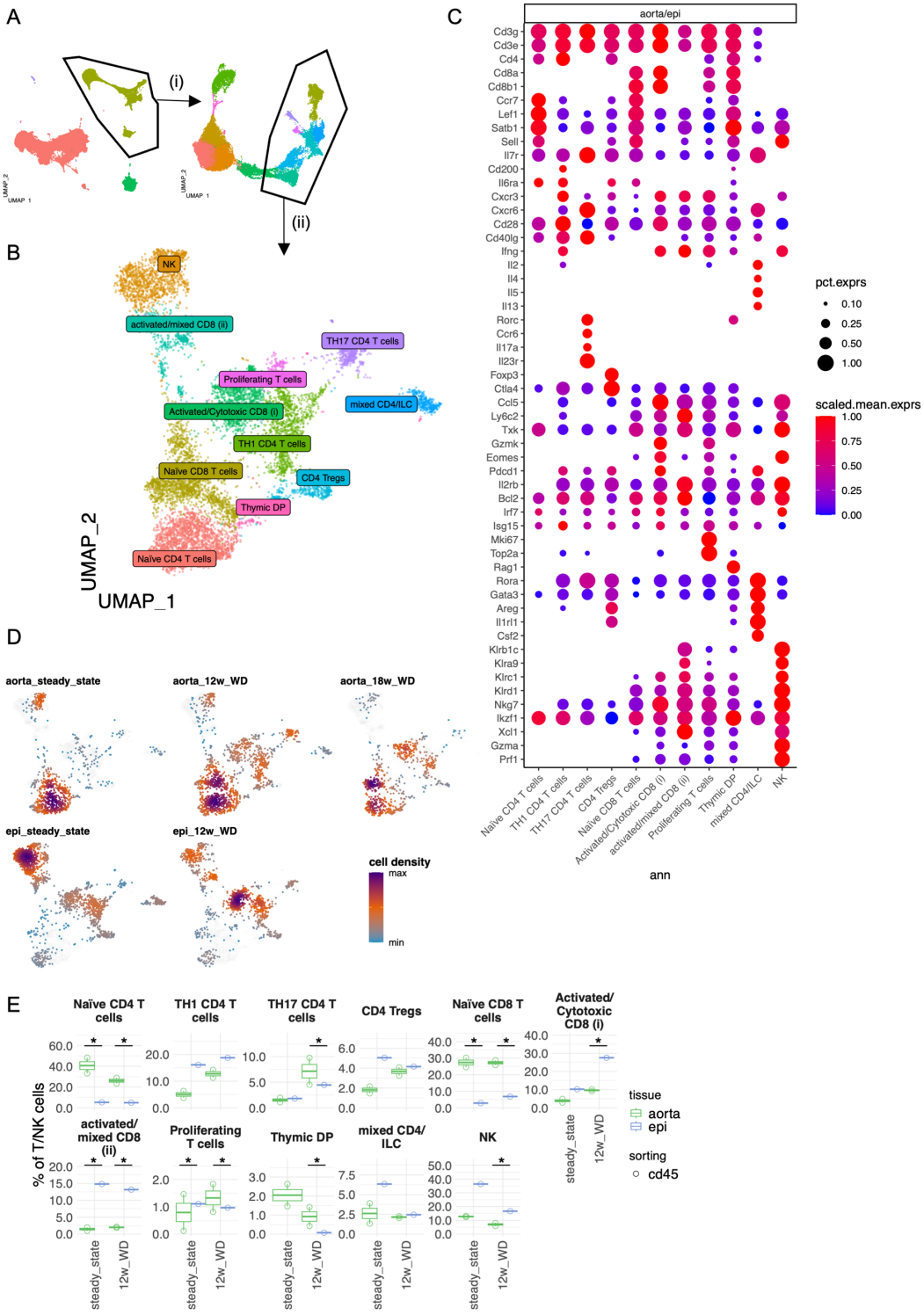


Figure 3.1: ***A combined T cell atlas of the aorta and epiWAT from mixed bone marrow chimeras (MBMCs) during metabolic disease progression.*** *scRNAseq was performed on CD45^{+} sorted WT and IRF5 $^{-/-}$ samples from MBMC aortas and epiWAT at steady state, 12w WD and 18w WD. A./B. Reanalysis strategy of T and NK cells. 31593 T and NK cells were reanalysed first(i). In a second step 12495 mature T cells (Rag1 negative/Itm2a negative (Figure S 10)) were reanalysed (ii) to improve resolution in the mature lymphocyte compartment. B. Leiden clustering of mature T and NK cells from the aorta and epiWAT identified 9 T cell cluster, 1 NK cell cluster and 1 ILC cluster. C. The dot plot shows the expression of selected cluster marker genes (BH-adjusted $P < 0.05$, two-sided Wilcoxon tests) and known cell-type marker genes. The colour of the dots represents the scaled average expression and their size reflects the percentage of cells within a cluster expressing the gene. Dots were only plotted for genes that were expressed in > 10% of the cluster. D. Cell density plots for the T cell compartment of the aorta (top) and epiWAT (bottom) at steady state, 12w WD and 18 w WD. E. The box plots show percentages of WT cells that were found in identified clusters. Composition in the epiWAT was compared to composition in the aorta at steady state and 12w WD using scCODA.*

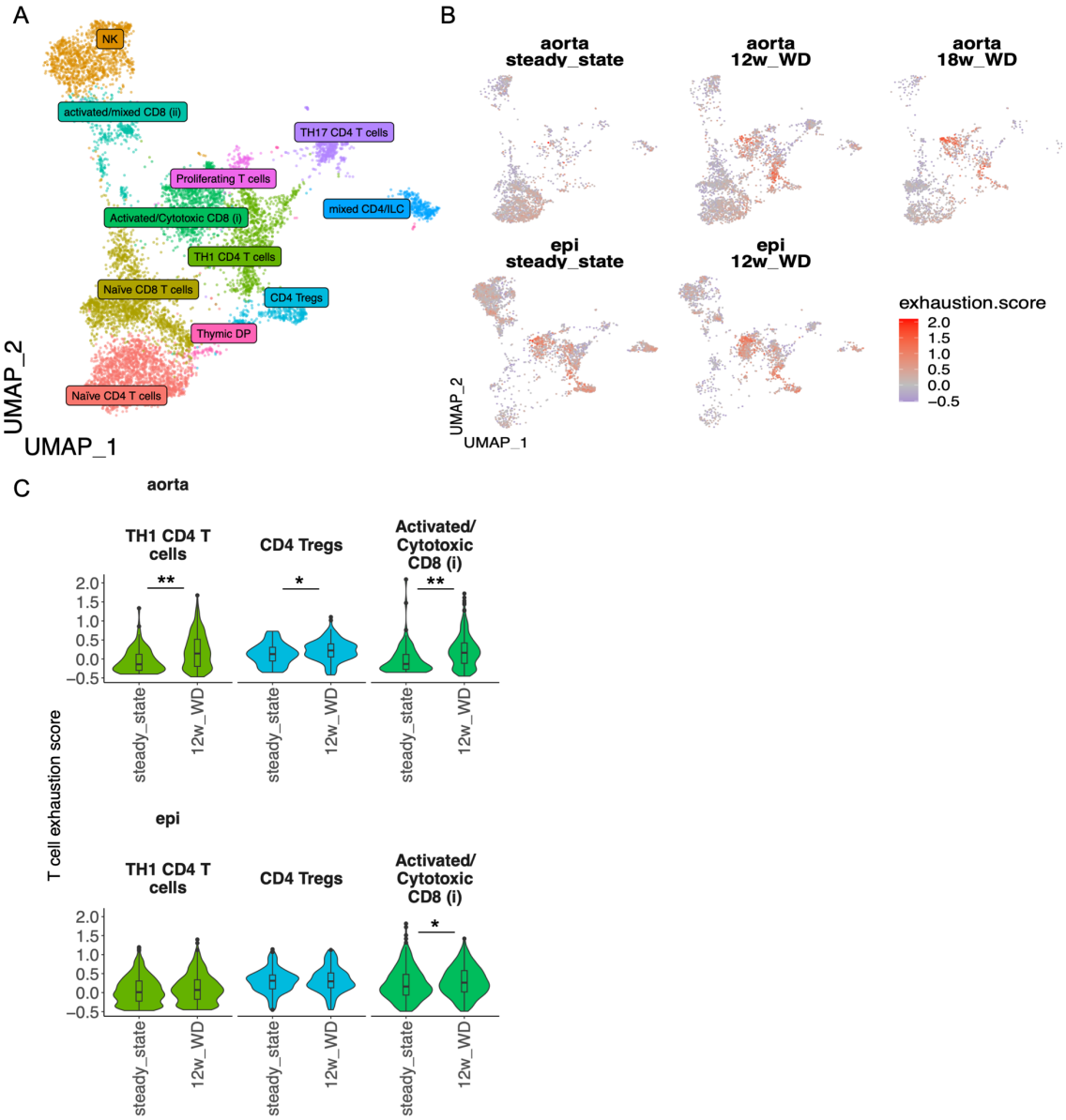


Figure 3.2: ***T cells in the aorta and epiWAT acquire exhaustion marker expression during metabolic disease progression.*** *scRNAseq was performed on CD45^{+} sorted WT and IRF5$^{-/-}$ samples from mixed bone marrow chimera (MBMC) aortas and epiWAT at steady state, 12w WD and 18w WD. A. Leiden clustering of mature T and NK cells form the aorta and epiWAT identified 9 T cell cluster, 1 NK cell cluster and 1 ILC cluster. B. UMAP representation of the analysis presented in (A.) split by time point and tissue (top: aorta, bottom: epiWAT) coloured by calculated T cell exhaustion score based on expression of Pdcd1, Tox, Entpd1, Tigit, and Lag3. C. Violin plots of T cell exhaustion score (BH-adjusted $P < 0.05$, two-sided Wilcoxon tests, *: P<0.05, **: P<0.001).*

3.3. Comparison of myeloid cells

3.3.1. A combined myeloid cells atlas of the aorta, epididymal white adipose tissue and blood during metabolic disease progression

Table 3.2 Overview of samples included to define the integrated aortic and epididymal white adipose tissue mononuclear phagocyte landscape.

tissue	disease time point	genotype	batch	number of mice in pool	Sorting strategy
aorta	steady state	WT	A	6	Live CD45+
aorta	steady state	KO	A	6	Live CD45+
epiWAT	steady state	WT	A	6	Live CD45+
epiWAT	steady state	KO	A	6	Live CD45+
aorta	12w WD	WT	B	4	Live CD45+
aorta	12w WD	KO	B	4	Live CD45+
epiWAT	12w WD	WT	B	4	Live CD45+
epiWAT	12w WD	KO	B	4	Live CD45+
blood	12w WD	WT	B	4	Live Lineage-Cd11b+
blood	12w WD	KO	B	4	Live Lineage-Cd11b+
aorta	steady state	WT	C	10	Live CD45+
aorta	steady state	KO	C	10	Live CD45+
epiWAT	steady state	WT	C	10	Live Lineage-Cd11b+CX3CR1+
epiWAT	steady state	KO	C	10	Live Lineage-Cd11b+CX3CR1+
blood	steady state	WT	C	10	Live Lineage-Cd11b+CX3CR1+
blood	steady state	KO	C	10	Live Lineage-Cd11b+CX3CR1+
aorta	12w WD	WT	D	7	Live CD45+
aorta	12w WD	KO	D	7	Live CD45+
epiWAT	12w WD	WT	D	7	Live Lineage-Cd11b+CX3CR1+
epiWAT	12w WD	KO	D	7	Live Lineage-Cd11b+CX3CR1+
blood	12w WD	WT	D	7	Live Lineage-Cd11b+CX3CR1+
blood	12w WD	KO	D	7	Live Lineage-Cd11b+CX3CR1+
aorta	18 w WD	WT	E	6	Live CD45+
aorta	18 w WD	KO	E	6	Live CD45+
epiWAT	18 w WD	WT	E	6	Live Lineage-Cd11b+CX3CR1+
epiWAT	18 w WD	KO	E	6	Live Lineage-Cd11b+CX3CR1+

Myeloid cells are central to metabolic disease progression, and monocytes are recruited to both the atherosclerotic plaque and the obese adipose tissue where they differentiate into macrophages and contribute to disease progression. Therefore, I next performed an integrated analysis of MNPs from the aorta (n=5 samples per genotype), epiWAT (n=5 samples per genotype) and blood (n=3 samples per genotype) from mixed bone marrow chimera across a time course of metabolic disease progression (Table 3.2) to compare MNP phenotypes that are shared and distinct in metabolic tissues and the blood. Overall, I identified 7 monocyte clusters (*Plac8*), 4 dendritic cell clusters (*Flt3, Dpp4*) and 12 macrophage clusters (*Adgre1*) (Figure 3.3A,C,E). As expected, the majority of cells from the blood clustered with monocytes (>99%) and only very few cells clustered with dendritic cells or macrophages (Figure 3.3B,Figure S 11A). No significant differences in monocyte, macrophage or dendritic cell abundance could be detected between the aorta and the epiWAT when comparing cell types at steady state or 12w WD using scCODA (Figure 3.3D). The majority of MNPs in the aorta and adipose tissue were macrophages (mean frequencies of MNPs at steady state: aorta=82.21%, epiWAT=72.03%) (Figure 3.3B-D).

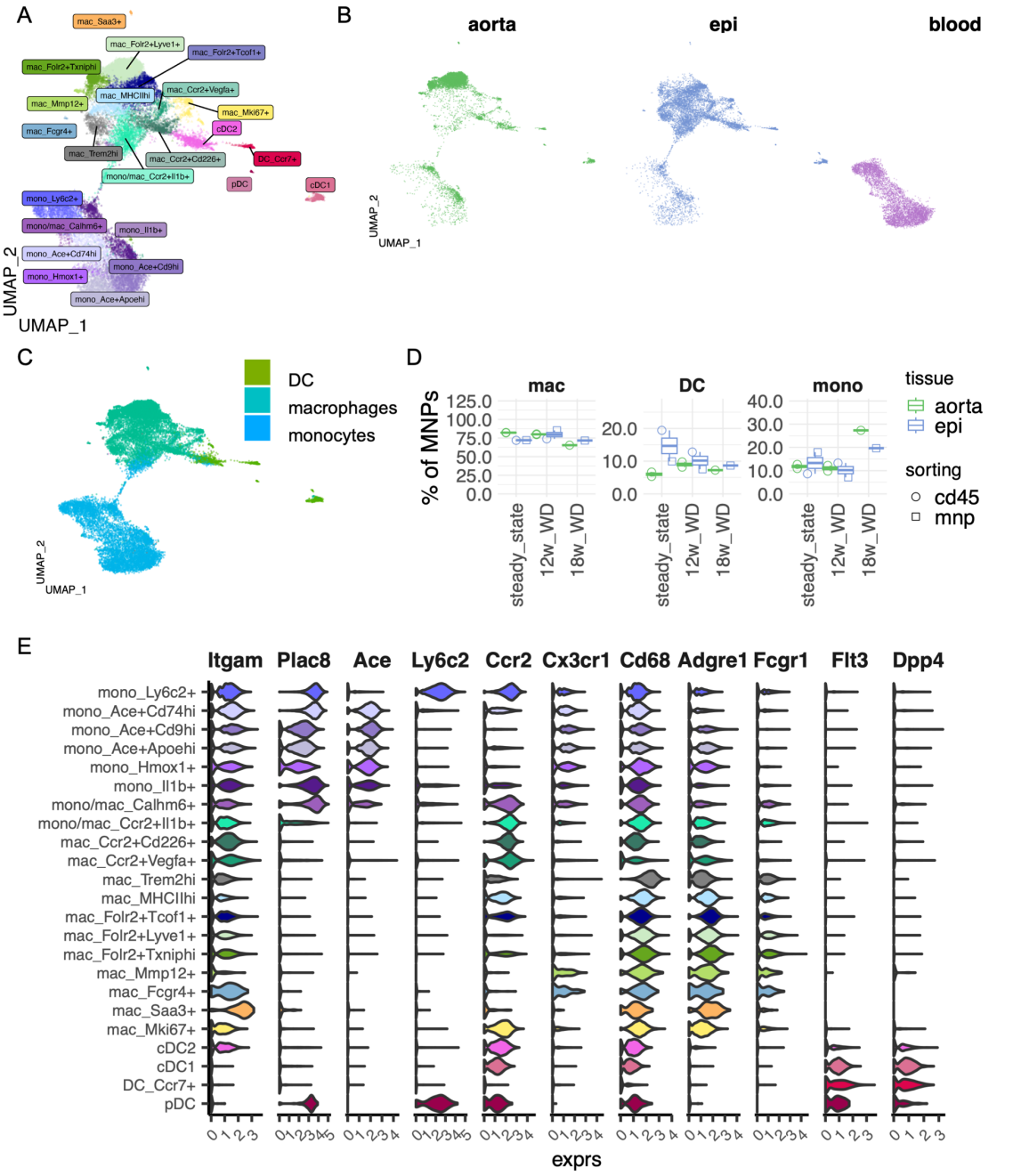


Figure 3.3: ***A combined mononuclear phagocyte atlas of the aorta and epiWAT from mixed bone marrow chimeras (MBMCs) during metabolic disease progression****. scRNAseq was performed on CD45^{+} sorted, Lineage^{-}CD11b^{+} sorted and Lineage^{-}CD11b^{+}CX3CR1^{+} WT and IRF5$^{-/-}$ samples from MBMC aortas, epiWAT and blood at steady state, 12w WD and 18w WD. A. Leiden clustering of 100024 MNPs identified 7 monocyte clusters, 4 dendritic cell clusters and 12 macrophage clusters. B. UMAP representation shown in (A.) faceted and coloured by tissue. C. UMAP representation shown in (A.) coloured by automatic cell type annotation using singleR and the ImmGen database as a reference. D. The box plots show percentages of WT cells that were found in identified clusters. No significant changes in composition were identified when comparing composition in the epiWAT to composition in the aorta at steady state and 12w WD using scCODA. E. The violin plots show the expression levels of known monocyte, macrophage and dendritic cell genes in each of the identified clusters.*

3.3.2. Dendritic cells

Consistent with the individual tissue analysis of the aorta and the epiWAT presented in Chapter 2, I identified 4 DC phenotypes also in the integrated computational study: cDC2s, cDC1s, *Ccr7*$^{+}$ DCs and pDCs (Figure S 12). At steady state and in disease, cDC1s were significantly more abundant in the MNP compartment of epiWAT samples. cDCs are abundant at steady state in the epiWAT[226] and have been shown to have anti-inflammatory function thereby contributing to tissue homeostasis[227]. DCs play an important role in bridging innate and adaptive immunity, hence this finding supports the higher abundance of ILCs and activated T cell phenotypes in the epiWAT at steady state (see 3.2). Even though the overall number of DCs per gram fat is not altered in obesity[123], inflammatory changes in the tissue environment during the onset of obesity result in inflammatory cDC activation[227]. Similarly, DCs in atherosclerosis have been attributed pro- and anti-atherogenic roles including through regulation of Treg responses[77,78].

3.3.3. Monocytes

In the multi-tissue integrated analysis, the identified monocytes clustered in 7 distinct populations: *Ly6c2*$^{+}$ monocytes, *Ace*$^{+}$*Cd74*^{hi} monocytes, *Ace*$^{+}$*Cd9*^{hi} monocytes, *Ace*$^{+}$*Apoe*^{hi} monocytes, *Hmox1*$^{+}$ monocytes and *Il1b*$^{+}$ monocytes and *Calhm6*$^{+}$ mono/macs. *Ly6c2*$^{+}$ monocytes, *Ace*$^{+}$*Cd74*^{hi} monocytes, *Ace*$^{+}$*Cd9*^{hi} monocytes, *Ace*$^{+}$*Apoe*^{hi} monocytes comprised the majority of monocytes in the blood and their gene signature have already been published for murine blood monocytes[139,228] (Figure 3.5A-B). I identified a small *Calhm6*$^{+}$ cluster with marker genes that were overrepresented in "IFN activation pathways including response to interferon-gamma" (OR 5.21) (Figure 3.5D), similar to the IFN responsive *Calhm6*$^{+}$ mono/mac cluster I identified in the adipose tissue (see 2.4.2). The *Calhm6*$^{+}$ cluster also expressed high levels of Major Histocompatibility Complex (MHC) genes (*H2-Ab1*, *H2-Eb1*, *H2-M3*) as well as *Ciita*, which encodes for the protein Class II transactivator (CIITA) and is a transcriptional

coactivator that regulates γ-interferon-activated transcription of MHC class I and II (Figure S 11B). Type I interferon activation pathways such as "cellular response to interferon-beta" (OR 11.2) were also overrepresented in the *Ly6c2*$^{+}$ monocyte cluster. *Ly6c2*$^{+}$ monocytes were increased at 12 w WD in the aorta, suggesting that this pathway is important in the biology of monocytes in metabolic disease (Figure 3.4C-D).

Hmox1^{+} monocytes expressed high levels of cathepsins (*Ctsb*, *Ctsd)* (Figure S 11B), markers of monocyte activation, suggesting an activated monocyte phenotype. *Hmox1* encodes for the enzyme heme oxigenase 1 (HO-1) that catabolises heme groups to carbon oxide and biliverdin. The antioxidative HO-1/carbon oxide pathway mediates inflammation resolution. Indeed, *Hmox1*$^{+}$ cluster marker genes were overrepresented in pathways such as "cell redox homeostasis", "cellular iron homeostasis" and "response to reactive oxygen species", suggesting an antioxidative role of Hmox1 monocytes (Figure 3.4C-D).

Ilb^{+} monocyte subset expressed inflammatory genes including *Tlr2, Plaur* and *Cebpb* (Figure S 11B). Interestingly, this monocyte subset was mostly tissue-associated and not circulatory; aortic and epiWAT monocytes reconstituted 96.87% of this cluster, and only few blood monocytes showed this inflammatory phenotype (Figure 3.4C). This highlights that circulating monocytes show distinct phenotype compared to tissue monocytes (whether aortic or adipose tissue derived). In fact, I found minimal conserved markers across the three tissues (data not shown) and inflammatory status (*Il1b*, *Plaur* expression) was the main segregating factor between tissue and blood monocytes. Compared to the tissue specific analyses in Chapter 2, tissue monocytes could not be distinguished by *Ly6c2* and *Ace* expression when clustered with blood monocytes, further suggesting that the inflammatory phenotype of tissue monocytes is the predominant feature of these cells.

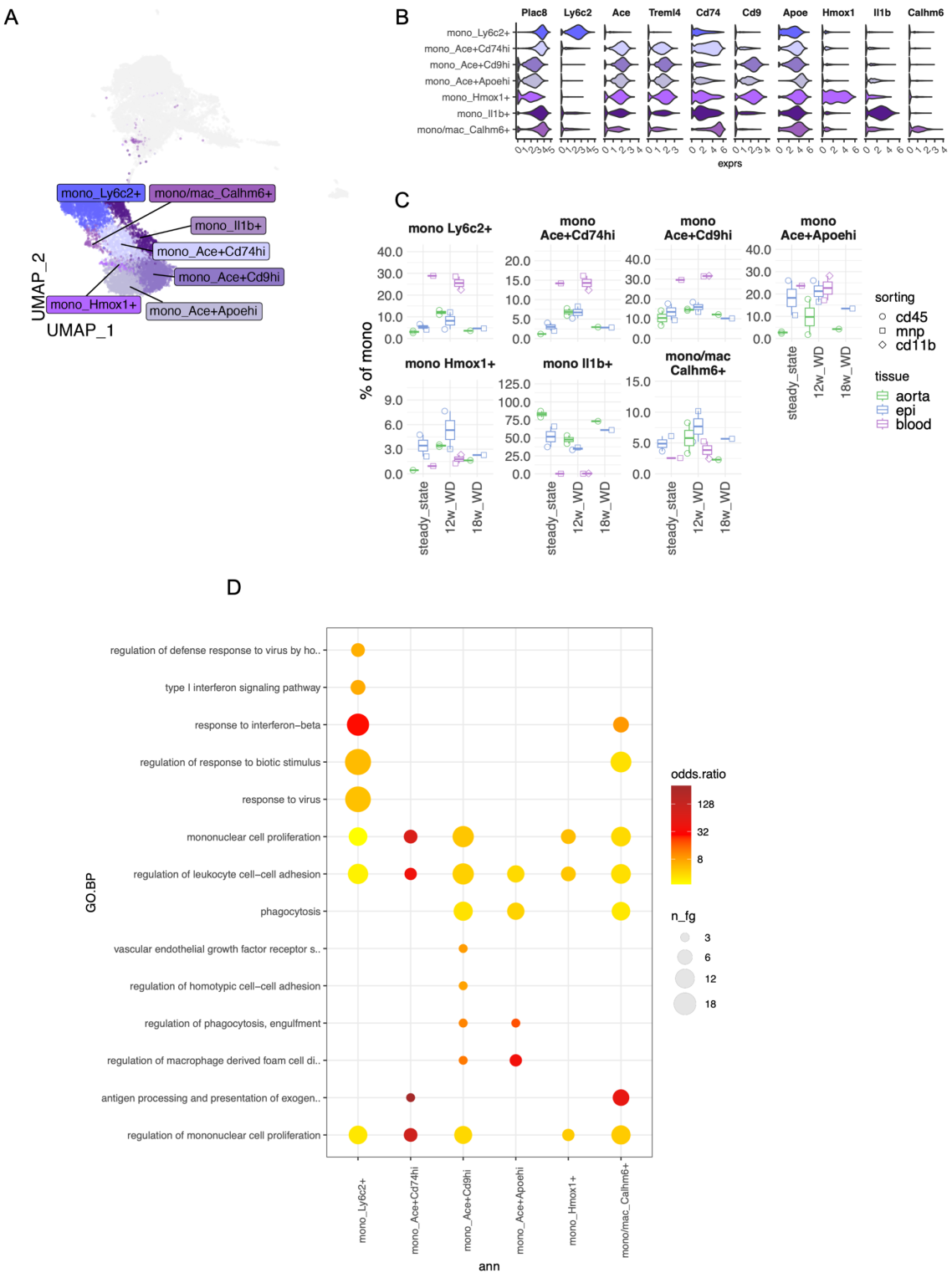


Figure 3.4: ***The combined single-cell landscape of monocytes in the aorta, epiWAT and blood using scRNAseq.*** *100024 mononuclear phagocytes (MNPs) from CD45$^+$ sorted, Lineage$^-$CD11b$^+$ sorted and Lineage$^-$CD11b$^+$CX3CR1$^+$ sorted WT and IRF5$^{-/-}$ samples from MBMC aortas, epiWAT and blood at steady state, 12w WD and 18w WD were analysed. A. Leiden clustering of the MNPs in the aorta identified 7 monocyte clusters. B. The violin plots show the expression levels of selected cluster marker genes (BH-adjusted P < 0.05, two-sided Wilcoxon tests) in each of the identified clusters. C. The box plots show the composition of WT cells in the monocyte compartment of the aorta, epiWAT and blood. D. The dot plot shows selected GO biological process categories that showed a significant overrepresentation in conserved cluster marker genes (Fisher test, BH adjusted p-value < 0.001). The colour of plots represents the odds ratio and the dot size represents number of differentially expressed genes that are part of this pathway category.*

Next, I compared the monocyte phenotype distribution between the epiWAT and the aorta using scCODA (Figure 3.5A). At steady state *Ace*$^{+}$*Apoe*^{hi} monocytes were more abundant in the epiWAT (mean frequency of MNPs=3.36%, mean frequency of monocytes=15.5%) than in the aorta (mean frequency of MNPs: 0.32%, mean frequency of monocytes=2.75%), while *Il1b*$^{+}$ monocytes were more abundant in the aorta (mean frequency of MNPs: aorta=9.82, epiWAT=7.52%, mean frequency of monocytes: aorta=82.32%, epiWAT=51.78%). *Ace*2^{+}*Apoe*^{hi} marker genes were overrepresented in pathways associated with phagocytosis (Figure 3.5D), i.e. "positive regulation of phagocytosis, engulfment" (OR 6.74). They expressed *Cd9, Cd36* and *Itgax (*Figure S 11*)*, markers of *Trem2*^{hi} LAMS and foamy monocytes found in the blood of hypercholesterolaemic mice[229]. *Ace*$^{+}$*Apoe*^{hi} monocytes share characteristics of previously described 'patrolling' *Ace*$^{+}$ monocytes that take up lipid, at steady state as well as during obesity, when entering the adipose tissue or atherosclerotic plaque[94]. Adipose tissue undergoes continuous lipolysis due to triglyceride turnover[40], which explains the role of these monocytes in adipose tissue even at steady state. However, in the aorta, monocyte recruitment is minimal at steady state which could explain the absence of *Ace*$^{+}$*Apoe*^{hi} monocytes in the aorta at this time point[119,120].

At 12w WD *Ly6c2*$^{+}$ monocytes (mean frequency of MNPs: aorta=1.31, epi=0.71%, mean frequency of monocytes: aorta=11.92%, epiWAT=7.00%) were more abundant in the aorta than in the epiWAT (Figure 3.5A). This finding is consistent with previous reports that suggest that monocyte recruitment is crucial in early atherogenesis for plaque formation[119] while in obesity a high contribution of cycling macrophages has been observed[40].

As discussed above, blood and tissue monocytes did not cluster together, suggesting potential differences in transcriptional status. To explore transcriptional differences between blood and tissue monocytes, I performed pseudobulk differential gene

expression analysis using edgeR (see 6.7.7). Reflecting the clustering segregation between blood and tissular monocytes described above, most genes differentially expressed between the aorta and the blood were also the same genes differentially expressed between the epiWAT and the blood (Figure 3.5B-E). Genes that were upregulated in both tissues regardless of the time point (steady state and disease) included complement cascade genes (*C3ar1, C5ar1),* receptors and mediators involved in monocyte recruitment *(Ccl2, Ccrl2 ,Ccr5, Ccl4, Cxcl2, Vegfa, Thbs1, Igf1*), markers of monocyte to macrophage/ DC maturation *(Nr4a2, Nr4a3, Cd14, Cd63)* and genes associated with inflammatory responses (*Il1b, Nlrp3, Osm, Il1rn)*, suggesting that tissue monocytes adopt a more activated and inflammatory phenotype once entering the tissue reflecting the monocyte compositional analysis described above (Figure 3.5D,E). This was consisted with previous reports that *Ly6c2*$^{+}$ monocytes are recruited to the epiWAT at steady state, where they acquire adipose tissue signatures and likely differentiate into CCR2^{+} macrophages[123]. Interestingly, genes that were upregulated in both tissues at 12 w WD but not at steady state included; inflammation regulatory genes *(Tnf, Cxcl10, Nfkbid, Nfkbia*), lysosome and lipid droplet- associated genes *(Ctsb, Lpl, Ctsl, Ehb1, Fabp5)* and genes involved in antigen presentation (*H2-Ab1, H2-Aa, H2-Eb1)* suggesting adaption to the proatherogenic/obesogenic environments in the tissues (Figure 3.5E). Overall, this suggested high similarity between transcriptional phenotypes of monocytes during tissue adaptation in aortas and adipose tissues with a limited number differentially expressed genes when comparing monocytes between the two tissues (Figure S 13). The few genes differentially expressed between the two tissues included the inflammatory genes *Il1b, Ccl2, Ccl4 and Tnf* (Figure S 13) consistent with differences in monocyte distribution at steady state.

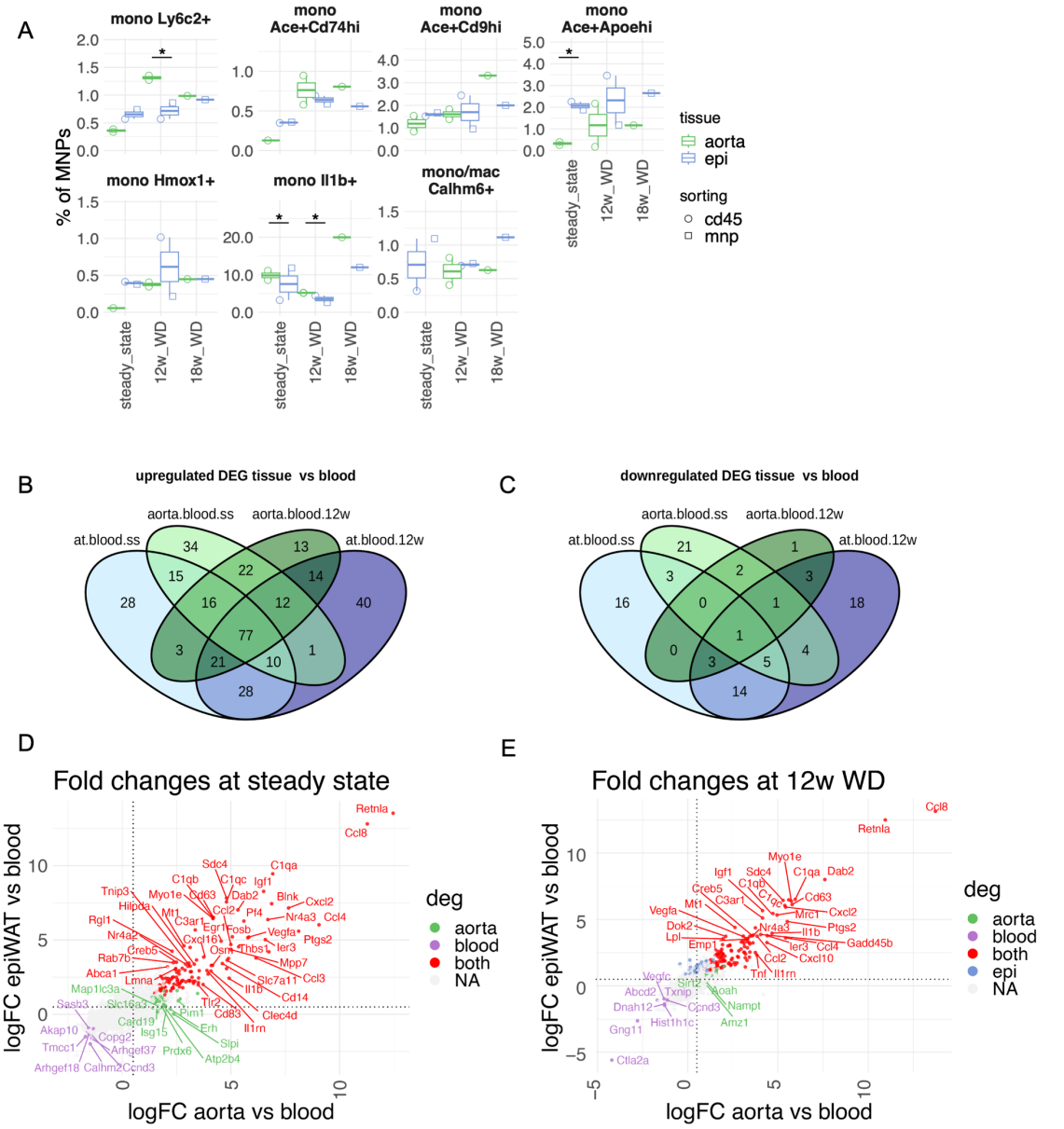


Figure 3.5 ***Monocytes transcriptionally adapt to the aorta and epiWAT microenvironments.*** *100024 mononuclear phagocytes (MNPs) from CD45$^+$ sorted, Lineage$^-$CD11b$^+$ sorted and Lineage$^-$CD11b$^+$CX3CR1$^+$ sorted WT and IRF5$^{-/-}$ samples from MBMC aortas, epiWAT and blood at steady state, 12w WD and 18w WD were analysed. A. The box plots show percentages of WT cells from the aorta and epiWAT that were found in identified clusters. Composition in the epiWAT was compared to composition in the aorta at steady state and 12w WD using scCODA. B. The Venn diagram shows the intersection and numbers of differentially upregulated genes when comparing aortic or epiWAT monocytes to blood monocytes at steady state or 12w WD. C. The Venn diagram shows the intersection and numbers of differentially downregulated genes when comparing aortic or epiWAT monocytes to blood monocytes at steady state or 12w WD. D./E. The scatter plots show log fold changes (logFC) of differentially expressed genes (BH adjusted p-value < 0.05, edgeR LRT test) between the aorta and blood (x-axis) and epiWAT and blood (y-axis) at steady state (D.) and 12w WD (E.). Differentially expressed genes are coloured by whether they are upregulated in both tissues (red), upregulated in the aorta (green), upregulated in the epiWAT (blue), or upregulated in the blood (violet). Differentially expressed genes were detected on pseudobulks using edgeR (LRT test, BH adjusted p value < 0.05, absolute logFC >0.5).*

3.3.4. Macrophages

Next, I investigated differences and similarities between the aorta and the epiWAT in the macrophage compartment (Figure 3.6). After integration of the blood, aorta and epiWAT, I identified 12 macrophage clusters that could be subdivided into 3 main groups: *Ccr2*^{hi} clusters (*Ccr2*$^{+}$*Il1b*$^{+}$ mono/macs, *Ccr2*$^{+}$*Cd226*$^{+}$ macrophages, *Ccr2*$^{+}$*Vegfa*$^{+}$); *Trem2*^{hi} macrophages and resident-like macrophage clusters including *MHCII*^{hi} macrophages, 3 *Folr2*$^{+}$ resident macrophage clusters (*Folr2*$^{+}$*Tcof1*$^{+}$ macrophages, *Folr2*$^{+}$*Lyve1*$^{+}$ macrophages, *Folr2*$^{+}$Txnip^{hi} macrophages), a *Mmp12*$^{+}$ and a *Fcgr4*$^{+}$ macrophage clusters; and *Mki67*$^{+}$ cycling macrophages (Figure 3.6A-B). In the integrated analysis, all clusters showed transcriptional similarities to clusters identified in the individual tissue analysis of the aorta and the epiWAT in Chapter 2 (Figure S 14). As expected, most clusters contained cells from both tissues, suggesting the existence of conserved transcriptional signatures (Figure 3.6C).

Compositional analysis with scCODA showed that at steady state *Ccr2*$^{+}$*Il1b*$^{+}$ mono/macs (mean frequency of MNPs: epiWAT=11.04%, aorta=1.68%) and *Ccr2*$^{+}$*Vegfa*$^{+}$ macrophages (mean frequency of MNPs: epiWAT=8.72%, aorta= 1.18%) were more abundant in the adipose tissue than in the aorta. In addition, *Ccr2*$^{+}$*Il1b*$^{+}$ mono/macs represented the biggest cluster in the epiWAT at 12w WD (mean frequency of MNPs: epiWAT=17.91%, frequency aorta=3.53%) (Figure 3.6C). This was consistent with previous reports highlighting the importance of CCR2 signalling in ATM expansion during obesity[38,39,230,231] as well as reports showing that Ly6C^{+} monocytes are recruited to the epiWAT at steady state, where they acquire adipose tissue signatures and likely differentiate into CCR2^{+} macrophages[123]. *Trem2*^{hi} LAMs were more abundant in the epiWAT at steady state (logFC abundance epiWAT/aorta=3.04) and at 12w WD (logFC abundance epiWAT/aorta=2.80) (Figure 3.6C), reflecting the high abundance of lipids in the adipose tissue.

MHCII^{hi} macrophages significantly increased in abundance in the epiWAT in disease and were more abundant in the epiWAT than in the aorta at 12w WD (mean frequency of MNPS: epiWAT=15.53%, aorta=0.92%) (Figure 3.6C). *MHCII*^{hi} macrophages also expressed high levels of *Trem2*, *Slamf9* and *Cd72* but not *Gpnmb* (Figure S 11C) consistent with a less "foamy" *Trem2* population recently identified in both steady state and disease in murine atherosclerotic plaques[117]. *MHCII*^{hi} macrophages might represent a less specialised lipid-associated macrophage population due to lack of expression of *Fabp4*, *Fabp5* and *Cd9* (Figure S 11C).

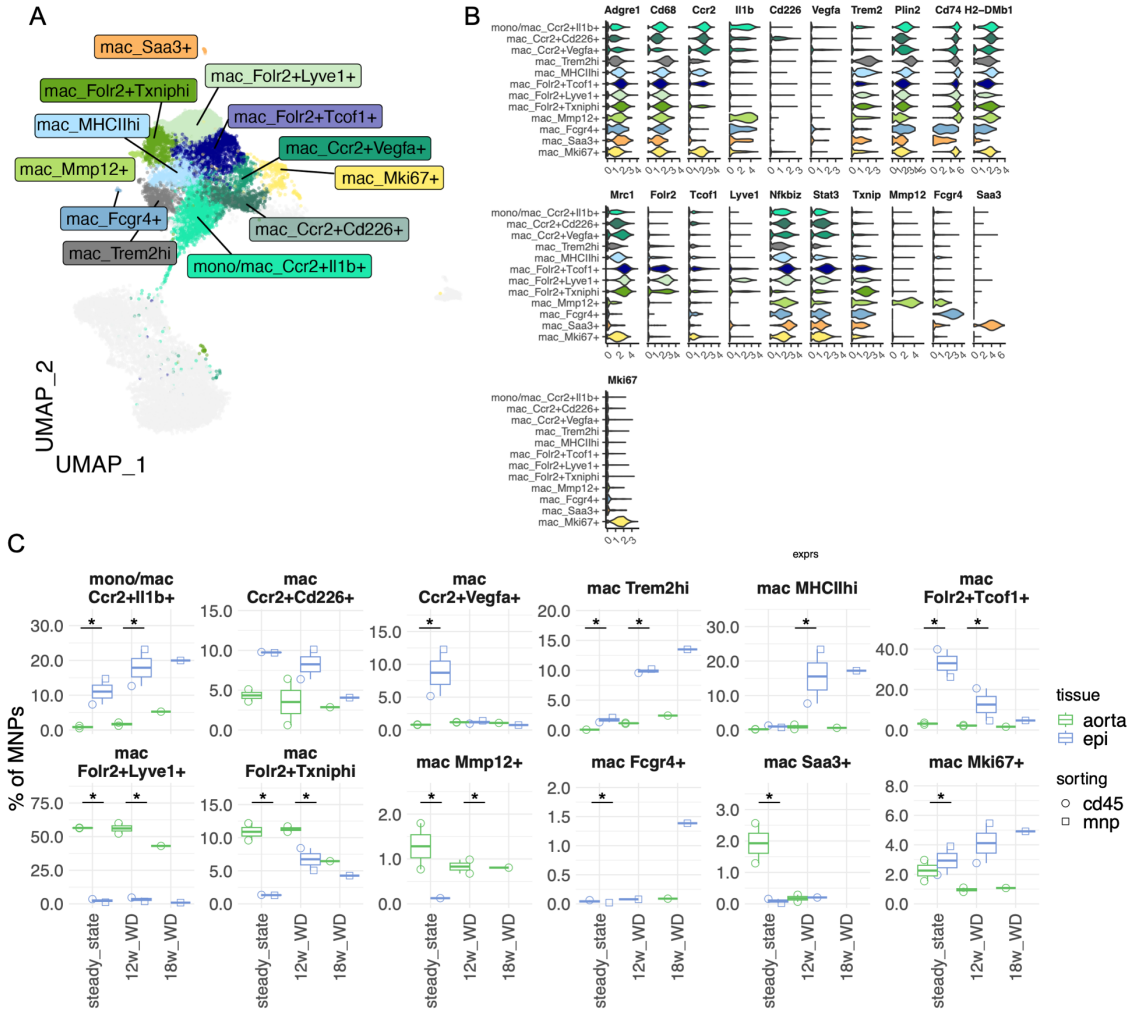


Figure 3.6: ***The combined single-cell landscape of macrophages in the aorta and epiWAT of mixed bone marrow chimeras (MBMCs) using scRNAseq.*** *100024 mononuclear phagocytes (MNPs) from CD45$^+$ sorted, Lineage$^-$CD11b$^+$ sorted and Lineage$^-$CD11b$^+$CX3CR1$^+$ sorted WT and IRF5$^{-/-}$ samples from MBMC aortas, epiWAT and blood at steady state, 12w WD and 18w WD were analysed. A. Leiden clustering of the MNPs in the aorta identified 12 macrophage clusters. B. The violin plots show the expression levels of selected cluster marker genes (BH-adjusted P < 0.05, two-sided Wilcoxon tests) in each of the identified clusters. C. The box plots show percentages of WT cells that were found in identified clusters. Composition in the epiWAT was compared to composition in the aorta at steady state and 12w WD using scCODA.*

The majority of cells in the aorta displayed resident-like *Folr2*$^{+}$*Lyve1*$^{+}$ (mean frequency of MNPs: steady state=56.48%, 12w WD=56.13%) and *Folr2*$^{+}$Txnip^{hi} macrophage phenotypes (mean frequency of MNPs: steady state=10.89%, 12w WD=11.29%), both when analysed separately and when integrated with epiWAT MNPs. Integration resulted in a decreased granularity in the aortic *Folr2*$^{+}$*Lyve1*$^{+}$ macrophage compartment compared to separate analysis of the aorta and only a small proportion of adipose tissue MNPs clustered with *Folr2*$^{+}$*Lyve1*$^{+}$ aortic macrophages (mean frequency of MNPS: steady state=2.37, 12w WD=3.29) (Figure 3.6C). In epiWAT, *Folr2*$^{+}$*Tcof1*$^{+}$ macrophages formed the largest resident macrophage cluster at steady state (mean frequency of MNPs: steady state =32.99%).

Mmp12^{+} macrophages were identified in all aortic samples, while *Fcgr4*$^{+}$ macrophages were only identified in the epiWAT suggesting the presence of tissue specific macrophage populations.

Overall, my data highlights differences in cluster distribution between the aorta and epiWAT at steady state and in disease that suggest differences in macrophage dynamics during homeostasis and metabolic disease progression.

3.3.4.1. Resident macrophages in the adipose tissue distinctly express CCR2

Since, resident macrophage in the aorta and the epiWAT clustered separately, I next explored transcriptional differences between *Folr2*$^{+}$ macrophage clusters from the aorta and the adipose tissue (Figure 3.7). First, I performed differential gene expression analysis on pseudobulks of *Folr2*$^{+}$ macrophages from the aorta and the epiWAT (see 6.7.7). At steady state 224 genes were upregulated in the epiWAT and 602 genes were upregulated in the aorta (BH adjusted $p<0.05$, fold change > 0.5) (Figure 3.7BCC). Consistent with homeostatic functions of *Folr2*$^{+}$ macrophages, fewer DEGs were detected at 12w WD and 18w WD (Figure 3.7B-C). Genes that were upregulated in the epiWAT at steady state and 12w WD included *Pparg, Lpl, Noct* and *Fabp4* (Figure 3.7D),

all part of the PPARγ signalling pathway, a pathway involved in lipid metabolism and cell proliferation[232]. The PPARγ pathway has been shown to regulate ATM maturation in the lean epiWAT thereby contributing to adipose tissue homeostasis[38,39,230,231]. In addition, epiWAT resident macrophages differentially expressed cell adhesion molecules including *Ccr2, Cd44, Cadm1* and *Fn1* at steady state and 12 w WD (Figure 3.7D). CCR2 and CD44 are important to adipose tissue physiology and metabolism; CCR2 plays a central role in ATM recruitment and proliferation, and CD44, in addition to being involved in functions associated with adhesion, migration and cell proliferation also displays metabolic functions and is involved in glucose and lipid metabolism[233]. Other differentially expressed genes in the epiWAT at steady were overrepresented in immune regulatory and transcriptional activation pathways including: "regulation of toll-like receptor 4 signalling pathway" (OR 13.32), "wound healing" (OR 3.92), and "histone methylation" (OR 11.50) (Table S 1) as well as phagocytosis (*Sirpb1c1, Prkgc* and *Tgm*). At 12 w WD, differentially upregulated genes in the epiWAT were overrepresented in pathways associated with adipose tissue homeostasis: "PPAR signalling pathway - Mus musculus (house mouse)" (OR 28.97), "lipid storage" (OR 12.76), "temperature homeostasis" (OR 6.55), "regulation of developmental growth" (OR 4.42) (Table S 2). Consistent with the proliferative transcriptional phenotype of *Folr2*$^{+}$*Tcof1*$^{+}$ macrophages, epiWAT *Folr2*$^{+}$ macrophages differentially expressed cell cycle and differentiation markers *Stmn1, Mcm6, Tcof1* at 12w WD, suggesting that proliferation of tissue resident ATMs was induced in disease.

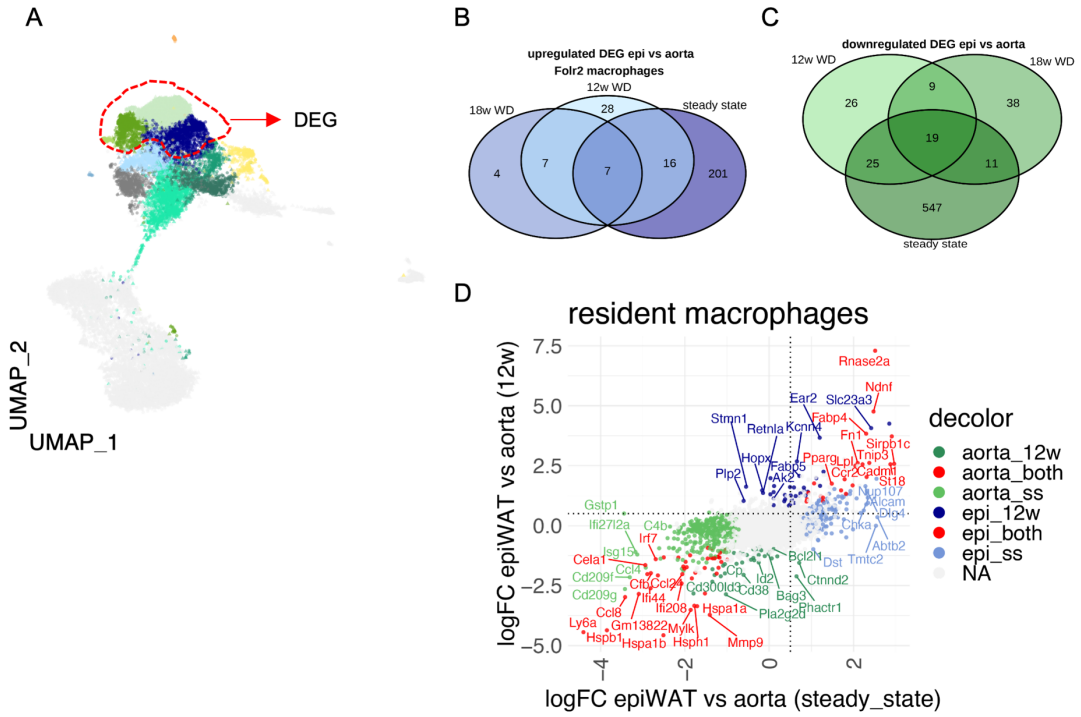


Figure 3.7: ***Resident macrophages in the aorta and epiWAT show tissue specific transcriptomes.*** *A. 100024 mononuclear phagocytes (MNPs) from CD45$^+$ sorted, Lineage$^-$CD11b$^+$ sorted and Lineage$^-$ CD11b$^+$CX3CR1$^+$ sorted WT and IRF5$^{-/-}$ samples from MBMC aortas, epiWAT and blood at steady state, 12w WD and 18w WD were analysed. Folr2$^+$ macrophage clusters (red dotted line) were subset for differential gene expression analysis. B. The Venn diagram shows the numbers of differentially upregulated genes when comparting epiWAT Folr2$^+$ macrophages to aortic Folr2$^+$ macrophages at steady state or 12w WD. C. The Venn diagram shows the numbers of differentially downregulated genes when comparting epiWAT Folr2$^+$ macrophages to aortic Folr2$^+$ macrophages at steady state or 12w WD. D. The scatter plots show log fold changes (logFC) of differentially expressed genes (edgeR LRT test, BH adjusted p-value < 0.05, absolute logFC >0.5) between the epiWAT and aorta at steady state (x-axis) and epiWAT and aorta at 12w WD (y-axis). Differentially expressed genes are coloured by whether they are differentially expressed at steady state and 12w WD (red), upregulated in the aorta at steady state (light green) or 12w WD (dark green), upregulated in the epiWAT at steady state (light blue) or 12w WD (dark blue).*

Differentially upregulated genes in the aorta were markers of tissue resident aortic macrophages and vascular macrophages including *Lyve1, Pf4, Cd209f* and *Cd209g* (Figure 3.7C-D) indicating that vascular associated macrophages are transcriptionally distinct from other tissue resident macrophage subsets. The differentially upregulated genes in the aorta at steady state were overrepresented in cytokine signatures and interferon response pathways including "response to interferon-alpha" (OR 6.85) and "cytokine activity" (OR 6.43) (Table S 1). At 12 w WD, DEGs that were upregulated in the aorta were overrepresented in immune activation pathways, such as "Lipid and atherosclerosis - Mus musculus (house mouse)" (OR 5.78), "regulation of inflammatory

response" (OR 3.38) and "pattern recognition receptor signaling pathway" (OR 4.72) (Table S 2). This suggests that aortic macrophages presented a more mature and activated macrophage phenotype than epiWAT macrophages. This is also in line with the heterogeneity of aortic resident macrophages identified in the separate analysis presented in 2.3.2. In contrast, resident-like *Folr2*$^{+}$ macrophage in the epiWAT displayed immune regulatory features, and adipose tissue inflammation might be driven by other macrophage clusters. Overall, this suggests that resident macrophages in the aorta and epiWAT have tissues specific functions.

To explore whether transcriptional differences in macrophage phenotypes were reflected in differences in surface marker expression, I performed CyTOF on MBMC at steady state and 12 WD (Figure 3.8A-B). Resident CD206^{+} macrophages from aorta and adipose tissue clustered separately (Figure 3.8D-E). The majority of CD206^{+} resident aortic macrophages showed a CD206^{+}CCR2^{-} phenotype. In contrast, epiWAT resident macrophages were CD206^{+}CCR2^{+} (Figure 3.8A-E). In summary, resident macrophages displayed a different phenotype both at the transcriptional and protein level between aorta and adipose tissue.

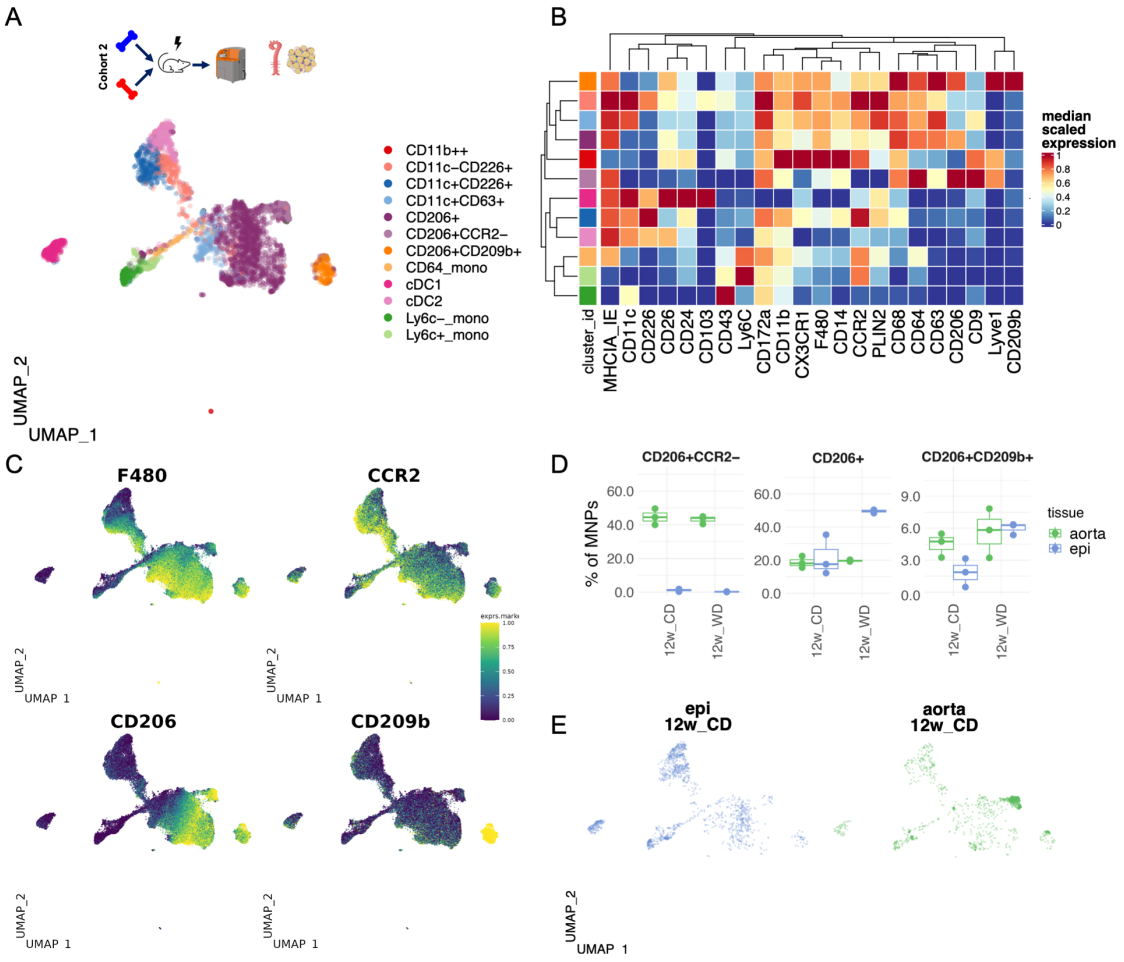


Figure 3.8: ***Resident macrophages in the adipose tissue distinctly express CCR2****. CyTOF was performed on aortas from mixed bone marrow chimeras (MBMCs) at steady state (12w chow diet (CD)) and 12wwestern diet (WD). A. Mononuclear phagocytes were analysed using FlowSOM clustering. Clusters were merged based on similarities of median marker expression. The analysis identified 3 monocyte, 2 dendritic cell and 6 macrophage clusters. B. Marker expression heatmap showing median scaled expression of surface markers used for clustering. C. Expression of selected markers that were used to identify CD206$^+$ macrophages. D. The boxplots show percentages of WT cells that were found in CD206$^+$ macrophage subsets. E. UMAP faceted by tissue at 12w CD after bone marrow transfer highlighting the different distributions of CD206$^+$ cells between the aorta and the epiWAT.*

3.3.4.2. *Itgax*$^+$ macrophages share transcriptional features in the aorta and epididymal white adipose tissue

CD11c$^+$ macrophage accumulation is a hallmark of obesity and atherosclerosis progression[43,44,119,128,211]. Therefore, I investigated *Itgax*$^+$ (gene coding for CD11c) macrophages in both the aorta and the epiWAT. I identified three *Itgax*$^+$ macrophage clusters: *Ccr2*$^+$*Cd226*$^+$ macrophages, *Trem2*^{hi} macrophages and *Mmp12*$^+$ macrophages. *Ccr2*$^+$*Cd226*$^+$ and *Trem2*^{hi} macrophages were present in aorta and epiWAT samples.

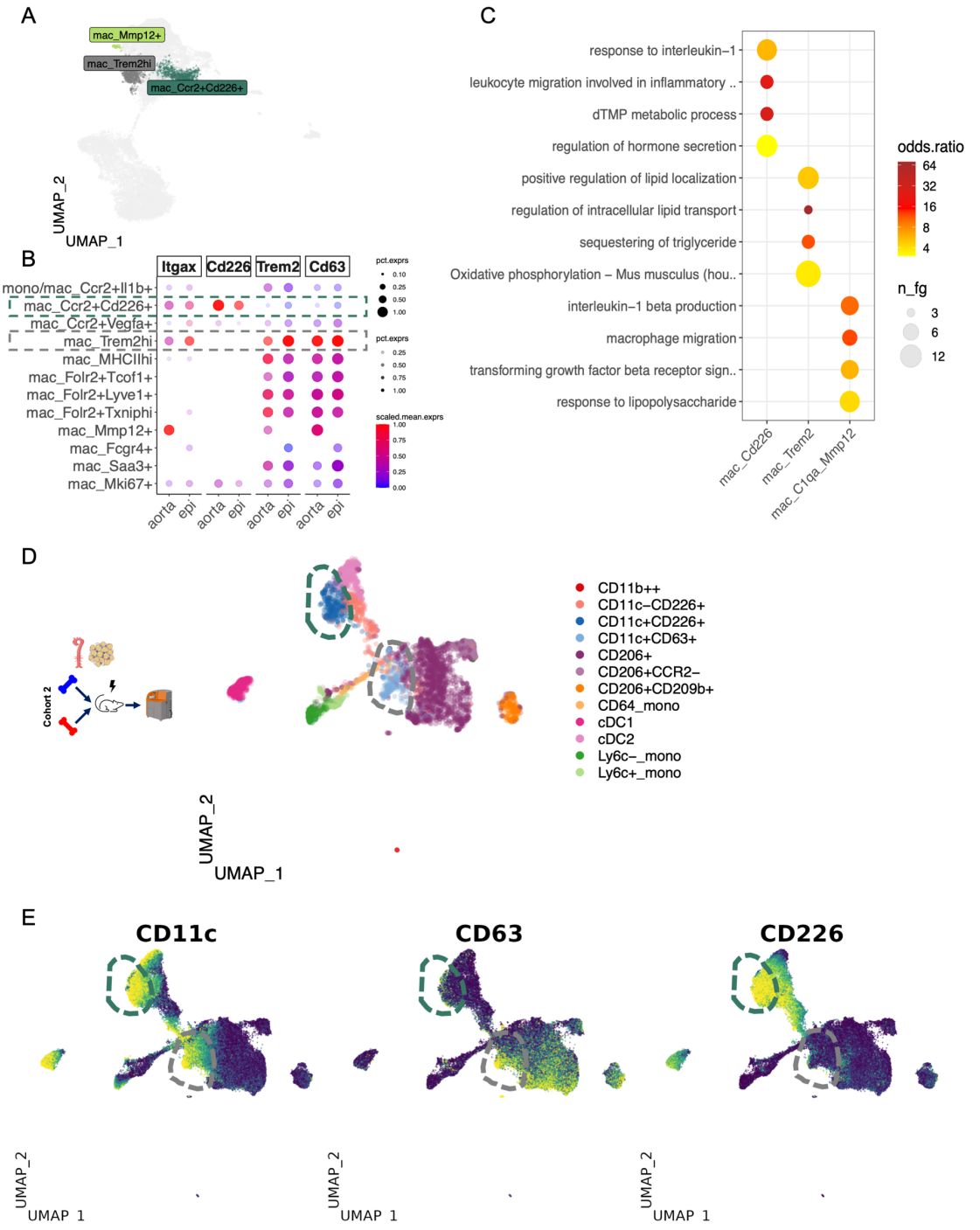


Figure 3.9: ***Two distinct CD11c$^+$ macrophage populations can be identified in the aorta and epiWAT using scRNAseq and CyTOF.*** *A. 100024 mononuclear phagocytes (MNPs) from CD45$^+$ sorted, Lineage$^-$ CD11b$^+$ sorted and Lineage$^-$CD11b$^+$CX3CR1$^+$ sorted WT and IRF5$^{-/-}$ samples from mixed bone marrow chimera (MBMC) aortas, epiWAT and blood at steady state, 12w WD and 18w WD identified three clusters expressing Itgax (encodes for CD11c). B. The dot plot shows the expression of selected cluster marker genes (BH-adjusted P < 0.05, two-sided Wilcoxon tests) that can be used to distinguish CD11c$^+$ macrophages. The colour of the dots represents the scaled average expression and their size reflects the percentage of cells within a cluster expressing the gene. Dots were only plotted for genes that were expressed in > 10% of the cluster. C. The dot plot shows selected GO biological process categories that showed a significant overrepresentation in conserved cluster marker genes (Fisher test, BH adjusted p-value < 0.05). The colour of plots represents the odds ratio and the dot size represents number of differentially expressed genes that are part of this pathway category. D/E. CyTOF was performed on aortas and epiWAT from MBMCs at steady state and 12w WD. Mononuclear phagocytes were analysed using FlowSOM clustering. E. Expression of selected surface markers that were used to distinguish two CD11c$^+$ macrophage subsets in the aorta and epiWAT (E.). CD11c$^+$CD226$^+$ macrophages are indicated by the green dotted line and CD11c$^+$CD63$^+$ macrophages are indicated by the grey dotted line.*

Conserved gene signatures across both tissues were overrepresented in cluster specific pathways, suggesting shared functional heterogeneity of CD11c$^+$ macrophages in metabolic tissues. *Ccr2*$^+$*Cd226*$^+$ macrophages showed an activated macrophage phenotype, while *Trem2*^{hi} macrophages displayed, as expected, a lipid homeostasis phenotype (Figure 3.9C). *Mmp12*$^+$ macrophages were mainly identified in the aorta at steady state (Figure 3.6C), in agreement with previous reports showing that Mac^{AIR} are replaced by monocyte derived macrophages upon high fat diet feeding[119]. Thus, I focussed on *Ccr2*$^+$*Cd226*$^+$ and *Trem2*^{hi} macrophages using distinctly expressed markers *Cd226* for the former and *Cd63* for the latter. First, I performed an integrated analysis of MNPs from 6 aortic and 2 epiWAT publicly available datasets as well as my MBMC dataset and validated the presence of both CD11c$^+$ macrophage subsets in non-irradiated mice (Figure S 15). I further validated the presence of the 2 CD11c$^+$ clusters at the protein level using CyTOF in both aorta and AT (Figure 3.9D-E). To understand CD11c$^+$ macrophage contribution to metabolic disease progression, I compared macrophage subset abundance at steady state and 12w WD. In the aorta CD11c$^+$CD63$^+$ macrophages, a proxy for *Trem2*^{hi} macrophages, expanded upon western diet feeding similar to what I identified in *Trem2*^{hi} macrophages using scRNAseq (Figure 3.10A). CCR2$^+$CD226$^+$ macrophages however did not change in abundance, suggesting that accumulating CD11c$^+$ macrophages in the aorta are LAMs (Figure 3.10A). Consistently with literature, CD206$^+$ resident-like macrophages did not change in their overall abundance at 12 WD, resulting in an overall shift towards a CD11c$^+$ macrophage phenotype in disease (Figure 3.10A). Similarly, in the epiWAT CD11c$^+$CD63$^+$ macrophages/*Trem2*^{hi} macrophages significantly increased at 12w WD in CyTOF and scRNAseq analysis, respectively. CCR2$^+$CD226$^+$ macrophages however show decreased abundance at 12 w WD in the epiWAT (Figure 3.10B). In contrast to the aorta CD206$^+$ resident-like epiWAT

macrophages expanded at 12w WD, suggesting that macrophage dynamics differ between the aorta and the epiWAT.

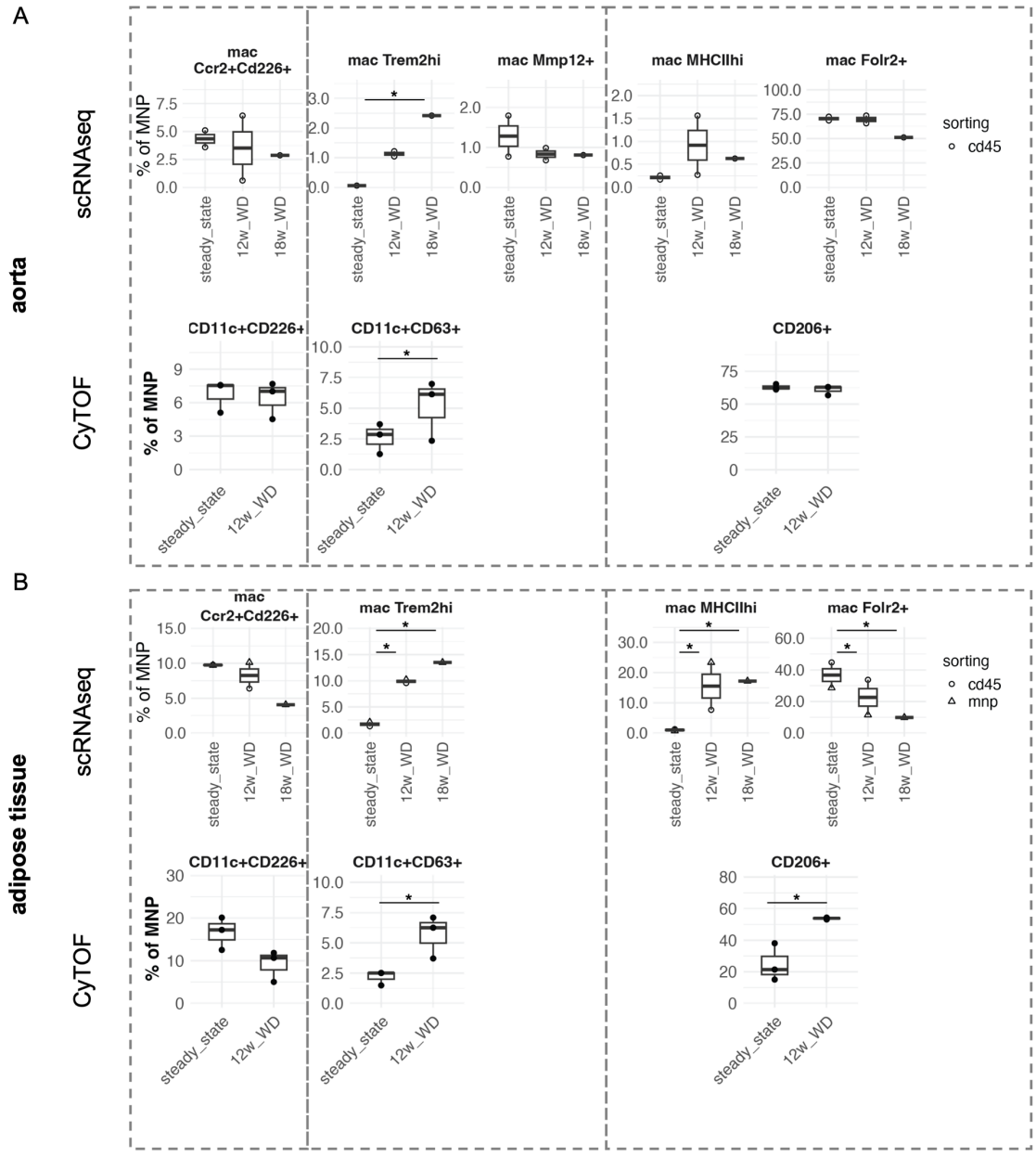


Figure 3.10 ***Macrophage dynamics in the aorta and epiWAT using scRNAseq and CyTOF.*** *Box plots show percentages of WT cells in macrophage clusters that were identified in the MNP compartment of the aorta (A.) and epiWAT (B.) in mixed bone marrow chimeras (MBMCs) using scRNAseq and CyTOF. Composition at steady state was compared to composition at 12w WD or 18w WD using scCODA.*

3.4. Discussion

In this chapter I aimed to define transcriptional similarities and differences in immune cells between the epiWAT and the aorta. First, I performed an integrated analysis of aortic and epiWAT T/NK cells. As described in Chapter 2, T cells in the aorta displayed, especially at steady state, more naïve phenotypes than in the epiWAT. Whereas at steady state, in the epiWAT NK cells and activated T cells constituted the majority of lymphocytes. However, in both tissues WD induced accumulation of activated CD4 and CD8 T cells. Even though T cell cluster abundance differed between the aorta and epiWAT, at 12w WD, I identified an increase in markers of T cell exhaustion in both tissues (*Pdcd1, Tox, Entpd1, Tigit*, and *Lag3*[224,225]*)*. T cell exhaustion has been reported in the atherosclerotic aorta and obese epiWAT in murine and human studies[47,65,220–222]. The inflammatory impairment of T cells in tissues during metabolic disease through exhaustion and senescence mechanisms could be physiological feedback to resolve the chronic low-grade inflammation[234]. Exhausted T cells are dysfunctional and secrete less cytokines, but might be also be implicated in dampening inflammatory responses[223]. It is unclear whether exhausted dysfunctional T cells contribute to metabolic disease progression. For example, PD1 deficiency resulted in increased atherosclerosis in mice[235,236], and PD1 blockade in cancer patients increased CVD[237]. In contrast, obesity is known to increase tumour progression through immunosuppression, metabolic and hormonal effects. Interestingly, PD1 blockade appears more effective to treat melanoma in obese mice and patients[238]. In the aorta, I also observed a significant increase in exhaustion gene scores in TH1 CD4 T cells and CD4 Tregs, consistent with a recently reported exTreg phenotype in mouse and human[63]. exTregs have also been reported in other autoimmune diseases. Interestingly, TH1 CD4 T cells and CD4 Tregs in the epiWAT did not show an increased expression of exhaustion markers, suggesting that self-antigenicity is more important in atherosclerosis. These observations suggest

impaired adaptive immune responses in both the aorta and epiWAT during metabolic disease progression.

For the myeloid analysis, I combined analysis of the aorta, epiWAT and blood and identified 7 monocyte, 4 DC and 10 macrophage subsets with distinct transcriptomic features that were shared between the two metabolic tissues in health and disease.

In metabolic disease, monocytes are recruited to the aorta and the epiWAT where they differentiate to macrophages driving metabolic tissue inflammation. Interestingly, tissue monocytes clustered separately from blood monocytes and differential gene expression analysis revealed shared transcriptional changes monocytes entering the aorta and the epiWAT when compared to blood monocytes, including chemokines and receptors indicative of monocyte recruitment and adhesion (i.e *C3ar1, C5ar1, Ccl2*) and inflammatory genes, such as *Il1b, Nlrp3*. In addition, at 12 w WD tissue monocytes upregulated lysosome and lipid droplet associated genes in both tissues (*Cstb, Lpl, Ctsl, Ehb1, Fabp5*) suggesting monocyte adaption to the tissue environment at steady state and in disease[123]. Aortic monocytes differentially expressed higher *Il1b, Ccl2, Ccl4*, and *Tnf* when compared to epiWAT monocytes, consistent with a higher abundance of $Ly6c2^{+}$ and $Il1b^{+}$ monocytes at steady state and in disease. In contrast, epiWAT monocytes showed higher abundance of $Ace^{+}Apoe^{hi}$ monocytes compared to the aorta, resembling foamy/phagocytic monocytes (high *Cd9, Itgax* expression). This might be due to the lipid-rich environment in the adipose tissue. Overall, tissue adaption signatures of monocytes were conserved across both tissues at steady state and disease, but differences in cluster distributions indicated differences in monocyte recruitment and contribution to disease progression between the aorta and the epiWAT.

Similarly, I also observed differences in the DC composition between the aorta and the epiWAT. The cDC1 cluster was more abundant in the epiWAT than in the aorta, consistent with the homeostatic role of cDCs in the lean adipose tissue. Nevertheless, DC

clusters were conserved across separate and integrated analysis, suggesting that DC functions are conserved between tissues.

In contrast, macrophages between both tissues showed higher heterogeneity. I identified 12 macrophage clusters, and most of them were present in both tissues except from *Mmp12*$^{+}$ macrophages (intimal resident Mac^{AIR}[119]) and *Fcgr4*$^{+}$ macrophages (phagocytic macrophages previously described in the adipose tissue[110]). *Ccr2*$^{+}$ macrophage clusters form the aorta and epiWAT clustered together, including *Ccr2*$^{+}$*Il1b*$^{+}$ mono/mac, *Ccr2*$^{+}$*Vegfa*$^{+}$ macrophages and *Ccr2*$^{+}$*Cd226*$^{+}$ macrophages. However, *Ccr2*$^{+}$*Il1b*$^{+}$ mono/macs and *Ccr2*$^{+}$*Vegfa*$^{+}$ macrophages were more abundant in the epiWAT, consistent with the reported importance of *Ccr2* for macrophage maintenance in the lean and obese adipose tissue[39,239,240]. In contrast, the majority of aortic macrophages displayed a *Folr2*$^{+}$*Lyve1*$^{+}$ macrophage phenotype that clustered separately from resident-like *Folr2*$^{+}$*Tcof1*$^{+}$ macrophages. Differential gene expression analysis in *Folr2*$^{+}$ macrophages between the aorta and the epiWAT indicated that epiWAT resident macrophages express higher levels of *Ccr2*, which I confirmed using CyTOF, and displayed a more stem-like phenotype. Ccl2, which is secreted by mature adipocytes[241] is required for macrophage proliferation in the epiWAT[40] through its interaction with its receptor CCR2. Therefore, *Ccr2* expression on resident epiWAT macrophages might contribute to macrophage proliferation or could suggest quicker turnover and dependence of monocyte recruitment than in the aortic resident macrophage compartment. Consistent with separate analysis of the aorta where I identified 10 *Folr2*$^{+}$ macrophage clusters, including homeostatic, phagocytic and inflammatory clusters (Chapter2), in disease aortic *Folr2*$^{+}$ macrophages upregulated genes associated with phagocytosis and macrophage activation, further supporting the notion that *Folr2*$^{+}$ macrophages in the aorta are highly heterogenous. In addition, the aorta harbours two anatomical distinct niches of resident macrophages: the intima and the adventitia, whereas in the adipose tissue displays one

continuous compartment and this difference could contribute to transcriptional differences between tissue resident macrophages. Overall, differences in macrophage cluster abundance in addition to phenotypic and transcriptional differences between resident macrophages suggest tissue specific functions of vascular associated *Folr2*$^{+}$*Lyve1*$^{+}$ macrophages and adipose tissue associated *Folr2*$^{+}$*Tcof1*$^{+}$ macrophages.

Disease-associated CD11c^{+} macrophages are known to be associated with atherosclerosis and obesity progression[38,109,211]. Here, I identify two distinct CD11c^{+} macrophages subsets that could be distinguished by CD226 and CD63 expression using scRNAseq and CyTOF. CD11c^{+}Cd63^{+} (*Trem2*^{hi}) macrophages specifically increase during metabolic disease progression in the epiWAT and the aorta. In contrast CD11c^{+}CD226^{+} (*Ccr2*$^{+}$*Cd226*$^{+}$) macrophages did not change in abundance in the aorta and even decreased at 12 w WD in the epiWAT, suggesting that not all CD11c^{+} macrophages in metabolic tissues are disease associated. In line with this, *Ccr2*$^{+}$*Cd226*$^{+}$ marker genes were overrepresented in activation pathways including response to interleukin-1 and leukocyte migration, suggesting immunoregulatory role.

In summary, MNPs in the epiWAT and aorta showed shared and distinct populations. In particular resident-like macrophages displayed tissue specific functions. In addition, compositional differences between the aorta and the epiWAT, especially in monocytes, the resident-like and the disease associated CD11c^{+} compartment, suggest tissue specific dynamics of macrophage accumulation and response to WD feeding. Therefore, elucidating functions using *in vivo* and *in vitro* experimental procedures of specific macrophage subsets that are either shared or distinct between the two tissues will help pinpoint new therapeutic targets.

Chapter 4. The role of IRF5 in shaping monocyte and macrophage heterogeneity during metabolic disease progression.

4.1. Introduction

IRF5 is a transcription factor that acts as a master regulator to induce a proinflammatory phenotype in macrophages[129]. IRF5 deficiency reduced atherosclerotic plaque burden in *Apoe*$^{-/-}$ mice[134,135], reduced plaque rupture frequencies in a mouse model of aortic ligation[136] and improved insulin sensitivity in diet induced obesity[137]. In atherosclerosis, IRF5 deficiency has been shown to reduces necrotic core size and was associated with a decrease in disease-associated CD11c^{+} macrophages[134,135]. In addition, IRF5 deficiency promoted expansion of CD206 resident/homeostatic macrophages over CD11c^{+} macrophage development in the inflamed colon[139]. IRF5 contributed to an altered macrophage phenotype in obesity: myeloid-specific IRF5 deficiency resulted in higher abundance of CD206^{+} macrophages in the obese epiWAT[137]. In addition, IRF5 regulates macrophage metabolism in response to short term high fat diet[138]. Together this suggests that IRF5 might act as an important regulator of macrophage activation in metabolic disease.

In addition, IRF5 is upregulated during monocyte[132] and neutrophil maturation[133]. Hypercholesterolaemia has been shown to induce emergency haematopoiesis, including extramedullary haematopoiesis in the spleen[27]. Hypercholesterolaemia and other risk factors of atherosclerosis, including inflammation, stress, sleep and aging affect the hematopoietic stem cell niche and result in a myeloid bias[26,27,81,84,242]. IRF5 genetic variants are associated with various autoimmune diseases, including systemic lupus erythematosus (SLE)[133]. Similar to atherosclerosis, murine and human haematopoiesis in SLE is skewed towards myelopoiesis[243,244] and IRF5 has been shown to be enriched in

$CD34^+$ bone marrow progenitors of SLE patients[245], suggesting a role in modulating inflammation beyond immune cell activation.

In this chapter I aim to uncover cell intrinsic effects of IRF5 deficiency on myeloid population in the context of metabolic disease.

4.2. IRF5 deficiency affects age dependent myelopoiesis

To investigate the cell intrinsic effects of IRF5 on myeloid populations in the context of metabolic disease in an unbiased model, $LDLR^{-/-}$ mice were irradiated and reconstituted with equal parts WT and $IRF5^{-/-}$ bone marrow cells and fed a chow diet for 3-4 weeks or western diet for 12 and 18 weeks to induce metabolic disease. Using mixed bone marrow chimeras (MBMCs), I aimed to assess cell intrinsic changes in the myeloid lineage depending on the IRF5 state without introducing the bias of supressed inflammation as seen in global IRF5 deletion.

I assessed the distribution of WT versus $IRF5^{-/-}$ myeloid cell reconstitution in both the circulation (blood) and in the studied tissues (aorta, epididymal adipose tissue) at all time points studied. $CD11b^+$ myeloid cells in the blood were equally reconstituted by WT (7.34±0.92% of leukocytes) and $IRF5^{-/-}$ (5.80±1.44% of leukocytes) cells at steady state. However, at 12 w and 18w WD, WT cells (13.21±2.28% of leukocytes) significantly outcompeted $IRF5^{-/-}$ cells (7.32±2.10% of leukocytes) (Figure 4.1A). Dominance of WT cells over $IRF5^{-/-}$ cells in the blood in disease was not driven by a specific myeloid subtype as WT cells outcompeted $IRF5^{-/-}$ cells in all subsets of myeloid cells, namely $Ly6C^{hi}$, $Ly6C^{lo}$ monocytes, neutrophils and eosinophils suggesting that IRF5 affected global myeloid development (Figure 4.1D).

In the aorta and adipose tissue, chimerism was assessed using pooled samples of 4-9 mice that were sorted for scRNAseq. Both tissues reflected the shift in chimerism seen in the blood; i.e. WT cells were more abundant than $IRF5^{-/-}$ myeloid cells at 12w WD, but not at steady state (Figure 4.1B).

To assess whether out-competition of IRF5$^{-/-}$ cells was driven by western diet feeding or was time dependent, I performed an additional set of mixed bone marrow chimera, where mice were fed a chow diet (CD) or a western diet (WD) for 12w weeks after 6-8w recovery and cells were collected from both control (CD) and experimental (WD) mice at the same time. Even though not significant due to low sample numbers, I observed a similar trend of higher abundance of WT cells compared to IRF5$^{-/-}$ cells in Ly6c^{hi}, Ly6c^{lo} monocytes, neutrophils and eosinophils in the blood of age-matched CD fed mice and WD fed mice (Figure 4.1E), showing that the genotype distribution of myeloid cells was not diet-dependent. This suggests a potential role of IRF5 in age dependent myelopoiesis. To explore whether IRF5 affected myeloid development in an earlier developmental stage, I investigated reconstitution efficiency in the bone marrow of MBMCs at steady state (CD for 3-4w after BMT), 12w CD and 12w WD. Consistent with previous reports[139], I observed no difference in reconstitution in CD45^{+} cells, long-term (LT) or short-term (ST) hematopoietic stem cells (HSCs), or myeloid progenitors cells including common myeloid progenitors (CMPs), granulocyte-monocyte progenitors (GMPs), granulocyte committed progenitors (GP), monocyte committed progenitors (MPs), common monocyte progenitors (cMoPs), monocyte-dendritic cell progenitors (MDPs) or bone marrow Ly6C^{hi} monocytes at either steady state or 12 w WD (Figure 4.2A-B). However, at both 12w CD and 12 w WD, I observed more IRF5$^{-/-}$ megakaryocyte-erythrocyte progenitors (MEPs) than WT cells (Figure 4.2B-C). CMPs diverge into MEPs (erythrocyte progenitors) and GMPs (myeloid progenitors). MEPs being more prevalent in IRF5$^{-/-}$ cells suggests that IRF5$^{-/-}$ cells might be more likely to differentiate into erythrocytes than myeloid cells, however, there were no significant changes in reconstitution in any of the myeloid progenitors. Therefore, further investigation is warranted to determine IRF5 causality on bone marrow cell maturation and differentiation.

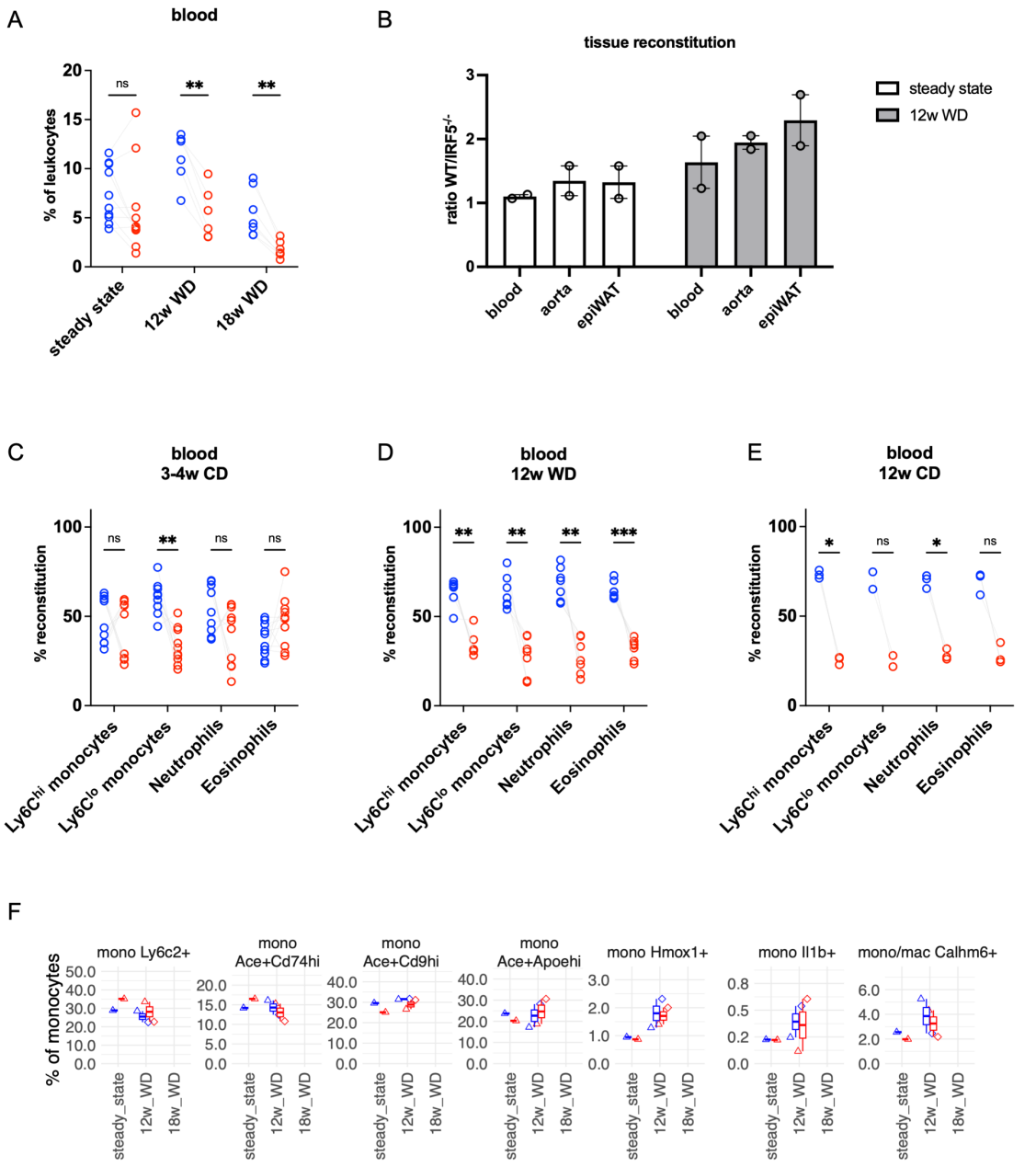


Figure 4.1: ***Myeloid WT cells outcompete IRF5$^{-/-}$ cells 20 weeks after bone marrow transfer in the blood, aorta and epiWAT.*** *A. Myeloid CD11b^{+} repopulation in the blood of mixed bone marrow chimeras (MBMCs) reconstituted with WT and IRF5$^{-/-}$ bone marrow was assessed using flow cytometry at steady state (3-4 chow diet (CD)), 12 weeks CD, 12 weeks western diet (WD) and 18 w WD (n=6-10 mice per time point from 2 independent experiments). B. Genotype reconstitution of myeloid cells (CD45^{+}Cd11b^{+}) from pooled MBMC samples that were used for scRNAseq was quantified at steady state (3-4 w CD) and 12w WD. Chimerism was quantified as ratio of WT/IRF5$^{-/-}$ cells (n=2 per tissue/time point). C-D. Reconstitution of myeloid subpopulations in blood at steady state (3-4 CD). (C.), 12 w WD (D.) (n=6-10 mice per time point from 2 independent experiments) and 12w CD (E.) (n=3 mice from 1 experiment). F. The box plots show the percentages of WT and IRF5$^{-/-}$ cells for monocyte clusters in the blood identified using scRNAseq data of mixed bone marrow chimera at steady state, 12w WD and 18w WD. No compositional differences between 12w WD and steady state were identified using scCODA. (A,C,D,E) Paired t-test with Holm-Šídák correction, ns: p>0.05, ***: p<0.05, ****: p<0.001.*

Differences in myeloid cell reconstitution in the blood 18-20w after BMT might also indicate differences in cell egress from the bone marrow or cell survival in the blood. At steady state Ly6C^{lo} monocytes were shown to be preferentially derived from WT progenitors[139]. In my scRNAseq dataset all monocyte subsets (*Ly6c2*$^{+}$ monocytes, *Ace*$^{+}$*Cd74*^{hi} monocytes, *Ace*$^{+}$*Cd9*^{hi} monocytes, *Ace*$^{+}$*Apoe*^{hi} monocytes, Hmox1^{+} monocytes, *Il1b*$^{+}$ monocytes and *Calhm6*$^{+}$ monocytes) were identified in WT and IRF5$^{-/-}$ cells in blood and both tissues (Figure 3.4). However, *Ace*$^{+}$*Cd9*^{hi} and *Ace*$^{+}$*Apoe*^{hi} monocytes, transcriptionally identified as Ly6c^{lo} blood monocytes, showed a small decrease in abundance of IRF5$^{-/-}$ cells in the blood at steady state (frequency of sorted monocytes: *Ace*$^{+}$*Cd9*^{hi} WT=29.5%, IRF5$^{-/-}$=25.04, *Ace*$^{+}$*Apoe*^{hi} WT=23.61%, IRF5$^{-/-}$ 20.20%) (Figure 4.1F). In turn, Ly6c^{hi} monocytes were slightly increased in IRF5$^{-/-}$ cells (frequency of sorted monocytes: WT=28.78%, IRF5$^{-/-}$=35.05). Even though more data and higher samples size are needed to investigate these effects, the data presented suggest that IRF5 deficiency might affect monocyte maturation and transition towards Ly6c^{lo} monocytes in the blood.

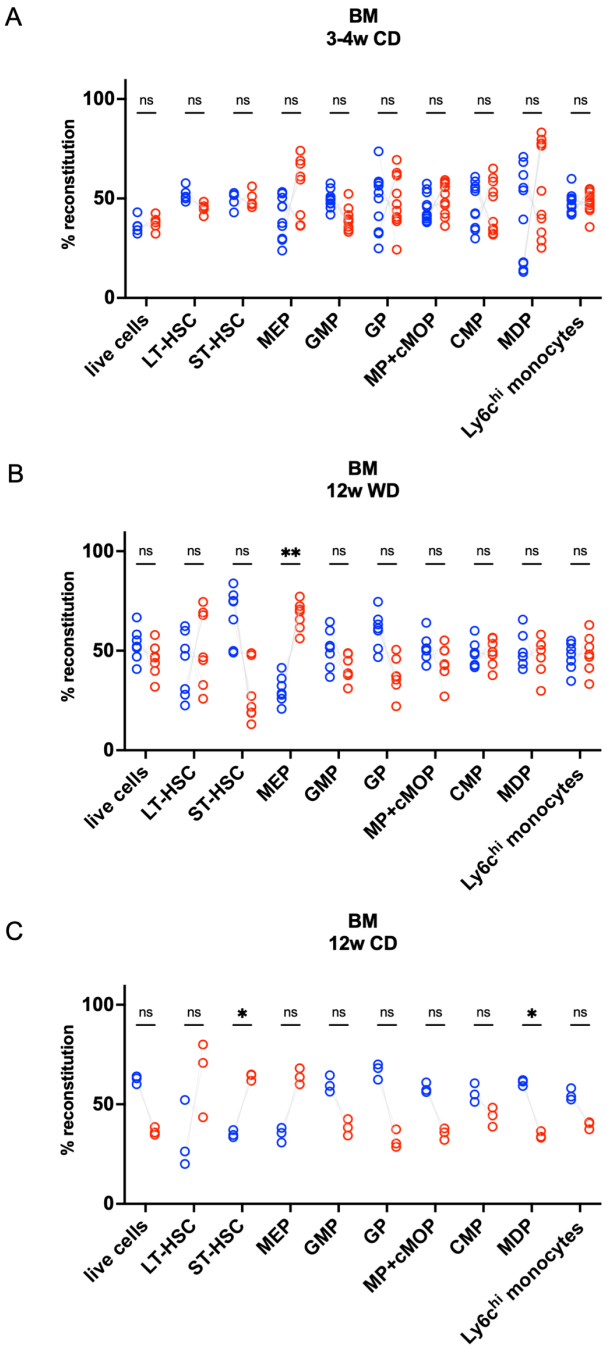


Figure 4.2: ***WT cells and IRF5$^{-/-}$ cells equally reconstitute the bone marrow of mixed bone marrow chimera.*** *A-C. Reconstitution of myeloid progenitors in the bone marrow from mixed bone marrow chimera (MBMC) reconstituted with WT and IRF5$^{-/-}$ bone marrow was assessed using flow cytometry at steady state (3-4 chow diet (CD)) (A.), 12 weeks western diet (WD) (B.) (n=6-10 mice per time point from 2 independent experiments) and 12 weeks CD (C.) (n=3 mice from 1 experiment). Long-term hematopoietic stem cells (LT-HSCs), short-term HSC (ST-HSC), common myeloid progenitors (CMPs), granulocyte-monocyte progenitors (GMPs), granulocyte committed progenitors (GP), monocyte committed progenitors (MPs), common monocyte progenitors (cMOPs), monocyte-dendritic cell progenitors (MDPs). Paired t-test with Holm-Šídák correction, ns: p>0.05, ***: p<0.05, ****: p<0.001.*

To assess the cell-intrinsic role of IRF5 on myeloid differentiation, I cocultured bone marrow-derived WT and IRF5$^{-/-}$ cells from mixed bone marrow chimera fed a western diet for 12 w. In both MCSF (monocyte colony stimulating factor) and GMCSF (granulocyte colony stimulating factor) cultures, the WT/IRF5$^{-/-}$ cell ratio increased after 7 days differentiation (Figure 4.3A-C). This might be due to 1) higher macrophage differentiation potential of WT compared to IRF5$^{-/-}$ cells, 2) higher proliferation potential of WT compared to IRF5$^{-/-}$ cells, 3) less apoptosis of WT compared to IRF5$^{-/-}$ cells. IRF5 has been shown to be upregulated downstream of GMCSF[129], suggesting that IRF5 might play a role in GMCSF dependent myeloid maturation. WT cells differentiated in the presence of GMCSF showed increased proliferation at day 3 of differentiation (Figure 4.3D,F) as assessed by BrdU incorporation. In contrast, proliferation and apoptosis in BMDMs (day 6 of differentiation) was not affected by macrophage genotype (Figure 4.3D-I). Overall, these data showed that IRF5 contribution to increase in macrophage cell number *in vitro* is most likely through progenitor proliferation and stimulating differentiation. To explore the effect of IRF5 deficiency on Ly6c^{hi} monocyte maturation to Ly6c^{lo} monocytes and macrophages *in vivo*, I performed slingshot pseudotime trajectory analysis on the blood, aorta and epiWAT at 12w WD (Figure 4.4). Pseudotime analysis with scVelo (see 2.3.2.1 and 2.4.2.1) suggested that infiltrating Ly6C^{+} monocytes were primarily predicted to become Ly6C^{-} monocytes or *Ccr2*$^{+}$*Il1b*$^{+}$ mono/macs with minimal contribution to other macrophage subsets in both the aorta and the epiWAT. Re-analysis of blood, aorta and adipose tissue cells from the clusters of interest defined 4 clusters: *Ly6c2*$^{+}$ monocytes, *Ace*$^{+}$*Cd74*^{hi} monocytes, *Ace*$^{+}$ monocytes and *Ccr2*$^{+}$*Ilb*$^{+}$ mono/macs (Figure 4.4A-C). Slingshot analysis identified two lineages: maturation of *Ly6c2*$^{+}$ monocytes to *Ccr2*$^{+}$*Ilb*$^{+}$ mono/macs (Lineage1) and maturation of *Ly6c2*$^{+}$ monocytes to *Ly6c2*$^{-}$ monocytes (Lineage2) (Figure 4.4B). In agreement with the fact that no compositional differences were detected between WT and IRF5$^{-/-}$ cells in these

populations at 12w WD (Figure 4.1F), distributions along pseudotime for both lineages were also not affected by genotype in all three tissues. This suggests that IRF5 deficiency does not affect *Ly6c2*$^{+}$ to *Ly6c2*^{lo}/*Ly6c2*$^{-}$ transition or *Ly6c2*$^{+}$ to *Ccr2*$^{+}$*Il1b*$^{+}$ mono/macs maturation in the blood or tissues *in vivo*. Overall, the data indicates that IRF5 might contribute to age related myelopoiesis by affecting GMCSF dependent proliferation during myeloid differentiation.

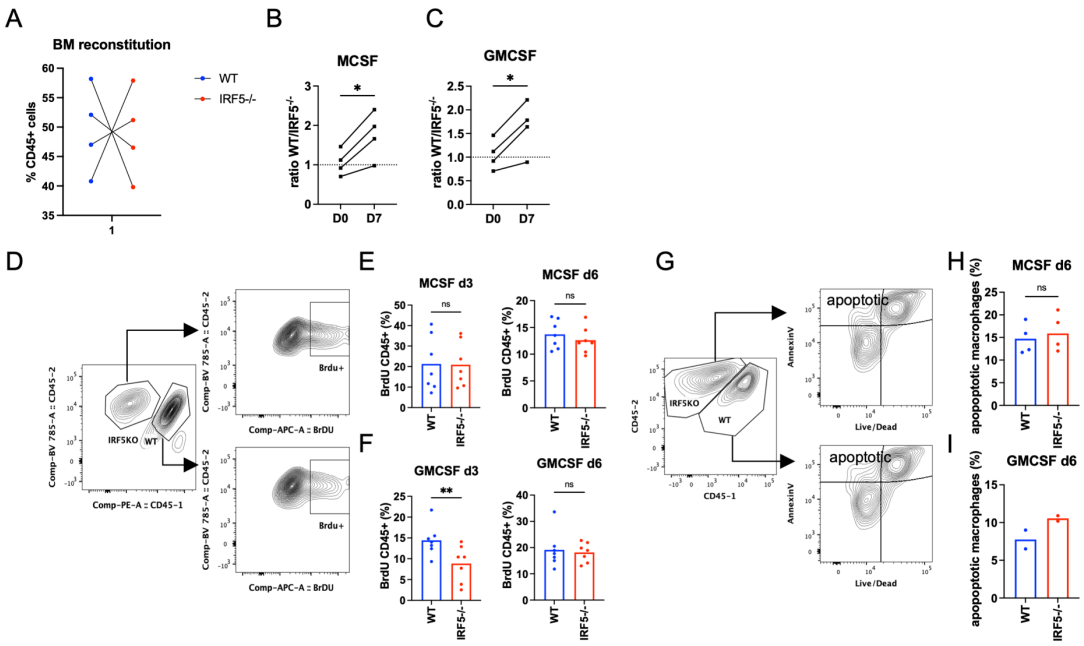


Figure 4.3: ***WT cells outcompete IRF5$^{-/-}$ bone marrow derived cells in vitro.*** *Bone marrow cells were isolated from mixed bone marrow chimera fed a western diet for 12w and differentiated in medium (10% FBS in RPMI) with either MCSF or GMCSF and adherent cells were analysed using flow cytometry. A.-C. Reconstitution of cells was assessed using flow cytometry before seeding (B.), after differentiation with MCSF (n=4) (B.), after differentiation with GMCSF (n=4) (C.). (B.-C.) Plots display the ratio of WT/IRF5$^{-/-}$ CD45^{+} cells at day 0 (D0) and day 7 (D7). D.-F. Cell proliferation was assessed at day 3 (d3) and day 6 (d6) of differentiation by incorporation of Bromodeoxyuridine (BrdU). Representative flow cytometry plots (D.) and proportions of BrdU^{+} cells cultured with MCSF (n=7, 2 independent experiments) (E.) or GMCSF (n=7, 2 independent experiments) (F.) are displayed. G.-I. Cell apoptosis was induced by incubation with 10 µM Camptothecin for 6h. Representative flow cytometry plots (G.) and proportions of Annexin V^{+} apoptotic macrophages differentiated with MCSF (n=4, 1 experiment) (H.) or GMCSF (n=2, 1 experiment) (I.) are displayed. B.-C. Paired t-test with Holm-Šídák correction. E.F.H. Unpaired t-test. ns: p>0.05, *: p<0.05, **: p<0.001*

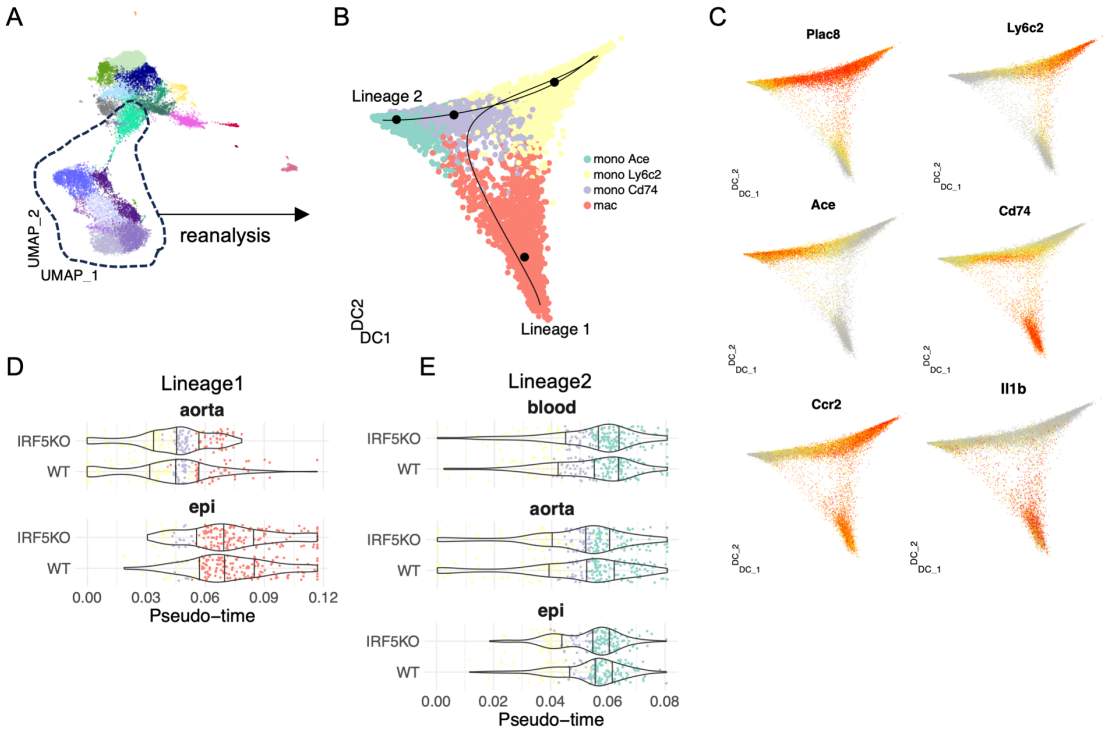


Figure 4.4: ***IRF5 deficiency does not affect monocyte maturation to Ly6C^{lo} monocytes or monocyte-derived macrophages in the blood, epiWAT or aorta.*** *A. WT and IRF5$^{-/-}$ monocyte and Ccr2^{+}Il1b^{+} monocyte/macrophage clusters (black dotted line) from aortas, epiWAT and blood from mixed bone marrow chimera at steady state, 12w WD and 18w WD were reanalysed for pseudotime analysis. B. Embedding of the cells in the first two dimensions of a diffusion map shows the two differentiation trajectories (solid lines) identified by the Slingshot pseudotime algorithm (with the Ly6c2 monocytes assumed to represent the root state). C. Expression of selected cluster marker genes. (D-E.) The violin plots show the progression of the WT and IRF5$^{-/-}$ (IRF5KO) cells through pseudotime in the aorta and epiWAT along the first trajectory (D.) and in the blood, aorta and epiWAT along the second trajectory (E.) as indicated in (B.) Differences in the distribution of cells along pseudotime trajectories between the genotypes were assessed with a Kolmogorov-Smirnov tests (P values were adjusted using the Bonferroni correction). No significant differences were identified (p>0.05). The position of the cells in pseudotime is shown on top of the violin plots. Cells are coloured by cluster as in (B). The positions of the 25th, 50th and 75th quantiles are indicated by the black vertical lines.*

4.3. IRF5 promotes accumulation of disease associated CD11c^{+}CD63^{+} macrophages in the aorta

To investigate whether IRF5 is a transcriptional regulator of CD11c^{+} macrophages in the aorta and epiWAT during metabolic disease progression, I compared macrophage cluster abundances between WT and IRF5$^{-/-}$ cells. Although there was no significant difference in CD11c^{+} macrophage abundance at steady state or disease in either of the tissues, *Trem2*^{hi} macrophage abundance was decreased in IRF5$^{-/-}$ cells in the aorta at 12w WD and to a lesser extent at 18 w WD (frequency of MNPs at 12w WD: WT=1.31±0.12%,

IRF5$^{-/-}$=0.75±0.14%; frequency of MNPs at 18w WD: WT=2.41%, IRF5$^{-/-}$=2.14%), but not in the adipose tissue (Figure 4.5A). I next confirmed this trend by performing CyTOF of non-competitive bone marrow chimera where LDLR$^{-/-}$ mice were either reconstituted with WT or IRF5$^{-/-}$ bone marrow cells. At 12w WD, CD11c^{+}CD63^{+} macrophages (protein markers for Trem2^{hi} LAMs) were significantly more abundant in the aorta of mice reconstituted with WT bone marrow than mice reconstituted with IRF5$^{-/-}$ bone marrow (6.70±0.57% in WT versus 4.17±1.35% in IRF5$^{-/-}$, scCODA composition analysis) (Figure 4.5D).

Differential gene expression analysis of WT and IRF5$^{-/-}$ macrophages suggested very few transcriptional differences between WT and IRF5 deficient macrophages, but *Trem2*^{hi} macrophages at 12w WD showed the most differentially expressed genes in the aorta supporting compositional changes observed in the aorta (Figure 4.5C). In the epiWAT no differentially expressed genes were detected at 12 w WD between WT and IRF5$^{-/-}$ *Trem2*^{hi} macrophages. WT Trem2^{hi} macrophages in the aorta differentially expressed the scavenger receptor CD36, and Lpl which encodes for lipoprotein lipase, indicating that IRF5$^{-/-}$ deficiency might affect lipid uptake (Figure 4.5C). In line with the transcriptional signature of WT cells, WT macrophages accumulated more DiL-oxLDL in an *in vitro* foam cell formation assay compared to IRF5$^{-/-}$ macrophages (Figure 4.5B).

Cxcl1 was upregulated in WT cells in the aorta and IRF5 deficiency is associated with reduced CXCL1 levels and consequently reduced neutrophil recruitment in mouse models of acute inflammation including antigen-induced inflammatory arthritis and lung injury[246,247]. However, neutrophil abundance was not affected in the atherosclerotic aorta or obese epiWAT, likely due to the chronicity of the diseases.

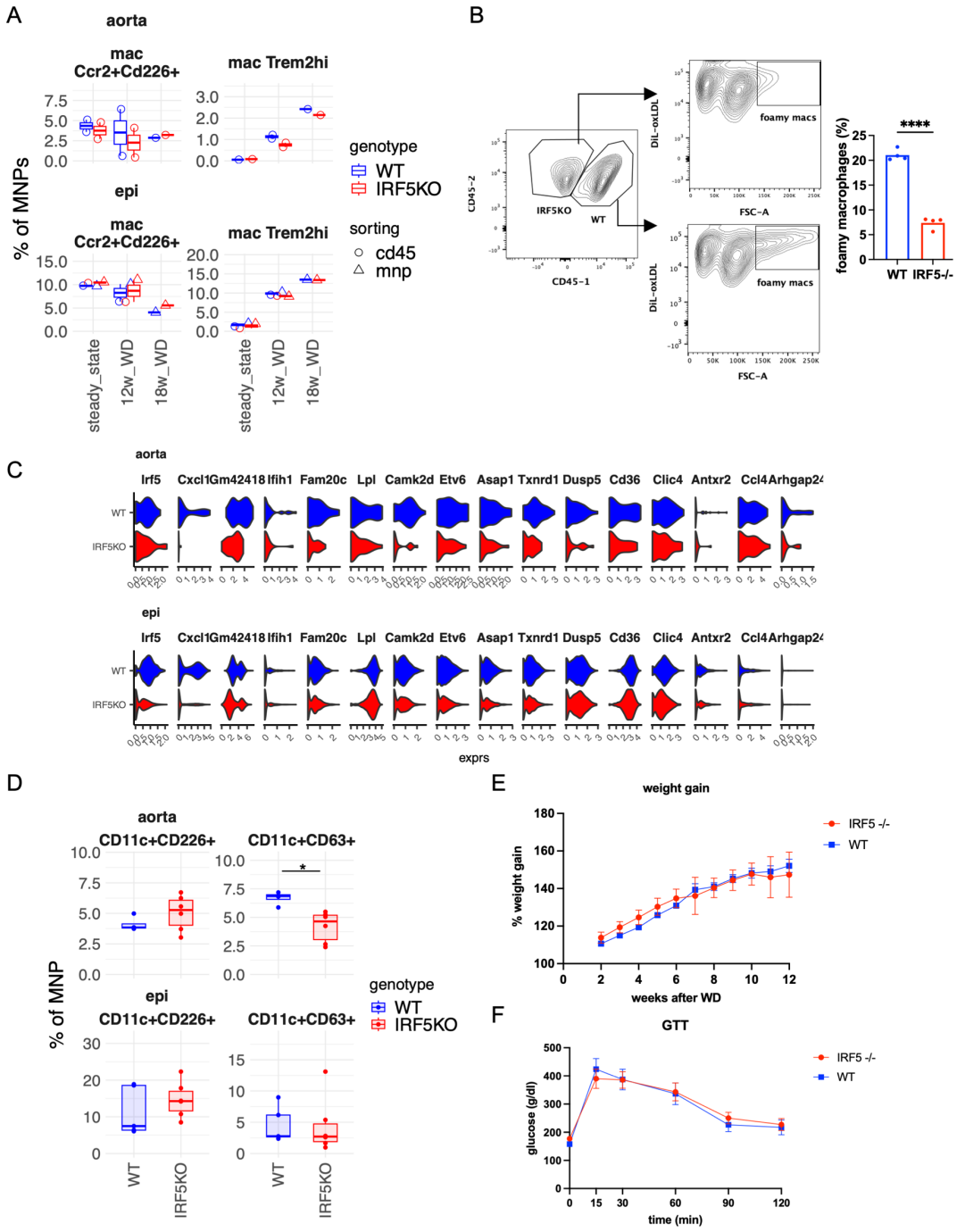


Figure 4.5: ***IRF5 promotes expansion of disease associated CD11c^{+}CD63^{+} macrophages in the atherosclerotic aorta****. A. The box plots show the percentages of WT and IRF5$^{-/-}$ cells for CD11c^{+} macrophage clusters in scRNAseq data of mixed bone marrow chimera at steady state, 12w WD and 18w WD. B. Bone marrow cells were isolated from mixed bone marrow chimera fed a western diet for 12w and differentiated in medium (10% FBS in RPMI) with MCSF and incubated with DiL-oxLDL (20µg/mL) for 24h. Adherent cells were analysed using flow cytometry. Representative flow cytometry plots and proportions of foamy macrophages are displayed (n=4, 1 experiment). Unpaired t-test. ns: p>0.05, *: p<0.05, **: p<0.001. C. The violin plots show expression levels in Trem2^{hi} macrophages in the aorta (top) and epiWAT (bottom) of differentially upregulated genes (edgeR, LRT test, BH corrected p value < 0.05, logFC >0.5) identified in the aorta when comparing Trem2^{hi} WT cells to Trem2^{hi} IRF5$^{-/-}$ at 12 w WD. D-F. CyTOF was performed on aortas and epiWAT from non-competitive bone marrow chimera reconstituted with either WT or IRF5$^{-/-}$ bone marrow and fed a western diet for 12 weeks. The box plots show the percentages of WT and IRF5$^{-/-}$ cells for CD11c^{+} macrophage clusters (D.). Body weight (E.) and glucose tolerance (F.) were not affected in mice reconstituted with IRF5$^{-/-}$ bone marrow. A./C. Composition in WT cells was compared to composition in IRF5$^{-/-}$ cells using scCODA.*

At steady state, IRF5$^{-/-}$ cells showed a decreased abundance of *Folr2*$^{+}$*Lyve1*$^{+}$ macrophages in the aorta (frequency of MNPs: WT=56.45±0.27%, IRF5$^{-/-}$ =49.01±4.87%), and *Folr2*$^{+}$Txnip^{hi} macrophages had more IRF5$^{-/-}$ cells (frequency of MNPs: WT=10.88±1.83%, IRF5$^{-/-}$=13.41±0.72%) (Figure S 16). These trends were not statistically significant, but, if confirmed in further validation experiments, they suggest that at steady state resident-like IRF5$^{-/-}$ macrophages may display a less activated macrophage phenotype in the aorta. In addition, similar to reports from the obese adipose tissue and inflamed gut[137,139], I also observed a small increase in abundance of *Folr2*$^{+}$*Lyve1*$^{+}$ macrophages in the aorta at 12w WD in the MBMC (frequency of MNPs at 12w WD: WT=56.12±5.43%, IRF5$^{-/-}$61.77±5.62%). However, no significant compositional shifts in the epiWAT were observed.

In summary, this indicates that IRF5 plays a role in regulating accumulation of disease associated CD11c^{+}Cd63^{+} (*Trem2*^{hi}) macrophages, while IRF5 deficiency results in accumulation of CD206^{+} resident-like (*Folr2*$^{+}$) macrophages in the aorta, but not the epiWAT.

4.4. Discussion

In this chapter, I investigated the cell intrinsic effects of IRF5 deficiency in the blood, aorta and epiWAT during metabolic disease progression. In MBMCs, WT cells outcompeted IRF5$^{-/-}$ cells over time in the blood, aorta and epiWAT, but not in the bone marrow. This suggests a role of IRF5 in hypercholesterolaemia/age related myelopoiesis and underlying mechanisms should be further explored using mouse models of emergency myelopoiesis. In addition, monocyte egress from the bone marrow and recruitment to the tissues could lead to the imbalance between WT and IRF5$^{-/-}$ cells in the blood and tissues. IRF5 deficient Ly6c^{hi} monocytes showed impaired chemotaxis in a mouse model of systemic lupus erythematosus[248]. A previous study of *Apoe*$^{-/-}$ mixed bone marrow chimera fed a high cholesterol diet for 12 weeks reported a shift in chimerism of

WT over IRF5$^{-/-}$ macrophages in atherosclerotic aortas[135]. Interestingly, WT cells also outcompeted IRF5$^{-/-}$ *in vitro*, but no difference in macrophage proliferation or apoptosis could be detected however WT exhibited a higher differentiation potential compared to IRF5$^{-/-}$ cells.

IRF5 deficiency in the aorta has been associated with a decrease in CD11c^{+} macrophages in the aorta[134] and inflamed gut[139]. Here, I show that IRF5 deficiency specifically resulted in a decrease in *Trem2*^{hi} LAMs in the aorta, but did not affect CD11c^{+}*Cd226*$^{+}$ macrophages. As reported previously[135], *Trem2*^{hi} IRF5$^{-/-}$ macrophages in the atherosclerotic aorta expressed lower levels of *Cd36* and IRF5$^{-/-}$ BMDMs showed decreased foam cell formation *in vitro*. In summary, the data presented here suggest potential roles of IRF5 in macrophage maturation, recruitment and foam cell formation. Surprisingly, IRF5 deficiency had no effect on cell composition in the epiWAT at steady state or in disease. Importantly, IRF5 deficiency in the context of obesity has not been associated with a decrease in CD11c^{+} abundance, but rather an increase of CD206^{+} macrophages[137]. Given the transcriptional differences between resident-like macrophages in the aorta and the epiWAT described in Chapter 2, differences in response to IRF5 deficiency between the tissues might reflect tissue specific monocyte-macrophage dynamics in the obese adipose tissue and the aorta.

Chapter 5. Discussion

Obesity is one of the biggest risk factors of atherosclerosis and cardiovascular disease and it is on the rise worldwide[140–142]. Obesity and atherosclerosis, even though traditionally acknowledged as lipid storage diseases, have been shown to depend on chronic inflammation[6,143]. Monocytes and macrophages are central to atherosclerosis and obesity progression. *In vitro*, monocyte derived macrophages subsets can be distinguished based on their differentiation environment and activation stimuli used. Importantly, *in vitro* macrophage phenotypes polarised with growth factors and stimuli relevant to atherosclerosis and obesity show distinct transcriptomes and surface markers beyond proinflammatory M1 macrophage and alternatively activated M2 macrophage polarisation. This includes M4 macrophages (differentiated in the presence of PF4)[249–251], Mox (polarised with oxidised phospholipids)[182]. However, the atherosclerotic plaque and obese adipose tissue represent diverse and dynamic microenvironments[252] and macrophage phenotypes seen *in vitro* might not exist *in vivo*. Functional, phenotypic, transcriptional and geographical heterogeneity of macrophages in the healthy and disease aorta and adipose tissue are becoming more and more appreciated through the help of single-cell studies[102–106,110,111,114,149]. Importantly, both diseases show accumulation of disease associated $CD11c^+$ macrophages[87,109,241,253], highlighting that macrophages across metabolic tissues share surface marker phenotypes. In atherosclerotic lesions, two $CD11c^+$ macrophage populations with distinct migratory and transcriptional phenotypes have been identified using reporter mice[107]. $CD11c^+$ adipose tissue macrophages express higher levels of proinflammatory cytokines compared to $CD11c^-$ macrophages[128], but *Trem2* foamy macrophages that express CD11c have been identified in atherosclerosis and obesity and are known to lack inflammatory gene expression programs[67,105]. In addition, integration of publicly available scRNAseq datasets from healthy and atherosclerotic murine aortas revealed the existence of two $Trem2^{hi}$ macrophage

populations (*Trem2*^{hi}*Gpnmb*^{hi}, *Trem2*^{hi}*Slamf9*^{hi})[117]. Overall, this suggests that CD11c^{+} cells constitute heterogenous populations.

To understand metabolic disease progression better, it is crucial to dissect how the tissue niche and metabolic disease stimuli might influence immune transcriptional states.

In this thesis, I aimed to investigate similarities and differences in the immune cell compartment between the aorta and epiWAT during a time course of metabolic disease progression using single-cell approaches.

Most single-cell studies are geared towards specific questions, and often focus on only one tissue and disease at a time. Mouse models of atherosclerosis and obesity often depend on feeding atherogenic high cholesterol or obesogenic high fat diets, respectively. Even though a meta-analysis of publicly available aortic scRNAseq datasets showed that most macrophage subsets were identified in both *Apoe*$^{-/-}$ and LDLR$^{-/-}$ mice[117], the biggest confounding factors when comparing results from different studies are genetic background and variation in diet composition.

To address these limitations, I performed a single-cell genomic investigation of immune cells in the aorta and epiWAT using mixed bone marrow chimera, allowing me to assess (i) myeloid transcriptional profiles in the aorta and epiWAT during metabolic disease progression, (ii) distinct and shared features of immune cells between the aorta and the epiWAT and, (iii) monocyte activation and differentiation programs and whether they are affected by IRF5 deficiency.

5.1. The aortic and adipose tissue *Folr2*$^{+}$ macrophage pools display divergent tissue specific transcriptional programs

Importantly, in the aorta and muscular arteries two distinct microanatomical niches exist, the artery's innermost layer, named intima, and the outermost layer, the adventitia. Both, the intima and the adventitia harbour tissue resident macrophages (TRMs) with either postnatal or embryonic origins, that are largely self-maintained through proliferation in

healthy ateries[119,121]. When the steady state is disrupted by disease, infection or genotoxic damage caused by irradiation a depletion of TRMs may occur and their niche can now be replenished by monocytes from the adult bone marrow. These monocytes have been shown to replicate transcriptional profiles and functions of TRMs in the lung and liver[254,255]. Embryonic derived *Tim4*$^{+}$*Lyve1*$^{+}$*Folr2*$^{+}$ (TLF) macrophages have been identified across multiple organs[118,256], including the epiWAT[118,123] and aorta[117,122]. Consistent with previous reports[119,121,149], I was able to identify resident adventitial *Lyve1*$^{+}$*Folr2*$^{+}$ macrophage clusters and a *Mmp12*$^{+}$ macrophage cluster expressing *Cd9*, *Cd72* , *Il1b* representing intimal resident macrophages (Mac^{AIR}) at steady state. At steady state and in disease the majority of macrophage clusters identified in the aorta displayed a *Lyve1*$^{+}$*Folr2*$^{+}$ phenotype consistent with resident adventitial macrophages. I identified a high heterogeneity in the resident-like macrophage compartment, including homeostatic/phagocytic clusters (*Folr2*$^{+}$*Lyve1*$^{+}$, *Folr2*$^{+}$Txniphi), inflammatory *Folr2*$^{+}$Nlrp3^{+} clusters (*Folr2*$^{+}$Mt2^{+}, *Folr2*$^{+}$Tlr2^{+}), interferon responsive clusters (IFN) suggesting various immunoregulatory functions for adventitial macrophages. After integration of my dataset with previously published datasets, at steady state resident-like macrophages from irradiated chimeras did not cluster together with resident macrophages from non-irradiated aortas. Differential gene expression analysis revealed that monocyte derived resident-like macrophages appeared more activated and lacked expression of bona fide tissue resident markers like *Timd4*, suggesting that not all transcriptional features of aortic TRMs can be acquired by monocyte derived cells. Adventitial resident macrophages have homeostatic functions including maintenance of vascular wall structure[122] and depletion of vascular resident macrophages results in atherosclerosis aggravation[149]. Hence, functional impairment or activation of adventitial resident macrophages after niche perturbation might affect atherosclerosis progression and health.

This might be relevant to patients undergoing radiotherapy, ageing or other processes that may cause damage to the resident macrophage niche.

In the epiWAT *Folr2*$^{+}$ macrophages were divided into a distinct vascular associated macrophage (*Folr2*$^{+}$*Lyve1*$^{+}$), stem-like homeostatic epiWAT TRMs (*Folr2*$^{+}$*Tcof1*$^{+}$) and phagocytic *Folr2*$^{+}$*Txnip*^{hi} macrophages. Integrated analysis with non-irradiated epiWAT single-cell datasets showed no differences in composition at steady state, suggesting that irradiation has a more pronounced effect on vascular macrophages. Similar to the aorta, DEG analysis revealed a higher expression of activation, proliferation and macrophage maturation markers in macrophages from chimeras, and higher expression of vascular associated macrophage genes in macrophages of non-irradiated mice[123], confirming the existence of a selective effect of genotoxic damage on vascular macrophages. After cross-tissue integration the majority of aortic TRMs clustered separately from epiWAT TRMs. Aortic TRMs at steady state and at 12 w WD differentially expressed genes associated with interferon response, immune activation, and phagocytosis, suggesting functional differences between aortic and adipose macrophages. In addition, epiWAT TRMs expressed higher levels of *Ccr2* than aortic TRMs. This finding was validated at the protein level using CyTOF. Our understanding on epiWAT TRM origin and maintenance at steady state is largely incomplete, with contrasting evidence collected so far, suggesting subset-dependent effects. It was recently indicated that murine epiWAT TRMs are embryonically derived and proliferate[257,258], but monocyte fate mapping suggested that ~50% of epiWAT TRMs were maintained through monocytes[112]. Three distinct TRM subsets with distinct origins and turnover kinetics in multiple murine tissues have been identified based on surface marker expression: TLF macrophages and MHCII^{hi} macrophages showed minimal to modest contribution of monocytes and depended on proliferation, while CCR2^{+} macrophages were continually replaced by monocytes[118]. The authors assessed macrophage turnover in the epiWAT and found that ~50% of CCR2^{+}

epiWAT TRMs were maintained by monocytes replacement. Overall, this suggests that CCR2 plays a role in epiWAT TRM maintenance through proliferation and monocyte recruitment. Consistent with the previously described ontogeny of arterial macrophages[120] and their expression of *Lyve1*[122], a metanalysis of publicly available murine scRNAseq aortic datasets confirmed that the majority of aortic macrophages displayed a TLF phenotype[117], suggesting differences in resident macrophage kinetics between the aorta and the adipose tissue. In summary, TRMs in the aorta and epiWAT have distinct transcriptional features suggesting tissues specific functions that should be further explored in the future. In addition, it is not known how TLF, MHCII^{hi} and CCR2^{+} macrophages contribute to tissue homeostasis, how different resident macrophage subsets interact with the tissue microenvironment and each other, and how differences in their abundance might affect their response to perturbations of the resident macrophage niche.

5.2. CD11c^{+} macrophages in the aorta and adipose tissue share fundamental transcriptional signatures but display differential regulation by IRF5

CD11c^{+} macrophages have been associated with metabolic disease progression[38,109], but their transcriptional regulation and function are still unknown. Using scRNAseq, I identified two distinct CD11c (*Itgax*) expressing clusters that were present in both the aorta and the epiWAT: *Trem2*^{hi} macrophages expressed *Itgax* and *Cd63* and *Ccr2*$^{+}$*Cd226*$^{+}$ macrophages expressed *Itgax* and *Cd226*. *Trem2*^{hi} macrophages had transcriptional features of LAMs that are known to accumulate in the atherosclerotic plaque and obese adipose tissue during metabolic disease progression. *Ccr2*$^{+}$*Cd226*$^{+}$ macrophages expressed *Il6* and conserved marker genes were overrepresented in pathways associated with macrophage activation. Using publicly available scRNAseq datasets I confirmed the presence of both CD11c^{+} macrophage subsets across mouse models of atherosclerosis and obesity. In addition, I validated the existence of CD11c^{+}CD63^{+} macrophages (a proxy for *Trem2*^{hi} macrophages) and CD11c^{+}CD226^{+} macrophages in both tissues as well as

their abundances in mixed bone marrow chimera using CyTOF. Importantly, in the aorta a net increase in CD11c$^+$ macrophage abundance was observed, whereas CD11c$^+$ macrophage abundance was unchanged in the epiWAT, suggesting different kinetics in disease progression in the aorta and adipose tissue. Diphtheria toxin mediated depletion of CD11c$^+$ myeloid cells reduced atherosclerosis lesion size[211] and global CD11c deficiency in CD11c$^{-/-}$*Apoe*$^{-/-}$ mice results in smaller lesions and reduced macrophage accumulation compared to *Apoe*$^{-/-}$ mice[213]. Similarly, CD11c$^+$ adipose tissue macrophages expressed higher levels of proinflammatory cytokines compared to CD11c- macrophages[128] and selective depletion of CD11c$^+$ ATMs improved insulin resistance in obesity[43]. Although these studies clearly establish an association between metabolic disease progression and CD11c$^+$ myeloid cells, functions of specific CD11c$^+$ macrophage subsets should be further investigated.

IRF5 is transcriptional regulator of pro-inflammatory macrophage polarisation and its deficiency resulted in decreased atherosclerotic plaque burden and improved insulin sensitivity in mouse models of atherosclerosis and obesity, respectively[134,135,137]. Hence, I hypothesised that IRF5 might act as regulator of a specific CD11c$^+$ macrophage subset. Indeed, IRF5 deficiency resulted in a decrease of *Trem2*hi/CD11c$^+$CD63$^+$ macrophages in the aorta, but not the epiWAT in competitive and non-competitive bone marrow chimera. This was further supported by transcription factor enrichment analysis in a metanalysis of publicly available murine scRNAseq datasets that identified enriched IRF5 activity in *Trem2*^{hi} macrophages and Mac^{AIR} [117]. *Trem2* macrophages in the obese epiWAT were not affected by IRF5 deficiency, in line with previous studies showing that IRF5 does not affect CD11c macrophages in obesity[137]. While my study identifies IRF5 as a driver of *Trem2*^{hi} macrophages in atherosclerosis, several questions remain unanswered. So far, I focussed on understanding conserved transcriptional programs between *Trem2*^{hi} macrophages between the aorta and the adipose tissue. The

atherosclerotic aorta and obese adipose tissue however display distinct tissue environments due to differences in tissue anatomy, lipid composition and tissue resident cell types. Therefore, contrasting transcriptional programs between the two tissues could help identify drivers of maladaptive lipid reprogramming. Another key question is the origin of *Trem2*^{hi} macrophages and their relationship to Mac^{AIR}. In line with fate mapping approaches[112,114], RNA velocity analysis suggested that *Trem2*^{hi} macrophages in the adipose tissue derive from monocytes and macrophage progenitors. However, in my analysis of aortic datasets no clear projection towards *Trem2*^{hi} macrophages could be identified. Fate mapping studies could reveal more details about *Trem2*^{hi} macrophage generation in the aorta and whether this process starts independently or sequential to Mac^{AIR} foam cell formation in early atherogenesis[119].

5.3. Future directions

In conclusion, I generated the first integrated single-cell immune atlas of the aorta and the epiWAT, highlighting shared and distinct transcriptomic features of metabolic disease progression in the lymphocyte and myeloid compartment.

Atherosclerosis and obesity are inflammatory diseases that depend on complex immune responses including adaptive and innate immune cell activation as well as their interplay at the immune synapse. In this thesis I mainly focussed on dissecting the myeloid immune cell compartment, but the presented analyses also suggested that, similar to the myeloid compartment, T cell transcriptional signatures might partly be conserved across metabolic tissues, even though subset abundance might differ between the tissues. In addition, the effect of tissue microanatomy could be further assessed by applying cell-cell communication analysis within the immune cell compartment and with non-immune cells. This could help identify new tissue specific and pan-tissue pathways helping the identification of new therapeutic targets.

Tissue specific compositions and transcriptomes of resident-like macrophages in the epiWAT and aorta at steady state and disease suggest functional differences during homeostasis and disease that are dictated by the tissue environment and/or specialised drivers. Disruption of the myeloid niche upon genotoxic damage such as irradiation has an important impact on aortic tissue in health and disease, as the monocyte to macrophage transition generates macrophage transcriptional states that are more inflammatory compared to their non-irradiated counterparts. This is less evident in the adipose tissues, highlighting the importance of understanding functional differences between co-existing tissue resident macrophages.

Even though shared $CD11c^+$ macrophage subsets were identified in the aorta and epiWAT, their difference in composition, transcriptional features and regulators in response to metabolic disease further highlight tissue specific myeloid dynamics during disease progression.

To further understand how tissue niche affects TRM and $CD11c^+$ macrophage phenotypes and functions, specific shared or distinct macrophage subsets should be further investigated using *in vivo* and *in vitro* experimental procedures. This will help pinpoint their contribution to disease progression. For example, specific depletion of *Trem2*^{hi} macrophages *in vivo*, could be achieved using a CD63 Cre driver line crossed with an inducible CD11c diphtheria toxin model. Mac^{AIR} that also express CD11c and CD63 and have a pro-atherogenic role, therefore time dependent depletion should be considered where depletion of $CD11c^+CD63^+$ macrophage is initiated after Mac^{AIR} have been displaced by monocytes. To further our understanding of how tissue niche and anatomy might affect macrophage phenotypes, functions and distributions, it will be important to identify spatial niche of specific populations. This could be achieved by performing RNAscope of cluster specific marker genes or using an unbiased spatial transcriptomic platform.

Chapter 6. Materials and Methods

6.1. Maintenance and breeding of mice

Animal procedures were performed according to UK Home Office regulations and institutional guidelines. All mouse strains on a C57BL/6J background were bred in individually ventilated cages under specific-pathogen free conditions. Mouse strains used were C57BL/6J wild type (WT) (JAX:000664); $LDLR^{-/-}$ (JAX: 002207) and $LDLR^{-/-}$ CD45.1 (generated by crossing $LDLR^{-/-}$ (JAX: 002207) and CD45.1 (JAX: 002014) mice). WT CD45.1, $IRF5^{-/-}$, $IRF5^{+/+}$ CD45.1 CX3CR1-$GFP^{+/+}$ and $IRF5^{-/-}$ CD45.2 CX3CR1-$GFP^{+/+}$ mice were provided by Prof. Irina Udalova. $IRF5^{+/+}$ CD45.1 CX3CR1-$GFP^{+/-}$ mice were generated by breeding $IRF5^{-/-}$ CD45.2 CX3CR1-$GFP^{+/+}$ with $IRF5^{-/-}$ mice and $IRF5^{+/+}$ CD45.1.2 CX3CR1-$GFP^{+/-}$ were generated by breeding $IRF5^{+/+}$ CD45.1 CX3CR1-$GFP^{+/+}$ with C57BL/6J wild type (WT) (JAX:000664) mice.

6.2. Genotyping

6.2.1. DNA extraction and polymerase chain reaction (PCR)

Genomic DNA (gDNA) was extracted from ear biopsies using RedExtract-N-Amp™ Tissue PCR Kit (Sigma-Aldrich) and amplified using Extract-N-Amp™ PCR ReadyMix™ (Sigma-Aldrich) according to manufacturer's instructions (Table 6.1,Table 6.2). gDNA was visualised in 1% agarose (ThermoFisher Scientific) gels in Tris-Acetate-EDTA (TAE) buffer (10x TAE buffer: 242g Tris-base, 57.1ml Glacial Acetic Acid, 18.6g, 100mM EDTA in 1L dH20) using SYBR DNA gel stain (ThermoFisher Scientific).

Table 6.1: PCR primers used for genotyping.

strain	common	WT	mutant
IRF5$^{-/-}$	CACGGTCTGCTCCTGTCTAA	CTTGAAGATGGTGTTGTCCC	CCTCCCCTACCCGGTAGAAT
CX3CR1-GFP	CCGCCCAGACGCCCAGACTA	AGCCGGAAGCCCAAGAGCATC	TGCTGCTGCCCGACAACCAC
LDLR$^{-/-}$	CCATATGCATCCCCAGTCTT	GCGATGGATACACTCACTGC	AATCCATCTTGTTCAATGGCCGATC

Table 6.2: PCR run parameters for genotyping.

		Cycles					
	Denaturing	**Cycle number**	**Denaturing**	**Annealing**	**Extension**	**Cycles**	**Completion**
IRF5$^{-/-}$	94°C 180s	1	95°C 30s	56°C 30s	72°C 60s	X35	72°C 600s
CX3CR1-GFP	94°C 120s	1	94°C 20s	65°C 15s (-1°C per cycle)	68°C 10s	X10	
		2	94°C 15s	60°C 15s	72°C 10s	X28	72°C 120s
LDLR$^{-/-}$	94°C 180s	1	94°C 30s	60°C 45s	72°C 45s	X35	72°C 120s

6.2.2. Blood sampling and flow cytometry

Blood samples were taken from tail veins using a 25G needle and collected in 100uL Alsever's solution (Sigma-Aldrich). Samples were washed in phosphate buffered saline (PBS) (Lonza) and red blood cells were lysed using RBC lysis buffer (Sigma-Aldrich) for 2 min at room temperature twice. Then cells were washed twice with PBS, stained for flow cytometry with CD45.1 and CD45.2 antibodies for 30 minutes at 4°C. The stained cells were washed twice with PBS and fixed in 200 µL 1x BD CellFix (BD Biosciences) for 10 minutes at 4 °C. Samples were analysed on the LSRII (BD Biosciences) or LSRFortessa X20 (BD Biosciences) flow cytometer.

6.3. *In vivo* experimental procedures

6.3.1. Competitive mixed bone marrow chimeras (MBMC)

8-14-week-old male WT CD45.1 or LDLR$^{-/-}$ CD45.1 mice were sublethally irradiated twice in a 4-hour interval using an X-ray irradiator (Gulmay; 1.8 Gy/min, 210 KV, 13 mA for 3 minutes). The irradiated mice received 3-5×10^6 bone marrow cells (50% WT, 50% IRF5$^{-/-}$) by tail vein injection 1 hour after the second irradiation. Antibiotic (Baytril, Bayer) was given for 2 weeks with drinking water. After 6-8 weeks recovery, mice were fed a chow diet for 3-12 weeks or obesogenic and atherogenic western diet (WD) for 12 weeks or 18 weeks. WD was purchased from ssniff Spezialdiäten (Germany) ((w/w%) Casein (24.00%), L-Cystine (0.30%), Maltodextrin (9.50%), Sucrose (20.16%), Cellulose (4.00%), Vitamin premix (1.00%), Mineral premix (6.00%), Choline chloride (0.25%), Butylated hydroxytoluene (0.01%), Cholesterol (0.25%), Pork lard (31.50%), Soybean oil (3.00%), Food dye Green (0.03%)).

6.3.2. Non-Competitive bone marrow chimeras (BMC)

8-12-week-old female LDLR$^{-/-}$ CD45.1 mice were sublethally irradiated twice in a 4-hour interval using an X-ray irradiator (Gulmay; 1.8 Gy/min, 210 KV, 13 mA for 3 minutes). The irradiated mice received 3-5×10^6 bone marrow cells (either WT or IRF5$^{-/-}$) by tail vein injection 1 hour after the last irradiation. Antibiotic (Baytril, Bayer) was given for 2 weeks with drinking water. After 6-8 weeks recovery, mice were a fed WD for 12 weeks.

6.3.3. Glucose tolerance testing

Mice were fasted for 4 h and were injected intraperitoneally with sterile filtered 1g/kg D-glucose (Sigma) solution. Repetitive glucose measurement were taken from the tail vein at baseline (before glucose injection), and at 15, 30, 60, 90 and 120 minutes after glucose injection using a glucometer (Abbot Freestyle Lite).

6.4. Single cell dissociation of murine tissues

6.4.1. Bone marrow

Femurs and tibias were dissected and disinfected for 1 min in 70% alcohol. The bone marrow was flushed with 5% FBS in RPMI-1640 (RPMI/FBS) and a 26G blunt cannula (Biochrome). For *in vitro* experiments red blood cells were lysed with Red Cell Lysis Buffer (Sigma-Aldrich) at room temperature for 2 minutes. Cells were washed with RPMI/FBS and filtered through a 70 µm cell strainer.

6.4.2. Blood leukocytes

The blood was harvested via tail vein bleeding (puncture with 23G needle) or cardiac puncture (27G needle). To prevent blood clotting, samples were stored with 100 µL heparin solution (200IU/mL) until ready for further processing. Erythrocytes were lysed by two 3 minute-incubations with 10 mL ice cold ACK lysis buffer (Gibco) followed by lysis buffer quenching with 15 mL ice cold RPMI/FBS. Cells were washed in cold medium and resuspended in PBS+ 0.1% bovine serum albumin.

6.4.3. Aorta

Single-cell suspensions of the aorta were prepared as previously reported[259]. In brief, hearts were slowly perfused with at least 10 mL of cold PBS (Lonza) to eliminate blood contamination before isolating the aorta. The whole aorta was dissected and the perivascular fat and cardiac muscle were removed. The aortic tissue was cut into small pieces and incubated at 37°C for 50 min with gentle shaking in RPMI/FBS containing DNase I (200 U/mL) (ThermoFisher Scientific), collagenase I (3.6 mg/mL) (Sigma-Aldrich), collagenase XI (0.1 mg/mL) (Sigma-Aldrich), hyaluronidase (0.15 mg/mL) (Sigma-Aldrich). Then cells were filtered through a 70 µm cell strainer.

6.4.4. Adipose tissue

Omental white adipose tissue and subcutaneous white adipose tissues were dissected carefully to avoid lymph nodes and then minced into small pieces. Tissues were digested with gentle shaking at 37 °C for 45-60 min in medium containing collagenase I (0.2% w/w) (Sigma-Aldrich) and vortexed every 15 min. Cells were washed twice with RPMI/FBS and the suspension was filtered through a 70 µm cell strainer.

6.5. Flow cytometry

Non-specific binding of antibodies was blocked by incubating cells with rat anti-mouse CD16/32 (BD Biosciences) followed by incubation with fluorochrome-conjugated antibodies recognising cell surface markers (Table 6.3). Cells were fixed with BD fix (BD Biosciences). Fortessa X-20 (BD Biosciences) flow cytometer was used for cell acquisition and data analysis was performed using FlowJo (v10.8.1).

Table 6.3: List of antibodies used for flow cytometry.

Antigen	Clone	Supplier
B220	RA3-6B2	Biolegend
CD115	AFS98	Biolegend
CD117	2B8	BD Biosciences
CD11b	M1/70	Biolegend
CD11c	N418	Biolegend
CD135	A2F10	Biolegend
CD138	281-2	Biolegend
CD150	W19132B	Biolegend
CD16/32	2.4G2	BD Biosciences
CD19	6D5	Biolegend
CD3	145-2C11	BD Biosciences
CD34	RAM34	eBiosciences
CD45.1	A20	Biolegend
CD45.2	104	Biolegend
CD64	X54-5/7.1	Biolegend
CD8	53-6.7	Biolegend
F4/80	BM8	Biolegend
Ly6C	HK1.4	Biolegend
Ly6G	1A8	Biolegend
NK1.1	S17016D	Biolegend
Sca1	D7	Biolegend
SiglecF	S17007L	Biolegend
TCRγδ	UC7-13D5	Biolegend
Ter119	Ter-199	Biolegend

6.6. *In vitro* experimental procedures

6.6.1. Bone marrow derived macrophages

Bone marrow progenitor cells were cultured in RPMI-1640 (Gibco) containing 10% FBS (Gibco), 10 units/mL penicillin (Gibco), 0.1 mg/mL streptomycin (Gibco), 2.5μg/mL amphotericin B (Gibco) and 50 μM 2-mercaptoethanol (Gibco), together with 100 ng/mL MCSF (PeproTech) or 20 ng/mL GMCSF (PeproTech). Medium was refreshed every 2 to 3 days. After 5-7 days differentiation, adherent cells were scraped, counted and replated ($5x10^5$ - $10x10^5$ cells/mL). Cells were then stimulated with DiL-oxLDL (20μg/mL) for 24 h (ThermoFisher Scientific).

6.6.2. Apoptosis Assay

BMDMs were incubated with 10 μM Camptothecin (Thermo Fisher) for 6h to induce apoptosis. Cells were washed twice with PBS and then scraped. The cell suspension was washed in FACS buffer (PBS+2% FBS) and unspecific binding was blocked by incubating cells with a rat anti-mouse CD16/32 antibody (BD Biosciences) for 10 min at 4°C followed by staining with fluorochrome conjugated antibodies for 1h at 4°C. Cells were washed twice in FACS buffer and then stained for Annexin V (Biolegend) following the manufacturer's protocol. Cells were fixed with BD CellFIX (1:10 in Annexin V binding buffer) for 10 min at 4°C. Cells were then washed with and resuspended in Annexin V binding buffer.

6.6.3. Proliferation Assay

The BrdU cell proliferation assay kit (BD Biosciences) was used as per manufacturer's protocol to asses macrophage proliferation: Cells were incubated for 3h at 37°C with 1mM BrdU. Cells were washed twice with PBS, scraped and washed once with FACS buffer in solution. Unspecific antibody binding was blocked with a rat anti-mouse CD16/32 antibody (BD Biosciences) for 10 min at 4°C followed by staining with

fluorochrome conjugated antibodies for 1h at 4°C. Cells were washed twice with FACS buffer and then fixed with BD Cytofix/Cytoperm for 30 min at 4°C. Cells were washed with BD Perm/Wash and stored at 4°C over night in FACS buffer. Between each of the following incubation steps cells were washed with BD Perm/Wash. First, cells were permeabilised with BD Cytoperm Permeabilization Buffer plus for 10 min at 4°C, and then incubated with BD Cytofix/Cytoperm for 5 min at 4°C. Next, cells were incubated with DNase for 1h at 37°C. Finally, cells were stained with APC anti-BrdU antibody for 20 min at room temperature. After washing, cells were resuspended in 1mL FACS buffer.

6.7. Single-cell RNA sequencing of mixed competitive bone marrow chimeras

6.7.1. Sample preparation

Single-cell suspensions from pooled (n=4-10 mice) aortas, epididymal adipose tissue and blood from MBMCs fed a chow diet for 3 weeks or western diet for 12 weeks or 18 weeks were prepared as described above. Cells were incubated for 30 min at 4°C with a rat anti-mouse CD16/32 (BD Biosciences) followed by incubation with fluorochrome-conjugated antibodies. Immune cells were sorted using an ARIA III flow cytometer (BD Biosciences). Multiple sorting strategies per tissue were applied to ensure good representation of cell types of interest in all tissues: live $CD45^+$ cells were sorted to acquire an overview of all immune cells in the aorta and adipose tissue; live $CD3^-CD19^-Terr119^-NK1.1^-TCR\gamma\delta^-CD138^-Ly6G^-SiglecF^-$(Lineage$^-$)$CD11b^+$ cells were sorted to acquire an overview of all monocytes in the blood; live Lineage$^-CD11b^+CX3CR1\text{-}GFP^+$ cells were sorted to enrich for monocyte derive macrophages in the adipose tissue and to enrich for monocytes in the blood (Table 6.4,Figure 6.1). In addition, similar cell numbers per genotype were sorted with the aim to uncover cell intrinsic effects of IRF5 deficiency during metabolic disease progression. Sample processing of FACS sorted cells for single-cell RNA sequencing was performed by Moustafa Attar. Sorted cells were washed with PBS+0.04% BSA before loading onto the Chromium 10x Genomics platform. Gene

expression libraries were prepared using the 10x Genomics Single Cell 3' Reagent Kits v2 following manufacturer user guide (CG00052). The final libraries were loaded on the Illumina HiSeq 4000 sequencing platform and sequenced with minimum depth of 30,000-50,000 reads/cell.

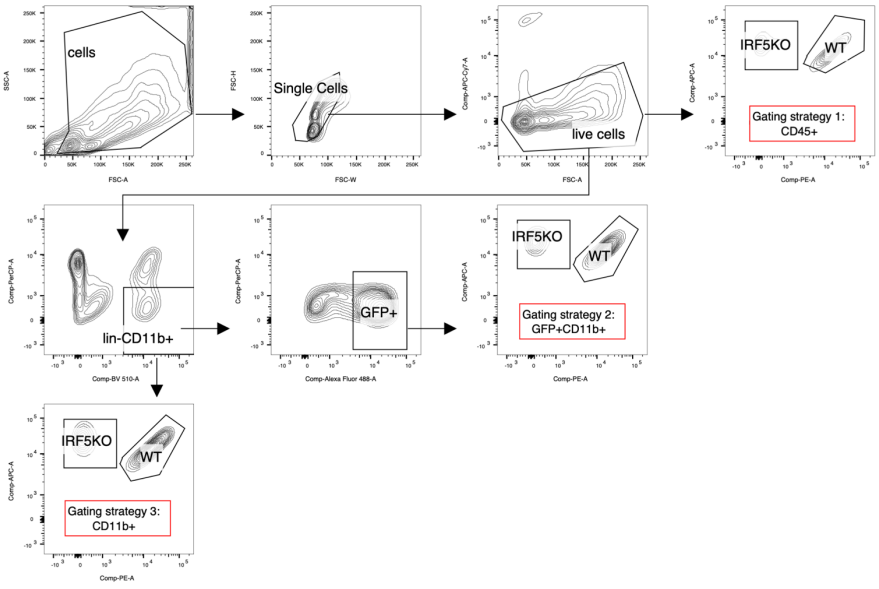


Figure 6.1: ***Representative sorting strategies for single-cell RNA sequencing analysis.***

Table 6.4: Overview of single-cell RNA sequencing samples and corresponding cellranger outputs.

tissue	disease time point	genotype	batch	number of mice in pool	Sorting strategy	Estimated number of cells	Mean reads per cell	Sequencing saturation
aorta	steady state	WT	A	6	Live $CD45^+$	1784	51020	94.34%
aorta	steady state	KO	A	6	Live $CD45^+$	1871	52377	94.67%
epiWAT	steady state	WT	A	6	Live $CD45^+$	8690	50803	73.06%
epiWAT	steady state	KO	A	6	Live $CD45^+$	4994	53654	75.40%
aorta	12w WD	WT	B	4	Live $CD45^+$	8259	48198	75.04%
aorta	12w WD	KO	B	4	Live $CD45^+$	5760	59690	84.11%
epiWAT	12w WD	WT	B	4	Live $CD45^+$	6681	52458	66.19%
epiWAT	12w WD	KO	B	4	Live $CD45^+$	5310	43203	63.94%
blood	12w WD	WT	B	4	Live Lineage-$Cd11b^+$	13412	25437	61.98%
blood	12w WD	KO	B	4	Live Lineage-$Cd11b^+$	6224	52476	71.86%
aorta	steady state	WT	C	10	Live $CD45^+$	9278	34994	79.61%
aorta	steady state	KO	C	10	Live $CD45^+$	9797	35953	81.55%
epiWAT	steady state	WT	C	10	Live Lineage-$Cd11b^+CX3CR1^+$	6507	47901	62.80%
epiWAT	steady state	KO	C	10	Live Lineage-$Cd11b^+CX3CR1^+$	7151	47041	65.71%
blood	steady state	WT	C	10	Live Lineage-$Cd11b^+CX3CR1^+$	7804	66912	82.42%
blood	steady state	KO	C	10	Live Lineage-$Cd11b^+CX3CR1^+$	7269	54480	78.54%
aorta	12w WD	WT	D	7	Live $CD45^+$	7868	78308	88.72%
aorta	12w WD	KO	D	7	Live $CD45^+$	5930	50171	90.03%
epiWAT	12w WD	WT	D	7	Live Lineage-$Cd11b^+CX3CR1^+$	6228	65943	72.83%
epiWAT	12w WD	KO	D	7	Live Lineage-$Cd11b^+CX3CR1^+$	8276	69861	82.54%
blood	12w WD	WT	D	7	Live Lineage-$Cd11b^+CX3CR1^+$	13650	34372	77.10%
blood	12w WD	KO	D	7	Live Lineage-$Cd11b^+CX3CR1^+$	7695	55106	76.78%
aorta	18 w WD	WT	E	6	Live $CD45^+$	5491	54541	81.27%
aorta	18 w WD	KO	E	6	Live $CD45^+$	5336	54464	83.35%
epiWAT	18 w WD	WT	E	6	Live Lineage-$Cd11b^+CX3CR1^+$	6439	53320	71.71%
epiWAT	18 w WD	KO	E	6	Live Lineage-$Cd11b^+CX3CR1^+$	6413	53051	74.65%

6.7.2. Data analysis strategy

Datasets were warehoused using cellhub (https://github.com/sansomlab/cellhub/). Sequence reads were aligned using the 10x Genomic cellranger multi pipeline (cellranger version 6.0.0) and the 10x mouse reference genome mm10 (GENCODE vM23/Ensembl98). For all downstream analysis cell counts were normalised and log1p transformed using Scanpy[260]. Highly variable genes (HVGs) were discovered using Scanpy highly_variable_genes function (flavour = 'seurat_v3', sorting HVGs first by "highly_variable_nbatches" and then by "highly_variable_rank") with analysis specific parameters. Clustering analyses were performed with pipeline_cluster.py (https://github.com/sansomlab/cellhub/).

6.7.3. Quality control and draft analysis

High quality cells with <5% mitochondrial reads and >200 genes were retained for downstream analysis (Figure 6.2). To assess the quality of the remaining cells, samples were integrated using scVI[261] on the full gene expression (GEX) space (batch_key=sample_id, covariates='ngenes', n_latent=50) and 3000 HVGs (batch_key='sample_id'). 10320 doublets were identified using Scrublet[262]. Doublets were defined as cells with scrublet score > median+2SD per sample or if >50% of cells within a cluster were identified as doublets. In addition, 5048 low quality cells identified as cells with a low number of UMIs and high percentage of mitochondrial genes and 522 contaminating non-immune cells (endothelial cells, fibroblasts, smooth muscle and platelets) were excluded from downstream analysis, resulting in 153213 immune cells that were reintegrated with 3000 HVGs (batch_key='sample_id') using scVI (batch_key=sample_id, n_latent=50). For draft analysis, major cell types (T cells, B cells, neutrophils, mononuclear phagocytes (MNPs)) were identified using low clustering resolution (pipeline_cluster.py). In short, an approximate neighbour graph was computed

on the scVI integrated latent space with scVelo[263] (n=20 neighbours, method='hnsw', Euclidean distance metric). The neighbour graph was used to compute UMAPs[264] and for Leiden[265] clustering across a range of resolutions. Clustering resolutions were compared using the clustree[266] package. Significant cluster markers were identified using the Scanpy rank_genes_groups function (Wilcoxon tests, Benjamini–Hochberg (BH)-adjusted P value < 0.05) and Gene set enrichment analysis of differentially expressed genes was performed using the gsFisher package (https://github.com/sansomlab/gsfisher/). Major cell types were identified using singleR[267] (ImmGenData and MouseRNAseqData as reference) and by known cell lineage marker expression and were subset for downstream analysis. Draft re-analyses of T/NK cells and MNPs per tissue were performed as described above and contaminating cell types as well as low-quality cells were excluded from downstream analysis resulting in a total of 145316 immune cells (aorta:49484 immune cells (12672 MNPs, 25905 T cells); epiWAT: 50927 immune cells (42445 MNPs, 5688 T cells), blood: 44907 MNPs) (Figure 6.3).

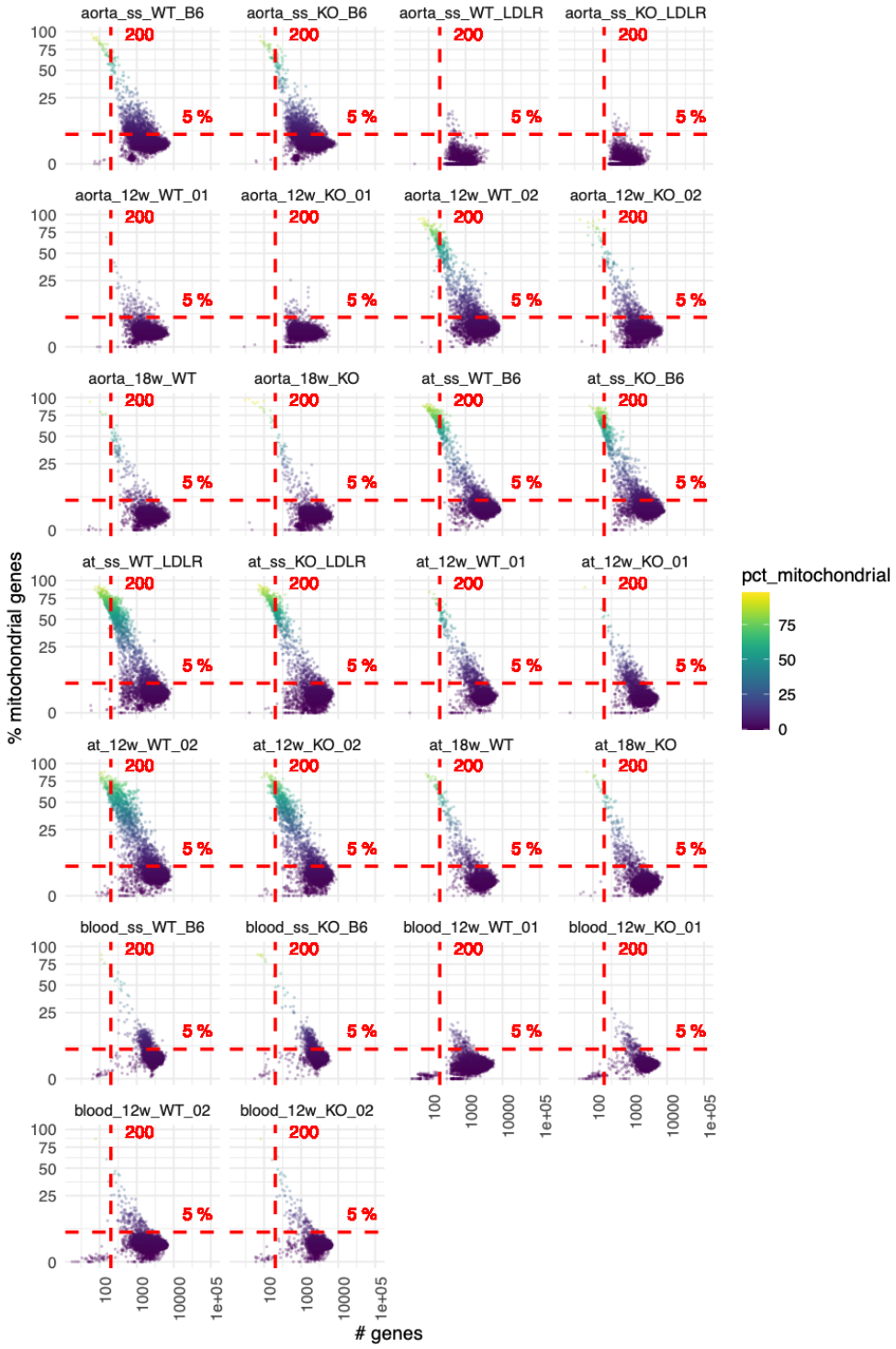


Figure 6.2: ***Scatter plot of number of genes and. % mitochondrial reads per sample coloured by % mitochondrial reads. Quality control filtering thresholds are indicated using red dotted lines.***

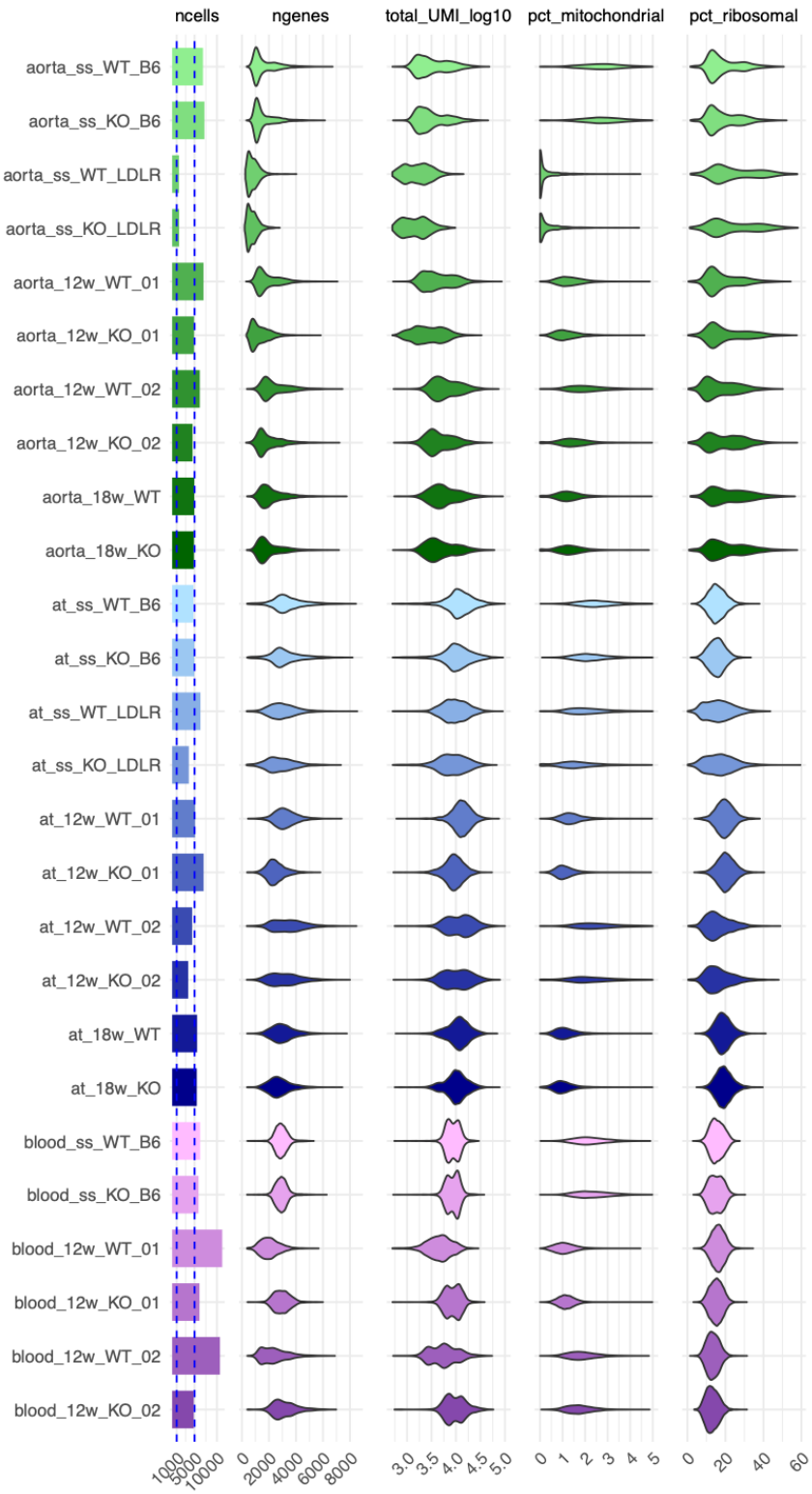


Figure 6.3: ***Overview of cell numbers and quality control metrics of scRNAseq samples.***

6.7.4. Resolving the immune cell landscape of the aorta and epididymal white adipose tissue

To resolve the CD45$^+$ immune cell landscapes of the aorta and adipose tissue, 4000 HVGs were discovered within tissues after excluding the union of the top 50 ambient genes for each analysis (batch_key='sample_id'). For integration with scVI (batch_key='sample_id', covariates [total_UMI, pct_mitochondrial], n_latent=50) the data was subset to HVGs. Clustering analysis was performed as described above on the full gene expression (GEX) space (epi: resolution 0.5, aorta: resolution 0.3). To improve subset delineation, mononuclear phagocytes and T/NK cells were reanalysed separately.

The majority of T cells in the aorta displayed a *Cd4*$^+$*Cd8a*$^+$*Rag1*$^+$ positive thymocyte-like phenotype (T0, T1, T2, T7, T8, T11, T12). *Rag1* is essential for T cell receptor recombination and is selectively expressed during thymic T cell maturation[268,269]. In addition, >50% of cells in *Rag1* positive clusters expressed *Cd4* and *Cd8a*. Even though adventitial CD4$^+$CD8$^+$ double positive T cells have been described before[219], the anatomic proximity of the thymus and aortic arch mark a challenge when dissecting aortas for single-cell analysis. Hence, *Rag1*$^+$ clusters amongst single positive immature and mature T cells, most likely also contain contaminating double positive thymocytes (T0, T1, T2, T12) and double positive cycling blasts (T7, T8, T11). In addition, cluster T3 expressed high levels of *Tox*, *Itm2a*, and *Ccr9* (not shown) which have been described to be upregulated in T cells undergoing selection in the thymus[270–272]. To improve clustering resolution of mature aortic T cells a sub analysis was performed after sub setting cells of interest (Figure 6.4).

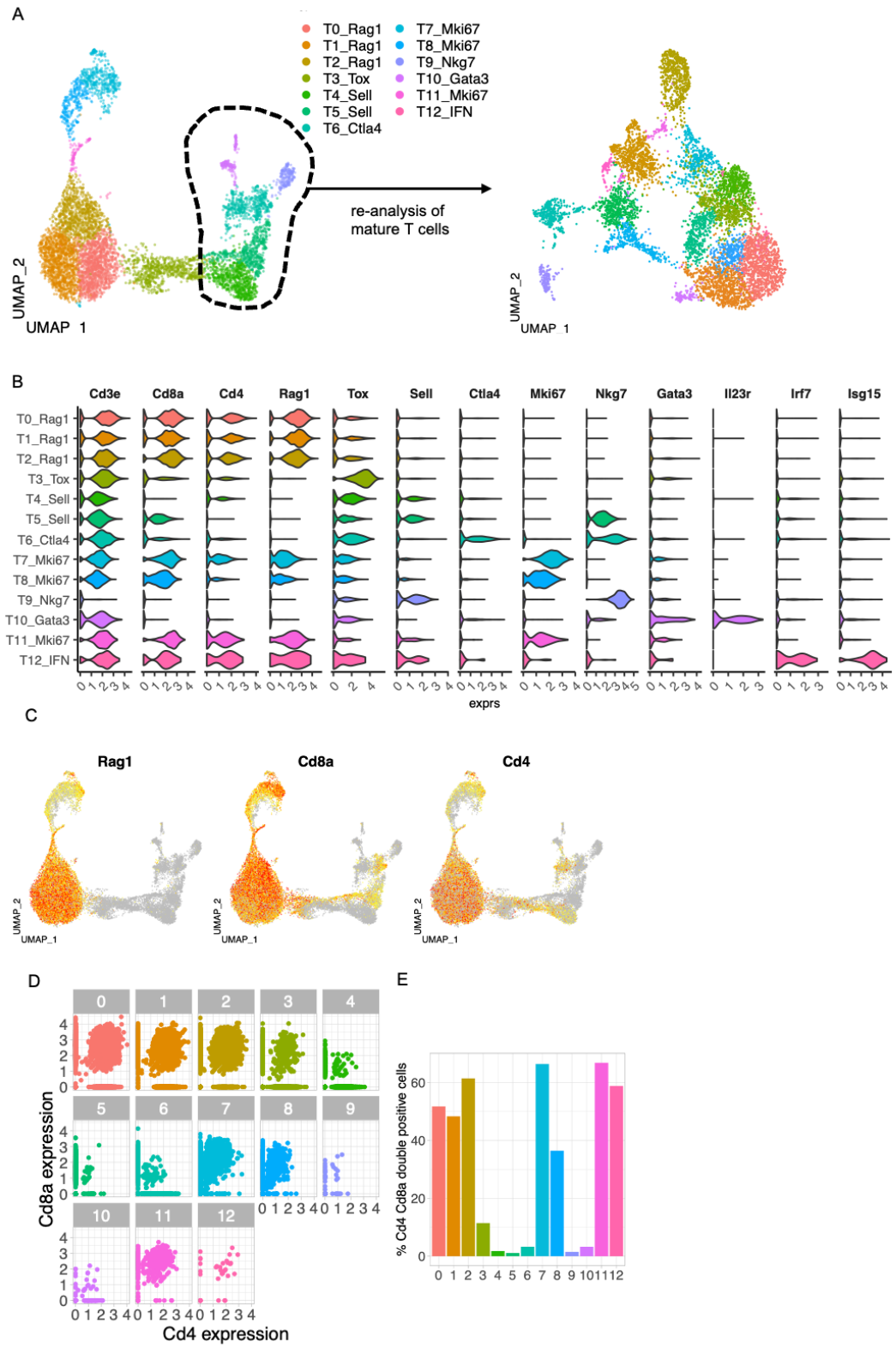


Figure 6.4: ***Subsetting of and reclustering of mature T cells in the aorta.*** *(A.) Subsetting strategy for reclustering of mature T cells. The left UMAP displays all cells identified as T/NK cells in the aorta. Mature T cell clusters (black dotted line) were subset and reanalysed to improve resolution of the mature T cell landscape in the aorta. The right UMAP shows reanalysed T cells. (B.) Violin plots showing selected cluster marker and known T cell marker genes in clusters identified in all T/NK cells in the aorta. (C.) Marker expression of Rag1, Cd8a and Cd4. Thymocyte like Rag1^{+} and Cd8a^{+}Cd4^{+} double positive cell clusters were excluded from downstream analysis. (D.) Scatter plot of Cd4 and Cd8a expression in clusters identified in initial T cell clustering analysis (A. top UMAP). D. Percentage of Cd4^{+}Cd8a^{+} double positive cells within each cluster identified in initial T cell clustering analysis (A. top UMAP).*

To achieve a similar clustering resolution in the *Ccr2*$^{+}$ macrophage compartment of epiWAT and aorta, a high cluster resolution of 2 was chosen for the aorta. Since this resulted in over clustering of the *Ccr2*$^{-}$ macrophage compartment, cell clusters were merged manually (Figure 6.5): cluster similarities were determined using hierarchical clustering of Pearson correlations calculated based on average scVI latent representations (Scanpy dendrogram function).

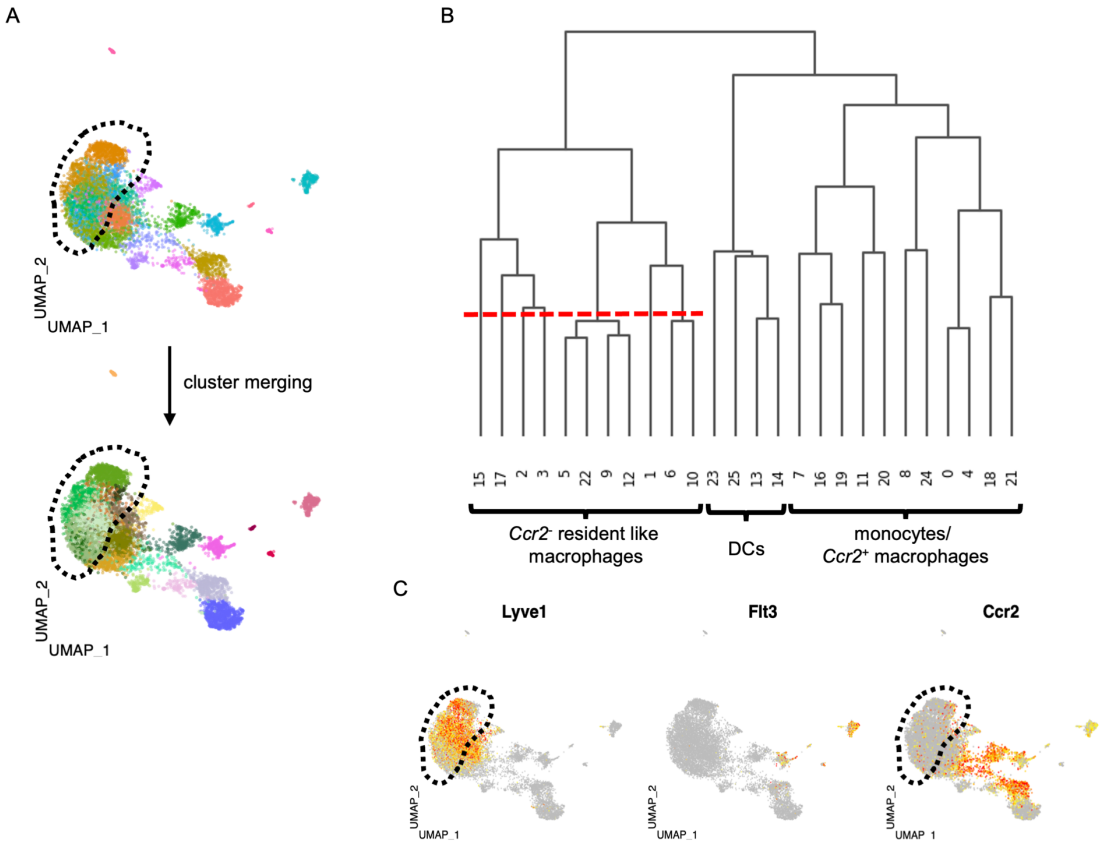


Figure 6.5: ***Merging strategy of aortic mononuclear phagocyte (MNP) clusters.*** *(A.) The top UMAP shows aortic MNPs clustered at resolution 2. The black dotted line highlights over clustered Ccr2*$^{-}$ *resident-like macrophages. The bottom UMAP is coloured by merged clusters. (B.) Dendrogram of hierarchical clustering of clusters identified at resolution 2. Pearson correlations were calculated based on mean scVI latent representations of cells. The dendrogram can be divided into three major parts: Ccr2*$^{-}$ *resident-like macrophages, dendritic cells (DCs), and monocytes/Ccr2*$^{+}$ *macrophages. The red dotted line indicates how clusters were merged. (C.) Marker expression for three populations described in (B). The black dotted line highlights the Ccr2*$^{-}$ *resident-like macrophage compartment.*

Table 6.5: Analysis parameters for sub analysis per tissue.

	aorta				**epiWAT**		
		number HVG	number of cells	cluster resolution	number HVG	number of cells	cluster resolution
MNPs		4000	12672	2	4000	42455	0.8
T/NK cells	T/NK cells	4000	25905	0.9	4000	5688	1.4
	mature T/NK cells	4000	6793	1.4			
CD45 cells		4000	49483	0.3	4000	50927	0.5

6.7.5. Comparison of the MNP landscapes of the aorta and epididymal white adipose tissue with community datasets

9 publicly available scRNAseq datasets from healthy or atherosclerotic mouse aortas and healthy or obese mouse epiWAT (Table S 3) were reanalysed and pre-processed as described above. Datasets were warehoused using cellhub (https://github.com/sansomlab/cellhub/). Sequence reads were aligned using the 10x Genomic cellranger multi pipeline (cellranger version 6.0.0) and the 10x mouse reference genome mm10 (GENCODE vM23/Ensembl98). High quality cells with <7.5% mitochondrial reads and >200 genes were retained for downstream analysis. Cell-hashed samples from Cottam et al. were demultiplexed using the GMM-Demux[273] algorithm. Across all community studies 42921 doublets identified using Scrublet and GMM-Demux, 609 contaminating non-immune cells (endothelial cells, fibroblasts, smooth muscle and platelets) and 768 low quality cells identified through draft analyses were excluded from downstream analyses. For both tissues, MNPs from the community datasets were combined with the datasets presented in this study; 4000 HVGs were discovered (batch_key='sample_id', span=0.8) per tissue after removing the union of the top 50 ambient RNA per sample and each tissue was integrated using scVI (batch_key = 'sample_id', covariates=['total_UMI', 'pct_mitochondrial'], n_latent=50, subset to

HVG). Clustering analysis was performed as described above (aorta: resolution 1.7, epi: resolution 0.8).

6.7.6. Cross-tissue integration of the aorta, epididymal white adipose tissue and blood

For cross tissue integration of MNPs, cells from the aorta, epiWAT and blood were combined for reanalysis. For cross tissue integration of T and NK cells, cells from the aorta and epiWAT were combined for reanalysis. To ensure accurate representation of cell states present at different disease time points (steady state, 12w WD and 18w WD), both genotypes (WT, IRF5$^{-/-}$) and tissues the union of 2000 HVGs per sample was used for downstream analyses (MNPs: 4467 HVGs, T/NK cells: 2133 HVGs). Samples were integrated with scVI (batch_key='sample_id', covariates=[total_UMI, pct_mitochondrial], n_latent=50, subset to HVG) and clustering analysis was performed. The majority of T cells in the aorta displayed a *Cd4*$^{+}$*Cd8a*$^{+}$ double positive thymocyte like phenotype. To improve clustering resolution in the mature aortic T cells a sub analysis was performed after subsetting cells of interest (4137 HVGs, 12495 cells). Cluster markers that were conserved across tissues were identified as the intersection of separate tests for cluster marker identification per tissue (Scanpy rank_genes_groups function, Wilcoxon tests, BH-adjusted P value < 0.05). T cell exhaustion scores were calculated using Scanpy score_genes and *Pdcd1, Tox, Entpd1, Tigit*, and *Lag3*.

6.7.7. Differential gene expression within clusters

Within cluster differential gene expression analysis was performed using edgeR[274]. For each cluster, samples containing at least 10 cells and genes that were expressed in 10% of cells within any of the samples were retained for downstream analysis. Samples were aggregated into per sample pseudobulks. Library sizes were normalised using the calcNormFactors() function. Common, Trended and Tagwise Negative Binomial

dispersions were calculated using estimateDisp(). If the dispersion could not be estimated due to limited sample numbers, common dispersion was set to 0.1. A gene wise negative binomial generalised log-linear model was fitted using glmFit(). Differentially expressed genes (DEGs) were identified using likelihood ratio tests for pairwise contrasts in the linear model (glmLRT, FDR<0.05, logFC>0.5). For differential gene expression between studies (Chapter 2) samples were subset for specific comparisons for each time points and dispersions, fits and DEGs were calculated per comparison. For differential gene expression between tissues (Chapter 3) dispersions, fits and DEGs were calculated together for the aorta, adipose tissue and blood. Gene set enrichment analysis was performed on DEGs using the gsFisher package (https://github.com/sansomlab/gsfisher/).

6.7.8. Composition analysis

6.7.8.1. Cell density plots

For visualisation cell density plots projected on UMAP representations were generated. For each tissue and time point 1000 cells were randomly sampled and cell density scores were calculated using the kde2d function from the MASS package[275].

6.7.8.2. scCODA

Composition analysis was performed using scCODA[165]. Significant compositional changes were identified as credible compositional changes that were observed >70% of cases by running tests with all clusters as reference (FDR=0.3).

6.7.9. Pseudotime analysis

6.7.9.1. scVelo

6.7.9.2. Preprocessing

For pseudotime analysis in scVelo[263] data was subset to monocyte and macrophage clusters. A sub analysis was performed for selected studies. If a study contained more

than one sample of interest, samples were integrated using scVI (batch_key=sample_id, covariates=[pct_mitochondrial,UMI], nlatent=50) after rediscovering 3000 HVGs (batch_key=sample_id). An approximate neighbour graph was computed on the scVI integrated latent space or the top 50 principal components with scVelo (n = 20 neighbours, method='hnsw', Euclidean distance metric) and the neighbour graph was used to compute UMAPs and for Leiden clustering (Cottam et al: resolution 0.8, Williams et al: resolution 1, Kim et al: resolution 0.8, Park et al: resolution 1.1). Clusters were annotated using cluster labels from the integrated analysis. If a study contained more than one disease time point of interest, 3000 HVGs were rediscovered (batch_key=sample_id) for each disease time point, and a separate neighbour graph and UMAP representation were calculated.

6.7.9.3. Velocity computation

Velocities were calculated using the standard scVelo workflow using the generalised dynamical model to solve full transcriptional dynamics. Raw spliced and unspliced counts were calculated using velocyto[276]. Counts were filtered (min_counts=30, min_counts_u=20), normalised and log1p transformed. First order moments were calculated, and velocities were calculated using the recover_dynamics function followed by the velocity function.

6.7.10. cellrank

To confirm velocities calculated using scVelo the cellrank[277] package combining a connectivity kernel and a velocity kernel (0.5+0.5) were used. Random walks from all identified clusters were visualised.

6.7.11. Slingshot

To investigate the role of IRF5 in monocyte maturation in metabolic disease, the dataset was subset to monocytes and *Ccr2*$^{+}$*Il1b*$^{+}$ mono/macrophages at 12w WD. For each tissue

3000 HVGs, neighbours, UMAP representation and clusters were recomputed as described above (epiWAT: resolution 0.5, aorta: resolution 0.4, epiWAT+aorta+blood: resolution 0.5). 50 diffusion components were calculated using the scanpy diffmap function and the slingshot[278] package was used to fit a minimum spanning tree to the full diffusion map. *Ly6c2*$^{+}$ monocytes were defined as a root clusters for lineage identification using getLineages() function and the getCurves() function was used to smooth lineage curves and calculate pseudo-time values along lineages for each cell.

6.8. Mass cytometry

6.8.1. Sample preparation

Metal-conjugated antibodies were either purchased from Fluidigm, or conjugated in house using the Maxpar X8 Metal Labelling Kit (Fluidigm) according to the manufacturer's instructions. All antibodies were titrated to determine the optimal staining concentration. Single cells from murine tissues were first stained with a Cisplatin DNA intercalator (Fluidigm) to distinguish live and dead cells followed by barcoding using the palladium-based 20-Plex Pd Barcoding Kit (Fluidigm) according to the manufacturer's instructions. Barcoded cells were then combined into a single tube for staining. Non-specific antibody binding was blocked with anti-rat CD16/32 (BD Biosciences) followed by staining with metal-conjugated antibodies for 30min at 4°C. The cells were then washed and permeabilised using the Foxp3/Transcription Factor Staining Buffer Set (Biolegend) according to manufacturer's protocol prior to staining with antibodies against intracellular markers for 30 min at 4°C. Cells were then fixed with 4% PFA for 10 min at room temperature. Finally, the stained cells were incubated with an Iridium DNA intercalator (Fluidigm) in Maxpar fix and perm buffer (Fluidigm) for 8-12 hours at 4°C. Prior to acquisition, cells were washed twice with cell staining buffer (Fluidigm) followed by two washes with water (Fluidigm) and filtered through 40µm cell strainer. EQ Four

Element Calibration Beads (Fluidigm) were added to the samples before introducing into a Helios mass cytometer (Fluidigm).

Table 6.6: List of CyTOF antibodies.

Metal	Antigen	Clone	Supplier	Used for MNP clustering
112	SiglecH	551	Biolegend	
113	CD163	ED2	BioRad	X
114	CD43	S11	Biolegend	X
116	CD63	NVG-2	Biolegend	X
141	Ly-6G/C	RB6-8C5	Fluidigm	
142	CD11c	N418	Fluidigm	X
143	Tim4	F31-5G3	Biolegend	X
144	XCR1	ZET	Biolegend	
145	NK1.1	PK136	Fluidigm	
146	CX3CR1	SA011F11	Biolegend	
147	CD45.2	104	Fluidigm	
148	Cd11b	M1/70	Fluidigm	
149	CD19	6D5	Fluidigm	
150	CD24	M1/69	Fluidigm	X
151	CD64	X54-5/7.1	Fluidigm	X
152	CD3	145-2C11	Fluidigm	
153	CD45.1	A20	Fluidigm	
154	CD103	2E7	Biolegend	X
155	Lyve1	ALY7	eBiosciences	X
156	CD14	Sa14-2	Fluidigm	X
158	CD206	C068C2	Biolegend	X
159	F4-80	BM8	Fluidigm	
160	CD26	DPP-4	Biolegend	X
161	TREM2	6E9	Biolegend	X
162	Ly-6C	HK1.4	Fluidigm	X
163	CCR2	SA203G11	Biolegend	X
164	CD172a	Sirpa	Biolegend	X
165	PLIN2	EPR3713	Abcam	X
166	CD209b	22D1	eBiosciences	X
167	SIGLECF	551	Biolegend	
168	CD8	53-6.7	Fluidigm	
169	GFP	5F12.4	Fluidigm	
170	CD90.2	20-H12	Biolegend	
171	CD226	'10e5	Biolegend	X
172	CD4	RM4-5	Fluidigm	
173	CD9	MZ3	Biolegend	X
174	KI67	11F6	Biolegend	X
175	CD68	FA-11	Biolegend	X
176	B220	RA3-6B2	Fluidigm	
194	CD44	IM7	Fluidigm	
198	CD49b	P1E6-C5	Fluidigm	
209	MHC IA/IE	M5/114.15.2	Fluidigm	X

6.8.2. Data Analysis

The analysis was performed in using the CATALYST package[279]. Raw fcs files obtained from barcoded samples were normalised using the normCytof() function and expression values were arcsinh-transformed (cofactor=5) using the prepData() function. Samples were debarcoded using the estCutoffs() and applyCutoffs() functions for (i) estimation of the cutoff parameter between positive and negative barcode population per sample and (ii) the separation of the samples based on estimated cut-offs and Mahalanobis distances. Events were gated on gaussian distributions followed by gating on $CD45^+$ live cells. Gated cells were clustered using all antibodies except from CD45.1 and CD45.2 based on the FlowSOM[280] and ConsensusclusterPlus[281] algorithms using the cluster() function. For $CD45^+$ analysis 25 metaclusters were then assigned to major cell types (T cells, B cells, mononuclear phagocytes and neutrophils). MNPs were selected and reclustered based on MNP cluster marker expression (Table 6.6). 30 MNP metaclusters were manually annotated and merged based on median marker expression. Cluster composition was analysed using scCODA as described for scRNAseq analysis.

1.1. Statistical analysis

Data were analysed using Prism V.9.5.0 (GraphPad). Statistical tests were performed as indicated in figure legends. Two-sided testing was used in unless indicated otherwise.

Appendix A Supplemental data

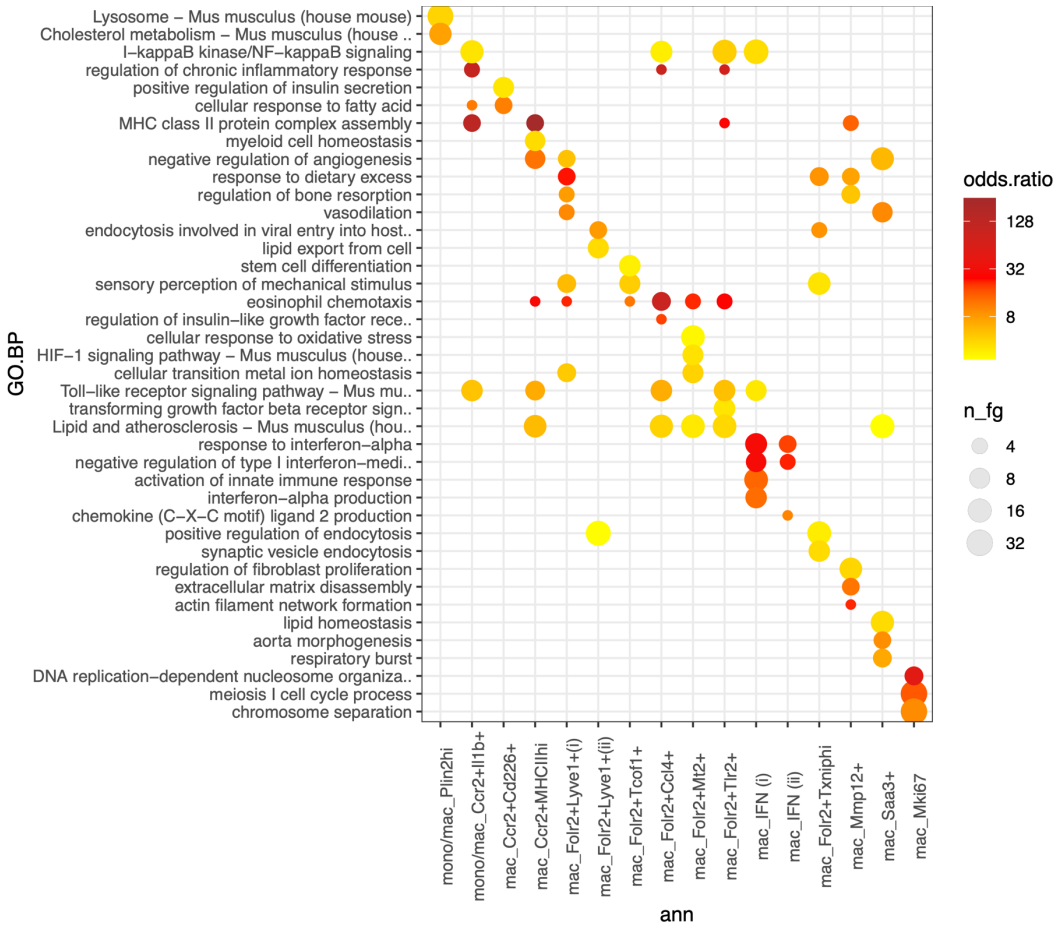


Figure S 1: ***Overrepresented gene sets in macrophage subsets identified in the aorta of mixed bone marrow chimeras (MBMCs).*** *The dot plot shows selected GO biological process categories that showed a significant overrepresentation in cluster marker genes that were identified for macrophage clusters in the aorta of mixed bone marrow chimera (Fisher test, BH adjusted p-value < 0.001). The colour of plots represents the odds ratio and the dot size represents number of differentially expressed genes that are part of this pathway category.*

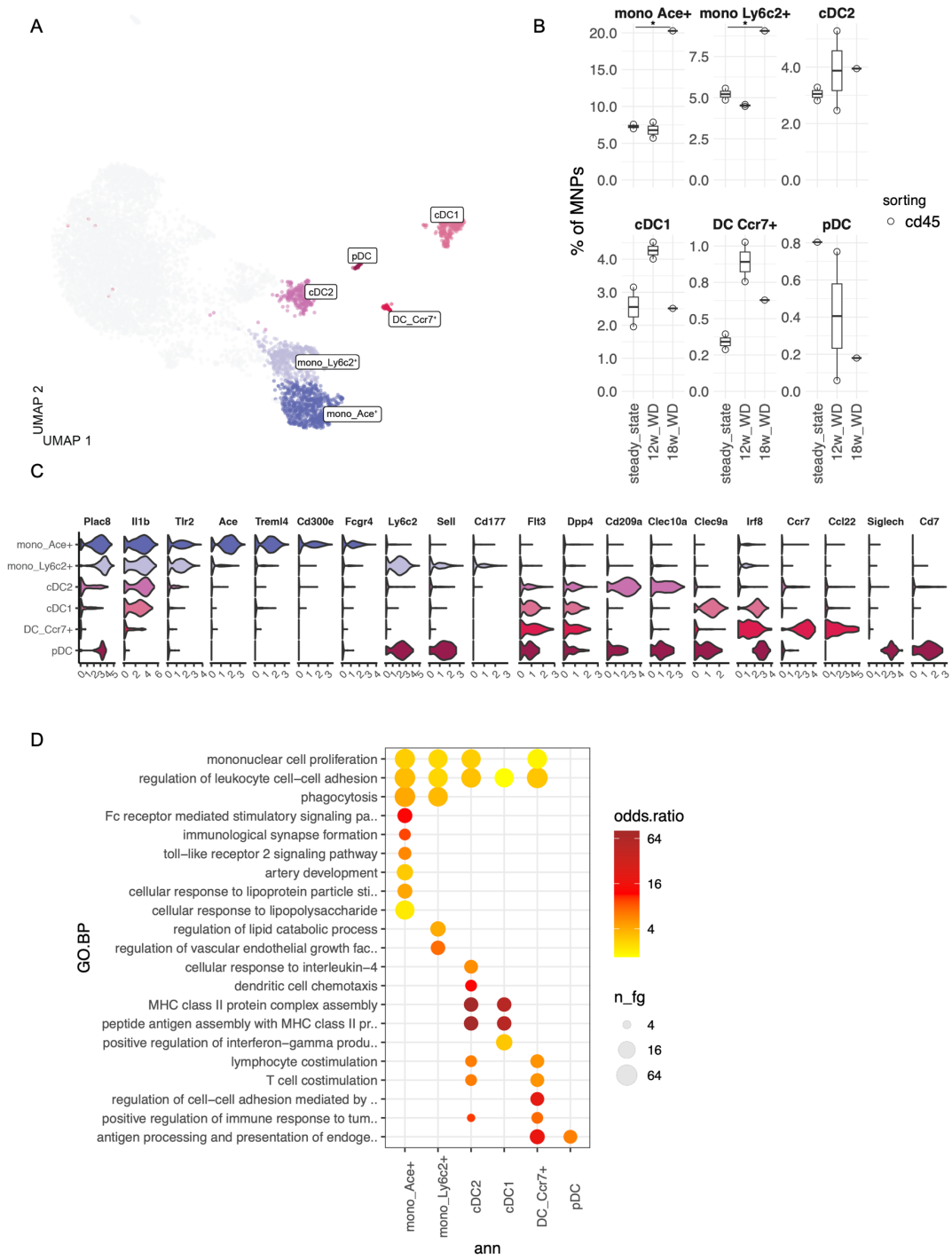


Figure S 2: ***The single-cell landscape of monocytes and dendritic cells in the aorta of mixed bone marrow chimeras (MBMCs).*** *12672 mononuclear phagocytes (MNPs) from CD45^{+} sorted WT and IRF5$^{-/-}$ samples from MBMC aortas at steady state (n=2 per genotype), 12w WD (n=2 per genotype), 18w WD (n=1 per genotype) were analysed. A. Leiden clustering of the MNPs in the aorta identified 2 monocyte and 4 dendritic cell clusters. B. The box plots show percentages of WT cells that were found in identified clusters. Composition at 12w WD and 18w WD were compared to steady state using scCODA. C. The violin plots show the expression levels of selected cluster marker genes (BH-adjusted $P < 0.05$, two-sided Wilcoxon tests) in each of the identified clusters.*

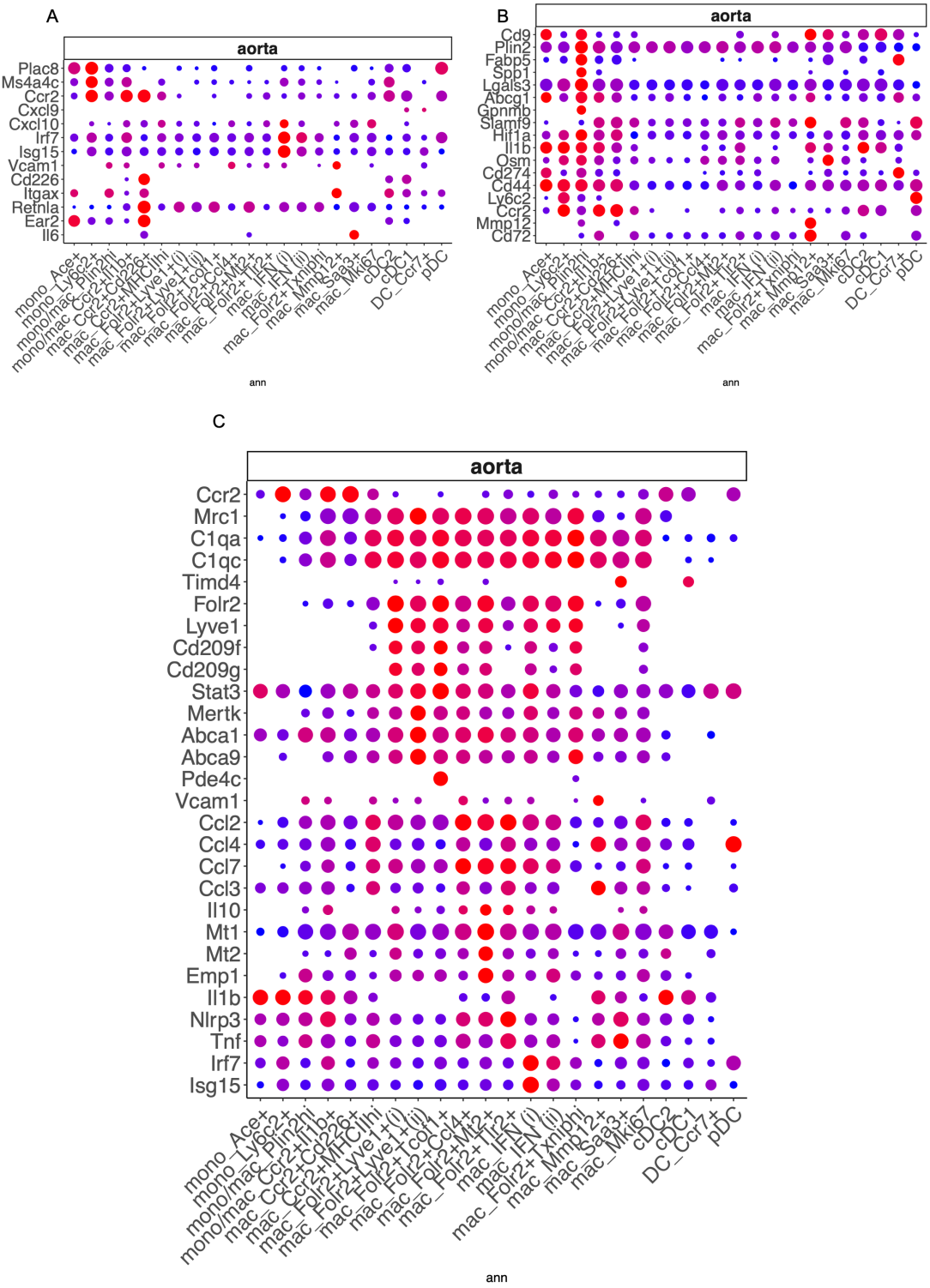


Figure S 3: ***Additional aortic mononuclear phagocyte marker genes****. The dot plots show the expression of selected cluster marker genes (BH-adjusted P < 0.05, two-sided Wilcoxon tests) and known mononuclear phagocyte marker genes for monocytes/macrophages (A.), lipid associated macrophages (B.) and resident macrophages (C.) identified in the analysis of scRNAseq data from aortas of mixed bone marrow chimeras (Figure 2.5). The colour of the dots represents the scaled average expression and its size reflects the percentage of cells within a cluster expressing the gene. Dots were only plotted for genes that were expressed in > 10% of the cluster.*

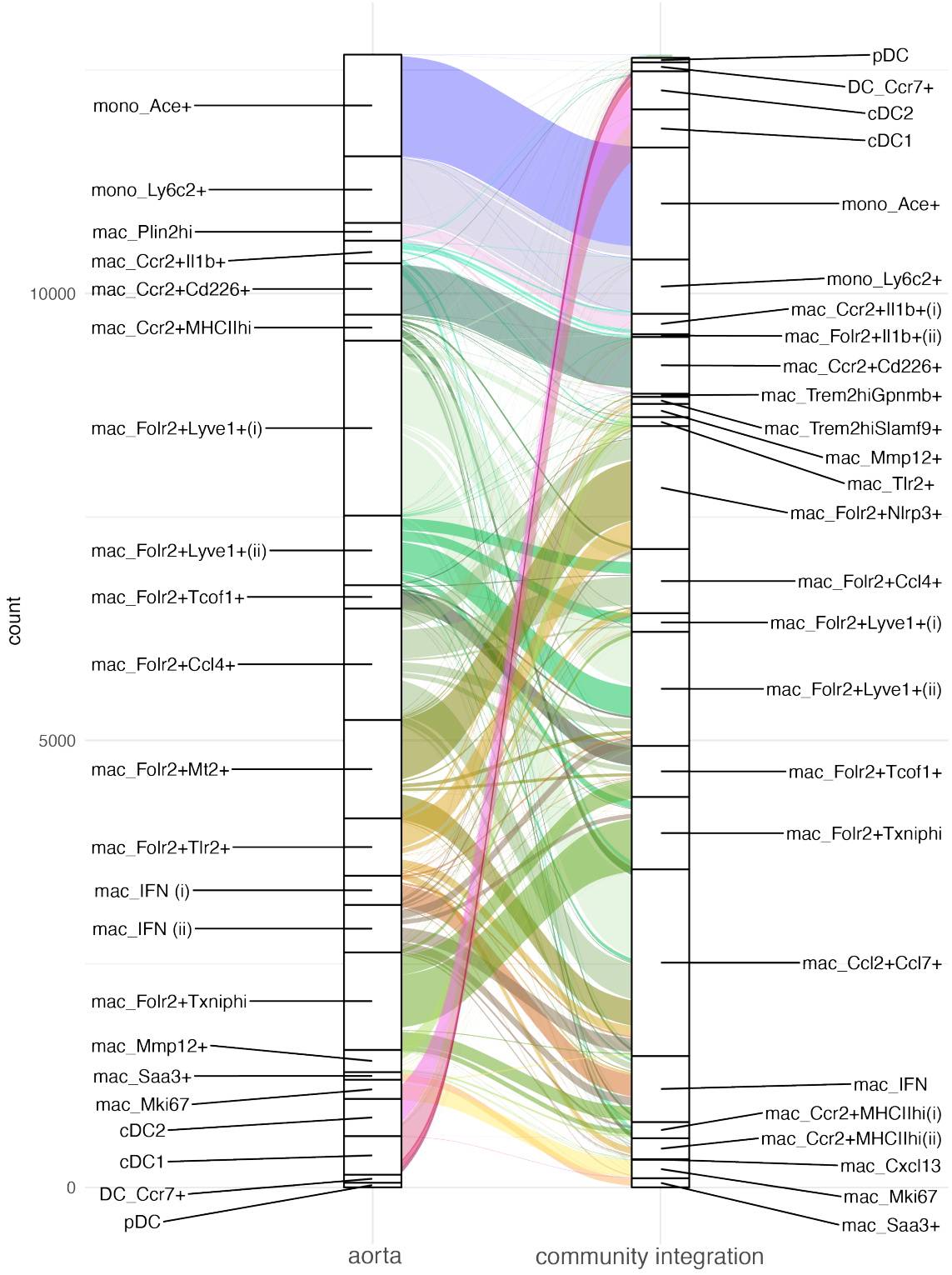


Figure S 4: ***Comparison of aortic myeloid clusters identified in analysis of mixed bone marrow chimeras (MBMCS) and integrated analysis with community aortic datasets.*** *The alluvial plot compares clusters identified in the analysis of MBMCs (left) with clusters identified in the integrated analysis of MBMCs combined with 6 publicly available datasets (community integration) (right). Alluvia are coloured by clusters identified in the community integration (Figure 7). Monocytes and dendritic cells show almost complete overlap between clusters in both analyses. Macrophages show also show high overlap in most clusters across analyses.*

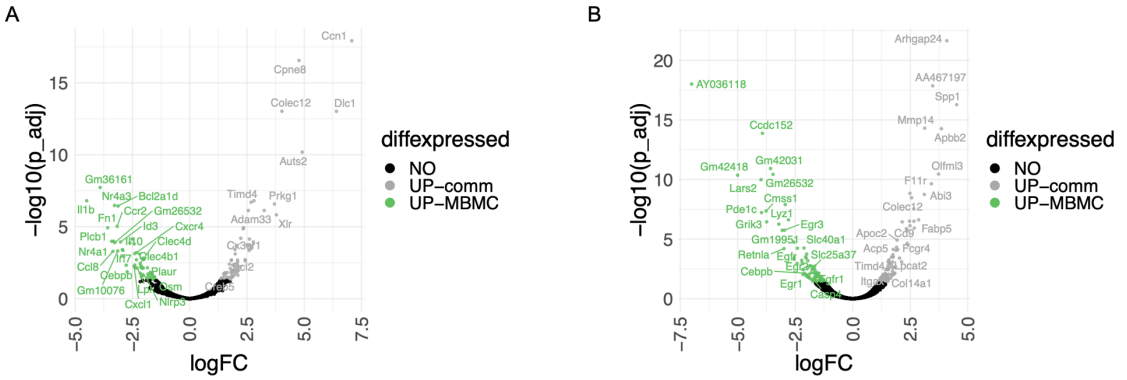


Figure S 5: ***Differential gene expression analysis between aortic macrophages clusters from mixed bone marrow chimeras (MBMCS) and community datasets.*** *Differentially expressed genes between macrophages from MBMCs and community datasets were identified using edgeR on pseudo bulk data (LRT test, FDR<0.05, absolute logFC >0.5). A-B. The Volcano plots show differentially expressed genes between macrophages from MBMCs and Williams et al at steady state (A). and differentially expressed genes between macrophages from MBMCs and Kim et al at 12 weeks diet (B). Differentially upregulated genes in community datasets are coloured in grey and differentially upregulated genes in MBMC macrophages are coloured in green. C-D.*

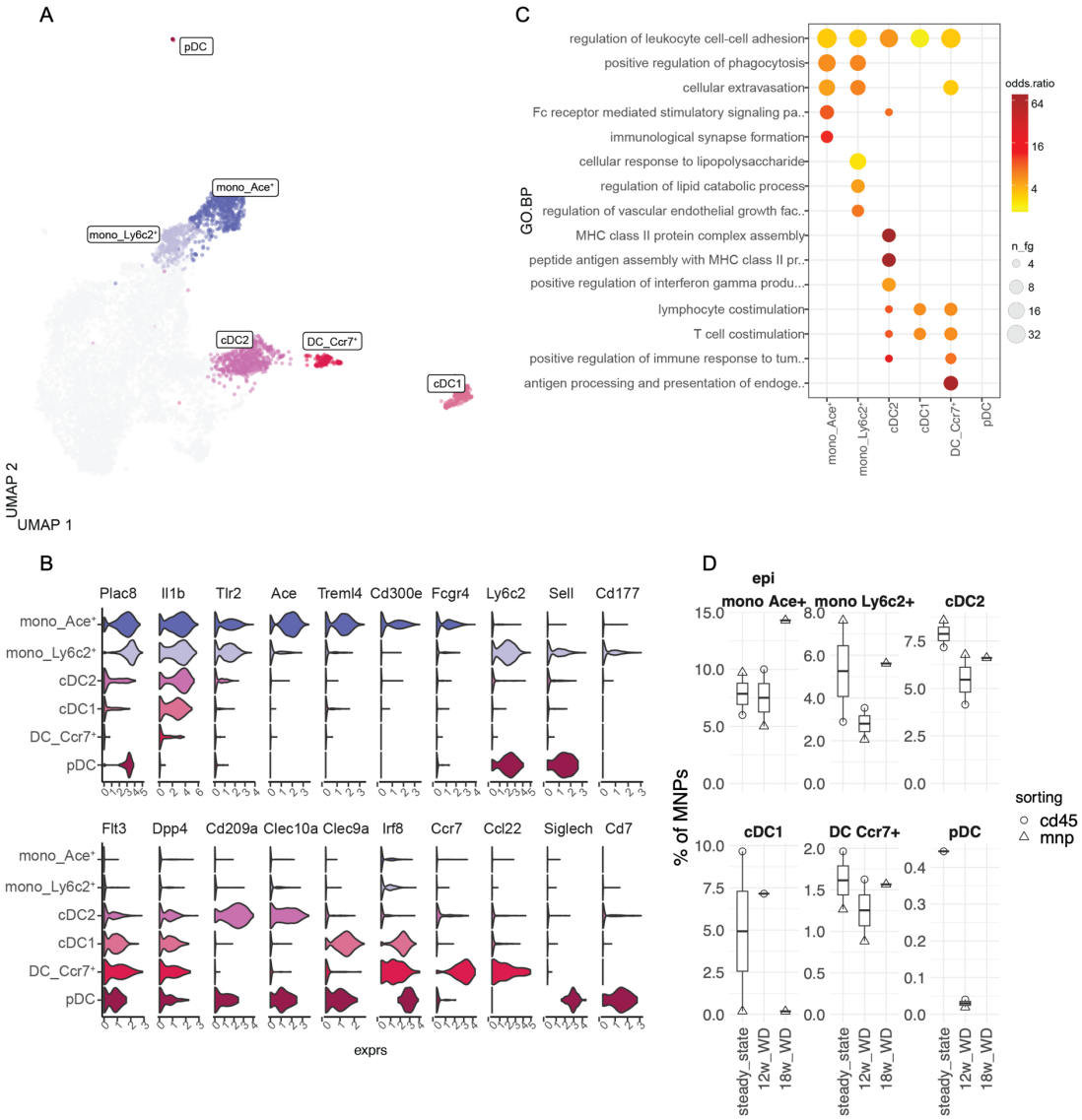


Figure S 6: ***The single-cell landscape of monocytes and dendritic cells in the epiWAT of mixed bone marrow chimeras (MBMCs).*** *42455 mononuclear phagocytes (MNPs) from CD45^{+} and Lin-CD11b^{+}CX3CR1^{+} sorted WT and IRF5$^{-/-}$ samples from epiWAT of MBMCs at steady state (n=1 per genotype and sorting strategy), 12w WD (n=1 per genotype and sorting strategy), 18w WD (n=1 per genotype sorted for Lin-CD11b^{+}CX3CR1^{+}) were analysed. A. Leiden clustering of the MNPs in the aorta identified 2 monocyte and 4 dendritic cell clusters. B. The dot plot shows selected GO biological process and KEGG categories that showed a significant overrepresentation in differentially expressed genes cluster marker genes (Fisher test, BH adjusted p-value < 0.001). The colour of plots represents the odds ratio and the dot size represents number of differentially expressed marker genes that are part of this pathway category. C. The violin plots show the expression levels of selected cluster marker genes (BH-adjusted P < 0.05, two-sided Wilcoxon tests) in each of the identified clusters. D. The box plots show percentages of WT cells that were found in identified clusters. Composition at 12w WD and 18w WD were compared to steady state using scCODA.*

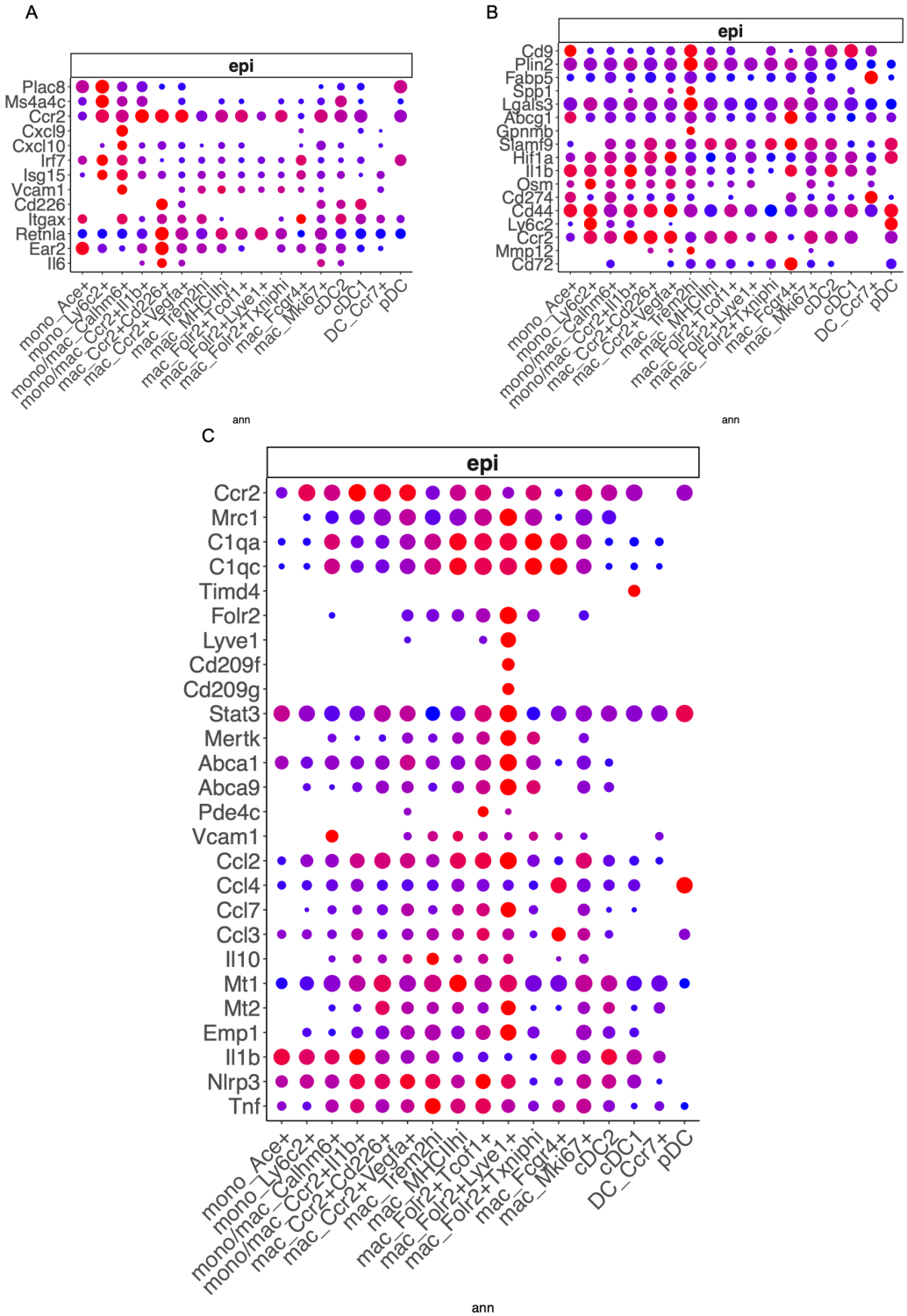


Figure S 7: ***Additional epiWAT mononuclear phagocyte marker genes****. The dot plots show the expression of selected cluster marker genes (BH-adjusted P < 0.05, two-sided Wilcoxon tests) and known marker genes for monocytes/macrophages (A.), lipid associated macrophages (B.) and resident macrophages (C.) identified in the analysis of scRNAseq data from epiWAT of mixed bone marrow chimeras (Figure 2.13). The colour of the dots represents the scaled average expression and their size reflects the percentage of cells within a cluster expressing the gene. Dots were only plotted for genes that were expressed in > 10% of the cluster.*

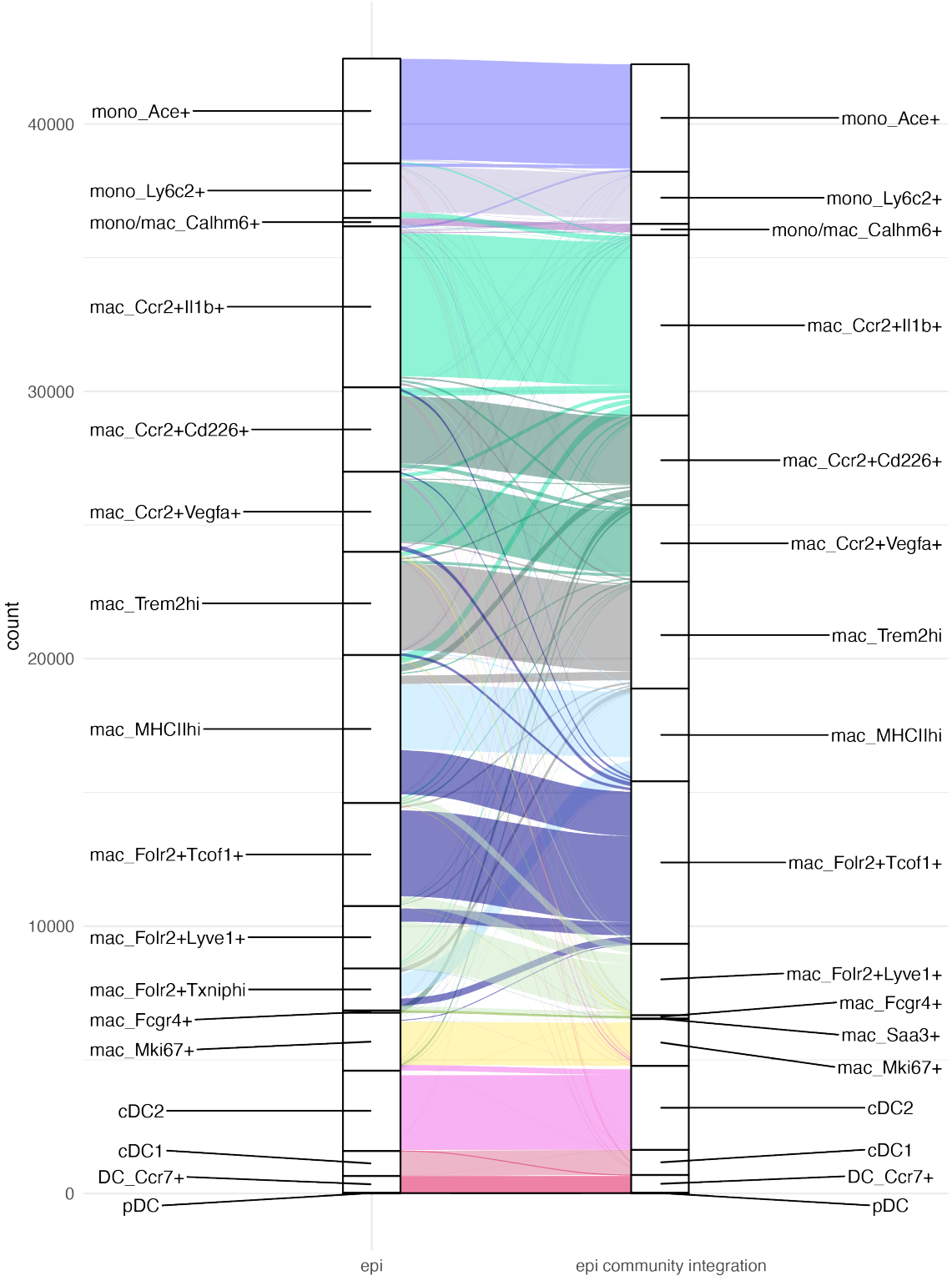


Figure S 8: ***Comparison of epiWAT myeloid clusters identified in analysis of mixed bone marrow chimeras (MBMCs) and integrated analysis with community epiWAT datasets.*** *The alluvial plot compares clusters identified in the analysis of MBMCs (left) with clusters identified in the integrated analysis of MBMCs combined with 6 publicly available datasets (community integration) (right). Alluvia are coloured by clusters identified in the community integration (Figure 7). Monocytes and dendritic cells show almost complete overlap between clusters in both analyses. Macrophages show also show high overlap in most clusters across analyses.*

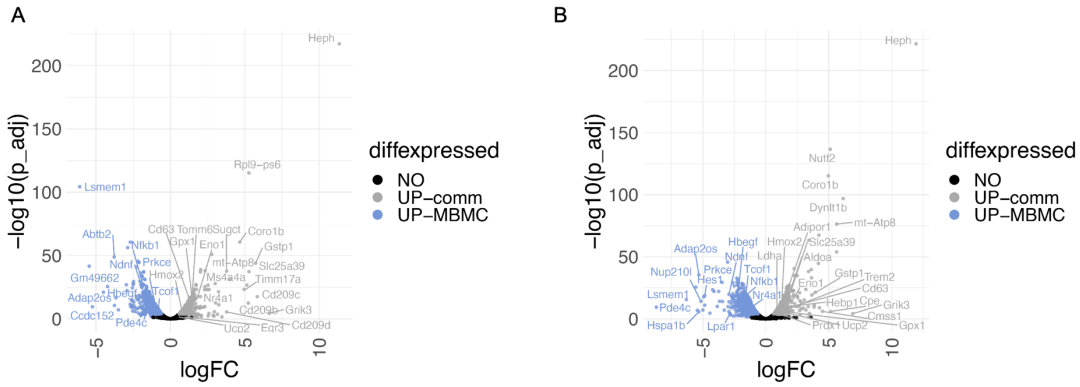


Figure S 9: ***Differential gene expression analysis between epiWAT macrophages clusters from MBMCS and community datasets.*** *Differentially expressed genes between macrophages from MBMCs and community datasets were identified using edgeR on pseudo bulk data (LRT test, FDR<0.05, absolute logFC >0.5). A-B. The Volcano plots show differentially expressed genes between macrophages from MBMC and Cottam et al at steady state (A) and in disease (>12 weeks diet) (B). Differentially upregulated genes in community datasets are coloured in grey and differentially upregulated genes in MBMC macrophages are coloured in blue.*

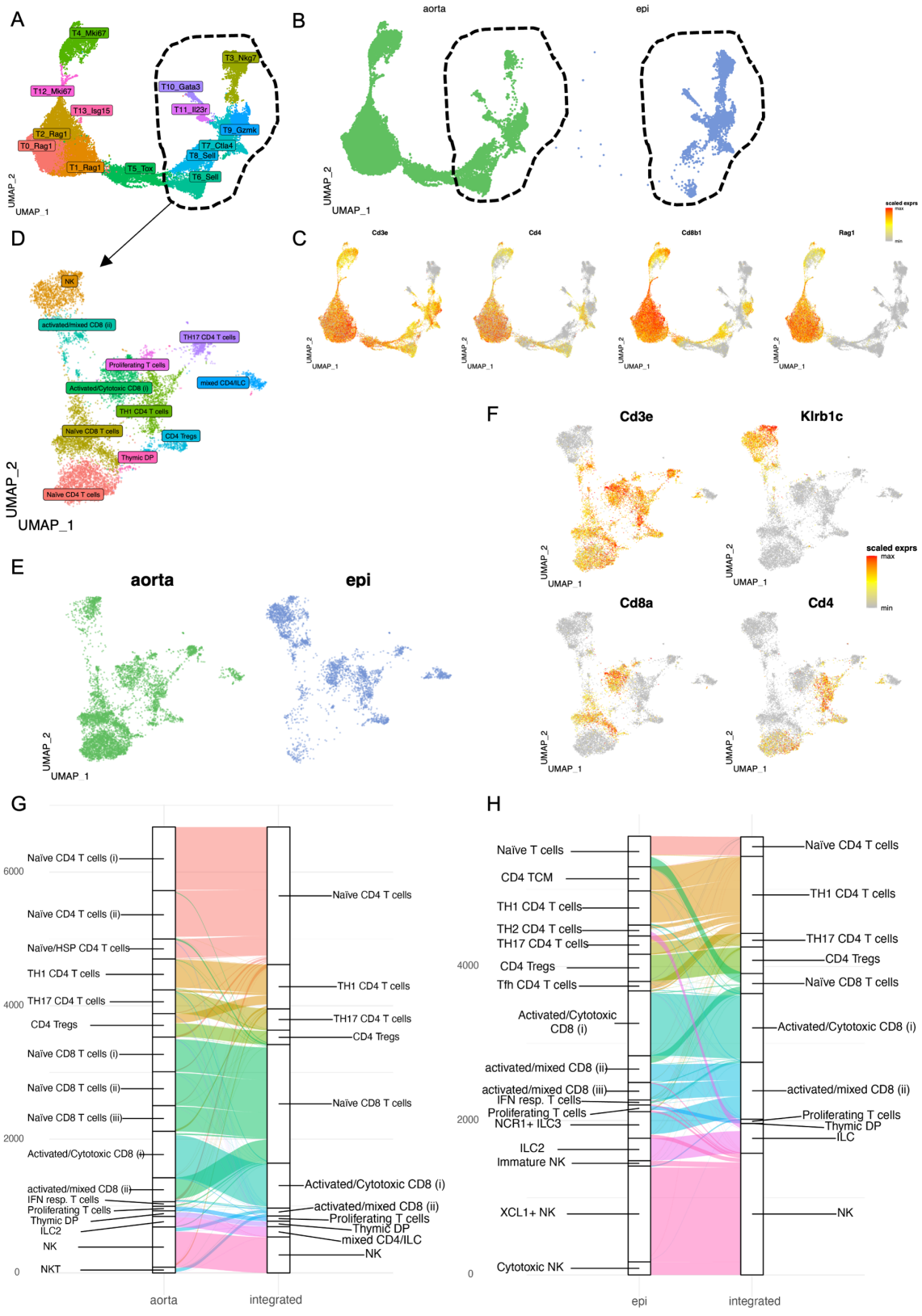


Figure S 10: ***Analysis strategy of combined T cell atlas of the aorta and epiWAT during metabolic disease progression.*** *scRNAseq was performed on CD45^{+} sorted WT and IRF5$^{-/-}$ samples from mixed bone marrow chimera (MBMC) aortas and epiWAT at steady state, 12w WD and 18w WD. A. Analysis of 31593 T and NK cells from the aorta and epiWAT revealed 14 T and NK cell clusters. The black dotted line indicates mature clusters that contained cells from aortic and epiWAT samples and were then reanalysed to improve resolution in the mature T cell compartment (D). B. UMAP representation of the analysis presented in (A.) faceted and coloured by tissue. C. Expression of selected T and NK cell markers used for cell type annotation in (A).* ***(continued page 162)***

(continued) *Figure S 10:* ***Analysis strategy of combined T cell atlas of the aorta and epiWAT during metabolic disease progression.*** *D. UMAP representation of the reanalysed mature T cell compartment. E. UMAP representation of the analysis presented in (D.) faceted and coloured by tissue. F. Expression of selected T and NK cell markers used for cell type annotation in (D). G. Alluvial plot comparing clusters identified in the analysis of the aorta (left) with clusters identified in the integrated analysis of the aorta and epiWAT (right). H. Alluvial plot comparing clusters identified in the analysis of the epiWAT (left) with clusters identified in the integrated analysis of the aorta and epiWAT (right). Alluvia flows are coloured by clusters identified in the integrated analysis (D.).*

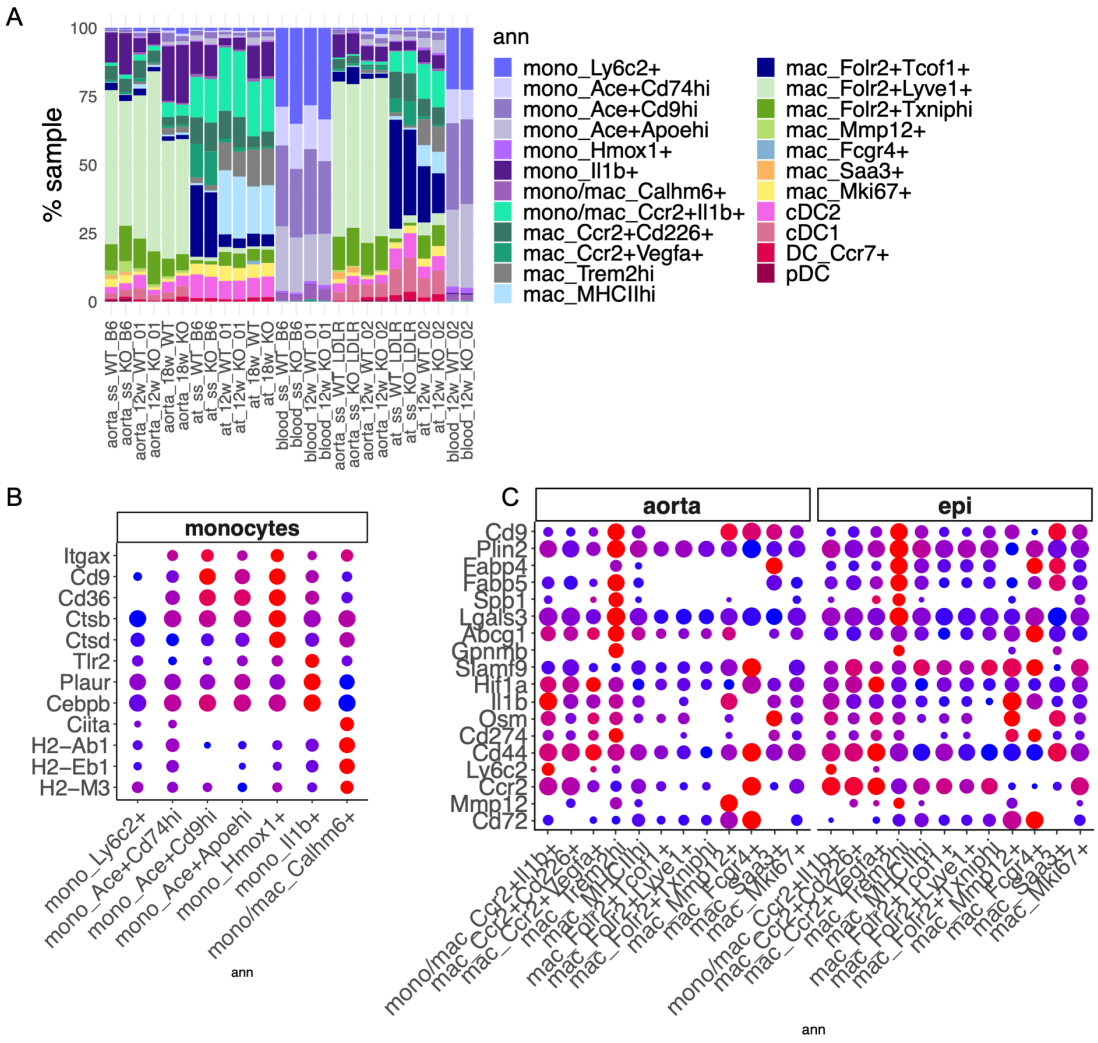


Figure S 11: ***Cluster composition per sample of mononuclear phagocyte clusters identified in combined analysis of blood, aorta and epiWAT and additional cluster marker genes for monocytes and macrophages.*** *A. scRNAseq was performed on CD45$^+$ sorted, Lin$^-$CD11b$^+$ sorted and Lin$^-$CD11b$^+$CX3CR-GFP$^+$ sorted WT and IRF5$^{-/-}$ samples from MBMC aortas, epiWAT and blood at steady state, 12w WD and 18w WD. Leiden clustering of 100024 MNPs identified 7 monocyte clusters, 4 dendritic cell clusters and 12 macrophage clusters. The bar plots show the cluster composition within each sample. B./C. The dot plots show the expression of selected cluster marker genes (BH-adjusted P < 0.05, two-sided Wilcoxon tests) and known marker genes for monocytes(B.), lipid associated macrophages (C.) The colour of the dots represents the scaled average expression and its size reflects the percentage of cells within a cluster expressing the gene. Dots were only plotted for genes that were expressed in > 10% of the cluster.*

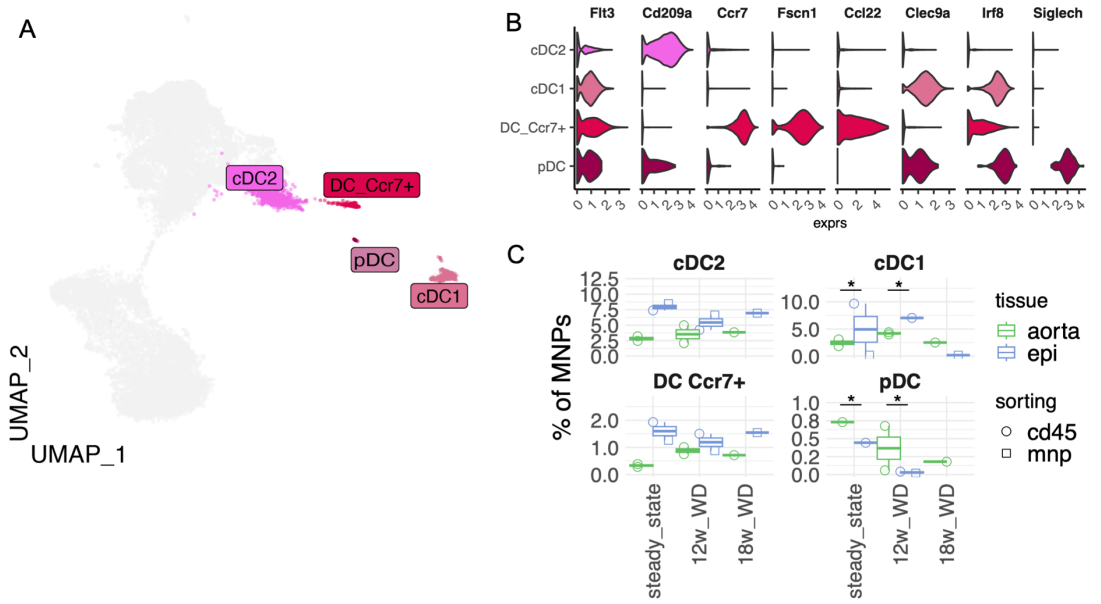


Figure S 12: ***The combined single-cell landscape of dendritic cells of the aorta and epiWAT using scRNAseq.*** *100024 mononuclear phagocytes (MNPs) from CD45+ sorted, Lin-CD11b+ sorted and Lin-CD11b+CX3CR1+ sorted WT and IRF5 -/- samples from MBMC aortas, epiWAT and blood at steady state, 12w WD and 18w WD were analysed. A. Leiden clustering of the MNPs in the aorta identified 4 dendritic cell clusters. B. The violin plots show the expression levels of selected cluster marker genes (BH-adjusted $P < 0.05$, two-sided Wilcoxon tests) in each of the identified clusters. C. The box plots show percentages of WT cells that were found in identified clusters. Composition in the epiWAT was compared to composition in the aorta at steady state and 12w WD using scCODA. D. The dot plot shows selected GO biological process categories that showed a significant overrepresentation in cluster marker genes (Fisher test, BH adjusted p-value < 0.001). The colour of plots represents the odds ratio and the dot size represents number of differentially expressed genes that are part of this pathway category.*

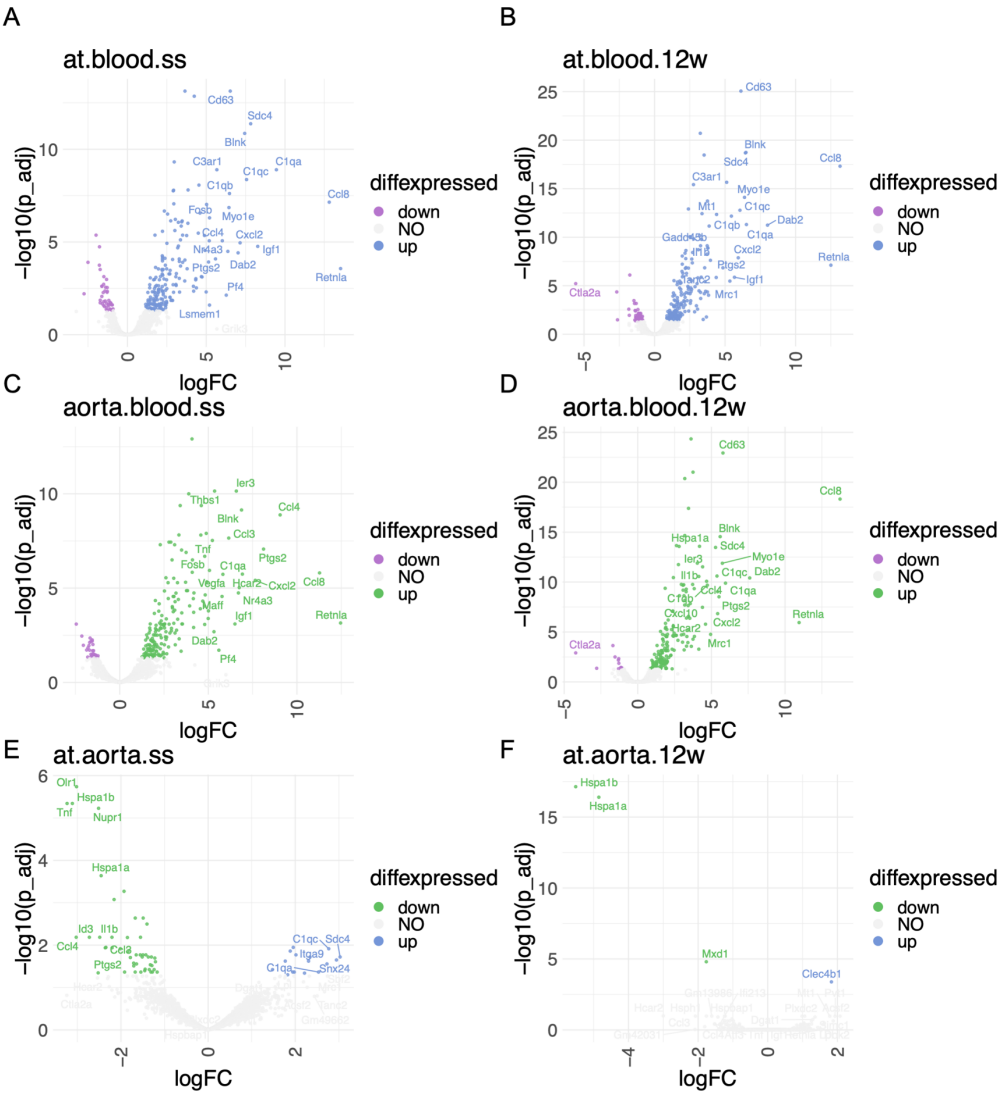


Figure S 13: ***Differential gene expression between monocytes of the aorta, epiWAT and blood at steady state and 12 w WD.***

The volcano plots show differentially expressed genes (BH adjusted p-value < 0.05, edgeR LRT test) between the epiWAT and blood (A.-B.), aorta and blood (C.-D), and epiWAT and aorta ((E.-F.) at steady state (A.,C.,E.) and 12w WD (B.,D.,F.). Differentially expressed genes are coloured by whether they are upregulated in upregulated in the aorta (green), upregulated in the epiWAT (blue), or upregulated in the blood (violet).

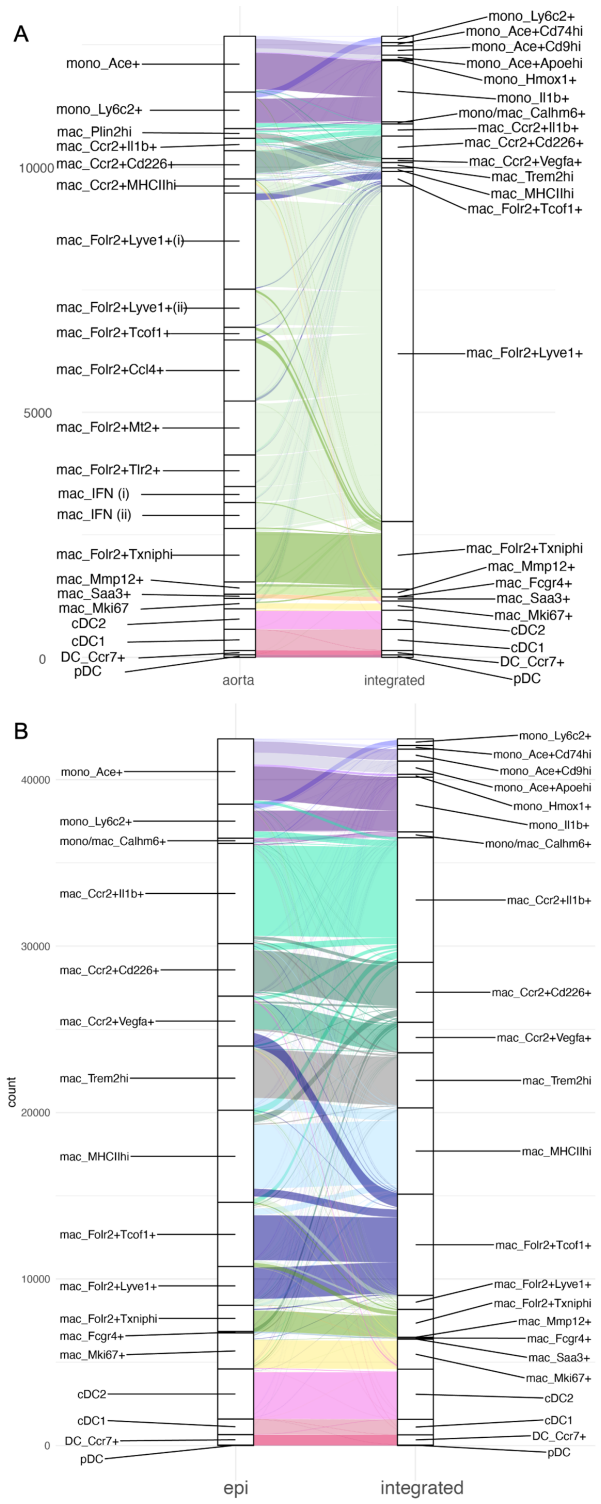


*Figure S 14**: Comparison of macrophage clusters identified in separate analysis of the aorta and epiWAT to integrated analysis of aorta, epiWAT and blood.** 100024 mononuclear phagocytes (MNPs) from CD45+ sorted, Lin-CD11b+ sorted and Lin-CD11b+CX3CR1+ sorted WT and IRF5 -/- samples from MBMC aortas, epiWAT and blood at steady state, 12w WD and 18w WD were analysed. A. Alluvial plot comparing clusters identified in the analysis of the aorta (left) with clusters identified in the integrated analysis of the aorta, epiWAT and blood (right). B. Alluvial plot comparing clusters identified in the analysis of the epiWAT (left) with clusters identified in the integrated analysis of the aorta, epiWAT and blood(right). Alluvia flows are coloured by clusters identified in the integrated analysis (Figure 3.3).*

upregulated	geneset_id	description	odds.ratio	p.adj	pathway.group
epiWAT	GO:0034143	regulation of toll-like receptor 4 signaling pathway	13.33	0.02	GO.BP
epiWAT	GO:0016577	histone demethylation	11.50	0.01	GO.BP
epiWAT	GO:0034142	toll-like receptor 4 signaling pathway	9.24	0.01	GO.BP
epiWAT	GO:0042060	wound healing	3.93	0.01	GO.BP
epiWAT	GO:0002262	myeloid cell homeostasis	3.21	0.04	GO.BP
epiWAT	GO:0010720	positive regulation of cell development	3.20	0.01	GO.BP
epiWAT	GO:0048872	homeostasis of number of cells	2.64	0.03	GO.BP
aorta	GO:0035456	response to interferon-beta	8.45	0.00	GO.BP
aorta	GO:0071357	cellular response to type I interferon	5.11	0.00	GO.BP
aorta	GO:0035455	response to interferon-alpha	6.85	0.00	GO.BP
aorta	GO:0005125	cytokine activity	6.44	0.00	GO.MF
aorta	GO:0005126	cytokine receptor binding	2.80	0.00	GO.MF

Table S 1: Gene set overrepresentation analysis of differentially expressed genes between Folr2^{+} macrophages of the aorta and epiWAT at steady state. The table shows selected GO (gene ontology) biological process and GO molecular function categories that showed a significant overrepresentation in differentially expressed genes (Fisher test, BH adjusted p-value < 0.05).

upregulated	geneset_id	description	odds.ratio	p.adj	pathway.group
epiWAT	path:mmu03320	PPAR signaling pathway - Mus musculus (house mouse)	28.9730715	0.00067646	KEGG
epiWAT	GO:0019915	lipid storage	12.765525	0.00522632	GO.BP
epiWAT	GO:0042060	wound healing	6.61099126	0.00550615	GO.BP
epiWAT	GO:0050727	regulation of inflammatory response	5.64428265	0.00771566	GO.BP
epiWAT	GO:0051235	maintenance of location	5.2880014	0.00887273	GO.BP
epiWAT	GO:0106106	cold-induced thermogenesis	7.73247108	0.01197953	GO.BP
epiWAT	GO:0001659	temperature homeostasis	6.5574529	0.01631015	GO.BP
epiWAT	GO:0048638	regulation of developmental growth	4.42238185	0.0231877	GO.BP
epiWAT	GO:0032640	tumor necrosis factor production	5.33609147	0.02486719	GO.BP
epiWAT	GO:0045444	fat cell differentiation	4.56331993	0.0337331	GO.BP
aorta	GO:0035456	response to interferon-beta	27.5285163	2.98E-07	GO.BP
aorta	path:mmu05417	Lipid and atherosclerosis - Mus musculus (house mouse)	5.78365739	0.00182876	KEGG
aorta	GO:0045765	regulation of angiogenesis	5.60643652	0.00407352	GO.BP
aorta	GO:0034341	response to interferon-gamma	4.91379626	0.02153151	GO.BP
aorta	GO:0050727	regulation of inflammatory response	3.3802604	0.03406671	GO.BP
aorta	GO:2001242	regulation of intrinsic apoptotic signaling pathway	4.76025949	0.01256405	GO.BP
aorta	GO:0002221	pattern recognition receptor signaling pathway	4.72007161	0.01289085	GO.BP

Table S 2: Gene set overrepresentation analysis of differentially expressed genes between Folr2^{+} macrophages of the aorta and epiWAT at 12w WD. The table shows selected GO (gene ontology) biological process and GO molecular function categories that showed a significant overrepresentation in differentially expressed genes (Fisher test, BH adjusted p-value < 0.05).

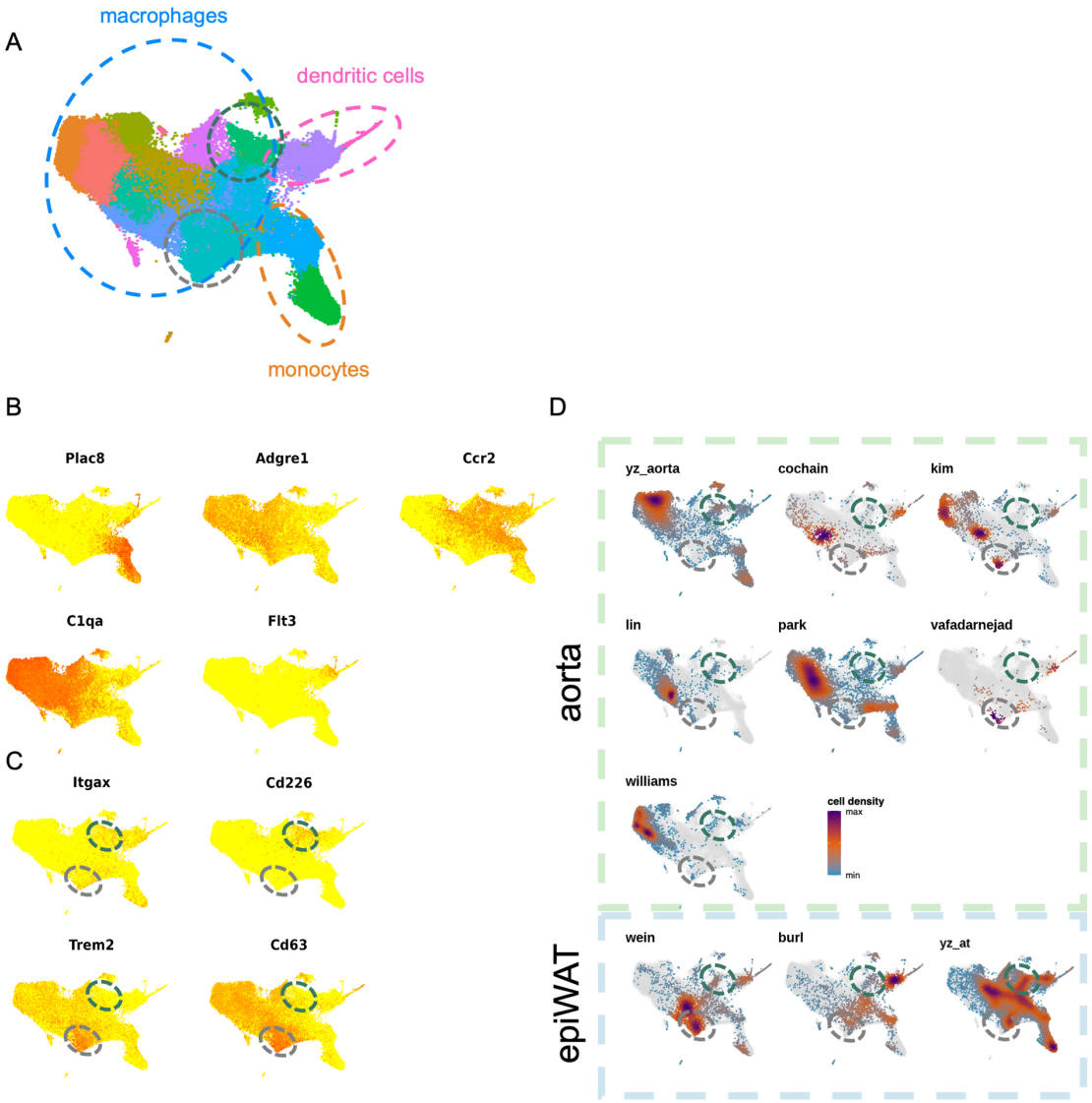


Figure S 15: ***Identification of Trem2^{hi} and Ccr2^{+}Cd226^{+} macrophages in publicly available scRNAseq datasets from the aorta and epiWAT.*** *A myeloid atlas was constructed by integrated analysis of 6 publicly available aortic scRNAseq datasets of healthy and atherosclerotic aortas, 2 publicly available epiWAT scRNAseq datasets of healthy and obese epiWAT and mononuclear phagocytes (MNPs) from WT and IRF5$^{-/-}$ samples from MBMC aortas. A. The UMAP shows the integrated dataset. Leiden clustering identified 2 monocyte clusters, 4 dendritic cell clusters and 11 macrophage clusters. Expression of selected cell type markers (B.), and cluster markers that are used to distinguish Itgax^{+} macrophages subsets (C.). Cell density plots for each study dataset. Trem2^{hi} macrophages are highlighted by the grey dotted line, Ccr2^{+}Cd226^{+} macrophages are highlighted by the green dotted line.*

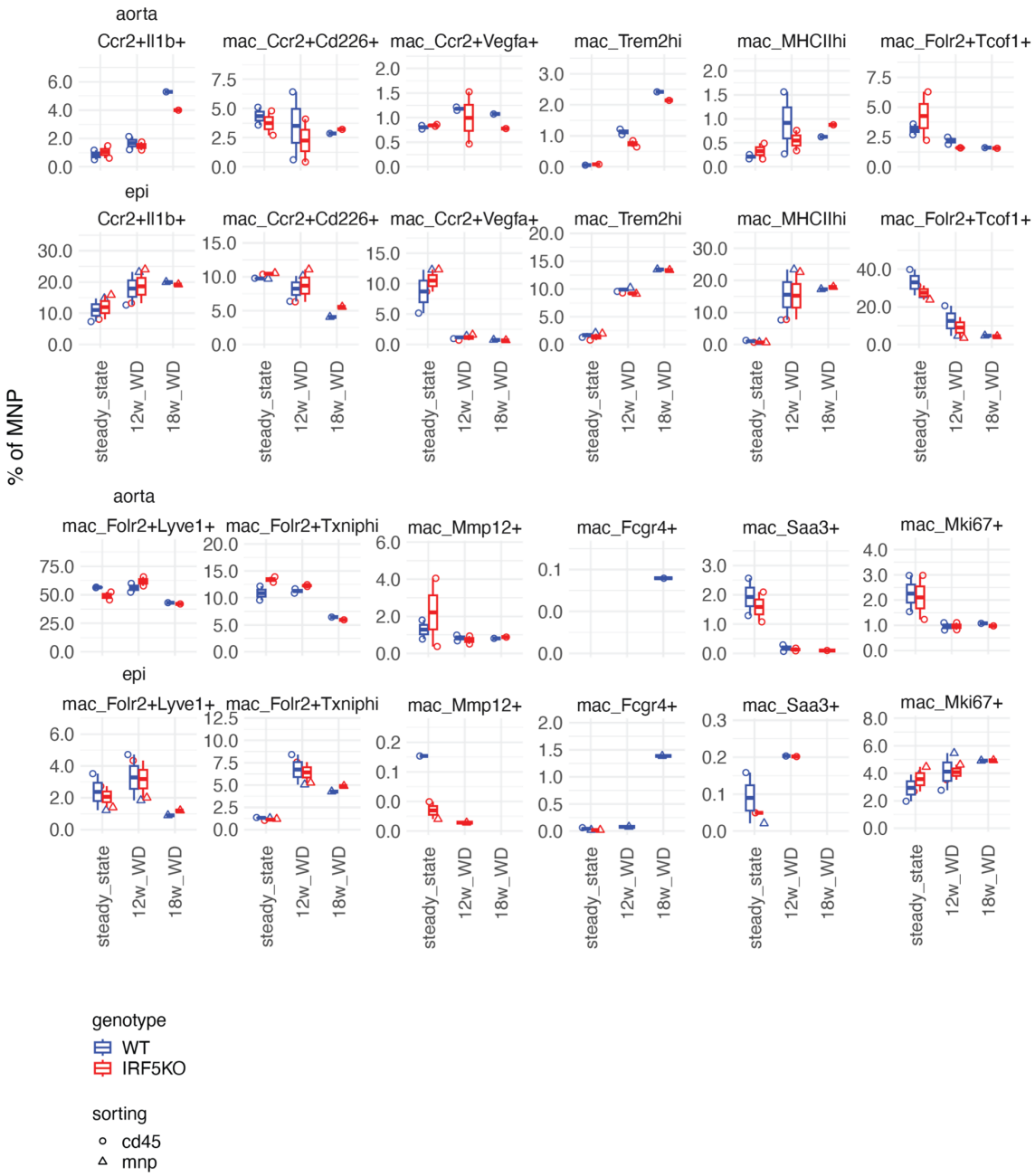


Figure S 16: ***Composition of WT and IRF5$^{-/-}$ macrophage clusters identified in combined analysis of the aorta and epiWAT of mixed bone marrow chimera during metabolic disease progression.***

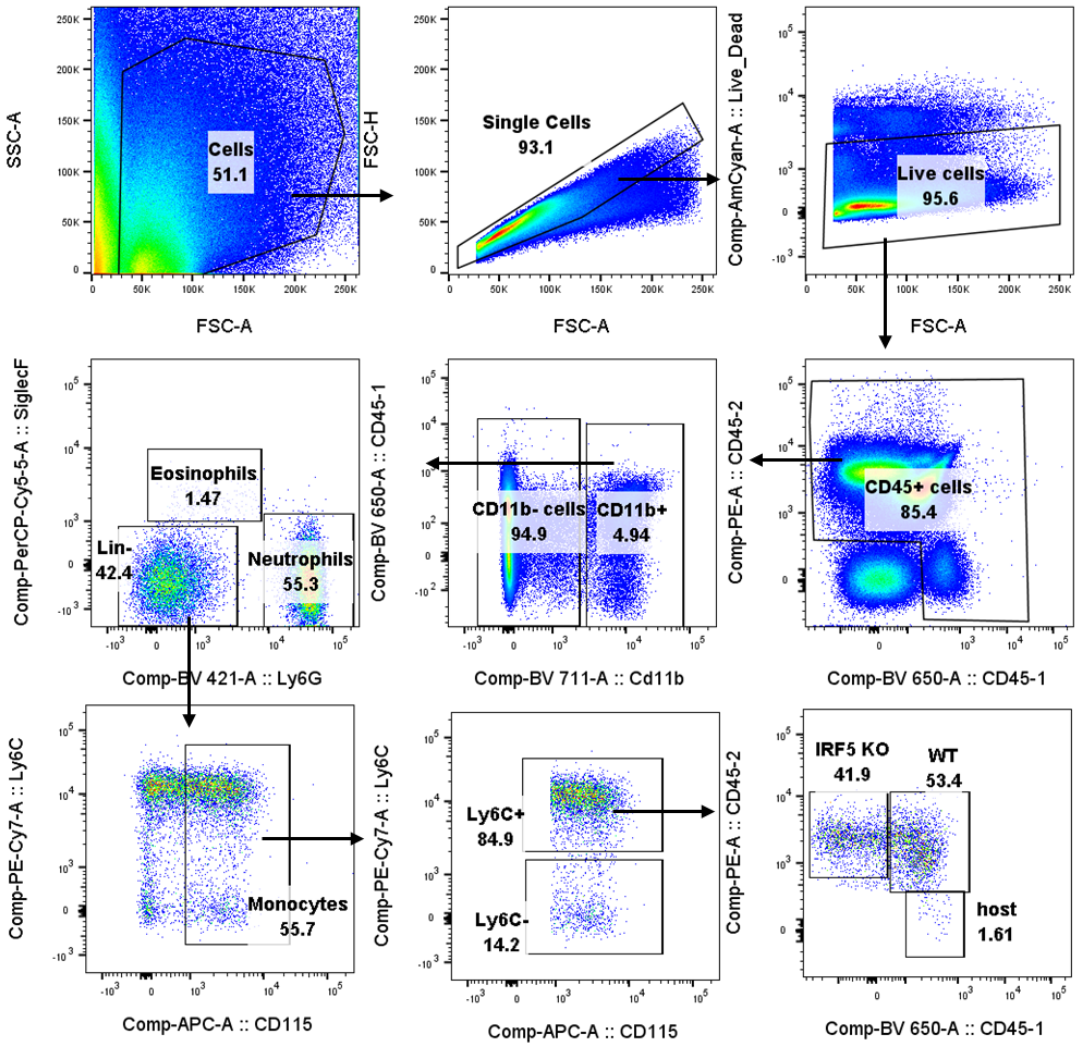


Figure S 17: ***Representative gating strategy for the myeloid populations in the blood of MBMCs.****For each cell population of interest reconstitution was measured by gating on WT and IRF5$^{-/-}$.*

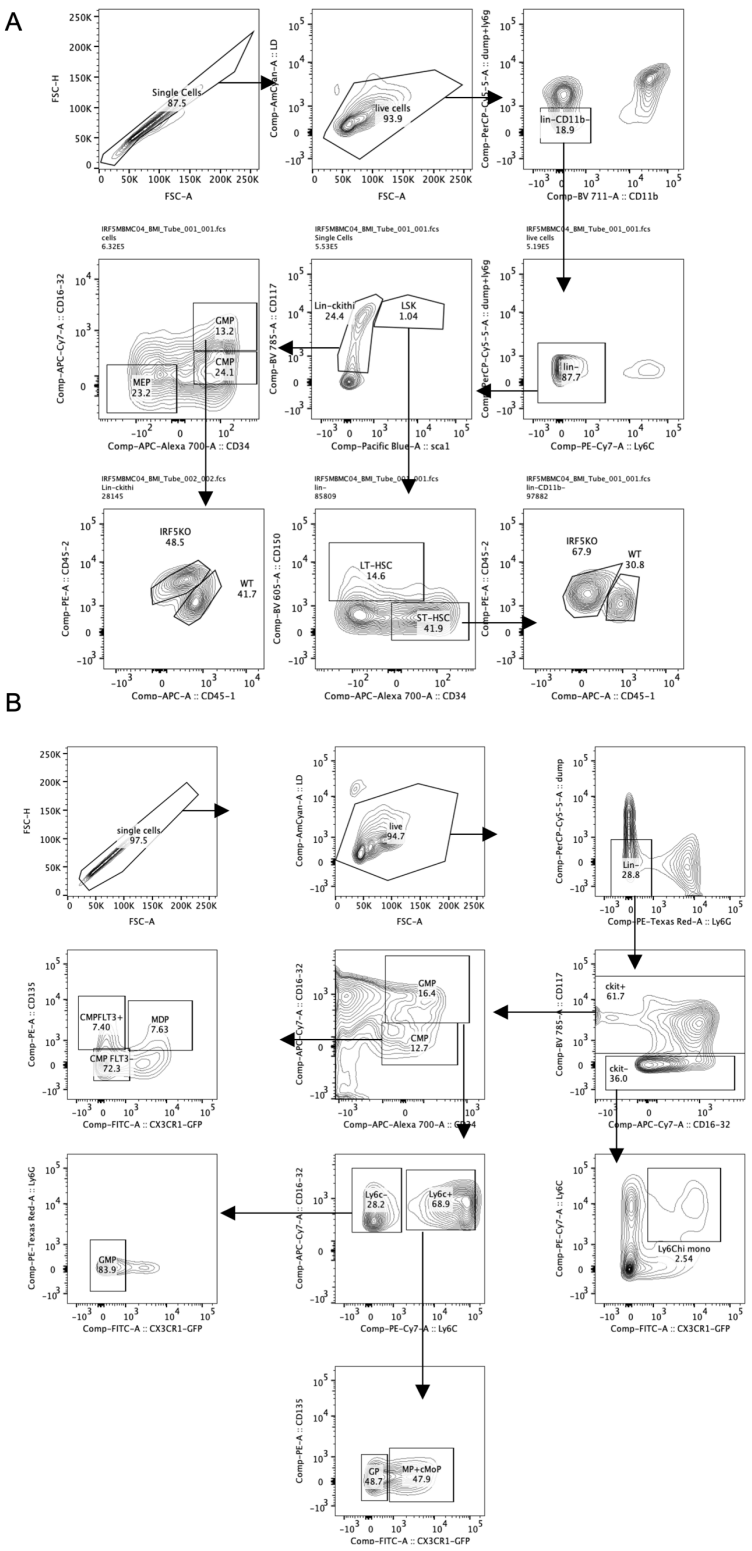


Figure S 18: ***Representative gating strategies for myeloid progenitors in the bone marrow.*** *A. Long-term A. Gating strategy for hematopoietic stem cells (LT-HSCs), short-term HSC (ST-HSC), common myeloid progenitors (CMPs), granulocyte-monocyte progenitors (GMPs). B. Gating strategy for granulocyte committed progenitors (GP), monocyte committed progenitors (MPs), common monocyte progenitors (cMoPs), monocyte-dendritic cell progenitors (MDPs) and Ly6C^{hi} monocytes. A-B. For each cell population of interest reconstitution was measured by gating on WT and IRF5$^{-/-}$.*

Table S 3: Overview of community datasets.

study	mouse strain	sex	tissue	sorting/ enrichment	age	feeding regime	diet supplier	disease time point	nsamples	technique	comment
burl	B6J	male	epiWAT	CD45+	8 w	NA	NA	steady state	1	scRNAseq	
cottam	B6J	male	epiWAT	CD45+	26 w	27 w chow diet	D12492 (Research Diets)	steady state	4	CITE seq	HTO 4 samples
cottam	B6J	male	epiWAT	CD45+	26 w	9w chow diet + 18 w HFD		late disease	4	CITE seq	HTO 4 samples
cottam	B6J	male	epiWAT	CD45+	26 w	18w HFD + 9 w chow diet		regression	4	CITE seq	HTO 4 samples
cottam	B6J	male	epiWAT	CD45+	26 w	9w HFD + 9w chow diet + 9w HFD		weight cycling	4	CITE seq	HTO 4 samples
weinstock	PCSK9 AAV	male	epiWAT	CD45+	32 w	26 w high fat diet	17052507i (Research diets)	late disease	1	scRNAseq	
weinstock	PCSK9 AAV	male	epiWAT	CD45+	32 w	24 w HFD + 2 w chow diet		regression	1	scRNAseq	
park	Apoe-/-	female	aorta	CD45+Cd11b+	20 w	12 w HFD	Special Diets Services (UK)	established disease	1	scRNAseq	
park	Apoe-/-	female	aorta	CD45+Cd11b+	24 w	16 w HFD		late disease	1	scRNAseq	
park	Apoe-/-	female	aorta	CD45+CD11b+Cd64+	20 w	12 w HFD		established disease	1	scRNAseq	
kim	Ldlr-/-	male	aorta	CD45+	18-20w	12 w HFD	AIN-76A (Test Diet)	established disease	1	scRNAseq	
kim	Apoe-/-	male	aorta	foamy cells	33-35 w	27 w HFD		late disease	1	scRNAseq	
cochain	Ldlr-/-	male	aorta	CD45+	17-19w	11 w chow diet	Altromin	steady state	1	scRNAseq	
cochain	Ldlr-/-	male	aorta	CD45+	17-19w	11 w HFD		established disease	1	scRNAseq	
cochain	Ldlr-/-	male	aorta	CD45+	17-19w	20 HFD		late disease	1	scRNAseq	
vafadarnejad	Ldlr-/-	male	aorta without macroscopically visible atherosclerotic plaques	CD45+	18w	10w HFD		established disease	1	scRNAseq	
vafadarnejad	Ldlr-/-	male	plaques	CD45+	18w	10w HFD		established disease	1	scRNAseq	
lin	PCSK9 AAV	male	aorta	CD11b+ tdTomato+	30 w	20w HFD	101977 (Dyet Inc)	late disease	1	scRNAseq	
lin	PCSK9 AAV	female	aorta	CD11b+ tdTomato+	NA	18w HFD + 2w chow diet		regression	1	scRNAseq	
williams	B6J	male	aorta	CD45+	11w	NA	TD.88137 (Envigo)	steady state	1	scRNAseq	
williams	Ldlr-/-	male	aorta	CD45+	11w	21d HFD		early disease	1	scRNAseq	

Appendix B Abbreviations

APC	antigen presenting cell
AT	adipose tissue
ATM	adipose tissue macrophage
BAT	brown adipose tissue
BH	benjamini hochberg
BMDM	bone marrow derived macrophages
BMC	bone marrow chimera
BP	biological process
BrdU	Bromodeoxyuridin
CAD	coronary artery disease
CD	chow diet
cDC	conventional dendritic cell
cMOP	common monocyte progenitors
CMP	common myeloid progenitor
CVD	cardiovascular disease
CyTOF	cytometry by time of flight
epiWAT	epididymal white adipose tissue
FC	fold change
gDNA	genomic DNA
GLP-1	glucagon-like peptide-1
GMCSF	granulocyte colony stimulating factor
GMP	granulocyte-monocyte progenitor
GO	gene ontology
GP	granulocyte committed progenitors
HSC	hematopoietic stem cell
LAM	lipid associated macrophage
LDL	low density lipoprotein
LT	long term
MCSF	monocyte colony stimulating factor
MDP	monocyte-dendritic cell progenitors
MEP	megakaryocyte-erythrocyte progenitors
MP	monocyte committed progenitors
Mac^{AIR}	aortic intimal resident macrophages
MBMC	mixed bone marrow chimera
MHC	histocompatibility complex class
MNP	mononuclear phagocyte
oxLDL	oxidised low density lipoprotein
OR	odds ratio
pDC	plasmacytoid dendritic cells
SAA	serum amyloid apolipoproteins
SAT	subcutaneous adipose tissue
scRNAseq	single-cell ribonucleic acid sequencing
SLE	systemic lupus erythematosus
ST	short term
TAE	Tris-Acetate-EDTA
TLF	$Tim4^{+}Lyve1^{+}Folr2^{+}$
TREM	triggering receptor expressed on myeloid cells
TXNIP	thioredoxin-interacting protein
UCP1	uncoupling protein 1
VAM	vascular associated macrophages

VSMC	vascular smooth muscle cell
WAT	white adipose tissue
WD	western diet
WT	wild type

Appendix C List of Publications

1. Engelen, S. E.*, Robinson, A. J. B.*, **Zurke, Y. X**.* & Monaco, C. Therapeutic strategies targeting inflammation and immunity in atherosclerosis: how to proceed? *Nat. Rev. Cardiol.* **19**, 522–542 (2022). (*co-first author)
2. Ahern, D. J. *et al.* A blood atlas of COVID-19 defines hallmarks of disease severity and specificity. *Cell* **185**, 916-938.e58 (2022).
3. Abdelmoez, A. M. *et al.* Cell selectivity in succinate receptor SUCNR1/GPR91 signaling in skeletal muscle. *Am. J. Physiol. Endocrinol. Metab.* **324**, E289–E298 (2023).
4. Engelen, S. E. *et al.* Lipoproteins act as vehicles for lipid antigen delivery and activation of invariant natural killer T cells. *JCI insight* **8**, (2023).
5. Dib, L. *et al.* Lipid-associated macrophages transition to an inflammatory state in human atherosclerosis, increasing the risk of cerebrovascular complications. *Nat. Cardiovasc. Res.* **2**, 656–672 (2023).
6. Kwok, A. J. *et al.* Neutrophils and emergency granulopoiesis drive immune suppression and an extreme response endotype during sepsis. *Nat. Immunol. 2023 245* **24**, 767–779 (2023).

Appendix D Bibliography

1. Roth, G. A. *et al.* Global Burden of Cardiovascular Diseases and Risk Factors, 1990-2019: Update From the GBD 2019 Study. *J. Am. Coll. Cardiol.* **76**, 2982–3021 (2020).
2. Bays, H. E. 'Sick Fat,' Metabolic Disease, and Atherosclerosis. *Am. J. Med.* **122**, S26–S37 (2009).
3. Kassi, E., Pervanidou, P., Kaltsas, G. & Chrousos, G. Metabolic syndrome: Definitions and controversies. *BMC Med.* **9**, 1–13 (2011).
4. Ng, M. *et al.* Global, regional, and national prevalence of overweight and obesity in children and adults during 1980-2013: A systematic analysis for the Global Burden of Disease Study 2013. *Lancet* **384**, 766–781 (2014).
5. Wolf, D. & Ley, K. Immunity and Inflammation in Atherosclerosis. *Circ. Res.* **124**, 315–327 (2019).
6. Hotamisligil, G. S. Inflammation, metaflammation and immunometabolic disorders. *Nature* **542**, 177–185 (2017).
7. Arnett, D. K. *et al.* 2019 ACC/AHA Guideline on the Primary Prevention of Cardiovascular Disease: A Report of the American College of Cardiology/American Heart Association Task Force on Clinical Practice Guidelines. *Circulation* **140**, e596–e646 (2019).
8. Neumann, F. J. *et al.* 2019 ESC Guidelines for the diagnosis and management of chronic coronary syndromes. *Eur. Heart J.* **41**, 407–477 (2020).
9. Ridker, P. M. *et al.* Antiinflammatory Therapy with Canakinumab for Atherosclerotic Disease. *N. Engl. J. Med.* **377**, 1119–1131 (2017).
10. Nidorf, S. M. *et al.* Colchicine in Patients with Chronic Coronary Disease. *N. Engl. J. Med.* **383**, 1838–1847 (2020).
11. Tardif, J.-C. *et al.* Efficacy and Safety of Low-Dose Colchicine after Myocardial Infarction. *N. Engl. J. Med.* **381**, 2497–2505 (2019).
12. Jastreboff, A. M. *et al.* Tirzepatide Once Weekly for the Treatment of Obesity. *N. Engl. J. Med.* **387**, 205–216 (2022).
13. Rubino, D. *et al.* Effect of Continued Weekly Subcutaneous Semaglutide vs Placebo on Weight Loss Maintenance in Adults With Overweight or Obesity: The STEP 4 Randomized Clinical Trial. *JAMA* **325**, 1414–1425 (2021).
14. Nauck, M. A. & Meier, J. J. Incretin hormones: Their role in health and disease. *Diabetes. Obes. Metab.* **20 Suppl 1**, 5–21 (2018).
15. Lee, Y. S. & Jun, H. S. Anti-Inflammatory Effects of GLP-1-Based Therapies beyond Glucose Control. *Mediators Inflamm.* **2016**, (2016).
16. Bendotti, G. *et al.* The anti-inflammatory and immunological properties of GLP-1 Receptor Agonists. *Pharmacol. Res.* **182**, 106320 (2022).
17. Pollack, R. M., Donath, M. Y., LeRoith, D. & Leibowitz, G. Anti-inflammatory Agents in the Treatment of Diabetes and Its Vascular Complications. *Diabetes Care* **39**, S244–S252 (2016).
18. Netea, M. G. *et al.* The effect of salicylates on insulin sensitivity. *J. Clin. Invest.* **108**, 1723–1724 (2001).
19. Libby, P., Ridker, P. M. & Maseri, A. Inflammation and atherosclerosis.

Circulation **105**, 1135–1143 (2002).

20. Stemme, S. *et al.* T lymphocytes from human atherosclerotic plaques recognize oxidized low density lipoprotein. *Proc. Natl. Acad. Sci. U. S. A.* **92**, 3893–3897 (1995).
21. Roy, P. *et al.* How the immune system shapes atherosclerosis: roles of innate and adaptive immunity. *Nat. Rev. Immunol.* **22**, 251–265 (2022).
22. Stewart, C. R. *et al.* CD36 ligands promote sterile inflammation through assembly of a Toll-like receptor 4 and 6 heterodimer. *Nat. Immunol.* **11**, 155–161 (2010).
23. Binder, C. J., Papac-Milicevic, N. & Witztum, J. L. Innate sensing of oxidation-specific epitopes in health and disease. *Nat. Rev. Immunol.* **16**, 485–497 (2016).
24. Engelen, S. E., Robinson, A. J. B., Zurke, Y. X. & Monaco, C. Therapeutic strategies targeting inflammation and immunity in atherosclerosis: how to proceed? *Nat. Rev. Cardiol.* **19**, 522–542 (2022).
25. Naghavi, M. *et al.* From vulnerable plaque to vulnerable patient: A call for new definitions and risk assessment strategies: Part I. *Circulation* **108**, 1664–1672 (2003).
26. McAlpine, C. S. *et al.* Sleep modulates haematopoiesis and protects against atherosclerosis. *Nature* **566**, 383–387 (2019).
27. Robbins, C. S. *et al.* Extramedullary hematopoiesis generates Ly-6C high monocytes that infiltrate atherosclerotic lesions. *Circulation* **125**, 364–374 (2012).
28. Ravussin, E. & Galgani, J. E. The Implication of Brown Adipose Tissue for Humans. *https://doi.org/10.1146/annurev-nutr-072610-145209* **31**, 33–47 (2011).
29. Harms, M. & Seale, P. Brown and beige fat: development, function and therapeutic potential. *Nat. Med.* **19**, 1252–1263 (2013).
30. Villarroya, F., Cereijo, R., Villarroya, J. & Giralt, M. Brown adipose tissue as a secretory organ. *Nat. Rev. Endocrinol.* **13**, 26–35 (2017).
31. Bartelt, A. & Heeren, J. Adipose tissue browning and metabolic health. *Nat. Rev. Endocrinol. 2013 101* **10**, 24–36 (2013).
32. Pellegrinelli, V., Carobbio, S. & Vidal-Puig, A. Adipose tissue plasticity: how fat depots respond differently to pathophysiological cues. *Diabetologia* **59**, 1075–1088 (2016).
33. Muir, L. A. *et al.* Adipose tissue fibrosis, hypertrophy, and hyperplasia: Correlations with diabetes in human obesity. *Obesity (Silver Spring).* **24**, 597–605 (2016).
34. Reilly, S. M. & Saltiel, A. R. Adapting to obesity with adipose tissue inflammation. *Nat. Rev. Endocrinol. 2017 1311* **13**, 633–643 (2017).
35. Weinstock, A., Silva, H. M., Moore, K. J., Schmidt, A. M. & Fisher, E. A. Leukocyte Heterogeneity in Adipose Tissue, including in Obesity. *Circ. Res.* 1590–1612 (2020) doi:10.1161/CIRCRESAHA.120.316203.
36. Weisberg, S. P. *et al.* Obesity is associated with macrophage accumulation in adipose tissue. *J. Clin. Invest.* **112**, 1796–1808 (2003).
37. Harman-Boehm, I. *et al.* Macrophage Infiltration into Omental Versus Subcutaneous Fat across Different Populations: Effect of Regional Adiposity and the Comorbidities of Obesity. *J. Clin. Endocrinol. Metab.* **92**, 2240–2247 (2007).
38. Weisberg, S. P. *et al.* CCR2 modulates inflammatory and metabolic effects of high-

fat feeding. *J. Clin. Invest.* **116**, 115–124 (2006).

39. Kanda, H. *et al.* MCP-1 contributes to macrophage infiltration into adipose tissue, insulin resistance, and hepatic steatosis in obesity. *J. Clin. Invest.* **116**, 1494–1505 (2006).
40. Amano, S. U. *et al.* Local proliferation of macrophages contributes to obesity-associated adipose tissue inflammation. *Cell Metab.* **19**, 162–171 (2014).
41. Cinti, S. *et al.* Adipocyte death defines macrophage localization and function in adipose tissue of obese mice and humans. *J. Lipid Res.* **46**, 2347–2355 (2005).
42. Sun, K., Kusminski, C. M. & Scherer, P. E. Adipose tissue remodeling and obesity. *J. Clin. Invest.* **121**, 2094 (2011).
43. Patsouris, D. *et al.* Ablation of CD11c-Positive Cells Normalizes Insulin Sensitivity in Obese Insulin Resistant Animals. *Cell Metab.* **8**, 301–309 (2008).
44. Wu, H. *et al.* CD11c expression in adipose tissue and blood and its role in diet-induced obesity. *Arterioscler. Thromb. Vasc. Biol.* **30**, 186–192 (2010).
45. Saigusa, R. *et al.* T cell subsets and functions in atherosclerosis. *Nat. Rev. Cardiol.* **17**, 387–401 (2020).
46. Ketelhuth, D. F. J. & Hansson, G. K. Adaptive Response of T and B Cells in Atherosclerosis. *Circ. Res.* **118**, 668–678 (2016).
47. Fernandez, D. M. *et al.* Single-cell immune landscape of human atherosclerotic plaques. *Nat. Med.* **25**, 1576–1588 (2019).
48. Kyaw, T. *et al.* Cytotoxic and proinflammatory CD8+ T lymphocytes promote development of vulnerable atherosclerotic plaques in ApoE-deficient mice. *Circulation* **127**, 1028–1039 (2013).
49. Hwang, Y. *et al.* Expansion of CD8+ T cells lacking the IL-6 receptor α chain in patients with coronary artery diseases (CAD). *Atherosclerosis* **249**, 44–51 (2016).
50. I, B. *et al.* Persistent accumulation of interferon-γ-producing CD8+CD56+ T cells in blood from patients with coronary artery disease. *Atherosclerosis* **224**, 515–520 (2012).
51. Van Duijn, J., Kuiper, J. & Slutter, B. The many faces of CD8+ T cells in atherosclerosis. *Curr. Opin. Lipidol.* **29**, 411–416 (2018).
52. Nishimura, S. *et al.* CD8+ effector T cells contribute to macrophage recruitment and adipose tissue inflammation in obesity. *Nat. Med.* **15**, 914–920 (2009).
53. Depuydt, M. A. C. *et al.* Single-cell T cell receptor sequencing of paired human atherosclerotic plaques and blood reveals autoimmune-like features of expanded effector T cells. *Nat. Cardiovasc. Res.* **2**, 112–125 (2023).
54. McLaughlin, T. *et al.* T-cell profile in adipose tissue is associated with insulin resistance and systemic inflammation in humans. *Arterioscler. Thromb. Vasc. Biol.* **34**, 2632–2636 (2014).
55. Liu, R. & Nikolajczyk, B. S. Tissue immune cells fuel obesity-associated inflammation in adipose tissue and beyond. *Front. Immunol.* **10**, 469118 (2019).
56. Winer, S. *et al.* Normalization of obesity-associated insulin resistance through immunotherapy. *Nat. Med. 2009 158* **15**, 921–929 (2009).
57. Maganto-García, E., Tarrio, M. L., Grabie, N., Bu, D. X. & Lichtman, A. H. Dynamic Changes in Regulatory T Cells Are Linked to Levels of Diet-Induced Hypercholesterolemia. *Circulation* **124**, 185–195 (2011).

58. Cipolletta, D., Cohen, P., Spiegelman, B. M., Benoist, C. & Mathis, D. Appearance and disappearance of the mRNA signature characteristic of Treg cells in visceral adipose tissue: Age, diet, and PPARγ effects. *Proc. Natl. Acad. Sci. U. S. A.* **112**, 482–487 (2015).

59. Feuerer, M. *et al.* Lean, but not obese, fat is enriched for a unique population of regulatory T cells that affect metabolic parameters. *Nat. Med. 2009 158* **15**, 930–939 (2009).

60. Ali, A. J., Makings, J. & Ley, K. Regulatory T Cell Stability and Plasticity in Atherosclerosis. *Cells 2020, Vol. 9, Page 2665* **9**, 2665 (2020).

61. Butcher, M. J. *et al.* Atherosclerosis-Driven Treg Plasticity Results in Formation of a Dysfunctional Subset of Plastic IFNγ+ Th1/Tregs. *Circ. Res.* **119**, 1190–1203 (2016).

62. Li, J. *et al.* CCR5+ T-bet+ FoxP3+ Effector CD4 T Cells Drive Atherosclerosis. *Circ. Res.* **118**, 1540–1552 (2016).

63. Freuchet, A. *et al.* Identification of human exTreg cells as CD16+CD56+ cytotoxic CD4+ T cells. *Nat. Immunol.* 1–14 (2023) doi:10.1038/s41590-023-01589-9.

64. Wolf, D. *et al.* Pathogenic Autoimmunity in Atherosclerosis Evolves From Initially Protective Apolipoprotein B100-Reactive CD4+T-Regulatory Cells. *Circulation* **142**, 1279–1293 (2020).

65. Wang, Z. *et al.* Pairing of single-cell RNA analysis and T cell antigen receptor profiling indicates breakdown of T cell tolerance checkpoints in atherosclerosis. **2**, (2023).

66. Zhou, X. *et al.* Instability of the transcription factor Foxp3 leads to the generation of pathogenic memory T cells in vivo. *Nat. Immunol. 2009 109* **10**, 1000–1007 (2009).

67. Zernecke, A. *et al.* Meta-analysis of leukocyte diversity in atherosclerotic mouse aortas. *Circ. Res.* **127**, 402–426 (2020).

68. Newland, S. A. *et al.* Type-2 innate lymphoid cells control the development of atherosclerosis in mice. *Nat. Commun.* **8**, (2017).

69. Koltsova, E. K. *et al.* Dynamic T cell-APC interactions sustain chronic inflammation in atherosclerosis. *J. Clin. Invest.* **122**, 3114–3126 (2012).

70. Reizis, B. Plasmacytoid Dendritic Cells: Development, Regulation, and Function. *Immunity* **50**, 37–50 (2019).

71. Kohli, K., Janssen, A. & Förster, R. Plasmacytoid dendritic cells induce tolerance predominantly by cargoing antigen to lymph nodes. *Eur. J. Immunol.* **46**, 2659–2668 (2016).

72. Merad, M., Sathe, P., Helft, J., Miller, J. & Mortha, A. The dendritic cell lineage: Ontogeny and function of dendritic cells and their subsets in the steady state and the inflamed setting. *Annu. Rev. Immunol.* **31**, 563–604 (2013).

73. Niessner, A. *et al.* Pathogen-sensing plasmacytoid dendritic cells stimulate cytotoxic T-cell function in the atherosclerotic plaque through interferon-α. *Circulation* **114**, 2482–2489 (2006).

74. MacRitchie, N. *et al.* Plasmacytoid Dendritic Cells Play a Key Role in Promoting Atherosclerosis in Apolipoprotein E–Deficient Mice. *Arterioscler. Thromb. Vasc. Biol.* **32**, 2569–2579 (2012).

75. Zernecke, A. Dendritic cells in atherosclerosis: Evidence in mice and humans.

Arterioscler. Thromb. Vasc. Biol. **35**, 763–770 (2015).

76. Yilmaz, A. *et al.* Emergence of dendritic cells in rupture-prone regions of vulnerable carotid plaques. *Atherosclerosis* **176**, 101–110 (2004).

77. Weber, C. *et al.* CCL17-expressing dendritic cells drive atherosclerosis by restraining regulatory T cell homeostasis in mice. *J. Clin. Invest.* **121**, 2898–2910 (2011).

78. Choi, J. H. *et al.* Flt3 signaling-dependent dendritic cells protect against atherosclerosis. *Immunity* **35**, 819–831 (2011).

79. Tsapogas, P. *et al.* In vivo evidence for an instructive role of fms-like tyrosine kinase-3 (FLT3) ligand in hematopoietic development. *Haematologica* **99**, 638–646 (2014).

80. Stefanovic-Racic, M. *et al.* Dendritic cells promote macrophage infiltration and comprise a substantial proportion of obesity-associated increases in CD11c + cells in adipose tissue and liver. *Diabetes* **61**, 2330–2339 (2012).

81. Swirski, F. K. *et al.* Ly-6Chi monocytes dominate hypercholesterolemia-associated monocytosis and give rise to macrophages in atheromata. *J. Clin. Invest.* **117**, 195–205 (2007).

82. Nagareddy, P. R. *et al.* Adipose tissue macrophages promote myelopoiesis and monocytosis in obesity. *Cell Metab.* **19**, 821–835 (2014).

83. Leuschner, F. *et al.* Rapid monocyte kinetics in acute myocardial infarction are sustained by extramedullary monocytopoiesis. *J. Exp. Med.* **209**, 123–137 (2012).

84. Schloss, M. J., Swirski, F. K. & Nahrendorf, M. Modifiable Cardiovascular Risk, Hematopoiesis, and Innate Immunity. *Circ. Res.* **126**, 1242–1259 (2020).

85. Combadière, C. *et al.* Combined inhibition of CCL2, CX3CR1, and CCR5 abrogates Ly6Chi and Ly6Clo monocytosis and almost abolishes atherosclerosis in hypercholesterolemic mice. *Circulation* **117**, 1649–1657 (2008).

86. Tabas, I. & Lichtman, A. H. Monocyte-Macrophages and T Cells in Atherosclerosis. *Immunity* **47**, 621–634 (2017).

87. Tacke, F. *et al.* Monocyte subsets differentially employ CCR2, CCR5, and CX3CR1 to accumulate within atherosclerotic plaques. *J. Clin. Invest.* **117**, 185–194 (2007).

88. Geissmann, F. *et al.* Development of monocytes, macrophages, and dendritic cells. *Science (80-.).* **327**, 656–661 (2010).

89. Hamers, A. A. J. *et al.* Human Monocyte Heterogeneity as Revealed by High-Dimensional Mass Cytometry. *Arterioscler. Thromb. Vasc. Biol.* **39**, 25–36 (2019).

90. Sunderkötter, C. *et al.* Subpopulations of Mouse Blood Monocytes Differ in Maturation Stage and Inflammatory Response. *J. Immunol.* **172**, 4410–4417 (2004).

91. Woollard, K. J. & Geissmann, F. Monocytes in atherosclerosis: Subsets and functions. *Nat. Rev. Cardiol.* **7**, 77–86 (2010).

92. Narasimhan, P. B., Marcovecchio, P., Hamers, A. A. J. & Hedrick, C. C. *Nonclassical Monocytes in Health and Disease*. *Annual Review of Immunology* vol. 37 439–456 (Annual Reviews Inc., 2019).

93. Carlin, L. M. *et al.* Nr4a1-dependent Ly6Clow monocytes monitor endothelial cells and orchestrate their disposal. *Cell* **153**, 362–375 (2013).

94. Marcovecchio, P. M. *et al.* Scavenger Receptor CD36 Directs Nonclassical Monocyte Patrolling Along the Endothelium During Early Atherogenesis. *Arterioscler. Thromb. Vasc. Biol.* **37**, 2043–2052 (2017).

95. Quintar, A. *et al.* Endothelial Protective Monocyte Patrolling in Large Arteries Intensified by Western Diet and Atherosclerosis. *Circ. Res.* **120**, 1789–1799 (2017).

96. Hu, Y. W. *et al.* Nur77 decreases atherosclerosis progression in apoE-/- mice fed a high-fat/high-cholesterol diet. *PLoS One* **9**, 87313 (2014).

97. Smith, P. K. *et al.* Measurement of protein using bicinchoninic acid. *Anal. Biochem.* **150**, 76–85 (1985).

98. Colin, S., Chinetti-Gbaguidi, G. & Staels, B. Macrophage phenotypes in atherosclerosis. *Immunol. Rev.* **262**, 153–166 (2014).

99. Stout, R. D. & Suttles, J. Functional plasticity of macrophages: reversible adaptation to changing microenvironments. *J. Leukoc. Biol.* **76**, 509–513 (2004).

100. Tabas, I. & Bornfeldt, K. E. Macrophage Phenotype and Function in Different Stages of Atherosclerosis. *Circ. Res.* **118**, 653–667 (2016).

101. Moore, K. J. & Tabas, I. Macrophages in the pathogenesis of atherosclerosis. *Cell* **145**, 341–355 (2011).

102. Vafadarnejad, E. *et al.* Dynamics of Cardiac Neutrophil Diversity in Murine Myocardial Infarction. *Circ. Res.* **127**, E232–E249 (2020).

103. Cochain, C. *et al.* Single-cell RNA-seq reveals the transcriptional landscape and heterogeneity of aortic macrophages in murine atherosclerosis. *Circ. Res.* **122**, 1661–1674 (2018).

104. Lin, J. Da *et al.* Single-cell analysis of fate-mapped macrophages reveals heterogeneity, including stem-like properties, during atherosclerosis progression and regression. *JCI insight* **4**, (2019).

105. Kim, K. W. K. *et al.* Transcriptome analysis reveals nonfoamy rather than foamy plaque macrophages are proinflammatory in atherosclerotic murine models. *Circ. Res.* **123**, 1127–1142 (2018).

106. Williams, J. W. *et al.* Single Cell RNA Sequencing in Atherosclerosis Research. *Circ. Res.* **126**, 1112–1126 (2020).

107. McArdle, S. *et al.* Migratory and dancing macrophage subsets in atherosclerotic lesions. *Circ. Res.* **125**, 1038–1051 (2019).

108. Winkels, H. & Wolf, D. Heterogeneity of T Cells in Atherosclerosis Defined by Single-Cell RNA-Sequencing and Cytometry by Time of Flight. *Arterioscler. Thromb. Vasc. Biol.* **41**, 549–563 (2021).

109. Cole, J. E. *et al.* Immune cell census in murine atherosclerosis: Cytometry by time of flight illuminates vascular myeloid cell diversity. *Cardiovasc. Res.* **114**, 1360–1371 (2018).

110. Weinstock, A. *et al.* Single-Cell RNA Sequencing of Visceral Adipose Tissue Leukocytes Reveals that Caloric Restriction Following Obesity Promotes the Accumulation of a Distinct Macrophage Population with Features of Phagocytic Cells. *Immunometabolism* **1**, (2019).

111. Burl, R. B. *et al.* Deconstructing Adipogenesis Induced by β3-Adrenergic Receptor Activation with Single-Cell Expression Profiling. *Cell Metab.* **28**, 300-309.e4 (2018).

112. Jaitin, D. A. *et al.* Lipid-Associated Macrophages Control Metabolic Homeostasis in a Trem2-Dependent Manner. *Cell* **178**, 686-698.e14 (2019).

113. Emont, M. P. *et al.* A single-cell atlas of human and mouse white adipose tissue. **603**, 926–933 (2022).

114. Cottam, M. A., Caslin, H. L., Winn, N. C. & Hasty, A. H. Multiomics reveals persistence of obesity-associated immune cell phenotypes in adipose tissue during weight loss and weight regain in mice. *Nat. Commun. 2022 131* **13**, 1–16 (2022).

115. Magalhaes, M. S. *et al.* Role of Tim4 in the regulation of ABCA1+ adipose tissue macrophages and post-prandial cholesterol levels. *Nat. Commun. 2021 121* **12**, 1–15 (2021).

116. Félix, I. *et al.* Single-Cell Proteomics Reveals the Defined Heterogeneity of Resident Macrophages in White Adipose Tissue. *Front. Immunol.* **12**, 2995 (2021).

117. Zernecke, A. *et al.* Integrated single-cell analysis-based classification of vascular mononuclear phagocytes in mouse and human atherosclerosis. *Cardiovasc. Res.* **119**, (2022).

118. Dick, S. A. *et al.* Three tissue resident macrophage subsets coexist across organs with conserved origins and life cycles. *Sci. Immunol.* **7**, 7777 (2022).

119. Williams, J. W. *et al.* Limited proliferation capacity of aortic intima resident macrophages requires monocyte recruitment for atherosclerotic plaque progression. *Nat. Immunol.* **21**, 1194–1204 (2020).

120. Weinberger, T. *et al.* Ontogeny of arterial macrophages defines their functions in homeostasis and inflammation. *Nat. Commun.* **11**, 1–16 (2020).

121. Ensan, S. *et al.* Self-renewing resident arterial macrophages arise from embryonic CX3CR1 + precursors and circulating monocytes immediately after birth. *Nat. Immunol.* **17**, 159–168 (2016).

122. Lim, H. Y. *et al. Hyaluronan Receptor LYVE-1-Expressing Macrophages Maintain Arterial Tone through Hyaluronan-Mediated Regulation of Smooth Muscle Cell Collagen*. *Immunity* vol. 49 326-341.e7 (Immunity, 2018).

123. Silva, H. M. *et al.* Vasculature-associated fat macrophages readily adapt to inflammatory and metabolic challenges. *J. Exp. Med.* **216**, 786–806 (2019).

124. Cho, C. H. *et al.* Angiogenic role of LYVE-1-positive macrophages in adipose tissue. *Circ. Res.* **100**, (2007).

125. Owsiany, K. M., Alencar, G. F. & Owens, G. K. Revealing the Origins of Foam Cells in Atherosclerotic Lesions. *Arterioscler. Thromb. Vasc. Biol.* **39**, 836–838 (2019).

126. Dib, L. *et al.* Lipid-associated macrophages transition to an inflammatory state in human atherosclerosis, increasing the risk of cerebrovascular complications. *Nat. Cardiovasc. Res.* **2**, 656–672 (2023).

127. Castoldi, A., De Souza, C. N., Saraiva Câmara, N. O. & Moraes-Vieira, P. M. The macrophage switch in obesity development. *Frontiers in Immunology* vol. 6 1 (2016).

128. Li, P. *et al.* Functional heterogeneity of CD11c-positive adipose tissue macrophages in diet-induced obese mice. *J. Biol. Chem.* **285**, 15333–15345 (2010).

129. Krausgruber, T. *et al.* IRF5 promotes inflammatory macrophage polarization and T H1-TH17 responses. *Nat. Immunol.* **12**, 231–238 (2011).

130. Saliba, D. G. *et al.* IRF5:RelA Interaction Targets Inflammatory Genes in Macrophages. *Cell Rep.* **8**, 1308–1317 (2014).

131. Krausgruber, T. *et al.* IRF5 is required for late-phase TNF secretion by human dendritic cells. *Blood* **115**, 4421–4430 (2010).

132. Hettinger, J. *et al.* Origin of monocytes and macrophages in a committed progenitor. *Nat. Immunol.* **14**, 821–830 (2013).

133. Khoyratty, T. E. *et al.* Distinct transcription factor networks control neutrophil-driven inflammation. *Nat. Immunol. 2021 229* **22**, 1093–1106 (2021).

134. Seneviratne, A. N. *et al.* Interferon regulatory factor 5 controls necrotic core formation in atherosclerotic lesions by impairing efferocytosis. *Circulation* **136**, 1140–1154 (2017).

135. Leipner, J. *et al.* Myeloid cell-specific Irf5 deficiency stabilizes atherosclerotic plaques in Apoe–/– mice. *Mol. Metab.* **53**, 101250 (2021).

136. Edsfeldt, A. *et al.* Interferon regulatory factor-5-dependent CD11c+macrophages contribute to the formation of rupture-prone atherosclerotic plaques. *Eur. Heart J.* **43**, 1864–1877 (2022).

137. Dalmas, E. *et al.* Irf5 deficiency in macrophages promotes beneficial adipose tissue expansion and insulin sensitivity during obesity. *Nat. Med.* **21**, 610–618 (2015).

138. Orliaguet, L. *et al.* Early macrophage response to obesity encompasses Interferon Regulatory Factor 5 regulated mitochondrial architecture remodelling. *Nat. Commun. 2022 131* **13**, 1–17 (2022).

139. Corbin, A. L. *et al.* IRF5 guides monocytes toward an inflammatory CD11c+ macrophage phenotype and promotes intestinal inflammation. *Sci. Immunol.* **5**, 6085 (2020).

140. Vaduganathan, M., Mensah, G. A., Turco, J. V., Fuster, V. & Roth, G. A. The Global Burden of Cardiovascular Diseases and Risk: A Compass for Future Health. *J. Am. Coll. Cardiol.* **80**, 2361–2371 (2022).

141. Hossain, P., Kawar, B. & El Nahas, M. Obesity and Diabetes in the Developing World — A Growing Challenge. *N. Engl. J. Med.* **356**, 213–215 (2007).

142. Fuster, J. J., Ouchi, N., Gokce, N. & Walsh, K. Obesity-induced changes in adipose tissue microenvironment and their impact on cardiovascular disease. *Circulation Research* vol. 118 1786–1807 (2016).

143. Libby, P. Inflammation in atherosclerosis. *Nature* **420**, 868–874 (2002).

144. Christ, A., Lauterbach, M. & Latz, E. Western Diet and the Immune System: An Inflammatory Connection. *Immunity* **51**, 794–811 (2019).

145. Bray, G. A., Kim, K. K. & Wilding, J. P. H. Obesity: a chronic relapsing progressive disease process. A position statement of the World Obesity Federation. *Obes. Rev.* **18**, 715–723 (2017).

146. Rohm, T. V., Meier, D. T., Olefsky, J. M. & Donath, M. Y. Inflammation in obesity, diabetes, and related disorders. *Immunity* **55**, 31–55 (2022).

147. Rocha, V. Z. & Libby, P. Obesity, inflammation, and atherosclerosis. *Nat. Rev. Cardiol.* **6**, 399–409 (2009).

148. Winkels, H. *et al.* Atlas of the immune cell repertoire in mouse atherosclerosis defined by single-cell RNA-sequencing and mass cytometry. *Circ. Res.* **122**, 1675–1688 (2018).

149. Park, I. *et al.* C-type lectin receptor CLEC4A2 promotes tissue adaptation of macrophages and protects against atherosclerosis. *Nat. Commun.* **13**, 215 (2022).

150. Gu, W. *et al.* Adventitial Cell Atlas of wt (Wild Type) and ApoE (Apolipoprotein E)-Deficient Mice Defined by Single-Cell RNA Sequencing. *Arterioscler. Thromb. Vasc. Biol.* **39**, 1055–1071 (2019).

151. Vijay, J. *et al.* Single-cell analysis of human adipose tissue identifies depot- and disease-specific cell types. *Nat. Metab.* **2**, 97–109 (2020).

152. Henriques, F. *et al.* Single-Cell RNA Profiling Reveals Adipocyte to Macrophage Signaling Sufficient to Enhance Thermogenesis. *Cell Rep.* **32**, 107998 (2020).

153. Depuydt, M. A. C. *et al.* Microanatomy of the Human Atherosclerotic Plaque by Single-Cell Transcriptomics. *Circ. Res.* **127**, 1437–1455 (2020).

154. Haldar, M. & Murphy, K. M. Origin, development, and homeostasis of tissue-resident macrophages. *Immunol. Rev.* **262**, 25–35 (2014).

155. Liu, C. *et al.* TREM2 regulates obesity-induced insulin resistance via adipose tissue remodeling in mice of high-fat feeding. *J. Transl. Med.* **17**, 300 (2019).

156. Nugent, A. A. *et al.* TREM2 Regulates Microglial Cholesterol Metabolism upon Chronic Phagocytic Challenge. *Neuron* **105**, 837-854.e9 (2020).

157. Xiong, X. *et al.* Landscape of Intercellular Crosstalk in Healthy and NASH Liver Revealed by Single-Cell Secretome Gene Analysis. *Mol. Cell* **75**, 644-660.e5 (2019).

158. Park, M. *et al.* Triggering receptor expressed on myeloid cells 2 (TREM2) promotes adipogenesis and diet-induced obesity. *Diabetes* **64**, 117–127 (2015).

159. Ryzhakov, G., Eames, H. L. & Udalova, I. A. Activation and function of interferon regulatory factor 5. *Journal of Interferon and Cytokine Research* vol. 35 71–78 (2015).

160. Manz, R. A., Thiel, A. & Radbruch, A. Lifetime of plasma cells in the bone marrow [3]. *Nature* **388**, 133–134 (1997).

161. Slifka, M. K., Antia, R., Whitmire, J. K. & Ahmed, R. Humoral immunity due to long-lived plasma cells. *Immunity* **8**, 363–372 (1998).

162. Choi, Y. S., Dieter, J. A., Rothaeusler, K., Luo, Z. & Baumgarth, N. B-1 cells in the bone marrow are a significant source of natural IgM. *Eur. J. Immunol.* **42**, 120–129 (2012).

163. Wu, D. *et al.* Eosinophils sustain adipose alternatively activated macrophages associated with glucose homeostasis. *Science (80-.).* **332**, 243–247 (2011).

164. Ben-Baruch Morgenstern, N. *et al.* Single-cell RNA sequencing of mast cells in eosinophilic esophagitis reveals heterogeneity, local proliferation, and activation that persists in remission. *J. Allergy Clin. Immunol.* **149**, 2062–2077 (2022).

165. Büttner, M., Ostner, J., Müller, C. L., Theis, F. J. & Schubert, B. scCODA is a Bayesian model for compositional single-cell data analysis. *Nat. Commun. 2021 121* **12**, 1–10 (2021).

166. Liu, J., Zhang, X., Cheng, Y. & Cao, X. Dendritic cell migration in inflammation and immunity. *Cell. Mol. Immunol. 2021 1811* **18**, 2461–2471 (2021).

167. Tang-Huau, T. L. *et al.* Human in vivo-generated monocyte-derived dendritic cells and macrophages cross-present antigens through a vacuolar pathway. *Nat. Commun. 2018 91* **9**, 1–12 (2018).

168. McAdam, K. P. W. J. & Sipe, J. D. Murine model for human secondary amyloidosis: Genetic variability of the acute-phase serum protein saa response to endotoxins and casein. *J. Exp. Med.* **144**, 1121–1127 (1976).

169. Fyfe, A. I. *et al.* Association between serum amyloid A proteins and coronary artery disease: Evidence from two distinct arteriosclerotic processes. *Circulation* **96**, 2914–2919 (1997).

170. Johnson, B. D. *et al.* Serum Amyloid A as a Predictor of Coronary Artery Disease and Cardiovascular Outcome in Women: The National Heart, Lung, and Blood Institute-Sponsored Women's Ischemia Syndrome Evaluation (WISE). *Circulation* **109**, 726–732 (2004).

171. Kosuge, M. *et al.* Serum amyloid A is a better predictor of clinical outcomes than C-reactive protein in non-ST-segment elevation acute coronary syndromes. *Circ. J.* **71**, 186–190 (2007).

172. Poitou, C. *et al.* Serum amyloid A: Production by human white adipocyte and regulation by obesity and nutrition. *Diabetologia* **48**, 519–528 (2005).

173. Yang, R. Z. *et al.* Decrease of circulating SAA is correlated with reduction of abdominal SAA secretion during weight loss. *Obesity* **22**, 1085–1090 (2014).

174. Yang, R. Z. *et al.* Acute-phase serum amyloid A: An inflammatory adipokine and potential link between obesity and its metabolic complications. *PLoS Med.* **3**, 0884–0894 (2006).

175. Thompson, J. C. *et al.* Serum amyloid A3 is pro-atherogenic. *Atherosclerosis* **268**, 32–35 (2018).

176. Chait, A. *et al.* Sexually Dimorphic Relationships among Saa3 (Serum Amyloid A3), Inflammation, and Cholesterol Metabolism Modulate Atherosclerosis in Mice. *Arterioscler. Thromb. Vasc. Biol.* **41**, E299–E313 (2021).

177. Den Hartigh, L. J. *et al.* Deletion of serum amyloid A3 improves high fat high sucrose diet-induced adipose tissue inflammation and hyperlipidemia in female mice. *PLoS One* **9**, e108564 (2014).

178. Riley, J. K., Takeda, K., Akira, S. & Schreiber, R. D. Interleukin-10 receptor signaling through the JAK-STAT pathway. Requirement for two distinct receptor-derived signals for anti-inflammatory action. *J. Biol. Chem.* **274**, 16513–16521 (1999).

179. Takeda, K. *et al.* Enhanced Th1 Activity and Development of Chronic Enterocolitis in Mice Devoid of Stat3 in Macrophages and Neutrophils. *Immunity* **10**, 39–49 (1999).

180. Schafer, P. H. *et al.* Phosphodiesterase 4 in inflammatory diseases: Effects of apremilast in psoriatic blood and in dermal myofibroblasts through the PDE4/CD271 complex. *Cell. Signal.* **28**, 753–763 (2016).

181. Gu, W., Sun, L., Wang, J. & Chen, X. The oncogenic role of treacle ribosome biogenesis factor 1 (TCOF1) in human tumors: a pan-cancer analysis. *Aging (Albany. NY).* **14**, 943–960 (2022).

182. Kadl, A. *et al.* Identification of a novel macrophage phenotype that develops in response to atherogenic phospholipids via Nrf2. *Circ. Res.* **107**, 737–746 (2010).

183. Wenzel, P. *et al.* Heme oxygenase-1 suppresses a pro-inflammatory phenotype in monocytes and determines endothelial function and arterial hypertension in mice and humans. *Eur. Heart J.* **36**, 3437–3446 (2015).

184. Patel, J., Douglas, G., Kerr, A. G., Hale, A. B. & Channon, K. M. Effect of irradiation and bone marrow transplantation on angiotensin II-induced aortic inflammation in ApoE knockout mice. *Atherosclerosis* **276**, (2018).

185. Ablamunits, V., Weisberg, S. P., Lemieux, J. E., Combs, T. P. & Klebanov, S. Reduced adiposity in ob/ob mice following total body irradiation and bone marrow transplantation. *Obesity* **15**, 1419–1429 (2007).

186. Schiller, N. K., Kubo, N., Boisvert, W. A. & Curtiss, L. K. Effect of γ-Irradiation and Bone Marrow Transplantation on Atherosclerosis in LDL Receptor-Deficient Mice. *Arterioscler. Thromb. Vasc. Biol.* **21**, 1674–1680 (2001).

187. Poglio, S. *et al.* Adipose tissue sensitivity to radiation exposure. *Am. J. Pathol.* **174**, (2009).

188. Honold, L. & Nahrendorf, M. Resident and Monocyte-Derived Macrophages in Cardiovascular Disease. *Circ. Res.* **122**, 113–127 (2018).

189. Cochain, C. & Zernecke, A. Macrophages in vascular inflammation and atherosclerosis. *Pflugers Arch. Eur. J. Physiol.* **469**, 485–499 (2017).

190. Cochain, C. *et al.* CD8+ T Cells Regulate Monopoiesis and Circulating Ly6Chigh Monocyte Levels in Atherosclerosis in Mice. *Circ. Res.* **117**, 244–253 (2015).

191. D, K. *et al.* CD8+ T cell activation predominate early immune responses to hypercholesterolemia in Apoe⁻(/)⁻ mice. *BMC Immunol.* **11**, (2010).

192. Kiran, S., Kumar, V., Murphy, E. A., Enos, R. T. & Singh, U. P. High Fat Diet-Induced CD8+ T Cells in Adipose Tissue Mediate Macrophages to Sustain Low-Grade Chronic Inflammation. *Front. Immunol.* **12**, (2021).

193. Swirski, F. K. *et al.* Monocyte accumulation in mouse atherogenesis is progressive and proportional to extent of disease. *Proc. Natl. Acad. Sci. U. S. A.* **103**, 10340–10345 (2006).

194. Rajavashisth, T. *et al.* Heterozygous osteopetrotic (op) mutation reduces atherosclerosis in LDL receptor- deficient mice. *J. Clin. Invest.* **101**, 2702 (1998).

195. Lessner, S. M., Prado, H. L., Waller, E. K. & Galis, Z. S. Atherosclerotic lesions grow through recruitment and proliferation of circulating monocytes in a murine model. *Am. J. Pathol.* **160**, 2145–2155 (2002).

196. Lumeng, C. N., DeYoung, S. M., Bodzin, J. L. & Saltiel, A. R. Increased inflammatory properties of adipose tissue macrophages recruited during diet-induced obesity. *Diabetes* **56**, 16–23 (2007).

197. Sanin, D. E. *et al.* A common framework of monocyte-derived macrophage activation. *Sci. Immunol.* **7**, 7482 (2022).

198. Vogel, D. Y. S. *et al.* Macrophages in inflammatory multiple sclerosis lesions have an intermediate activation status. *J. Neuroinflammation* **10**, (2013).

199. Grajchen, E., Hendriks, J. J. A. & Bogie, J. F. J. The physiology of foamy phagocytes in multiple sclerosis. *Acta neuropathologica communications* vol. 6 (2018).

200. Keren-Shaul, H. *et al.* A Unique Microglia Type Associated with Restricting Development of Alzheimer's Disease. *Cell* **169**, 1276-1290.e17 (2017).

201. Remmerie, A. *et al.* Osteopontin Expression Identifies a Subset of Recruited Macrophages Distinct from Kupffer Cells in the Fatty Liver. *Immunity* **53**, 641-657.e14 (2020).

202. Ramachandran, P. *et al.* Resolving the fibrotic niche of human liver cirrhosis at single-cell level. *Nature* **575**, 512–518 (2019).

203. Hou, J. *et al.* TREM2 sustains macrophage-hepatocyte metabolic coordination in nonalcoholic fatty liver disease and sepsis. *J. Clin. Invest.* **131**, (2021).

204. Li, A. C. & Glass, C. K. The macrophage foam cell as a target for therapeutic intervention. *Nature Medicine* vol. 8 (2002).

205. Vedeler, C. A., Nyland, H. & Matre, R. In situ characterization of the foam cells in early human atherosclerotic lesions. *Acta Pathol. Microbiol. Immunol. Scand. - Sect. C Immunol.* **92**, 133–137 (1984).

206. Shapiro, H. *et al.* Adipose tissue foam cells are present in human obesity. *J. Clin. Endocrinol. Metab.* **98**, (2013).

207. Bacarella, N. *et al.* Whole Body Irradiation Induces Diabetes and Adipose Insulin Resistance in Nonhuman Primates. *Int. J. Radiat. Oncol. Biol. Phys.* **106**, (2020).

208. Werner, Y. *et al.* Cxcr4 distinguishes HSC-derived monocytes from microglia and reveals monocyte immune responses to experimental stroke. *Nat. Neurosci.* **23**, 351–362 (2020).

209. Hernandez, G. E. *et al.* Aortic intimal resident macrophages are essential for maintenance of the non-thrombogenic intravascular state. *Nat. Cardiovasc. Res.* **1**, 67 (2022).

210. Chen, Q. & Ruedl, C. Obesity retunes turnover kinetics of tissue-resident macrophages in fat. *J. Leukoc. Biol.* **107**, 773–782 (2020).

211. Paulson, K. E. *et al.* Resident intimal dendritic cells accumulate lipid and contribute to the initiation of atherosclerosis. *Circ. Res.* **106**, 383–390 (2010).

212. Jongstra-Bilen, J. *et al.* Low-grade chronic inflammation in regions of the normal mouse arterial intima predisposed to atherosclerosis. *J. Exp. Med.* **203**, 2073–2083 (2006).

213. Wu, H. *et al.* Functional role of CD11c+ monocytes in atherogenesis associated with hypercholesterolemia. *Circulation* **119**, 2708–2717 (2009).

214. Hilgendorf, I., Swirski, F. K. & Robbins, C. S. Monocyte Fate in Atherosclerosis. *Arterioscler. Thromb. Vasc. Biol.* **35**, 272–279 (2015).

215. Boring, L., Gosling, J., Cleary, M. & Charo, I. F. Decreased lesion formation in CCR2(-/-) mice reveals a role for chemokines in the initiation of atherosclerosis. *Nature* **394**, 894–897 (1998).

216. Dahlman, I. *et al.* A unique role of monocyte chemoattractant protein 1 among chemokines in adipose tissue of obese subjects. *J. Clin. Endocrinol. Metab.* **90**, 5834–5840 (2005).

217. Sartipy, P. & Loskutoff, D. J. Monocyte chemoattractant protein 1 in obesity and insulin resistance. *Proc. Natl. Acad. Sci. U. S. A.* **100**, 7265–7270 (2003).

218. Christiansen, T., Richelsen, B. & Bruun, J. M. Monocyte chemoattractant protein-1 is produced in isolated adipocytes, associated with adiposity and reduced after weight loss in morbid obese subjects. *Int. J. Obes.* **29**, 146–150 (2005).

219. Winkels, H. *et al.* CD4 and CD8 double positive T cell progenitors in mediastinal adipose tissue and the aortic arch differentiate to CD4 T cells. *J. Immunol. Conf. Immunol. Conf.* **204**, (2020).

220. Porsche, C. E., Delproposto, J. B., Geletka, L., O'Rourke, R. & Lumeng, C. N.

Obesity results in adipose tissue T cell exhaustion. *JCI Insight* **6**, (2021).

221. Shirakawa, K. *et al.* Obesity accelerates T cell senescence in murine visceral adipose tissue. *J. Clin. Invest.* **126**, 4626–4639 (2016).
222. Shirakawa, K. *et al.* Negative legacy of obesity. *PLoS One* **12**, e0186303 (2017).
223. Blank, C. U. *et al.* Defining 'T cell exhaustion'. *Nat. Rev. Immunol.* **19**, 665–674 (2019).
224. van der Leun, A. M., Thommen, D. S. & Schumacher, T. N. CD8+ T cell states in human cancer: insights from single-cell analysis. *Nat. Rev. Cancer* **20**, 218–232 (2020).
225. Sade-Feldman, M. *et al.* Defining T Cell States Associated with Response to Checkpoint Immunotherapy in Melanoma. *Cell* **175**, 998-1013.e20 (2018).
226. Ferrante, A. W. The immune cells in adipose tissue. *Diabetes, Obes. Metab.* **15**, 34–38 (2013).
227. Macdougall, C. E. *et al.* Visceral Adipose Tissue Immune Homeostasis Is Regulated by the Crosstalk between Adipocytes and Dendritic Cell Subsets. *Cell Metab.* **27**, 588-601.e4 (2018).
228. Mildner, A. *et al.* Genomic Characterization of Murine Monocytes Reveals C/EBPβ Transcription Factor Dependence of Ly6C− Cells. *Immunity* **46**, 849-862.e7 (2017).
229. Xu, L. *et al.* Foamy monocytes form early and contribute to nascent atherosclerosis in mice with hypercholesterolemia. *Arterioscler. Thromb. Vasc. Biol.* **35**, 1787–1797 (2015).
230. Muir, L. A. *et al.* Rapid adipose tissue expansion triggers unique proliferation and lipid accumulation profiles in adipose tissue macrophages. *J. Leukoc. Biol.* **103**, 615 (2018).
231. Zheng, C. *et al.* Local proliferation initiates macrophage accumulation in adipose tissue during obesity. *Cell Death Dis. 2016 73* **7**, e2167–e2167 (2016).
232. Ahmadian, M. *et al.* Pparγ signaling and metabolism: The good, the bad and the future. *Nat. Med.* **19**, 557–566 (2013).
233. Weng, X., Maxwell-Warburton, S., Hasib, A., Ma, L. & Kang, L. The membrane receptor CD44: novel insights into metabolism. **33**, 318–332 (2022).
234. Fang, L. *et al.* Tumor accomplice: T cell exhaustion induced by chronic inflammation. *Front. Immunol.* **13**, (2022).
235. Cochain, C. *et al.* Programmed cell death-1 deficiency exacerbates T cell activation and atherogenesis despite expansion of regulatory T cells in atherosclerosis-prone mice. *PLoS One* **9**, e93280 (2014).
236. Bu, D. X. *et al.* Impairment of the programmed cell death-1 pathway increases atherosclerotic lesion development and inflammation. *Arterioscler. Thromb. Vasc. Biol.* **31**, 1100–1107 (2011).
237. Lutgens, E. & Seijkens, T. T. P. Cancer patients receiving immune checkpoint inhibitor therapy are at an increased risk for atherosclerotic cardiovascular disease. *J. Immunother. Cancer* **8**, 300 (2020).
238. Wang, Z. *et al.* Paradoxical effects of obesity on T cell function during tumor progression and PD-1 checkpoint blockade. *Nat. Med.* **25**, 141–151 (2019).
239. Huan, T. *et al.* A systems biology framework identifies molecular underpinnings

of coronary heart disease. *Arterioscler. Thromb. Vasc. Biol.* **33**, 1427–1434 (2013).

240. Ramkhelawon, B. *et al.* Netrin-1 promotes adipose tissue macrophage retention and insulin resistance in obesity. *Nat. Med.* **20**, 377–384 (2014).

241. Lumeng, C. N., Bodzin, J. L. & Saltiel, A. R. Obesity induces a phenotypic switch in adipose tissue macrophage polarization. *J. Clin. Invest.* **117**, 175–184 (2007).

242. Poller, W. C., Nahrendorf, M. & Swirski, F. K. Hematopoiesis and cardiovascular disease. *Circulation Research* vol. 126 1061–1085 (2020).

243. Grigoriou, M. *et al.* Transcriptome reprogramming and myeloid skewing in haematopoietic stem and progenitor cells in systemic lupus erythematosus. *Ann. Rheum. Dis.* **79**, 242–253 (2020).

244. Niu, H. *et al.* The function of hematopoietic stem cells is altered by both genetic and inflammatory factors in lupus mice. *Blood* **121**, 1986–1994 (2013).

245. Kokkinopoulos, I. *et al.* Patrolling human SLE haematopoietic progenitors demonstrate enhanced extramedullary colonisation; implications for peripheral tissue injury. *Sci. Reports 2021 111* **11**, 1–14 (2021).

246. Zec, K. *et al.* Macrophages in the synovial lining niche initiate neutrophil recruitment and articular inflammation. *J. Exp. Med.* **220**, (2023).

247. Weiss, M. *et al.* IRF5 controls both acute and chronic inflammation. *Proc. Natl. Acad. Sci. U. S. A.* **112**, 11001–11006 (2015).

248. Yang, L., Feng, D., Bi, X., Stone, R. C. & Barnes, B. J. Monocytes from Irf5−/− Mice Have an Intrinsic Defect in Their Response to Pristane-Induced Lupus . *J. Immunol.* **189**, 3741–3750 (2012).

249. Erbel, C. *et al.* CXCL4-induced plaque macrophages can be specifically identified by co-expression of MMP7+S100A8+ in vitro and in vivo. *Innate Immun.* **21**, 255–265 (2015).

250. Gleissner, C. A. *et al.* CXCL4 downregulates the atheroprotective hemoglobin receptor CD163 in human macrophages. *Circ. Res.* **106**, 203–211 (2010).

251. Gleissner, C. A., Shaked, I., Little, K. M. & Ley, K. CXC chemokine ligand 4 induces a unique transcriptome in monocyte-derived macrophages. *J. Immunol.* **184**, 4810–4818 (2010).

252. Park, I., Kassiteridi, C. & Monaco, C. Functional diversity of macrophages in vascular biology and disease. *Vascul. Pharmacol.* **99**, 13–22 (2017).

253. Llodrá, J. *et al.* Emigration of monocyte-derived cells from atherosclerotic lesions characterizes regressive, but not progressive, plaques. *Proc. Natl. Acad. Sci. U. S. A.* **101**, 11779–11784 (2004).

254. Scott, C. L. *et al.* Bone marrow-derived monocytes give rise to self-renewing and fully differentiated Kupffer cells. *Nat. Commun.* **7**, 1–10 (2016).

255. van de Laar, L. *et al.* Yolk Sac Macrophages, Fetal Liver, and Adult Monocytes Can Colonize an Empty Niche and Develop into Functional Tissue-Resident Macrophages. *Immunity* **44**, 755–768 (2016).

256. Chakarov, S. *et al.* Two distinct interstitial macrophage populations coexist across tissues in specific subtissular niches. **363**, (2019).

257. Waqas, S. F. H. *et al.* Neuropeptide FF increases M2 activation and self-renewal of adipose tissue macrophages. *J. Clin. Invest.* **127**, 2842–2854 (2017).

258. Hassnain Waqas, S. F. *et al.* Adipose tissue macrophages develop from bone

marrow–independent progenitors in Xenopus laevis and mouse . *J. Leukoc. Biol.* **102**, 845–855 (2017).

259. Hu, D., Yin, C., Mohanta, S., Weber, C. & Habenicht, A. Preparation of Single Cell Suspensions from Mouse Aorta. *Bio-Protocol* **6**, (2016).
260. Wolf, F. A., Angerer, P. & Theis, F. J. SCANPY: Large-scale single-cell gene expression data analysis. *Genome Biol.* **19**, 15 (2018).
261. Lopez, R., Regier, J., Cole, M. B., Jordan, M. I. & Yosef, N. Deep generative modeling for single-cell transcriptomics. *Nat. Methods 2018 1512* **15**, 1053–1058 (2018).
262. Wolock, S. L., Lopez, R. & Klein, A. M. Scrublet: Computational Identification of Cell Doublets in Single-Cell Transcriptomic Data. *Cell Syst.* **8**, 281-291.e9 (2019).
263. Bergen, V., Lange, M., Peidli, S., Wolf, F. A. & Theis, F. J. Generalizing RNA velocity to transient cell states through dynamical modeling. *Nat. Biotechnol. 2020 3812* **38**, 1408–1414 (2020).
264. McInnes, L., Healy, J. & Melville, J. UMAP: Uniform Manifold Approximation and Projection for Dimension Reduction. (2018).
265. Traag, V. A., Waltman, L. & van Eck, N. J. From Louvain to Leiden: guaranteeing well-connected communities. *Sci. Reports 2019 91* **9**, 1–12 (2019).
266. Zappia, L. & Oshlack, A. Clustering trees: a visualization for evaluating clusterings at multiple resolutions. *Gigascience* **7**, 1–9 (2018).
267. Aran, D. *et al.* Reference-based analysis of lung single-cell sequencing reveals a transitional profibrotic macrophage. *Nat. Immunol. 2019 202* **20**, 163–172 (2019).
268. Turka, L. A. *et al.* Thymocyte expression of RAG-1 and RAG-2: Termination by T cell receptor cross-linking. *Science (80-.).* **253**, 778–781 (1991).
269. Li, Y. *et al.* Development of double-positive thymocytes at single-cell resolution. *Genome Med.* **13**, 1–18 (2021).
270. Park, J. E. *et al.* A cell atlas of human thymic development defines T cell repertoire formation. *Science (80-.).* **367**, (2020).
271. Mingueneau, M. *et al.* The transcriptional landscape of αβ T cell differentiation. *Nat. Immunol.* **14**, 619–632 (2013).
272. Karimi, M. M. *et al.* The order and logic of CD4 versus CD8 lineage choice and differentiation in mouse thymus. *Nat. Commun.* **12**, 1–14 (2021).
273. Xin, H. *et al.* GMM-Demux: sample demultiplexing, multiplet detection, experiment planning, and novel cell-type verification in single cell sequencing. *Genome Biol.* **21**, 1–35 (2020).
274. McCarthy, D. J., Chen, Y. & Smyth, G. K. Differential expression analysis of multifactor RNA-Seq experiments with respect to biological variation. *Nucleic Acids Res.* **40**, 4288–4297 (2012).
275. Venables, W. N. & Ripley, B. D. *Modern Applied Statistics with S Fourth edition by*. *World* vol. 53 (2002).
276. La Manno, G. *et al.* RNA velocity of single cells. *Nat. 2018 5607719* **560**, 494–498 (2018).
277. Lange, M. *et al.* CellRank for directed single-cell fate mapping. *Nat. Methods* **19**, 159–170 (2022).
278. Street, K. *et al.* Slingshot: Cell lineage and pseudotime inference for single-cell

transcriptomics. *BMC Genomics* **19**, 1–16 (2018).

279. Nowicka, M. *et al.* CyTOF workflow: Differential discovery in high-throughput high-dimensional cytometry datasets. *F1000Research* vol. 6 748 https://bioconductor.org/packages/release/workflows/vignettes/cytofWorkflow/inst/doc/cytofWorkflow.html (2017).

280. Van Gassen, S. *et al.* FlowSOM: Using self-organizing maps for visualization and interpretation of cytometry data. *Cytom. Part A* **87**, 636–645 (2015).

281. Wilkerson, M. D. & Hayes, D. N. ConsensusClusterPlus: A class discovery tool with confidence assessments and item tracking. *Bioinformatics* **26**, 1572–1573 (2010).